Organic Photodiodes and Their Optoelectronic Applications

by

Hyunsoo Kim

A dissertation submitted in partial fulfillment
of the requirements for the degree of
Doctor of Philosophy
(Electrical and Computer Engineering)
in The University of Michigan
2017

Doctoral Committee:

      Professor Jerzy Kanicki, Chair
      Professor L. Jay Guo
      Professor Jinsang Kim
      Professor Jamie D. Philips

To my beautiful wife, and family

ACKNOWLEDGEMENTS

First and foremost, I sincerely thank my research advisor, Prof. Jerzy Kanicki, for his support throughout my Ph.D study in the University of Michigan. Without his guidance, the six year journey was impossible for me and might be tumbled down at the middle of the period. He taught me in such a unique way to think more critically and deeply, broaden the knowledge, and learn how to write. I also appreciated his endless patience, respect to students, and encouragement which helped me to overcome many difficulties and frustrations during the period.

I also gratefully thank my doctoral committee, Prof. L Jay Guo, Prof. Jinsang Kim, and Prof. Jamie D. Phillips for their time and guidance through my doctoral work. My previous advisor, Prof. Guo has expressed constant encouragement and support even after I moved my research group. My fabrication skills and broad experience on nano science were mostly taught by him. Without him, I was not able to reach this stage of life. Prof. Kim has been a role model among Korean graduate student society and I really appreciated his thoughtfulness and consideration to students. Prof. Phillips was not only a good researcher but also the best lecturer to me as I remember I really enjoyed his solar cell class a lot. I also specially express my gratitude to Prof. Ganago who was my GSI instructor throughout the period. He always cared about my research and

health during the semester when I was busy doing both teaching and research work. He was very good friend and supporter during my doctoral journey.

I would like to thank Kanicki group members and friends in the University of Michigan for their help and friendship. First of all, I was lucky to work with talented former and current Kanicki group members : Chumin Zhao, Aunnasha Sengupta, Eric Yu, Mao-Hsun Cheng, Che-lin Huang, Soo Chang Kim, and Prof. Agnieszka Pawlicka. I also need to express my thankfulness to former Guo group members : Jaeyong Lee, Kyu-Tae Lee, Taehee Jang, Sangeon Lee, Taehwa Lee for their friendship and support. I am especially feeling grateful to OCM group members : Kyusang Lee, Jaesang Lee, Byeongseop Song, Jongchan Kim, Joosung Moon, Byungjun Lee, Changyeong Jeong and Prof. Stephen Forrest for their friendship and support on my research.

Most importantly, I have indebted to my parents, my sisters, and my wife for their endless support and unconditional love. I would never have completed my Ph.D without their sacrifice and patience for such a long period. Especially, I would like to express my sincere thankfulness and love to my wife, Jungwon Choi, for her support and endurance in the time of long distance relationship and when I was remotely writing the dissertation at Palo Alto. She continuously encouraged me that I can do this when I was discouraged, and she was always with me whenever I was working on the thesis including weekends and holidays. Finally, I thank to my God who allowed me to finish it.

TABLE OF CONTENTS

LIST OF FIGURES

LIST OF TABLES

LIST OF APPENDICES

ABSTRACT

Recently, organic photodiodes (OPDs) have been acknowledged as a next-generation device for photovoltaic and image sensor applications due to their advantages of large area process, light weight, mechanical flexibility, and excellent photoresponse. This dissertation targets for the development and understanding of high performance organic photodiodes for their medical and industrial applications for the next-generation.

As the first research focus, A dielectric / metal / dielectric (DMD) transparent electrode is proposed for the top-illumination OPDs. The fabricated DMD transparent electrode showed the maximum optical transmittance of 85.7% with sheet resistance of 6.2 Ω/sq. In the second part of the thesis, a development of novel transfer process which enables the dark current suppression for the inverted OPD devices will be discussed. Through the effort, we demonstrated OPD with high D* of 4.82 x 10^{12} cm·Hz$^{1/2}$W^{-1} at reverse bias of 1.5 V with dark current density (J_{dark}) of 7.7 nA/cm^2 and external quantum efficiency (EQE) of 60 %. Additionally in the third part, we investigate a high performance low-bandgap polymer OPD with broadband spectrum. By utilizing the novel transfer process to introduce charge blocking layers, significant suppression of the dark current is achieved while high EQE of the device is preserved. A low J_{dark} of 5 nA/cm^2 at reverse bias of 0.5 V was achieved resulting in the highest D* of 1.5 x 10^{13} cm·Hz$^{1/2}$W^{-1}. To investigate the benefit for the various OPD applications, we developed a novel 3D printing technique to fabricate OPD on hemispherical concave substrate. The techniques allowed the direct patterning of the OPD devices on hemispherical substrates without excessive strain or deformation. Lastly, a simulation of the OPD stacked a-ITZO TFT active pixel sensor (APS) pixel with external transimpedance amplifier (TIA) readout circuit was performed.

Chapter 1.

Introduction

1.1 Motivation

Over the last two decades, organic semiconductors have been extensively studied because of their easy deposition method, large-area process, and fine material tunability [1,2]. Due to the unique properties of the organic semiconductors, the opportunities to develop next-generation electronic devices using organic materials have emerged. Organic semiconductors virtually can be utilized to replace all the kinds of the electronic devices including transistors [3,4], light emitting diodes [5–7], photovoltaics [1,8,9], photodiodes [2,10], antennas [11], and etc as shown in Figure 1.1.
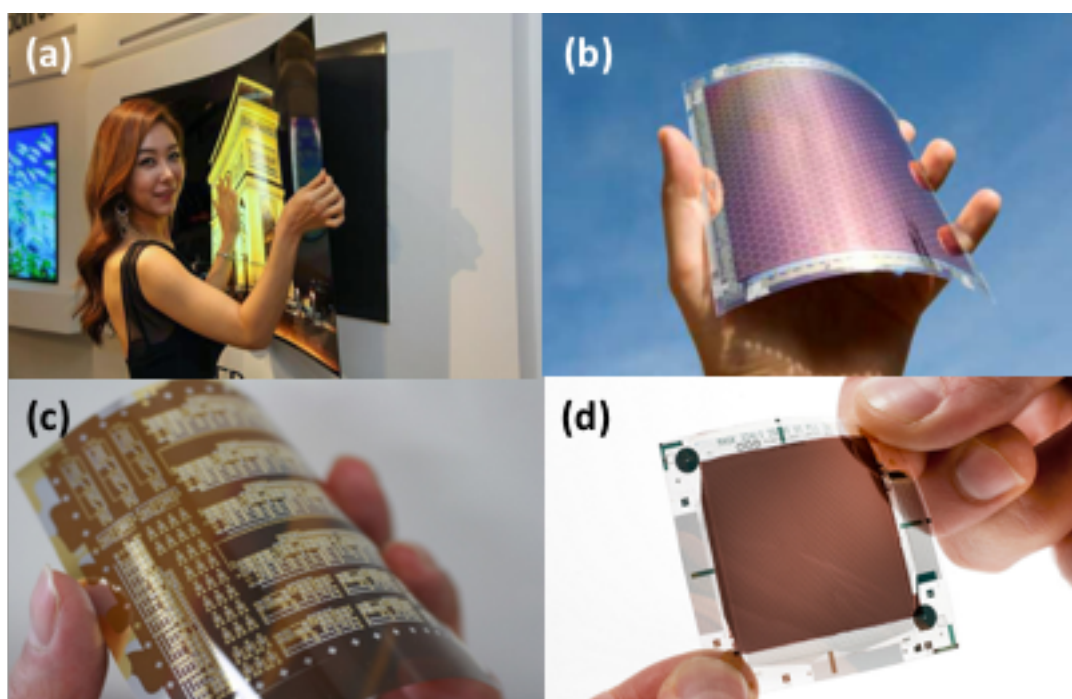
Figure 1.1 Examples of various electronic devices based on organic semiconductors (a) LG paper-like OLED TV [12] (b) ITO-free organic photovoltaic devices [13] (c) organic transistor array on plastic substrate [14] (d) organic photodetector array on flexible substrates [15].

The most successful adaptation of the organic semiconductors to industry so far was organic light emitting diodes (OLEDs) for display and lighting applications. Samsung and LG demonstrated the active matrix OLEDs (AMOLEDs) display technology can be a great successor of the conventional liquid crystal display (LCD) for mobile phone and TV applications, respectively [16,17]. The great expansion of the OLED market these days encouraged further development of the other organic devices for various applications.

In contrast to OLEDs, organic photodiodes (OPDs) utilize the organic semiconductor to absorb incident light and convert it to electric current. Since the inorganic photodiodes such as silicon photodetector technology suffer from its inherent bottleneck for cost reduction or easy fabrication process, organic semiconductor provides a huge potential for mass production of inexpensive photovoltaic cells or large area imager. Furthermore, the ability to fabricate the device on flexible substrates with low temperature provides a freedom to develop new kinds of photodetector using organic semiconductor materials.

The technological advantages on flexibility and large-area processability of the OPD could be particularly desirable when it is utilized in X-ray digital imager application. Since X-ray imager requires the size to be equal or larger than the target object, a facile spin-coating / blade-coating deposition of the organic active layer on the active matrix array can be beneficial in such an application. Moreover, the imager integrated with OPD can be made in flexible or curved form so it can significantly enhance the comfortableness of the patients being examined.

In this context, the main focus of the thesis will be the investigation of various OPD structures for the applications of the X-ray digital imager and next generation imaging devices. The strategies to enhance key features for the high performance OPDs such as low dark current, high quantum efficiency will be mainly emphasized throughout the thesis. In addition, the structural modification to enable the integration of OPD to conformal / arbitrary backplane will be discussed. Before proceed to the next chapter, we begin with a brief review of organic semiconductors and optoelectronic devices for better conceptual understanding for readers.

1.2 Physics of Organic Semiconductors

Organic materials are basically molecular solids bonded by van der Waals interaction between discrete molecules mainly consisted of carbon and hydrogen atoms. They can be largely classified into two categories : small-molecules and polymers. The classification of the organic materials are based on the molecular weights. (e.g. small molecules < ~500, polymers > ~2000). The optical and electronic properties of the organic materials can be easily tailored by chemical synthesis, providing ultimate variations in terms of material properties and combinations.

To transform the generic organic materials into organic semiconductors, the conjugated system of the carbon atoms needs to be employed. The conjugated system is a chain of carbon atoms with alternating single and double or single and triple bonds. The optoelectronic properties of organic semiconductors are mainly attributed to the π-conjugated system along the carbon atoms. In the conjugated systems, the carbon atoms form sp^2 hybridization, where the sp^2 orbitals are arranged in a planar trigonal structure with 120° angles and the p_z orbital is perpendicular to the sp^2 plane as shown in Figure 1.2(a). A σ bond is formed by the orbital overlap of two sp^2 orbitals from two carbon atoms. The remaining electrons in the p_z orbitals overlap and form the π-bond, creating a delocalized electron density. The energy difference between the bonding and anti-bonding π-orbitals is much smaller compared to σ-bond which contributes to semiconducting properties. The energy diagram of the interaction of two sp^2 hybridized carbon atoms is visualized in Figure 1.2(b). The electrons in the π-orbital are delocalized and spread over the entire backbone of the organic semiconductor molecule. The interaction of the p_z orbital of the two carbon atoms in a repeating molecular chain results in splitting the resultant and formation of two energy levels: The Highest Occupied Molecular Orbital (HOMO) and Lowest Unoccupied Molecular Orbital (LUMO). The electronic

properties of the organic material are determined mainly by the π-electrons in HOMO, as they are the most-easily excited into the lowest unfilled π^* orbitals, LUMO. A schematic of the delocalization of the orbitals and bonds is shown in Figure 1.2(c).
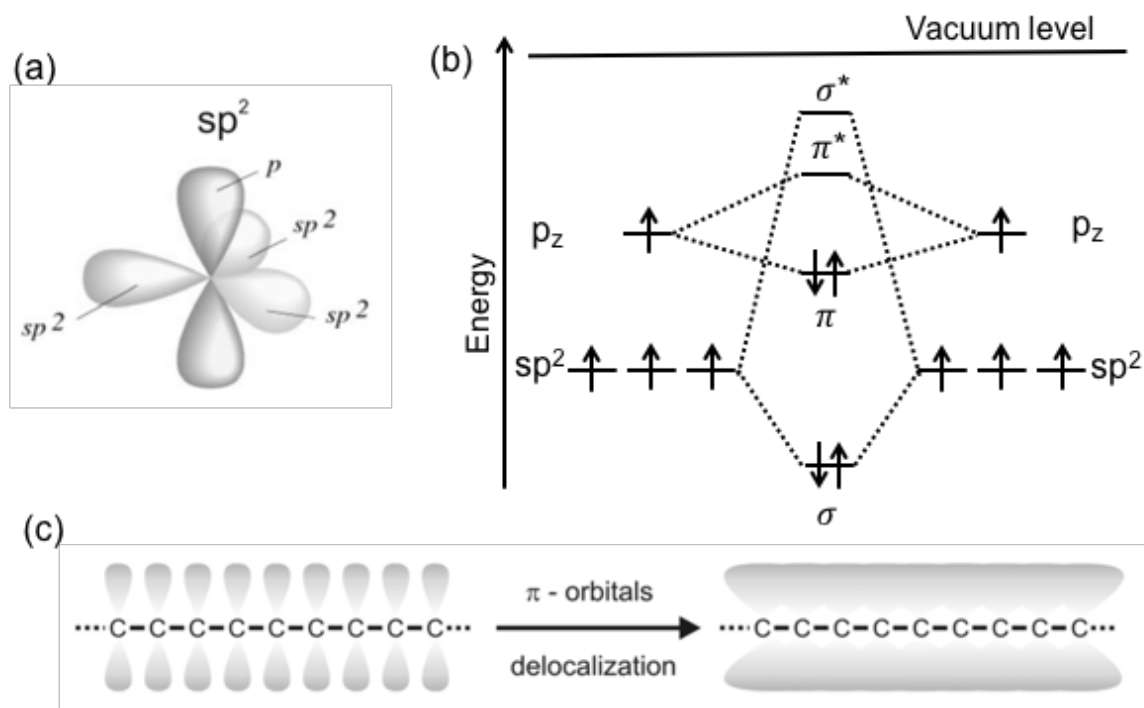
Figure 1.2 Schematic view of the organic molecule structures (a) sp^2 hybridization architecture with the angle between hybrid orbitals of 120° (b) Energy diagram of two sp^2 hybridized carbon atoms with sp^2 and p$_z$ orbital forming a non-bonding orbital, σ and π molecular orbital. The interaction of two carbon atoms (C = C) results in splitting of the p$_z$ orbital into π and π^* molecular orbitals. (reproduced from [18]) (c) Schematic view of the delocalization of the π - molecular orbitals through the carbon backbone.

While the organic semiconductor atoms are strongly bounded by covalent bonds, the organic molecules are rather bounded by van der Waals forces as dipole-dipole or dipole-induce dipole interactions. This weak intermolecular interaction results in short-range molecular arrangement and amorphous phase of the organic semiconductors. This intermolecular interaction of the organic molecules can be described by the empirical Lennard-Jones expression in Equation 1-1 [19],

$$U(r) = U_{att}(r) + U_{rep}(r) = -\frac{A}{r^6} + \frac{B}{r^{12}} \tag{1-1}$$

where $U(r)$ is Lennard-Jones potential, $U_{att}(r)$ is attractive force at long ranges, $U_{rep}(r)$ is repulsive force at shorter ranges due to orbital overlapping, r is the intermolecular distance while A and B are constants. As shown in Equation 1-1, the intermolecular bonds via van der Waals forces between organic molecules are much weaker compared to covalent bonds of inorganic materials case such as silicon. Since the intermolecular interaction in organic molecules is weak, the organic molecules are more independent and isolated compared to covalently bonded inorganic counterparts. Therefore, when an organic molecules are excited by thermal agitation or absorbed photons, it will create a so called exciton rather than a free electron and hole pair [20]. The looser intermolecular interaction between organic molecules leads to hopping process dominated charge transport along the organic solids, resulting in significantly lower charge carrier mobility in the order of 10^{-2} to 10^{-6} cm^2/Vs [21].

An exciton is an electrically neutral quasiparticle which forms a bound state of an electron and a hole attracted by the Coulombic force. Based on its size relative to the intermolecular distance, there are three types of excitons: Frenkel excitons, Wannier- Mott excitons and charge transfer (CT) excitons [21]. Frenkel excitons are tightly bounded electron-hole pair separated by a distance R, smaller than or close to the lattice constant a, that is R ≤ a. As shown in Figure 1.3, the Frenkel exciton is localized at a single site so it has strong Coulombic interaction due to the absence of strong dipoles (Figure 1.3(a)). Because of the weak Coulombic screening, the relative dielectric constant is usually small (e.g. 3~6) [22]. The CT excitons, with an increased delocalization, usually have a radius of two or more lattice constants (Figure 1.3(b)). The Frenkel excitons and CT excitons are seen commonly in organic semiconductors with a typical binding energy of 0.1 eV to 2 eV when the exciton binding energy can be expressed as

$$E_B(r) = \frac{q^2}{4\pi\varepsilon_o\varepsilon_r r} \tag{1-2}$$

where E_B is the binding energy, q is the electric charge, ε_o is the vacuum permittivity, ε_r is the relative dielectric constant and r is the electron-hole separation. As the radius of exciton becomes larger than lattice spacing, R>>a, there is a third type of highly delocalized exciton, named Wannier-Mott exciton, with a much smaller binding energy of a few meV. It is usually observed in inorganic semiconductors (Figure 1.3(c)).
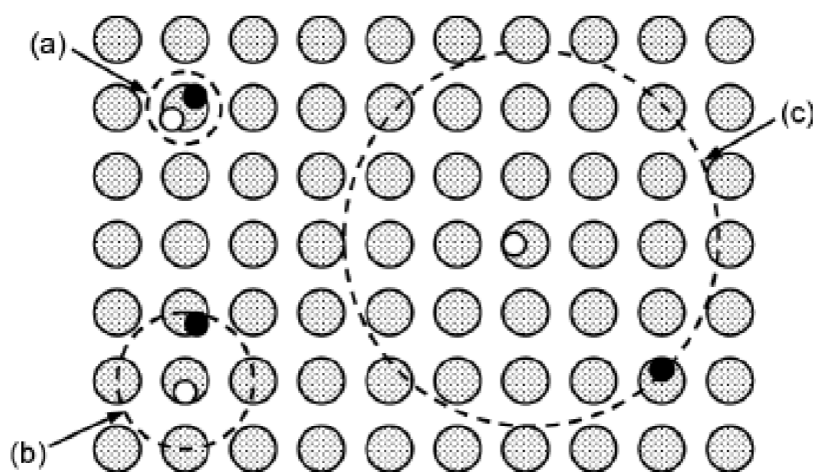
Figure 1.3 Schematic diagram of the various types of excitons in semiconductors and insulators. (a) Frenkel excitons, localized on a single molecule with distance $R \leq a$. (b) charge transfer (CT) excitons, slightly delocalized over two or more molecules. (c) Wannier-Mott excitons, highly delocalized with distance R>> (reproduced from [21]).

Exciton energy transfer (movement) can include energy migration between either same or different molecular species. Exciton migration in an organic solid is essentially a thermally activated hopping process and it can be further divided into one of three mechanisms: Cascade energy transfer, Förster energy transfer and Dexter energy transfer. During the Cascade energy transfer process, the exciton in the donor recombines and emits a photon, which is identical with a photon reabsorption process. Förster energy transfer, so called resonant energy transfer, requires the overlap between emission spectrum of donor and absorption spectrum of acceptor. As seen in Figure 1.4, the donor molecule is initially at an excited state and the acceptor molecule stays at a ground state. Energy transfer occurs from a donor to an acceptor by dipole-

dipole coupling during the transition of the donor to the ground state and the acceptor to the excited state. The Förster transfer rate can be described by [23]

$$K_{D \to A}^{F\ddot{o}rster} \propto -\frac{1}{\tau_D R^6} \int \frac{c^4}{\omega^4 n_0^4} F_D(\omega)\sigma(\omega)d\omega \qquad (1\text{-}3)$$

where τ_D is the donor lifetime, n_0 is the solvent index of refraction, $F_D(\omega)$ is the fluorescence spectrum of the donor, and $\sigma(\omega)$ is the normalized acceptor absorption cross section of the acceptor. The Förster radius depends on the spectral overlap between the donor emission and acceptor absorption. Förster transfer can occur at a distance at $< \sim 100$ Å, which is shorter than the range of the photon reabsorption process, which can exceed 100 Å.
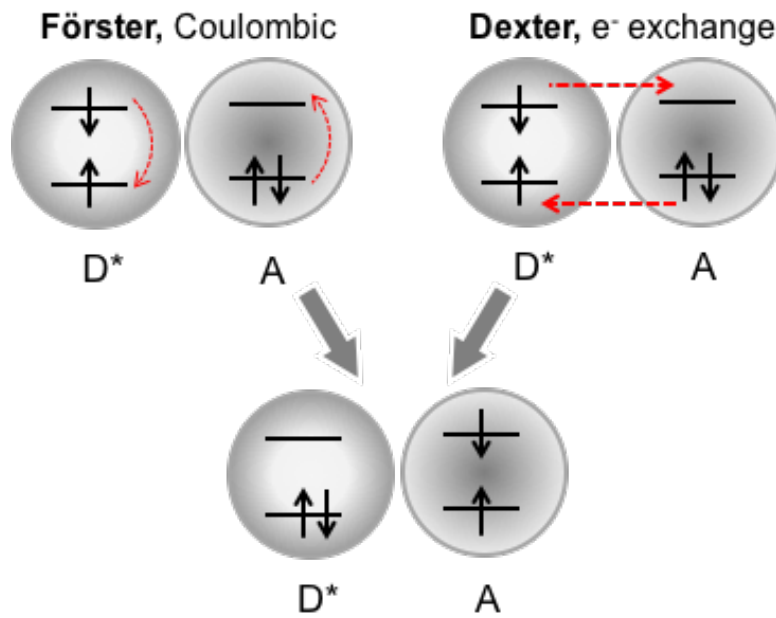
Figure 1.4 Schematic representation of two types of energy transfer between a donor (D) and an acceptor (A) molecule: Förster energy transfer (left) and Dexter energy transfer (right). The symbol * represents the excited state.

A third type of energy transfer, Dexter transfer is the diffusion of the exciton or direct exchange of the charges from donor to acceptor. It requires wavefunction overlap between the donor and the acceptor, therefore it only occurs over a very short distance typically in ~ 20 Å. The Dexter transfer rate is given by:

$$K_{D \to A}^{Dexter} \propto \exp\left(-\frac{2R}{L}\right) \int F_D(\omega)\sigma(\omega)d\omega \qquad (1\text{-}4)$$

where L is the effective Bohr radius. Dexter energy transfer involves the direct transfer of an electron from the LUMO of the donor molecule to the LUMO of the acceptor molecule with the transfer of a hole from the HOMO of the acceptor to the HOMO of the donor. This interaction relies on the overlap of donor and acceptor electron wavefunctions as well as the overlap of emission and absorption spectra.

Because the Frenkel excitons generated in organic semiconductor are tightly bounded and hard to be dissociated, the working principle of the charge generation process in the OPD is significantly different from inorganic counterparts. In general, an effective exciton dissociation can occur at the interfaces between materials which have distinct electron affinities and ionization potentials. The materials with lower electron affinity is so called electron donor while the material with higher electron affinity is called electron acceptor. The physical origin of these charge transfers is attributed to the reduction of the electrochemical energy of the system to result in thermodynamically more favorable states. With an assist of external electrical field or adaptation of heterojunction interface, the exciton can be effectively dissociated into a free electron and a hole. In a heterojunction configuration, there are total four steps for photocurrent generation as shown in Figure 1.5 [24]. In a heterojunction, the energy difference between the HOMO of the donor and LUMO of the acceptor is typically smaller than the E_B of the exciton, providing enough energy for the charge dissociation. Under light absorption, (i) excitons are generated by photon absorption (absorption efficiency, η_A), (ii) excitons diffuse to the electron acceptor-donor interface (diffusion efficiency, η_{Diff}), (iii) the diffused excitons dissociate into electron-hole pairs (charge transfer efficiency, η_{CT}). (iv) Finally, the electrons and holes are collected by cathode and anode (charge collection efficiency, η_{CC}), respectively, generating photocurrent in the OPD. The resulting total external quantum efficiency can be expressed as EQE = $\eta_A \eta_{Diff} \eta_{CT} \eta_{CC}$ [24].
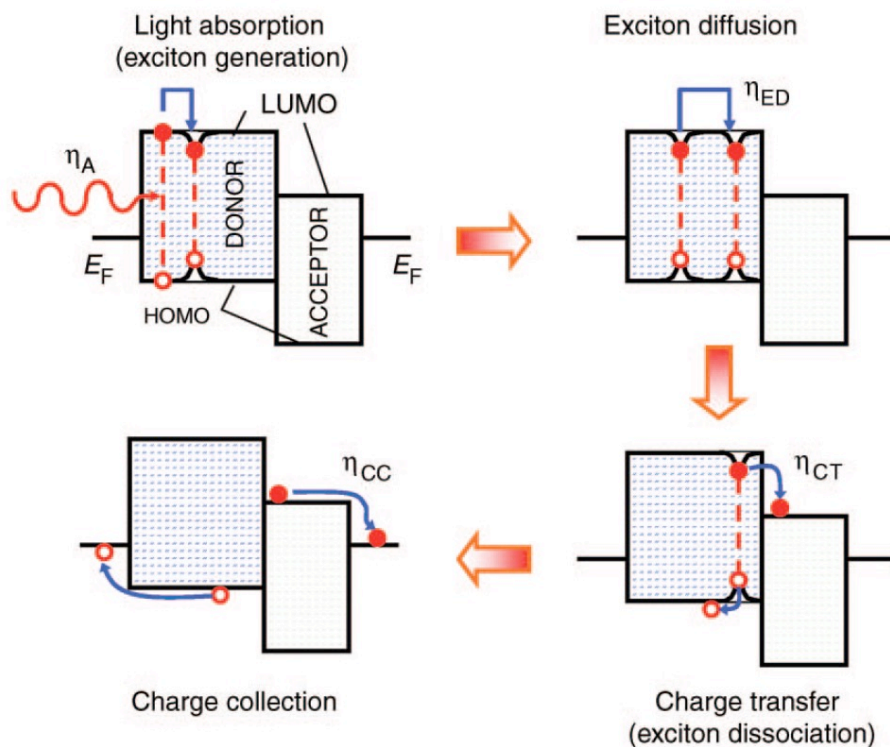
Figure 1.5 Schematic of steps in the photocurrent generation process. The horizontal lines to the left and right indicate the Fermi energies (E_F) of the anode and cathode contacts, respectively. The boxes correspond to the donor and the acceptor energy gaps. Red dots are electrons and red circles are holes. The dashed lines between them represent excitons. The dip in the energy levels in the vicinity of the exciton represents its binding energy ($\sim 0.5 - 1$ eV) (reproduced from [24]).

Last but not least, it is worthwhile to briefly discuss about the photophysics of the organic semiconductors. Not surprisingly, the absorption and emission properties of organic semiconductors are governed by the behavior of excitons. The optical transitions in organic solids are basically dominated by electronic transitions, with additional broadening of the absorption and emission spectra by the vibrational and rotational transitions of the molecules [20]. The weak van der Waals force in the intermolecular structure acts as the high oscillator strength when molecules interact with light. This behavior enables the absorption coefficient of the organic solids in the visible wavelength range reaches above $\sim 10^5$ cm^{-1} which makes a typical absorption length below ~ 100 nm. This provides the opportunity to make ultrathin

organic photodetectors device with high performance. The summary of key properties comparison between organic and inorganic semiconductors is shown in Table 1.1.

Table 1.1 Comparison of organics and inorganics optoelectronic properties [25]

Properties	Organics	Inorganics
Charge Transport	Polaron Hopping	Band Transport
Bonding	van der Waals	Ionic / Covalent
Excitons	Frenkel	Wannier-Mott
Exciton Radius	~ 10 Å	~ 100 Å
Binding Energy	$500 \sim 800$ meV	$10 \sim 100$ meV
Mobility	< 0.1 cm^2/Vs	~ 1000 cm^2/Vs
Absorption coefficient	$10^5 \sim 10^6$ cm^{-1}	$10^4 \sim 10^5$ cm^{-1}

1.3 Deposition Methods of Organic Semiconductors

The organic semiconductor is usually processed in relatively low temperature ($<$ 300 ^{o}C) due to its complex molecular structure and fragile nature caused by the weaker van der Waals bonding network as we mentioned in the previous section. The deposition process of the organic semiconductor materials can be mainly divided into two categories, (i) vacuum thermal evaporation (VTE) and (ii) solution process.

The VTE process is suitable for the deposition of small molecule organic semiconductor materials due to its difficulty to be dissolved in a solvent [26]. The process relies on a thermal sublimation process when the material is heated so it should be executed under high vacuum environment around 1×10^{-6} torr or higher. The high vacuum condition can eliminate possible contamination issue during the deposition process caused by the presence of oxygen, moisture, or other possible contaminants which can react with the organic semiconductor materials during

the deposition process. The pre-purified small molecule organic materials are first placed in a baffled boat (typically based on highly resistive metal e.g. Tungsten or Tantalum) connected to electrodes inside the chamber. The materials are then evaporated by increasing the temperature of the boat with Joule heating by flowing electric current through the boat. The evaporation rate should be kept low (< 3 Å/s) to have a uniform film and prevent the material decomposition due to high temperature above glass transition temperature of the organic material [27]. One of the advantage of VTE process is the precise control of the film thickness and composition ratio. The thickness of the organic materials is monitored by quartz crystal balances in real time during deposition process and can be interrupted in rapid manner by closing shutters, which allows sub-nm control of the film thickness. The schematic of the VTE system is shown in Figure 1.6.
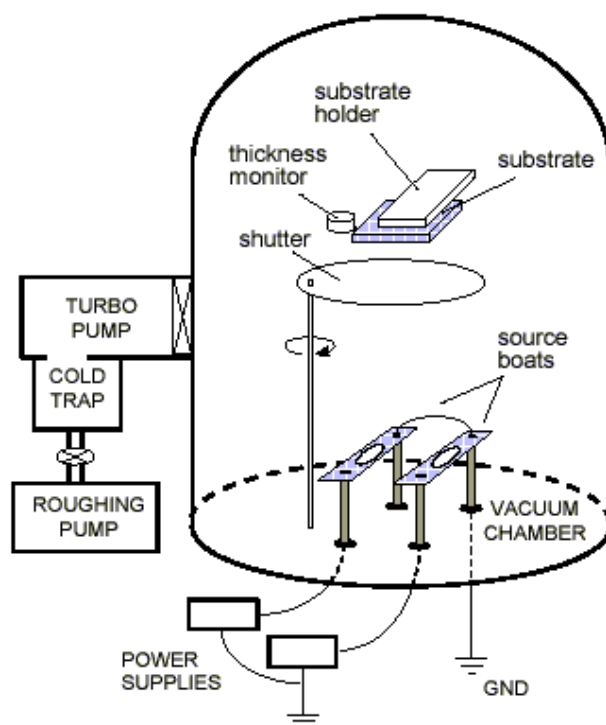
Figure 1.6 Schematic of the vacuum thermal evaporation (VTE) system. In a high vacuum chamber enabled by vacuum pumps, the material is evaporated upwards the substrate located in a rotatable substrate holder. The mechanical shutter precisely control the thickness of the films while oscillating quartz is used for the deposition rate monitoring [28].

On the other hand, the polymer organic materials, different from the small molecule organic materials, a rapid molecular weight reduction of the polymer will take place with increasing temperature leading to material property degradation due to breaking of backbone bonds, breakage of side groups or molecules, etc [29]. In other words, when the temperature of the material increases, polymers usually pass through a glass transition temperature, T_g, before it reaches the sublimation temperature to start the evaporation, severely altering the properties of the original polymer semiconductor materials. Therefore, in contrast to the aforementioned VTE process which is suitable for small molecule organic semiconductor device fabrication, the solution process has its advantage on the deposition of polymer organic materials due to inherent thermodynamic instability of the polymer materials. The following subsections will introduce a few representative solution process techniques of the polymer materials that have been adopted for the organic semiconductor device fabrications.

1.3.1 Spin Coating

Spin coating process is the most universal process with long history which allows to deposit uniform thin films on flat substrate. It is well known process for the photoresist deposition for conventional photolithography process. The spin coating process can be divided into four stages: (i) deposition, (ii) spread, (iii) spin-off and (iv) evaporation (Figure 1.7). A droplet of solution is dispensed on the substrate during the deposition stage. During the spread stage, the solution flows radially outward driven by centrifugal force. In the spin-off stage, excess liquid flows to the perimeter and leaves as droplets. As the film become thinner, the rate of removal of excess solution by spin-off process slows down. This is because the film becomes thinner, the flow resistance got bigger, increasing viscosity since the concentration of the non-volatile components become dense. In the final stage, evaporation takes over as the primary mechanism of film formation.
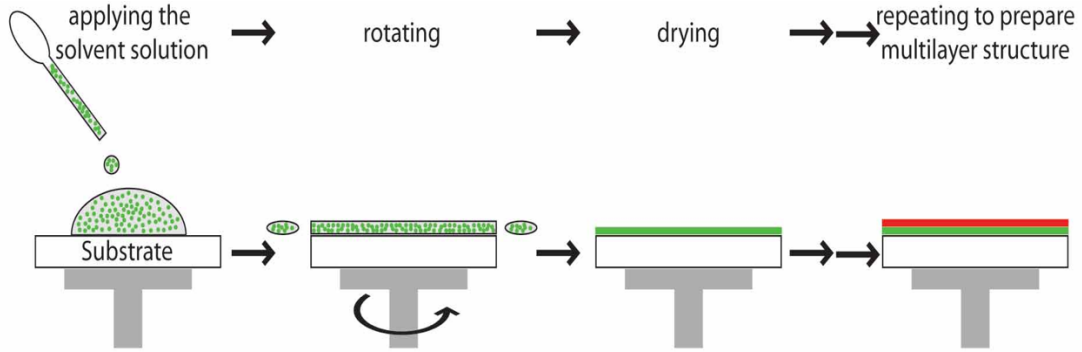
Figure 1.7 Schematic of steps of the spin coating process.

The final film thickness and morphology depend on several parameters such as viscosity, density, surface tension of the solution and etc. The spin-coating condition such as acceleration, rotational speed, time and atmospheric pressure will also affect the properties of the film. Analytically, the thickness of the final film can be anticipated by the following relationship [30],

$$h_f \propto x \left(\frac{\mu}{\rho\omega}\right)^{\frac{1}{2}} \tag{1-5}$$

where h_f is the final film thickness, x is the rate of the solids contacting on the substrate, μ is the viscosity of solution, ρ is the concentration, and ω is the angular speed.

Organic devices based on polymer semiconductor materials will confront a major disadvantage when the stacks of the device become more complex. This is because the organic solution for each layer can dissolve the other layers if solvent with similar properties are chosen for such a sequential coating process. The limitation can be overcome by cross-linking each layer [31,32] or using orthogonal solvents [33,34] for each layer. In addition, during the spin-coating process, most of the solution is wasted and the material utilization ratio is less than 5 % generally. Therefore, the spin coating process is considered to be suitable for academic research purpose but not for the industry level fabrication process.

1.3.2 Blade Coating

The blade coating method is common fabrication standard in various area including organic semiconductor or printing industry. First of all, the substrate will be placed under the blade. The gap between the blade and the substrate can be adjusted using micro-level scalable screw gauges. Next, the polymer solution will be deposited at the bottom of the blade which is then driven over the substrate with a constant drawing speed. Finally, the thinned film formed on the substrate is ready and the rest of the solvent will be evaporated to yield a final film. Contrary to spin coating where the film thickness is inversely proportional to the spin rate, the film thickness during the blade coating will increase with higher blade speed. The film thickness in blade coating is also related to viscosity of the solution, surface tension of the solution, and curvature radius of the downstream meniscus R. The R can be expressed with pressure difference between P_1 and P_2, and the relationship can be expressed as,

$$h = 1.34 \left(\frac{\mu V_{blade}}{\sigma} \right) (P_2 - P_1) \tag{1-6}$$

where μ is the viscosity of solution, V_{blade} is the blade speed, and σ is the surface tension. The schematic of the blade coating process is shown in Figure 1.8.
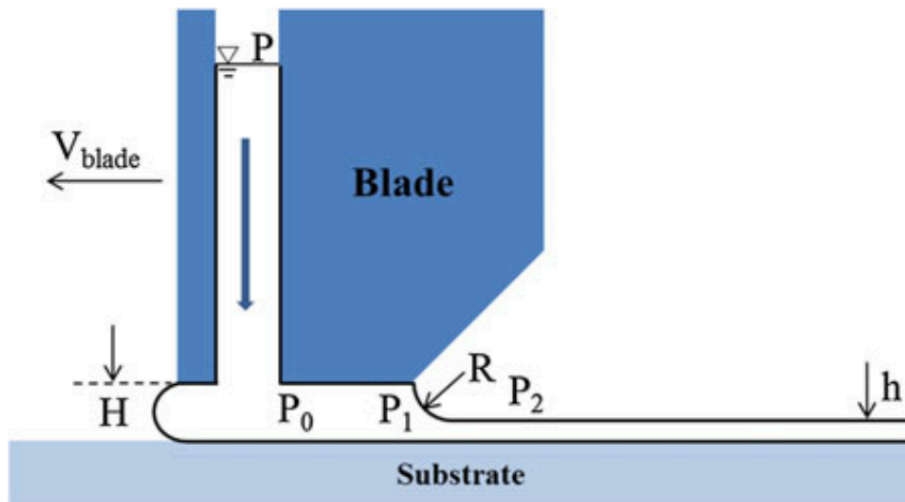
Figure 1.8 Schematic of the blade coating process (adapted from [35]).

Because the blade coating is fast process with controllable solution supply ratio, a large amount of solution will be preserved after the coating which is suitable for the industrial application. One of the disadvantages of the blade coating process is that difficulty on patterning the deposited layer. This drawback is similarly applicable to the aforementioned spin coating process. Moreover, the homogeneity over large areas larger than 1 cm^2 is relatively poor compared to spin-coating process due to different drying speed over the large area.

1.3.3 Inkjet Printing

Compared to the spin coating and blade coating method mentioned above, the ink-jet printing process is an attractive technology for organic electronics due to the controlled solution deposition of patterns and delivery of small quantities of the target materials [36–40]. To facilitate this technology, there are two general types of inkjet printing method ; the first one is continuous and the other one is drop-on-demand (DOD). The biggest difference between those technologies is the frequency of droplets generation.
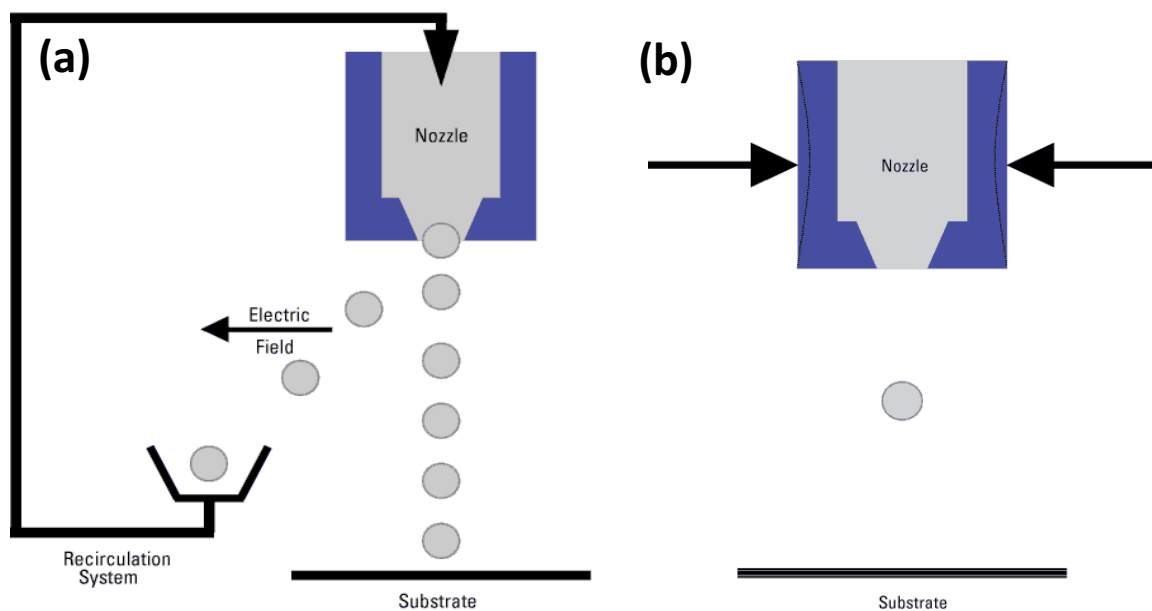
Figure 1.9 Schematic of ink-jet printing method (a) continuous (b) drop-on-demand.

In continuous ink jet printing system, droplets are continuously generated with constant amount of electric charges induced [41]. As shown in Figure 1.9 (a), the charged droplets are ink-jetted from a nozzle continuously toward the substrate. By applying external electric field perpendicularly to the direction of the ink-jetting route, the charged droplets are either landed to the substrate for printing, or they are redirected to a recirculation system. Thus, while the droplets are generated in continuous manner, they can be directed to the substrate only when the patterning is required.

In DOD ink jet printing system, droplets are ejected only when they are needed to be printed. One of the method in this category is thermal inkjet printing, namely, bubble jet printer, which employs thermal energy to generate the ink droplets. Ink drops are ejected from a nozzle by the high pressure due to thermal expansion induced by heat [42]. Alternatively, the droplets can be ejected mechanically through the application of an acoustic pulse or electrically stimulating a piezoelectric force to elicit a deformation of the chamber, which will generate a liquid droplet as shown in Figure 1.9 (b) [38]. One of the advantage of inkjet printing lies on its modularity. Individual printing nozzles can be combined into a single printing head. Multiple printing heads can be combined within a single printer system. This modular nature allows flexibility on printing methods ; printing more than one kind of ink at the same time or printing in large area by laterally combining multiple print heads.

1.4 Organic Photodiodes

1.4.1 Organic Solar Cells

One of the most vigorously studied area for the application of the organic semiconductor is for photovoltaics. The most appealing reason for that is because the organic semiconductor materials can be possibly deposited in low temperature, ambient environment with large area

and cheap price. Since Tang et al, developed the first heterojunction organic solar cell (OSC) device with 1% power conversion efficiency [9], the efficiency increased dramatically up to ~13.2 % with state-of-art tandem cell structures [43]. The most famous material (workhorse) for the OSC research was Poly(3-hexylthiophene-2,5-diyl) : Phenyl-C_{61}-butyric acid methyl ester (P3HT:PCBM) system materials [44]. These days many state-of-art low bandgap polymer OSCs are developed to comprise wider spectrum of illuminated solar radiation [45]. Even though there are more technical barrier for commercialization such as stability, life time issues, OSCs have high potential to be next-generation photovoltaic alternative.

1.4.2 Organic Photodetectors

In contrast to solar cells which is basically aiming to convert solar energy to electrical energy as much as possible, photodetectors need to target for precise detection of lower level of photons. Recently, organic photodetectors (OPDs) have been acknowledged as a next-generation device for image sensor applications due to wide spectrum response [32,46,47], low dark current density [48,49], excellent photoresponse [50,51] and fast response time [10]. Moreover, the low-temperature processability on the large area / arbitrary shaped substrates enables the OPDs to make innovative / next-generation sensors which is impossible using inorganic counterparts.

Most importantly, one of the interesting applications of OPDs is for digital imaging. The flexibility and light-weight capability of the OPDs provides a unique advantage to next-generation applications such as flexible digital x-ray detectors [52], near IR OPD imager [53] or artificial eyes utilizing hemispherical photodetector arrays [54]. For example, Xu et al demonstrated a passive matrix of OPDs on hemispherical focal plane detector array [55]. A plastic substrate is adopted in order to mimic the function of the human eye, where the spherical shape allows focus through a single lens. The integration in a hypothetical imaging system with

11×13 array of $(500 \ \mu m)^2$ detectors are successfully fabricated on a 1 cm radius plastic substrate. Bilayer OPDs based on a copper phthalocyanine (CuPc) electron donor and C_{60} fullerene electron acceptor were deposited between patterned Au anode and thin Ag cathode stripes. To enable the non-conventional shaped OPD structure, they adapted a transfer technique based on elastomeric stamps with cold-welding technique. The fabricated OPDs showed a spectral responsivity of 65 mA/W with specific detectivity of $5 \times 10^{10} \ cmHz^{1/2}/W$. Meanwhile, Ng et al. demonstrated an OPD can be successfully implemented on active-matrix array based on the passive pixel architecture [56]. An organic layer of the poly[2-methoxy-5-(2-ethylhexyloxy)-1,4-phenylene-vinylene] (MEH-PPV) and $PC_{61}BM$ photoactive mixed blend was deposited on top of a flexible amorphous silicon TFT backplane with 180×180 pixels, with a 75 ppi. The transparent top-electrode was formed by spin-coating ITO nano-particles dispersion on top of the photoactive layer. The dark currents lower than 1 nA/cm^2 at reverse bias of 4 V, comparable to standard silicon p-i-n photodiodes, were achieved by a very thick 4 μm blend layer. The external quantum efficiency (EQE) of the integrated detector was 35 %, with Noise Equivalent Power (NEP) of 30 pW/cm^2 with 100 ms integration time.

By tuning the properties of the organic active layer materials, even near infrared (NIR) image using the OPD was successfully demonstrated by Rauch et al. [53]. The ternary blended, nanocrystalline PbS quantum-dot sensitized P3HT:PCBM OPDs integrated with an amorphous silicon TFT backplane showed EQE up to 50% at a reverse bias 8 V. The photoactive film was solution processed with the 256×256 pixels with a 154 μm pitch active matrix backplane and a fill factor of 83.3%. A specific detectivity of $2.3 \times 10^9 \ cmHz^{1/2}/W$ with a 3 dB cutoff frequency of 2.5 kHz.

Besides all the aforementioned excellent works to utilize the OPD to imager applications, our main object in this thesis is to investigate the possibilities to enhance the performance of OPDs further by various approaches such as modification of the device structure or development of the new process.

1.5 Thesis Organization

In Chapter 2, we begin with the discussion on top-illumination OPDs with inverted structure. The development of the high efficient structure of top-illumination OPD is crucial for the vertically stacked OPD image sensor application. A dielectric / metal / dielectric (DMD) structure to replace conventional transparent electrodes such as ITO was discussed by both optical simulation and experimental measurement. Chapter 3 discusses a development of novel transfer process which enables the dark current suppression for the inverted OPD structure with high performance. Accurate analyses of the bilayer and interdiffused heterojunction organic devices are successfully fabricated and discussed by various optoelectrical measurement and modeling methods. In Chapter 4, we report a high performance low-bandgap polymer OPD with broadband spectrum. By utilizing the novel transfer process developed in our lab, significant suppression of the dark current is achieved while high quantum efficiency of the device is preserved by employing charge blocking layers to typical BHJ devices. In Chapter 5, for the first time, we report the fabrication of hemispherical organic photodiode arrays on curved concave glass substrate using three dimensional (3D) printed shadow mask. A novel 3D mask enabled by additive manufacture technologies and a 3D elastomeric stamp are utilized to successfully fabricate the OPD on curved surface. Chapter 6 reported the simulation result of the OPD integrated with active pixel sensor (APS) pixel circuit using metal oxide TFTs and external transimpedance amplifier (TIA) readout circuit. The performances of the proposed system such as current gain or voltage gain are evaluated and compared with exiting previous works. Lastly, the thesis concludes with Chapter 7, which summarized the major contributions and findings of this work. Several recommendations for future research are suggested at the end of the thesis.

Chapter 2.
Inverted Organic Photodetectors with DMD Top Illumination Transparent Anode

2.1. Introduction

Among various organic materials for an indirect type X-ray imager application, P3HT:PCBM bulkheterojunction (BHJ) blend system proved itself as the best candidate [57–61] and few groups successfully demonstrated X-ray imager with the active matrix backplane organic photodiode combination. Ng et al. used 4 μm thick MEHPPV : PCBM BHJ blend layer as photoactive layer in combination with a flexible a-Si TFT backplane to realize an imager array with 35% external quantum efficiency [56]. They used solution processed ITO nanoparticles as top transparent electrodes which had a very high sheet resistance of 1MΩ/sq, resulting in significant current loss during signal readout. Alternatively, Tedde et al. demonstrated a concept of active pixel sensor (APS) imager with three a-Si:H TFTs integrated with the OPD. The utilization of the APS provided on-pixel amplification up to 10 compared to passive pixel sensor (PPS) [57]. They adapted conventional structure of OPDs with top Ca/Al transparent cathode. In case of use of the low-workfunction metals as transparent top electrode, even though the encapsulation post-process can prevent the degradation of the electrode and active layer, the long-term stability of the devices cannot be guaranteed if delicate encapsulation process is not used. In this context, the inverted organic solar cell or photodiode architectures are investigated to enhance the device stability in air by adapting the high workfunction metal such as Au, Ag, or poly(3,4-ethylenedioxythiophene) polystyrene sulfonate (PEDOT:PSS) as top transparent electrodes [62–68]. Although a large number of

works have been reported for inverted type organic solar cells [62–66] or inverted type organic photodetector with bottom illumination [67], still few inverted type organic photodetectors with top illumination geometry have been reported so far. For example, Baierl et al demonstrated the inverted type P3HT:PCBM OPD with PEDOT:PSS as a top electrode [69,70]. However, the PEDOT:PSS suffers from a high acidity, hygroscopic behavior, resulting in inferior stability [71]. Alternatively, ultra-thin metallic films can also be used as a transparent electrode in OPV and OPD application [57,58,72,73]. In such configuration, the reflection from the metal surface is too high and a large portion of incident light can be wasted. To suppress such high reflections, an optically transparent dielectric material can be employed as an anti-reflection layer, leading to the Dielectric / Metal / Dielectric (DMD) multilayer electrode configuration. Although a number of papers on the application of the DMD transparent electrode on organic solar cell have been published [74–78], to our best knowledge, no research on the top anode, top-illumination OPD with the DMD configuration has been reported so far. In this chapter, we demonstrate a top-anode, top-illumination OPD with engineered MoO_3 / Ag / MoO_3 DMD semi-transparent electrode that could be used for large-area imager application. Especially, optical simulation and experimental measurement are conducted to investigate the effect of the DMD semi-transparent electrode on the OPD. Additionally, electrical characteristics including current-voltage properties, quantum efficiency, noise equivalent power, and detectivity of the fabricated OPDs are evaluated.

2.2. Experimental

2.2.1. Device Fabrication

Low-cost soda lime glass substrates (Asahi glass) were cleaned by acetone, isopropyl alcohol, and deionized water by sonication for 5 minutes for each process, and treated by oxygen plasma for 5 minutes subsequently. 100 nm of aluminum layer was thermally

evaporated with shadow mask for patterning bottom cathode. ZnO sol-gel solution was prepared by dissolving 0.5 M of zinc acetate dihydrate ($Zn(CH_3COO)_2 \cdot 2H_2O$, Sigma Aldrich) as a precursor in 2-methoxyethanol (2ME, Sigma Aldrich) solvent. 0.5 M of mono-ethanolamine was added as a stabilizer and the mixture was vigorously stirred at a temperature of 60 °C for 4 hours. The solution was then cooled down and aged for more than 24 hours. The synthesized ZnO solution was spin-coated on top of the patterned cathode layer with spin-coating speed of 2000 rpm for 30 seconds and annealed at 150 °C for 20 minutes, yielding 40 nm thickness of ZnO layer. The substrates were transferred into a glove box with nitrogen atmosphere for deposition of photoactive layer. 25mg of P3HT (Rieke Metals) and 25mg of PCBM (American Dye Source, Purity: >99.5%) were mixed into 1mL of dichlorobenzene (DCB) and stirred by magnetic bar overnight for the BHJ solution. The solution was filtered by 0.45 μm syringe filter and then spin-coated onto the ZnO layer with different spin-coating speed to give an active layer thickness of 200 nm, 320 nm and 450 nm to fabricate OPDs with different active layer thickness. To prevent complete drying of P3HT:PCBM film, the spin-coating timing was adjusted for each process. The active layers were then solvent-assisted annealed [79] for 30 minutes to 1 hour to ensure fully dried films in N_2 atmosphere. The substrates were transferred into thermal evaporator with top-anode shadow mask on it to deposit 5 nm MoO_3, 10 nm silver and 35 nm MoO_3 subsequently to finish the fabrication. All the devices were encapsulated with a thin slide glass sealed by UV curable epoxy resin. The device size was 0.04 cm^2 with square shape.

2.2.2. Device Measurement

Optical transmittance and absorbance spectra of the semitransparent DMD, DM multilayer, and P3HT:PCBM BHJ film were measured using Agilent CARY-5E UV-vis spectrometer. Optical reflectance of the DMD, DM electrode were measured by Filmmetrics

F20 thin-film measurement system. Sheet resistances of the electrodes are measured by 4-point probe method. A solar simulator (Oriel) equipped with Xenon lamp and band pass filter with peak wavelength 546nm (FWHM = 2nm), was used for the current density-voltage (J-V) characteristic measurement under illumination. The irradiance of the illuminated light was measured by Newport power meter. The J-V characteristics of all the organic photodiode under illumination and dark conditions were measured by HP2416A semiconductor measurement system with a probe station in a dark Faraday cage. External Quantum Efficiency (EQE) was measured with a setting of lock-in amplifier (Stanford Research Systems SRS 830), monochromator with a 100W halogen tungsten lamp, light chopper, and UV-enhanced silicon photodetector (Newport UV808) for calibration.

2.2.3. DMD Electrode Optical Simulations

We carried out the optical simulations by using the transfer matrix method to find an optimized DMD electrode structure and calculate an optical absorption in the photoactive region [22,80]. The transfer matrix method is based on boundary conditions for the electric field across isotropic, homogeneous interfaces from one layer to the following medium. Given the field of the initial layer medium, the field at the next medium can be obtained from a matrix calculation. Thus an optical property, such as transmittance, reflectance, and absorption, of an entire OPD structure (i.e., multiple stacks) can be calculated by a matrix multiplication procedure. A spectroscopic ellipsometer (M-2000, J. A. Woollam) was employed to measure dielectric constants of all the layers, all of which were used in the optical simulation. To further explain that high transmittance is due to minimized reflectance of the DMD structure, the admittance loci diagram technique is used, which is widely used to study the thin film coating performance [81]. The admittance diagram is a visual representation of the evolution of surface admittance from the substrate interface to the incident medium interface, which contains all the

information necessary for the calculation of reflectance. The characteristic admittance Y of a material is defined as $Y=H/E$ where H is the magnetic field and E is the electric field. Because there is no direct magnetic effects at optical frequencies, we can get a simple relationship between the characteristic admittance and complex refractive index as $y = (n - ik)$ in free space with unit of 1/377 Siemens [S]. Note that the admittance and the complex refractive index of a material are not physically identical when they become numerically equal in this case.

2.3. Results and Discussion

2.3.1. DMD Electrode Simulation, Characterization and Optimization

The DMD electrode has a great advantage over other transparent top electrode, such as (i) the DMD electrode has anti-reflection MoO_3 dielectric layer on top, which maximizes the transmission of the light of interest, and (ii) the passivation of the top electrode with the additional MoO_3 layer allows direct deposition (e.g. thermal evaporation [82]) of CsI(Tl) scintillator materials, which is beneficial in achieving higher scintillator gain [61].

Figure 2.1 Device structure of the inverted OPD with top illumination. The thickness for each layer indicates the optimized values for the fabricated OPD.
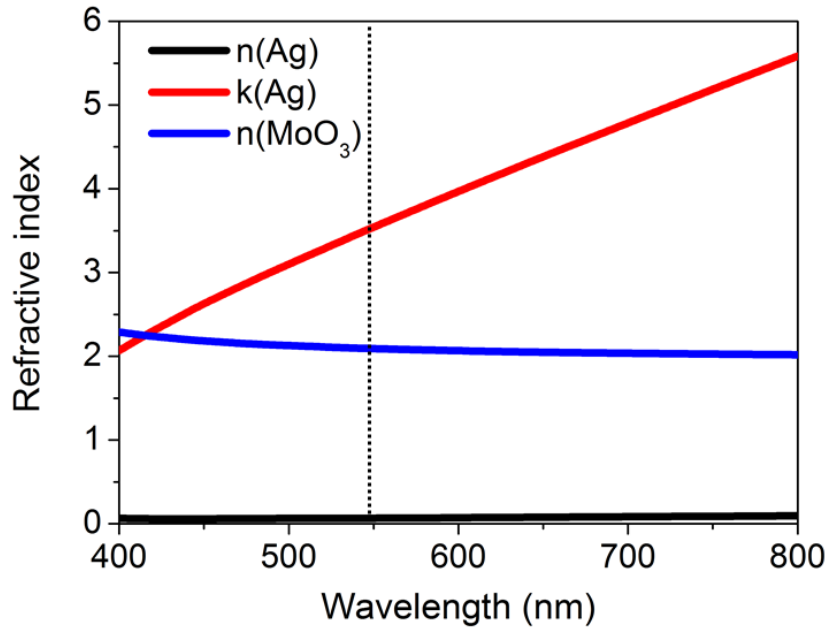
Figure 2.2 Measured refractive indices of Ag and MoO$_3$ plotted from 400 nm to 800 nm wavelength. Extinction coefficient of MoO$_3$ is omitted in the graph due to negligible value.

Table 2.1 A summary of the complex refractive indices of P3HT:PCBM, ZnO, MoO$_3$, Al, and Ag at 546nm wavelength measured by the ellipsometer

Materials	n	k
P3HT:PCBM	2.0918	0.4128
ZnO	1.5361	0
MoO$_3$	2.0941	0.0067
Al	0.9445	6.6304
Ag	0.0672	3.5076

Figure 2.1 shows the schematic of the fabricated inverted-type OPD with top illumination. To find optimum layer thicknesses ensuring that a maximum amount of incident light can pass through the top DMD multilayer transparent electrode, an optical simulation is carried out based on refractive indices of all the layers in the OPD design measured by a spectroscopic ellipsometer. The measured refractive indices of MoO$_3$ and Ag layers over

wavelength from 400 nm to 800 nm are shown in Figure 2.2. The index values of all the layers in the OPD at the wavelength of 546 nm are summarized in Table 2.1.

Prior to determining the optimum thickness of each layer of the DMD electrode, we need to fix the Ag interlayer which ensures both a low sheet resistance and a high optical transmittance. Figure 2.3(a) shows the variation of the sheet resistance of the DMD structure with MoO_3 5 nm / Ag varied / MoO_3 35 nm on glass as a function of the thickness of the Ag interlayer. As shown in the figure, silver thickness higher than 9 nm gives sheet resistance under 10 Ω/sq which is suitable for a large area imager. High sheet resistance of 24 Ω/sq of the DMD layer with 8 nm Ag thickness shown in the figure can be attributed to the discontinuous film morphology with aggregated Ag islands formation [83].

Meanwhile, the significant decrease of the R_{sh} for Ag thickness above 9 nm assures the formation of the continuous metal film. We fixed Ag thickness to 10 nm for the DMD multilayer; the sheet resistance of the DMD film was 6.2 Ω/sq, which is much lower than 10 Ω/sq of standard ITO. Next, to find the optimum thickness of the bottom and top MoO_3 dielectric layer for light transmission, the transfer matrix method approach was applied to the whole OPD structure with varying top and bottom MoO_3 thickness. Figure 2.3(b) shows a simulated contour plot of the light absorption in the P3HT:PCBM active layer of the OPD structure as functions of top and bottom MoO_3 thickness. Fixed thickness of Al = 100 nm, ZnO = 40 nm, P3HT:PCBM = 320 nm, and Ag = 10 nm are used. In this simulation, a monochromatic light at the wavelength 546nm is chosen since it corresponds to an emission peak of the CsI(Tl) scintillator [61]. As can be seen from the figure, the highest absorption in the active layer can be achieved when the top MoO_3 layer thickness is around 35 nm, indicating light absorbance over 90 % by P3HT:PCBM film. Since the bottom MoO_3 layer not only transmits the incident light but also transports the photogenerated charges [75,83], it is required to optimize this thickness for both light transmission and carrier transport. From the simulation

data we can conclude that the maximum absorption is attained with a combination of bottom MoO$_3$ = 70 nm and top MoO$_3$ = 35 nm. However, we need to limit the thickness of the bottom MoO$_3$ layer to 5 nm to ensure the efficient charge transport in the interlayer.
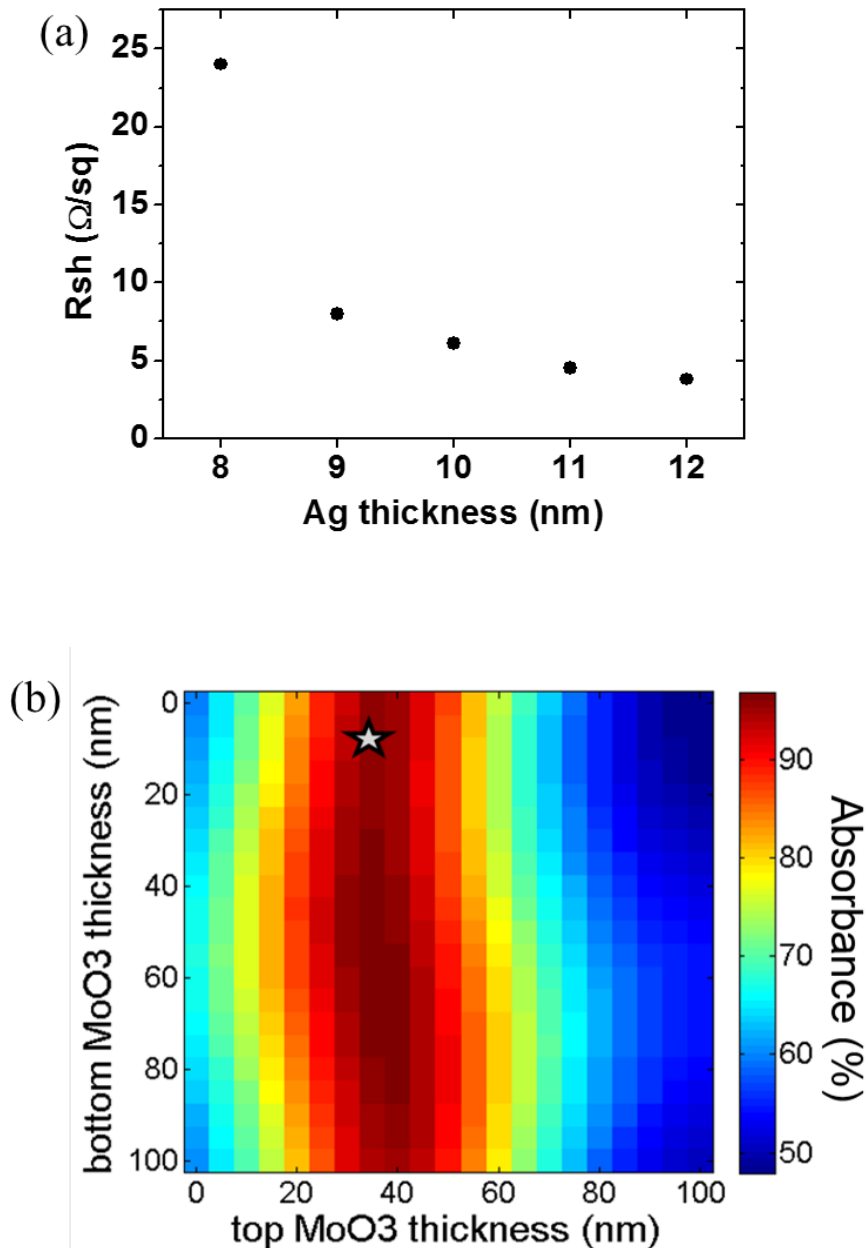
Figure 2.3 (a) Sheet resistance of the MoO$_3$ 5 nm / Ag varied / MoO$_3$ 35 nm structure fabricated on glass as a function of the thickness of the Ag interlayer (b) Simulated 2D absorption spectrum with different bottom and top MoO$_3$ thickness in DMD structure with fixed Ag layer thickness of 10 nm. The color bar represents the absorption in P3HT:PCBM at 546 nm.

Finally, for optimum OPD performance, we decided that the bottom MoO_3 layer should be fixed to 5 nm with 10 nm of Ag interlayer and 35 nm of top MoO_3 layer. The star in Figure 2.3(b) indicates the suggested optimum light absorption point of the OPD structure. This choice is expected to guarantee a high charge transport efficiency and a high absorption of the incident light above 90 % in the active layer at the same time [75,83].
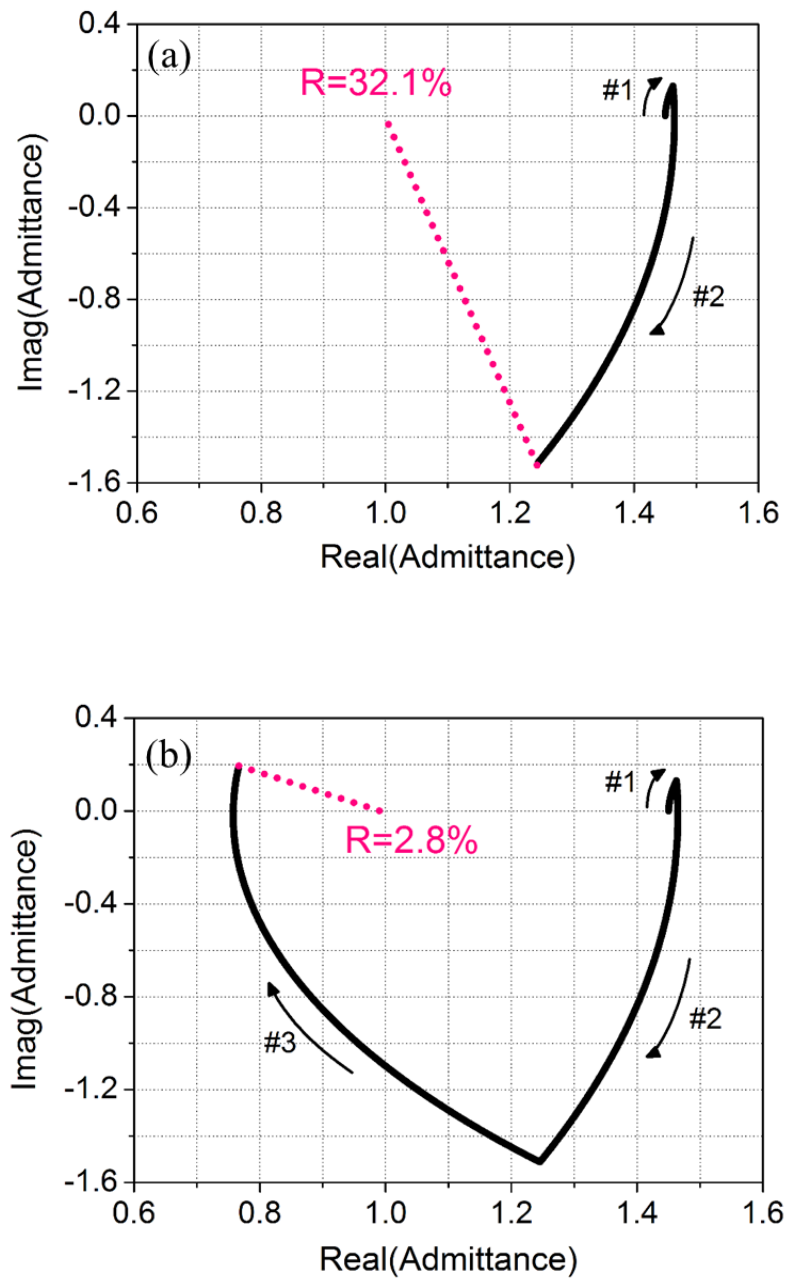
Figure 2.4 Admittance diagrams of (a) MoO_3 (5 nm, #1)/ Ag (10 nm, #2) DM and (b) MoO_3 (5 nm, #1)/ Ag (10 nm, #2)/ MoO_3 (35 nm, #3) DMD multilayers on glass substrates. The arrows indicate the increasing thickness of each layer from the glass substrates.

Additionally, we investigated the influence of the dielectric layer in the DMD electrode on the light reflection properties by studying an optical admittance of the multilayer system [84,85]. The admittance diagram helps to understand more clearly how the variation of each multilayer results in the minimum reflectance of the DMD structure. Figure 2.4 presents the admittance diagrams of the multilayer transparent electrodes of Ag 10 nm / MoO_3 5 nm / glass and MoO_3 35 nm / Ag 10 nm / MoO_3 5 nm / glass substrate at 546nm wavelength, respectively. The loci for perfect electric conductors and optically transparent dielectric materials are represented by a series of circular arcs while the semiconductors result in a spiral locus. As the thickness of each medium increases, the optical admittance of the layer is computed that leads to a rotation of the admittance on either circles or spirals and the corresponding locus is plotted on the complex plane. The starting point of the admittance diagram is (1.45, 0) that corresponds to a glass substrate and the subsequent admittance is determined by both the refractive index and thickness of the material. For example, in Figure 2.4(a), 5 nm of MoO_3 (#1) leads to the admittance rotating from (1.45, 0) toward (1.463, 0.131). After that, 10 nm of Ag (#2) results in the rotation of admittance to (1.245, -1.511). When the termination point of the whole multilayer system ends at (1, 0) that corresponds to air, a perfect impedance matching occurs, thus giving rise to zero reflection. This implies that reducing the difference between the final admittance point and the air enables the transmission efficiency of the DMD electrode to be enhanced by suppressing the light reflections. For the structure without the top MoO_3 film, the termination point is (1.245, -1.511) that is not close to the air, resulting in 32.1 % reflections (R), which can be calculated by the following expression.

$$R = \left(\frac{Y_0 - Y_1}{Y_0 + Y_1}\right)\left(\frac{Y_0 - Y_1}{Y_0 + Y_1}\right)^* \qquad (2\text{-}1)$$

where Y_o and Y_1 are the optical admittance of the incident medium (i.e. air) and the termination point, respectively [85].

In contrast, in Figure 2.4(b), the admittance attained from the multilayer structure with the top MoO_3 layer (#3) ends at (0.766, 0.183), which is much close to the point of the air, thereby leading to highly suppressed reflections of 2.8%. Such highly reduced reflections can also be explained by a small index contrast between air and MoO_3 as compared to the contrast between air and metallic layer.
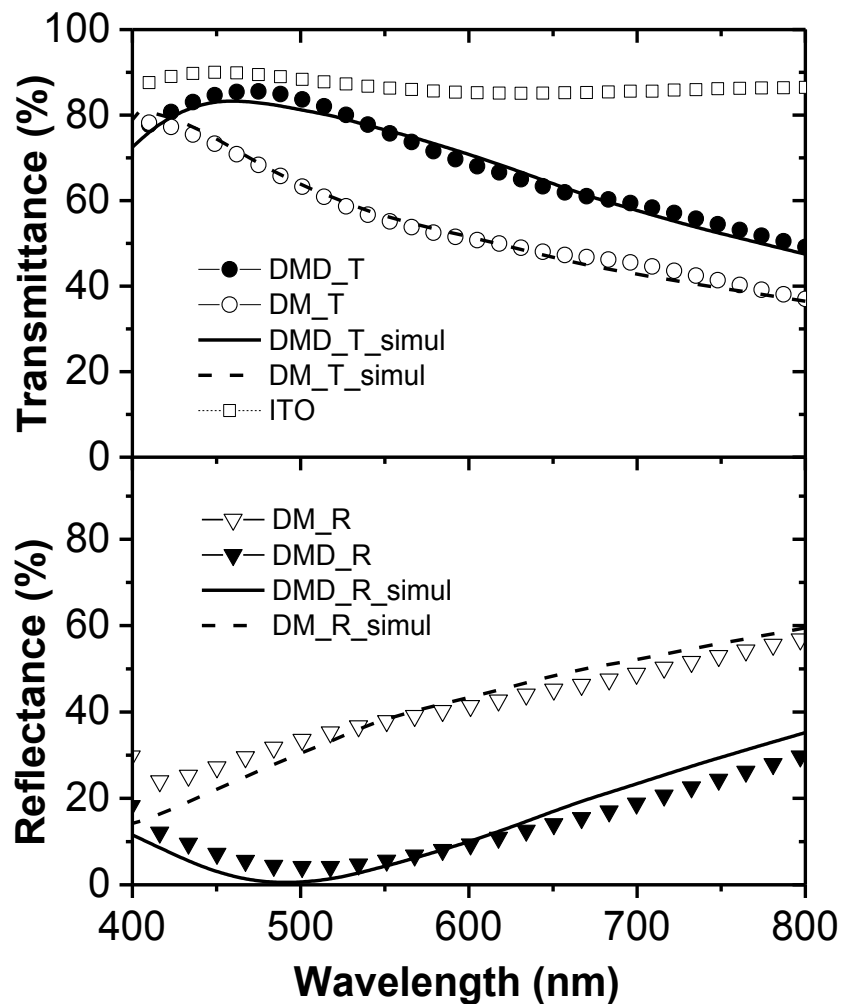
Figure 2.5 Experimental and simulated optical transmittance and reflectance spectra of the optimal DMD (MoO_3 5 nm/ Ag 10 nm/ MoO_3 35 nm) and DM (MoO_3 5 nm/ Ag 10 nm) multilayer. Transmission spectra (top) shows excellent match with experimental spectra (DMD : closed circle, DM : open circle) with simulation plot (DMD : solid line, DM : dashed line). Transmission spectrum of ITO film (open square) is included for comparison. Reflectance spectra (bottom) is shown with experimental spectra (DMD : closed triangle, DM : open triangle) with simulation plot (DMD : solid line, DM : dashed line) in good agreement.

Figure 2.5 shows excellent agreement between simulated data obtained by the transfer matrix method and the experimental optical transmission and reflectance spectra of the both MoO_3 5 nm / Ag 10 nm / MoO_3 35 nm DMD and MoO_3 5nm / Ag 10nm DM electrodes on glass substrates at normal incidence. It is noticed that the maximum light transmittance of 85.7 % is achieved at 468 nm wavelength for the DMD electrode on glass. We also note that the light transmittance of the optimized DMD electrode is comparable with that of a standard ITO glass (Delta technologies, R_{sheet} ~ 11 Ω/sq), as included in Figure 2.5. The transmittance of the DMD electrode at 546 nm wavelength was 76.8 %, which is much higher than that of DM electrode of 56 % at same wavelength. On the other hands, the measured reflectance of the DMD multilayer at 546 nm wavelength was 5.4 % while the DM structure showed 37.6 % of the reflectance value. These measured reflectance values are in excellent agreement with the calculated reflectance values from both the simulated reflectance spectrum in Figure 2.5 and the admittance diagram in Figure 2.4.

2.3.2. Device Physics of the Inverted DMD OPD

The inverted OPD incorporates several functional layers including cathode (Al), electron transfer layer (ETL, ZnO), bulkheterojunction (BHJ, P3HT:PCBM) photoactive layer, hole transfer layer (HTL, bottom MoO_3), anode (Ag), and anti-reflection layer (top MoO_3). Figure 2.6(a) shows flat band diagram of the OPD with corresponding energy levels for each layer. The superpositioned layers in BHJ region with solid line and dashed line represent energy band of P3HT electron donor and PCBM electron acceptor, respectively. Note that the good alignment of the conduction band of the ZnO layer (4.4eV [86]) with the lowest unoccupied molecular orbital (LUMO) level of PCBM (4.3eV [87]) and the conduction band of the MoO_3 layer (5.5eV [88]) with the highest occupied molecular orbital (HOMO) level of P3HT (5.0eV [87]) forms favorable energy level match between buffer layers and BHJ active layer.
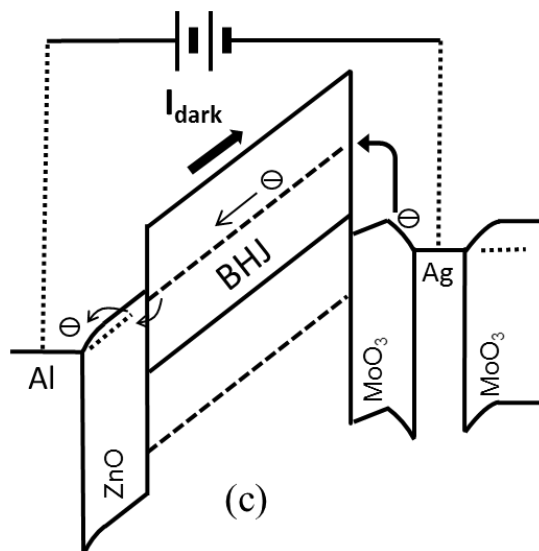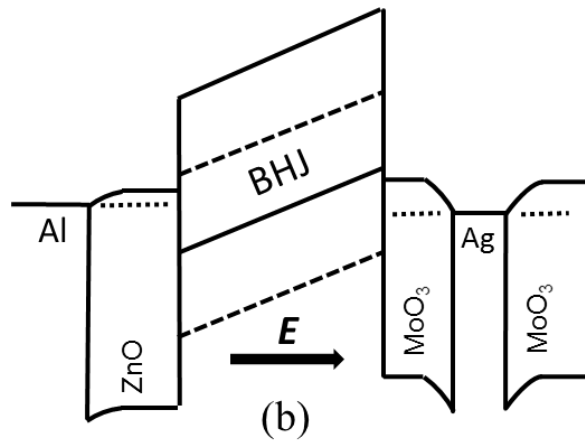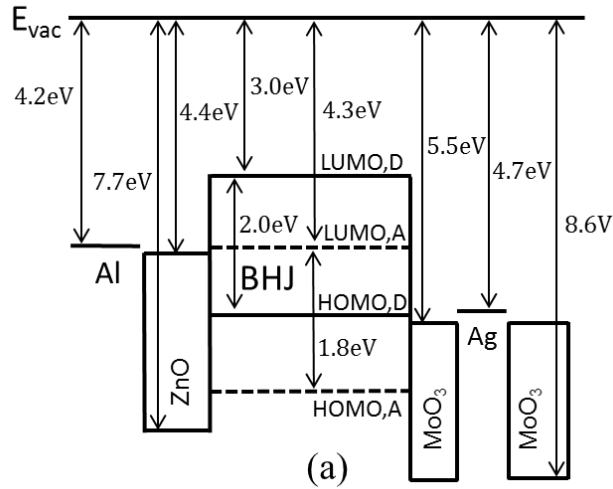
Figure 2.6 (a) Flat band energy diagram of the inverted type P3HT:PCBM OPD under open circuit condition. D indicates the P3HT electron donor while A is PCBM electron acceptor. (b) Schematic band diagram of the inverted type OPD in equilibrium under dark condition. (c) Band diagram of the OPD with reverse bias under dark condition. The arrows show the carrier injection mechanism at each electrode and the direction of dark current.

Under equilibrium condition, we assume that ZnO and MoO_3 layer forms ohmic contact with Al cathode and Ag anode, respectively. The device band bending under equilibrium condition is depicted in Figure 2.6(b). Although both ZnO and MoO_3 buffer layers employed in the OPD structure are n-type semiconductor [68,88], the high work function difference between ZnO (Φ_{ZnO} = 4.7eV [86]) and MoO_3 (Φ_{MoO3} = 5.7eV [88]) makes electrons on ZnO cathode side migrate to MoO_3 anode side, establishing the internal electric field inside the BHJ active layer as shown in the figure. Under light illumination condition, the internal E-field allows photo-generated electrons and holes in the active layer drift to the ZnO cathode and MoO_3 anode, respectively, which is the generation principle of the short circuit current when the OPD works in photovoltaic regime with zero bias.

When the OPD is reverse biased, (positive bias to Al/ZnO cathode and negative bias to MoO_3/Ag) in dark condition, as shown in Figure 2.6(c), the reverse dark saturation current is mainly generated by undesired charge injection through electrodes, which can be minimized by formation of energetic barriers on each electrode by ZnO and MoO_3 layer [89]. To decrease the dark current at cathode side, the ZnO layer is employed as a hole blocking layer (HBL) to increase the injection barrier for holes to BHJ active layer as $\Delta E_{cathode}$ = valence band of ZnO (7.7eV [68]) − Φ_{Al} (4.2eV) = 3.5 eV. On the other hand, the energetic barrier for carrier injection on anode side is ΔE_{anode} = Φ_{MoO3} (5.7eV) - $LUMO_{PCBM}$ (4.3eV) = 1.4 eV, which has lower barrier than cathode side. Due to its lower energetic barrier formed on active layer / MoO_3 interface, the dominant carrier injection will occur at the anode side.

Under light illumination, (i) excitons are generated by photon absorption in P3HT electron donor, and (ii) excitons diffuse to the electron acceptor-donor interface. (iii) The diffused excitons dissociate into electron-hole pairs due to internal electric field. (iv) Finally, the electrons and holes transport by hopping between localized states and collected by cathode and anode, respectively, generating photocurrent in the OPD [90].

2.3.3. Electrical Characteristics of the Inverted DMD OPDs

To validate the suitability of the P3HT:PCBM BHJ layer for the indirect type imager with CsI(Tl) scintillator, absorption coefficient of the fabricated P3HT:PCBM film is compared with the emission spectra of CsI(Tl) scintillator in Figure 2.7(a). The absorption coefficient α was derived from the measured absorption spectrum of the P3HT:PCBM layer with thickness of 200 nm deposited on glass and optical density. The emission spectrum of CsI(Tl) scintillator shown in Figure 2.7(a) is adapted from reference [91]. As shown in the figure, the absorption coefficient of the P3HT:PCBM film overlaps well with the emission spectrum of the CsI(Tl) scintillator.

(b) 950μW/cm² @ 546nm

Jp(200nm)
Jd(200nm)
Jp(320nm)
Jd(320nm)
Jp(450nm)
Jd(450nm)
Jd(200nm)simul
Jd(320nm)simul
Jd(450nm)simul
Jd(320nm)ideal

(c)

200nm
320nm
450nm
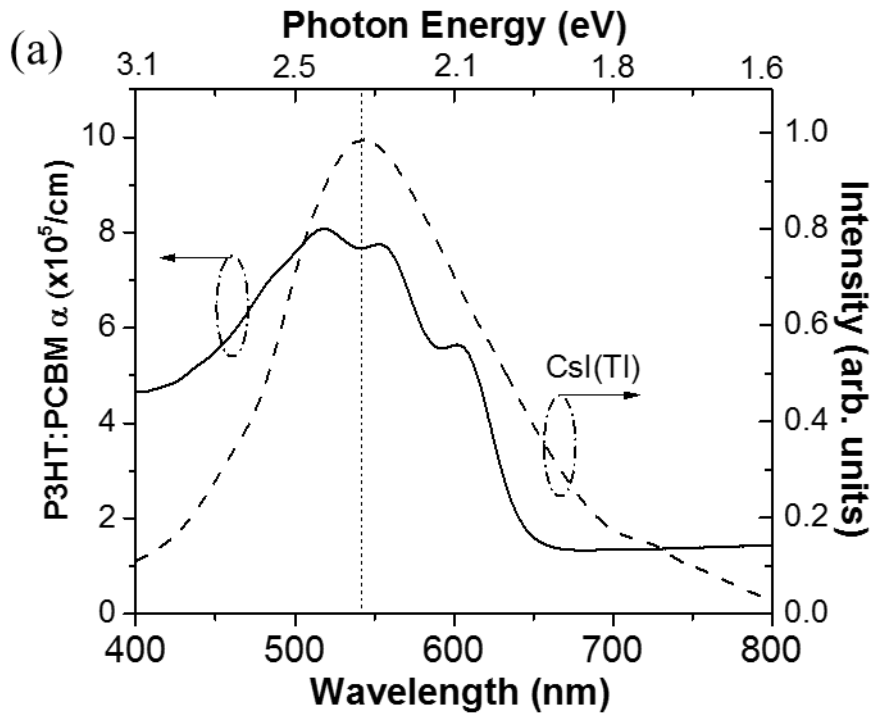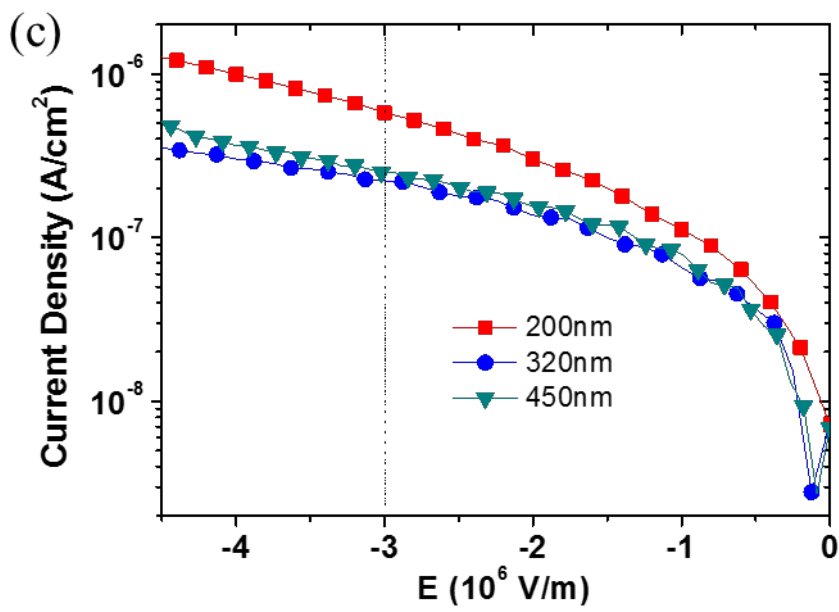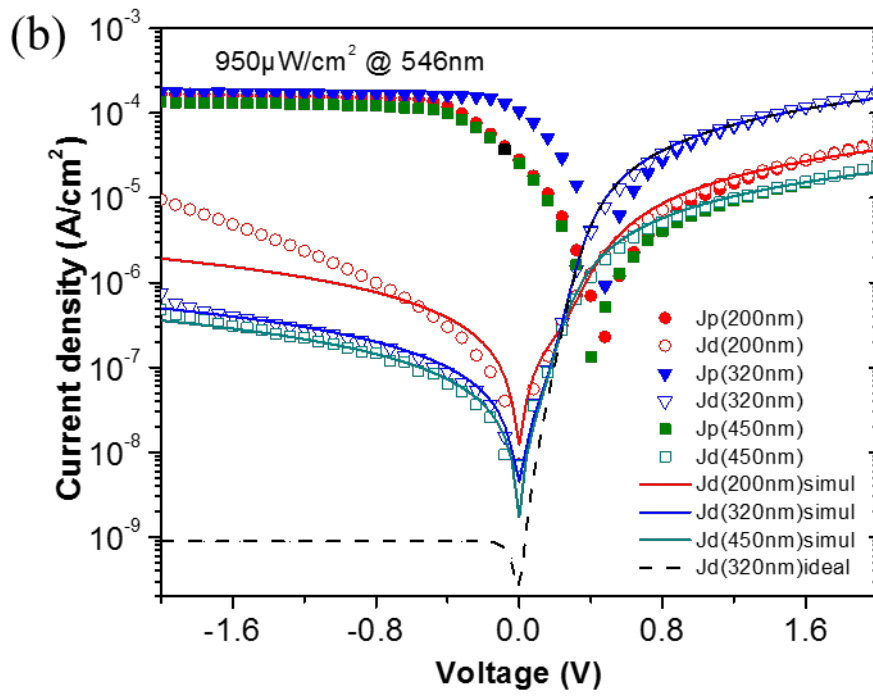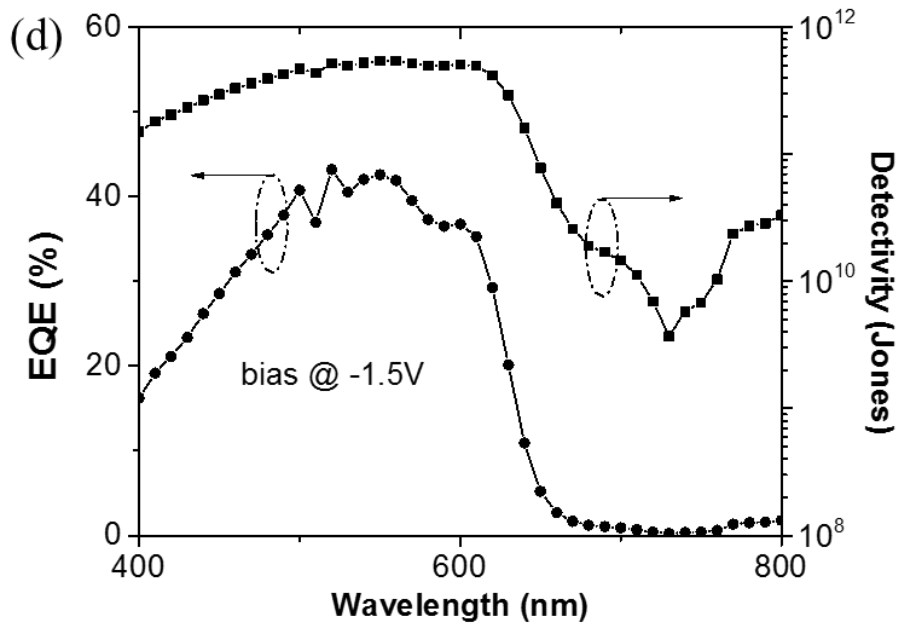
Figure 2.7 (a) The absorption coefficient plot of P3HT:PCBM active layer from wavelength 400 nm to 800 nm. (solid line) Emission spectra of CsI(Tl) scintillator is included for comparison. (dashed line) (b) Experimental and fitted current density (J) versus voltage (V) characteristics under dark condition and irradiance of 950 μW/cm^2 light illumination with 546 nm wavelength of the OPDs with different thickness of the photoactive layer. Open symbols represent measured dark currents when solid symbols are photo responses. The solid lines are fitted dark current densities from non-ideal diode equation. The dashed line represents ideal J-V curve when the shunt resistance R$_{sh}$ is infinite. (c) Dark current density (J$_{dark}$) measurement plot as function of the internal electric field for the OPDs with different active layer thickness. (d) External Quantum Efficiency (EQE) of the OPD with 320 nm thickness active layer at reverse bias of 1.5V. The right axis indicates specific detectivity of the OPD according to wavelength from 400 nm to 800 nm.

To optimize device performance, the inverted OPDs with different thickness of the active layers of 200 nm, 320 nm and 450 nm were fabricated and investigated. Figure 2.7(b) shows the current density (J) versus voltage (V) characteristics of the inverted OPDs with different active layer thicknesses. The figure confirms that the dark current value of the OPDs increases with decreased active layer thickness and increased reverse bias voltage. The trends indicate that the carrier injection occurs from device contact to photoactive layer and the injection mechanism is attributed to electric-field assisted electron injection from the MoO$_3$/Ag contact to the LUMO level of PCBM where the lowest energetic barrier exists [49,89]. To validate the E-field driven injection mechanism, the dark current densities are plotted as a

function of the internal E-field in Figure 2.7(c) with a relationship E = V/d, where E is the internal E-field, V is applied reverse bias and d is thickness of each active layer. In the figure, note that the J_{dark} = 2.22x10^{-7}A/cm^2 of 320 nm active layer device is almost identical with J_{dark} = 2.49x10^{-7}A/cm^2 of 450 nm device at E = 3x10^6 V/m with negligible error. It is worthwhile to emphasize that the J_{dark} of 320 nm device is even smaller than J_{dark} of 450nm device at E=3x10^6 V/m compared to the trend of higher J_{dark} of 320nm device than J_{dark} of 450 nm device in Figure 2.7(b). The bigger variation of J_{dark} of 200 nm device in the figure can be possibly originated from imperfect and unfavorable BHJ morphology with pin-holes developed due to thin active layer [89,92]. However, the data is still acceptable since the J_{dark} of 200 nm device is 5.8x10^{-7}A/cm^2 at E=3x10^6 V/m, which is only about two times bigger than J_{dark} value of 320 nm and 450 nm devices at same E-field, when the J_{dark} value of 200 nm device at 1.5 V reverse bias is >10 times bigger than J_{dark} of 320 nm and 450 nm device at the same bias.

To probe existence of traps inside active layers in each device, the dark J-V characteristics of the OPDs are fitted using the non-ideal diode equation given by [93],

$$J_d(V) = J_O \left[\exp\left(\frac{q(V - J_d(V)R_S)}{nkT} \right) - 1 \right] + \frac{V - J_d(V)R_S}{R_{sh}} \qquad (2\text{-}2)$$

where J_d is total dark current density, J_o is reverse dark saturation current density, n is ideality factor, k is Boltzmann constant, T is temperature, R_S is series resistance, and R_{sh} is shunt resistance. The fitted curves are included in Figure 2.7(b) showing a very good agreement to experimental data. The fitting of Equation 2-2 to the dark J-V characteristics yielded n = 1.95, R_{sh} = 1 MΩ for 200 nm device, n = 1.6, R_{sh} = 4 MΩ for 320 nm device, n = 1.5, R_{sh} = 5.5MΩ for 450 nm device, respectively. The ideality factor deviating from unity is the evidence of deeply trapped carrier or trap-assisted recombination mechanism [94,95]. The larger ideality factor values for thinner active layer devices rationalize that more pin-holes and defects in thinner active films induced more trap-assisted recombination sites inside films. The increasing shunt resistance values from 1 MΩ to 5.5 MΩ with thicker active layer also support the fact

that the current leakage inside the active layer decreases with thicker film. From the fitted parameters and Equation 2-2, we can estimate the theoretical limit of the total dark current density $J_{d,min}$ of fabricated OPD by setting the shunt resistance R_{sh} value to infinite, meaning there is no shunt leakage through the device. The dashed line in Figure 2.7(b) represents the ideal J-V curve of the OPD and the corresponding $J_{d,min}$ value converges to $9x10^{-10}$ A/cm^2, which is identical to the value of reverse dark saturation current density J_o.

For the OPD, the figures of merit which need to be evaluated include external quantum efficiency (EQE), responsivity ($\mathcal{R}$), noise equivalent power (NEP), specific detectivity (D*), and linear dynamic range (LDR). One of the most fundamental properties of the photodetector is the responsivity, which is defined as the photocurrent per unit incident optical power, which gives the equation [96],

$$\mathcal{R} = \frac{i_{ph}}{P_{opt}} = \frac{\eta q \lambda}{hc} = \frac{\eta \lambda [nm]}{1239.89[nmW/A]} \text{ [A/W]} \tag{2-3}$$

where i_{ph} is the output photocurrent of the detector, P_{opt} is the incident optical power on the detector, η is quantum efficiency, q is electron charge, λ is wavelength of interest, h is plank constant, and c is the light velocity. Note that responsivity $\mathcal{R}$ is directly related to external quantum efficiency η by a factor of $q\lambda/hc$, and it can be used to determine the photogenerated current in response to the light wavelength of interest. Noise equivalent power (NEP, in W/Hz$^{1/2}$) is defined as the incident power at a particular wavelength required to produce a photodetector current equal to the root-mean-squate (rms) noise current in a photodetector. In other words, it is the amount of incident light required to make a signal-to-noise ratio (SNR) to unity, and given by [97],

$$NEP = \frac{\sqrt{\langle I_N^2 \rangle / B}}{\mathcal{R}} \tag{2-4}$$

where I_N is the noise current, B is the bandwidth and $\mathcal{R}$ is the responsivity. The noise current is generated from various mechanisms. The representative noise sources are classified as

thermal (Johnson) noise, shot noise, and 1/f (flicker) noise [98]. When we assume that the shot noise current associated to the dark current is dominant over the thermal noise under reverse bias [97], NEP can be expressed as,

$$NEP = \frac{\sqrt{\langle I_N^2 \rangle}}{R} = \frac{\sqrt{2qI_D}}{R} \; [\text{W/Hz}^{1/2}] \tag{2-5}$$

where I_D is the dark current of the photodetector and $2qI_D$ is the shot noise power spectral density. Because the mean square noise of the photodectector is proportional to the detector bandwidth, the NEP of a detector is proportional to the square root of the detector bandwidth, $NEP \propto \sqrt{B}$, and the NEP is generally specified in terms of the NEP for a bandwidth of 1 Hz as $NEP/\sqrt{B}$ which corresponds to Equation 1-8 with unit of $\text{W/Hz}^{1/2}$. From the equation, it is obvious that the lower dark current yields smaller NEP value, while higher responsivity is desirable for lower NEP.

In general, it is more convenient to define the inverse of the NEP as another figure of merit, called detectivity, defined as $D = 1/\text{NEP}$. However, since the detectivity is still dependent on the size of the photodetector, it is beneficial to normalize the detectivity to unit area to accurately compare the performance with other detectors, and it is called specific detectivity D^*, written as

$$D^* = \frac{\sqrt{AB}}{NEP} \tag{2-6}$$

expressed in Jones or $\text{cm}\sqrt{Hz}/\text{W}$, where A is the area of the photodetector. Another important figure of merit of photodiode is linearity of sensitivity of linear dynamic range (LDR). LDR can be defined as [46]

$$LDR = 20\log \left(\frac{J_{ph}^*}{J_d}\right) \; [\text{dB}] \tag{2-7}$$

where J_{ph}^* is the photocurrent density measured at light intensity of 1mW/cm^2 and J_d indicates dark current density.

Table 2.2 summarized the OPDs' figures of merit including J_{dark}, Responsivity ($\mathcal{R}$), External Quantum Efficiency (EQE), Noise Equivalent Power (NEP), and Specific Detectivity (D*). $\mathcal{R}$ and EQE are calculated by Equation 2-3 and NEP and D* are derived from Equation 2-5 and 2-6, respectively. In the table, even though the dark current of OPD with 450 nm active layer thickness showed lowest value of 2.95×10^{-7} A/cm^2 compared to 3.81×10^{-7} A/cm^2 of OPD with 320 nm active layer and 4.25×10^{-6} A/cm^2 of OPD with 200 nm active layer at reverse bias of 1.5V, higher responsivity of 320 nm OPD (0.18 A/W) than 450 nm OPD (0.14 A/W) yielded the highest specific detectivity of 5.25×10^{11} Jones among all the devices. This value is comparable to the value (D* = 8.8×10^{11} Jones) reported by Tedde et al. in their bottom-illuminated spray coated OPDs [99] and even higher than the detectivity value of 3.15×10^{11} Jones reported by Arredondo et al. in their ITO-free inverted P3HT:PCBM photodetectors [100]. Figure 2.7(d) shows the measured EQE of the OPD with 320 nm active layer along with specific detectivity D* plotted according to the wavelength in logarithmic scale. The EQE and D* were measured under reverse bias 1.5V. The peak EQE value of 42.6% at 546 nm wavelength in the figure shows good agreement with the calculated value in Table 2.2.

Table 2.2. Comparison of photodiode figures of merit with different thickness of P3HT:PCBM active layer of 200nm, 320nm and 450nm

P3HT:PCBM thickness	J_{dark} @ -1.5V	Responsivity @ -1.5V	EQE @ -1.5V	NEP (W/Hz$^{1/2}$)	D* (Jones)
200nm	4.25×10^{-6} A/cm^2	0.17 A/W	38 %	1.37×10^{-12}	1.46×10^{11}
320nm	3.81×10^{-7} A/cm^2	0.18 A/W	42 %	3.81×10^{-13}	5.25×10^{11}
450nm	2.95×10^{-7} A/cm^2	0.14 A/W	31 %	4.46×10^{-13}	4.49×10^{11}
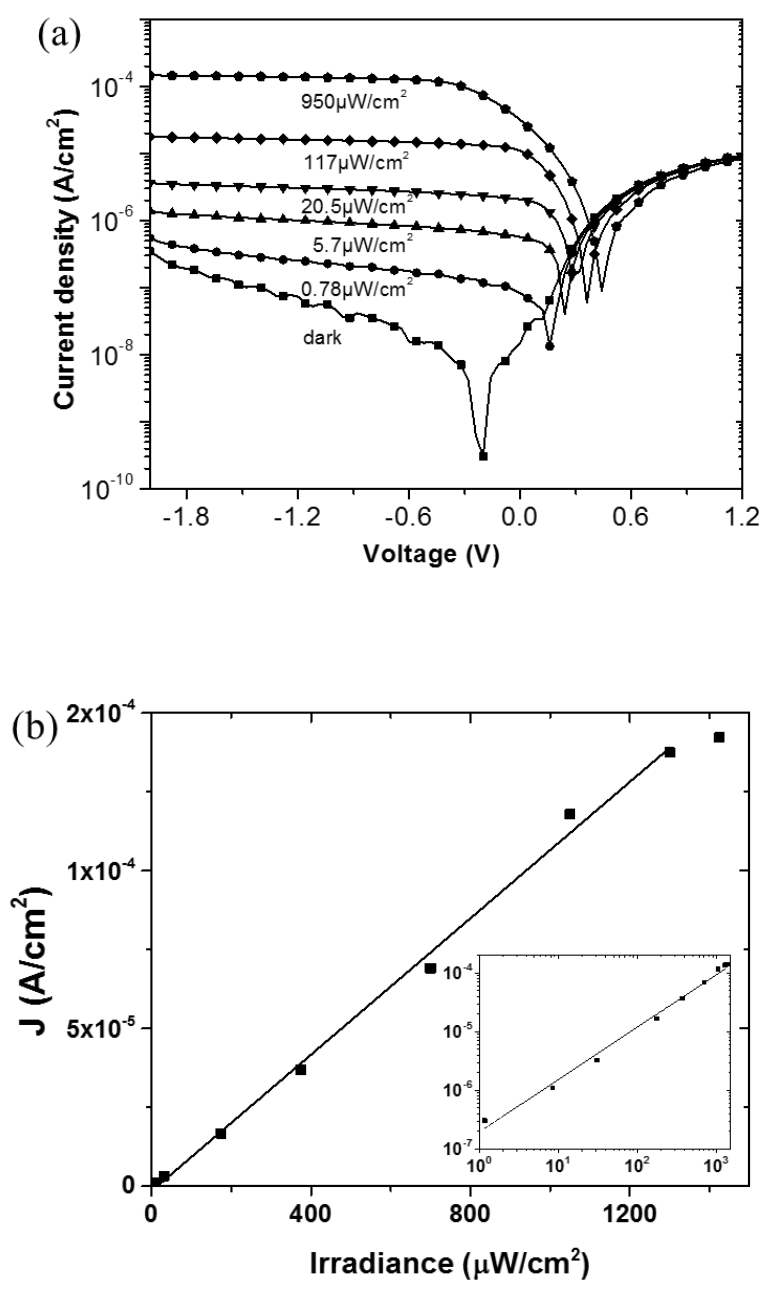
Figure 2.8 (a) J-V curve of the OPD with 320 nm active layer under various light intensity at 546nm light wavelength. (b) Linear dynamic range (LDR) plot of the OPD with 320nm active layer thickness measured at reverse bias of 1.5V. The photocurrent density J is the summation of dark current and photo-generated current, $J = J_{dark} + J_{ph,}$ when the irradiance is 546nm wavelength monochromatic illumination. The inset is the LDR plot in logarithmic scale.

Figue 2.8(a) shows the J-V characteristics of OPD with 320 nm active layer for various

light intensities of the 546 nm wavelength illumination. The graph clearly shows that the OPD

can response to light irradiance from 950 $\mu W/cm^2$ down to 780 nW/cm^2. While the

photocurrent at the negative bias increases with higher light intensity, the photocurrent at positive bias 1 V has no variation, indicating the series resistance R_S of the OPD is not affected by the irradiance. Figure 2.8(b) shows fitted linear dynamic range (LDR) of the photocurrent according to input irradiance in Figure 2.8(a) at reverse bias of 1.5 V. The lower limit of the range was defined by the dark current value of the OPD, which is 3.8×10^{-7} A/cm^2 for the OPD with 320nm active layer. The photocurrent is found to be increased linearly with irradiance of 546nm wavelength up to 1mW/cm^2. The LDR graph can be expressed as a linear equation, J [A/cm^2] = αP_{in} [μW/cm^2] + β with coefficients α = 0.108 [A/W] and β = -1.51×10^{-6} [A/cm^2], where J is the photocurrent and P_{in} is input irradiance. Note that the minimum J value in the equation is limited by the dark current value of the OPD. The calculated LDR of the OPD from Equation 1-5 was 60 dB, comparable to the LDR of InGaAs photodetectors [46], which is sufficient for the high contrast imaging.

2.4. Conclusion

In conclusion, we suggested the inverted OPD with MoO$_3$/Ag/MoO$_3$ semi-transparent electrode with top illumination. The DMD top transparent electrode for the OPD is simulated and optimized to acquire the best light absorption condition for CsI(Tl) scintillator light emission spectrum of 545 nm wavelength. The fabricated DMD transparent electrode showed the maximum optical transmittance of 85.7% with R_{sheet} = 6.2 Ω/sq, which is suitable for large area imager application. Moreover, P3HT:PCBM active layer was optimized for the inverted OPD structure to yield the high detectivity of 5.25×10^{11} Jones. The OPD with inverted structure will enhance the stability of the OPD significantly when the top incoupling MoO$_3$ layer allows direct deposition of scintillator material over OPD. The OPDs with such structure are ready-to-be integrated on various applications especially to cost-effective large area X-ray imager.

Chapter 3
Bilayer Interdiffused Heterojunction Organic Photodiode by Double Transfer Stamping Method

3.1. Introduction

BHJ system has been the preferred choice for the active layer in the OPD structure since it can be introduced as one-step deposition of a polymer : fullerene blend from solution [2,8]. Performance of the BHJ type OPDs typically depends on various process parameter, such as the blending ratio of donor and acceptor materials, the solvents used, thermal annealing conditions, etc [101]. It is known that the choice of the solvent system largely affect the vertical segregation of the donor and acceptor materials, greatly influencing the opto-electronic performance of the BHJ devices [102]. The co-existence (e.g. two materials present at the same time) of the electron donor and acceptor materials on both cathode / anode interface had made difficult on effective suppression of the dark injection current due to ill-defined metal / organic materials interface [2]. The vertical material composition can be controlled somehow by both careful solvent selection [102] and surface energy treatment of the substrate [103,104]. But these approaches cannot completely remove the co-existence problem of the electron donor and acceptor materials at electrodes when BHJ is used. Substantial dark current suppression can be achieved, in principle, by controlling donor / acceptor (D/A) vertical segregation using the double-layered active layer structure [49,105]. However, realization of the polymer / fullerence multilayered structures using solution process needs special techniques due to the difficulty of finding "orthogonal" solvents for each material. Typical polymer and fullerene derivative materials can be easily dissolved in halogenated solvents such as chlorobenzene (CB),

dichlorobenzene (DCB) or dichloromethane (DCM). So far, the most popular method to realize the bilayer heterojunction was successive spin-coating deposition of the electron acceptor material dissolved in DCM on polymer film since the solvent typically has lower solubility with polymer materials [106–109]. However, this method can easily allow partial penetration of the D/A materials to counter-electrodes forming macroscopically undesirable films. Moreover, low solubility of the fullerene derivatives in DCM solvent circumvents the preparation of highly concentrated solution, limiting the range of spin-coatable active layer thickness [107]. Alternatively, float-casting method was introduced but surface of the polymer materials can be easily contaminated and degraded by water molcules and cannot guarantee conformal contact between films [110,111]. The bilayer can also be realized utilizing middle-stage substrate treated with releasing agent, but this method incorporates surface contamination which possibly introduce unfavorable interface traps [112,113]. To minimize the contamination, the lamination process using a polydimethylsiloxane (PDMS) stamp treated by O_2 plasma was introduced by Chen et al which enabled the polymer films casting directly on the PDMS [114]. However, this method not only causes serious damage to the surface structure due to the plasma treatment but also makes difficult to detach the polymer film from the PDMS stamp for transfer process due to increased adhesion energy between the stamp and polymer film. Spray-coating [99] or hot-cast method [60] are also developed as unconventional coating methods. However, these methods are difficult in defining exact layers of each active material, therefore they can not guarantee a well-defined bilayer of the heterojunction.

The key concept used in this chapter is taking advantage of the interdiffusion of the electron acceptor molcules into the electron donor polymer induced by thermal annealing process, verified by Treat et al [115] . They described the evolution of the blend morphology of the P3HT / PCBM BHJ films starting from a bilayer film fabricated by the float-casting technique. They found that PCBM molecular species interdiffuse into the amorphous regions of P3HT during thermal annealing, resulting in a homogeneous BHJ system when the

temperature increased up to 150 °C with an estimated interdiffusion coefficient of 3 x 10^{-10} cm^2/s. Even though they succeeded to elucidate a miscibility and detailed interdiffusion behavior in the polymer: fullerene bilayer system, no fabrication of an actual photodiode was followed using this approach. This was due to serious contamination and degradation of the films during the float-casting method. However their work clearly indicated that if the annealing temperature and time are deliberately controlled, we could achieve an optimized vertically segregated heterojunction active layer.

To address these problems, we introduce double transfer stamping (DTS) to promote interdiffusion between donor and acceptor layers to form well-defined interdiffused bilayer heterojunction (BiHJ) OPDs sandwiched between doner and acceptor layers that are in direct contact with their respective metal electrodes. The thermal annealing step is used to enable interdiffusion between the donor and acceptor layers, forming the active layer. Using this approach, we demonstrate an inverted interdiffused P3HT/PCBM bilayer photodiode whose dark current density is 7.7 ± 0.3 nA/cm^2 with an external quantum efficiency of 60 ± 1 % and a peak specific detectivity of (4.8 ± 0.2) x 10^{12} cm·$Hz^{1/2}W^{-1}$.

3.2. Experimental

3.2.1 PDMS Stamp and Solutions Preparation

The PDMS stamps were prepared by mixing the Sylgard 184 silicone elastomer (Dow Corning) and a curing agent in clean roon (43 % relative humidity, 20 °C temperature) environment [116]. Various ratios of Sylgard : curing agent by mass were prepared to yield a different surface energy of the stamps. The two components were mixed homogenerously for 10 minutes and degassed in vacuum chamber at the pressure of ~ 0.4 psi for six hours before being poured onto plastic weighing boats and cured at room temperature for three days. The PDMS stamps were gently peeled off from the boats and then cut into pieces (~ 1.5 x 1.5 cm^2).

The thickness of the PDMS stamps were typically ~5 mm. The PDMS stamps were attached to backing glass wafers for a conformal transfer process. The polyethylenimine ethoxylated (PEIE) layer was used to form a low workfunction cathode [117]. The PEIE solution was prepared by dissolving 5 wt% of PEIE (Sigma Aldrich) in 2-methoxyethanol (2ME, Sigma Aldrich) solvent in ambient atmosphere. Two kinds of active layer solution were prepared in glove box (O_2, H_2O level < 0.5 ppm) : (1) P3HT solution : 14 mg of P3HT (Rieke Metals, ~91 % regioregularity) was dissolved in 1.5 mL of CB; and (2) PCBM solution : 25 mg of PCBM (American Dye Source, Purity: > 99.5%) was dissolved in 1 mL of CB. All the solution were filtered by 0.45 μm syringe filter and then stirred by magnetic bar overnight at 70 ^{o}C for homogeneous solutions.

3.2.3 Device Fabrication

Figure 3.1 summarizes schematic illustration of the proposed DTS fabrication process of the BiHJ OPD device. Before starting the device fabrication, we need to prepare a receiving glass substrate. The ITO-coated glass substrates (Delta Technologies, LTD) were cleaned by acetone, isoropyl alcohol, and deionized water by sonication for 5 minutes respectively, and subsequently by oxygen plasma for 5 minutes.

Next a low-work function cathode was prepared by spin-coating of PEIE on top of the ITO coated glass [117]. The spin-coating speed of 2000 rpm for 60 seconds and thermal annealing at 100 ^{o}C for 10 minutes in air yielded < 10 nm thick PEIE layer. Then the substrates were transferred into the glove box for deposition of photoactive layers. The PCBM in CB solution was spin-coated for 60 seconds to form ~ 90 nm thick electron acceptor layer on the top of PEIE/ITO substrate. The spin-cast process allowed enough time for CB solvent to vaporize and no further thermal annealing process was added. Next, two PDMS stamps with

different surface energies were prepared by mixing different ratio of Sylgard elastomer and curing agent.
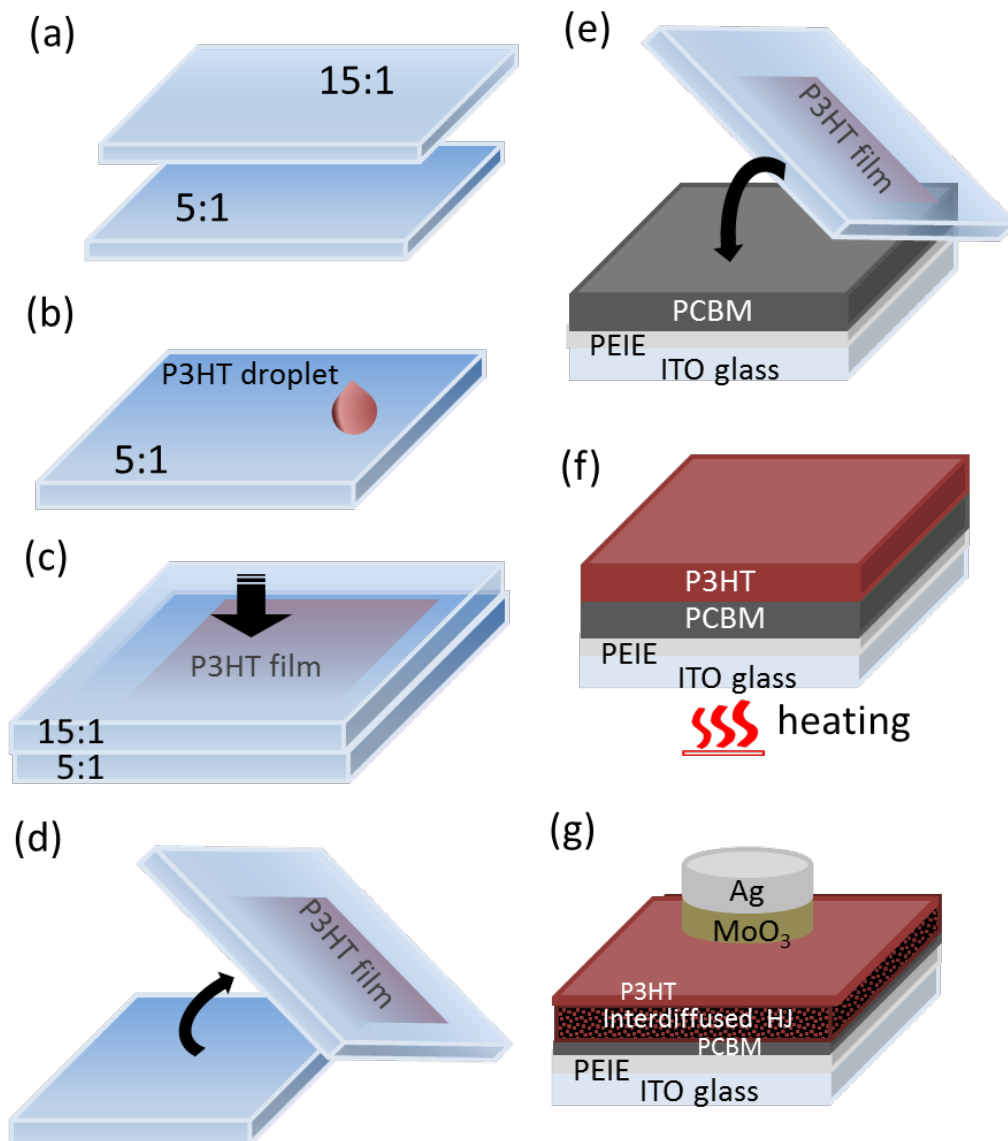
Figure 3.1. Schematic illustration of proposed Double Transfer Stamping (DTS) process for fabricating bilayer heterojunction organic photodiode : (a) Prepare PDMS stamps with different surface energy. (b) Drop-cast P3HT solution droplet on a PDMS stamp with lower surface energy. (c) Squeeze down the solution with higher surface energy PDMS stamp to form a uniform film. (d) Detach PDMS stamp (in this stage, whole film is transferred to 15:1 stamp due to higher surface energy). (e) Transfer the P3HT film from stamp onto prepared substrate. (f) Substrate heating to allow interdiffusion of PCBM into P3HT (g) Completion of the deivce fabrication by depositing MoO_3 / Ag anode. All the processes are done inside glove box to prevent any degradation induced by oxygen and water molecules.

To fabricate the PDMS stamp having suitable surface energy, advancing contact angles were measured by dropping P3HT in CB solution on various PDMS surfaces for the elastomer to curing agent mixing ratios varying from 5:1 to 20:1. The advancing contact angles measured using a goniometer in air are shown in Figure 3.2.
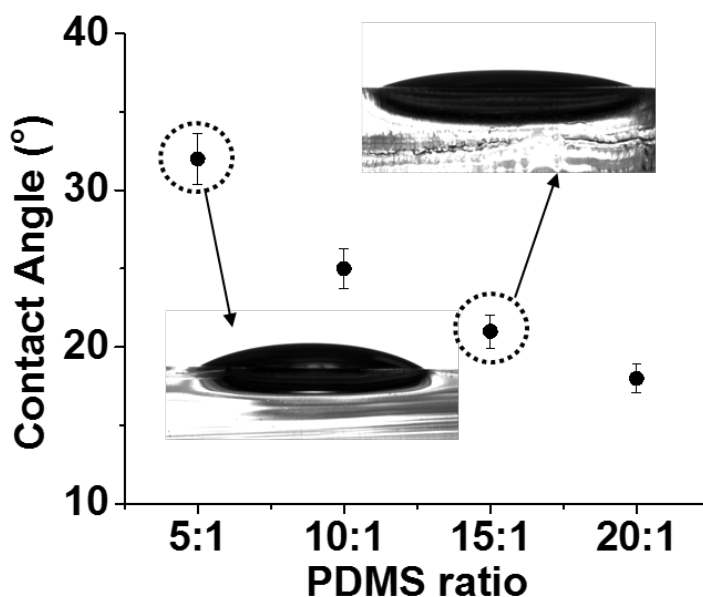
Figure 3.2 Advancing contact angle measurement on PDMS stamps with different mixing ratio of PDMS to Sylgard and curing agent combined. The P3HT dissolved in CB was used for these measurements.

It is clear that the contact angle is decreasing from 33° to 18° when the composition of the elastomer in PDMS stamps increases from 5:1 to 20:1. The decrease of P3HT contact angle indicates formation of a less hydrophobic surface for higher PDMS ratio. The PDMS stamps having less curing agent (cross-linker) have a lower contact angles; e.g. higher PDMS surface energy. However, if the content of the cross-linker is too low, the PDMS modulus of elasticity becomes too small making difficult the fabrication of stamp with required stiffness. Therefore, for the DTS process, we chose PDMS stamps with 15:1 and 5:1 ratios. Next the P3HT solution was drop-casted in the glove box on 5:1 PDMS stamp followed by quick squeeze with 15:1 PDMS stamp to form a uniform polymer film between two stamps having different surface

energies (e.g. adhesion). After few seconds, needed for solvent evaporation into the gas permeable stamp, the 15:1 PDMS stamp was detached. During this process step the whole polymer film is transferred from 5:1 to 15:1 stamp having a higher adhesion energy. The thickness of printed (formed) polymer film measured by surface profilometer was 90 ± 5 nm. Next the polymer film formed on the 15:1 stamp was stamped (printed) onto PCBM/PEIE/ITO substrate to form a P3HT / PCBM bilayer structure. A perfect P3HT film transfer from the 15:1 stamp onto the PCBM surface was accomplished due to much higher adhesion energy between P3HT solution and PCBM surface, verified by the contact angle measurement of P3HT in CB droplet on PCBM surface which showed a complete wetting behavior. Once this transfer is completed the bi-layer is subjected to thermal annealing with temperature ranging from 70 ^{o}C to 150 ^{o}C allowing PCBM molecules to diffuse into the P3HT film [115]. The thermal annealing time for all the devices was adjusted to 5 minutes to realize well defined diffusion region between PCBM and P3HT. The thickness of the P3HT / PCBM bilayer was kept to ~ 190 nm. Finally, the interdiffused devices were transferred into thermal evaporator built in glove box to complete the device fabrication by depositing MoO$_3$ / Ag anode; Circular shadow mask with 1 mm diameter was used to deposit 15 nm MoO$_3$ and 100 nm silver electrode subsequently.

Figure 3.3 shows schematic of device structures of (a) as-cast bilayer OPD before thermal annealing process and (b) BiHJ OPD after thermal annealing process. The interdiffusion of the PCBM into P3HT layer allows formation of well defined layer between PCBM and P3HT layers. By varying annealing temperature and time an optimized interdiffusion layer with well defined morphology can be formed. As shown in the figure, the inverted device structure incorporates several functional layers including low-work function cathode (PEIE/ITO), hole blocking layer (PCBM), BiHJ (interdiffused) active layer, electron blocking layer (P3HT), hole transport layer (HTL, MoO$_3$), and anode (Ag).
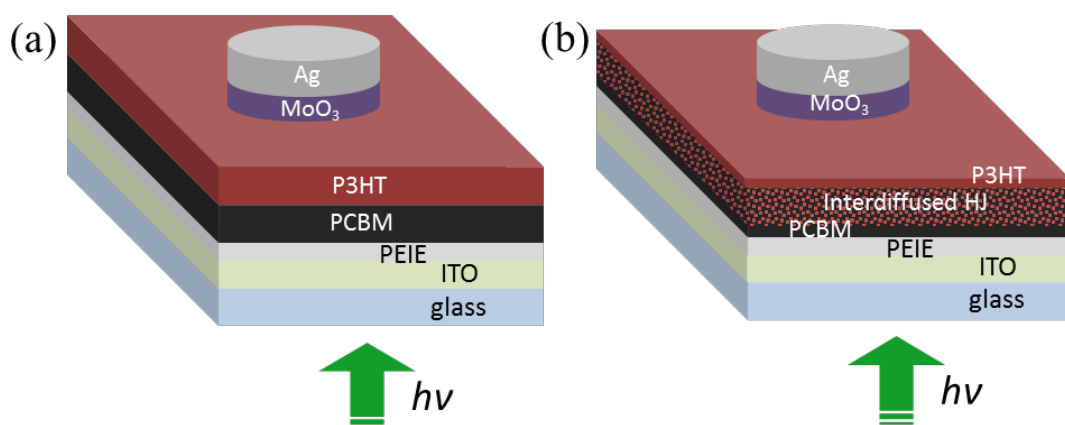
Figure 3.3 Device structure of (a) As-cast bilayer OPD before thermal annealing (b) Bilayer interdiffused heterojunction (BiHJ) OPD after thermal annealing process. Bottom illumination was used for the OPDs.

3.2.4 Measurements and Simulations

A contact angle measurement was done by a contact angle goniometer (Ramé-Hart) in clean room (43 % relative humidity, 20 $^{\circ}$C temperature) . A static sessile drop method was used to measure the advancing angle of the P3HT in CB solution droplet on the PDMS stamps. The calculation of contact angles from the captured data was performed by a built-in software. Optical absorbance spectra of the BiHJ films were measured by Agilent CARY-5E UV-vis spectrometer.
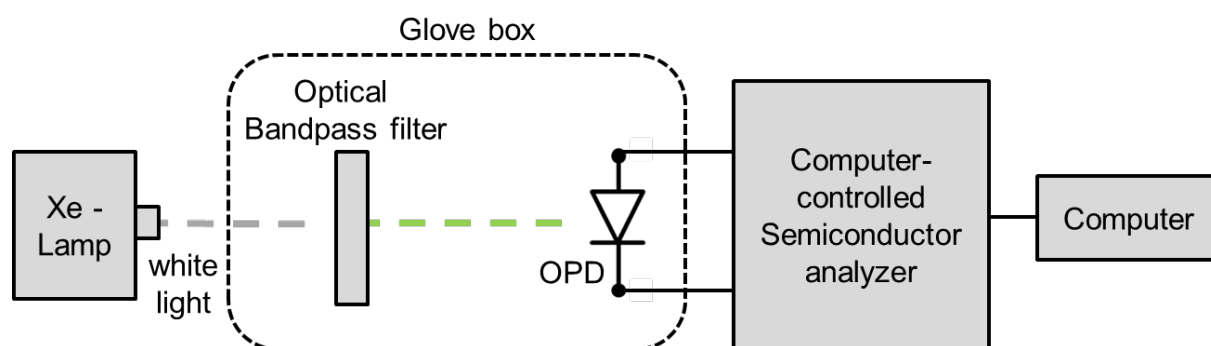
Figure 3.4 Schematic of the J-V measurement setup.

The dark current density – voltage (J-V) characteristics of the OPDs were measured by HP2416A semiconductor measurement system with a probe station in a dark Faraday cage at room temperature in air. For the J-V measurement of the OPDs under illumination, a combination of a solar simulator (Oriel) equipped with Xenon lamp, a band pass filter with peak wavelength at 546nm (FWHM = 10 nm) and 4156C semiconductor parameter analyzer located outside the glove box was used. The experimental scheme is shown in Figure 3.4. The measured devices were located inside the glove box and illumination was done through ITO side. A liquid light guide (Newport, 5mm diameter) and a broadband mirror were used for the device (circular 1mm diameter) bottom illumination. The optical intensity of the illuminated monochromatic light was measured by a radiant power meter (70260, Newport) using the same configuration. For the solar cell J-V characterization, simulated AM 1.5G illumination at 1 sun intensity (100 mW/cm^2) was used.

The schematic of EQE measurement set-up is shown in Figure 3.5. First of all, incident light from a halogen tungsten lamp passing through a monochromator is chopped by a light chopper at 200 Hz outside the glove box and illuminated on the device inside the glove box through the fiber optic cable.
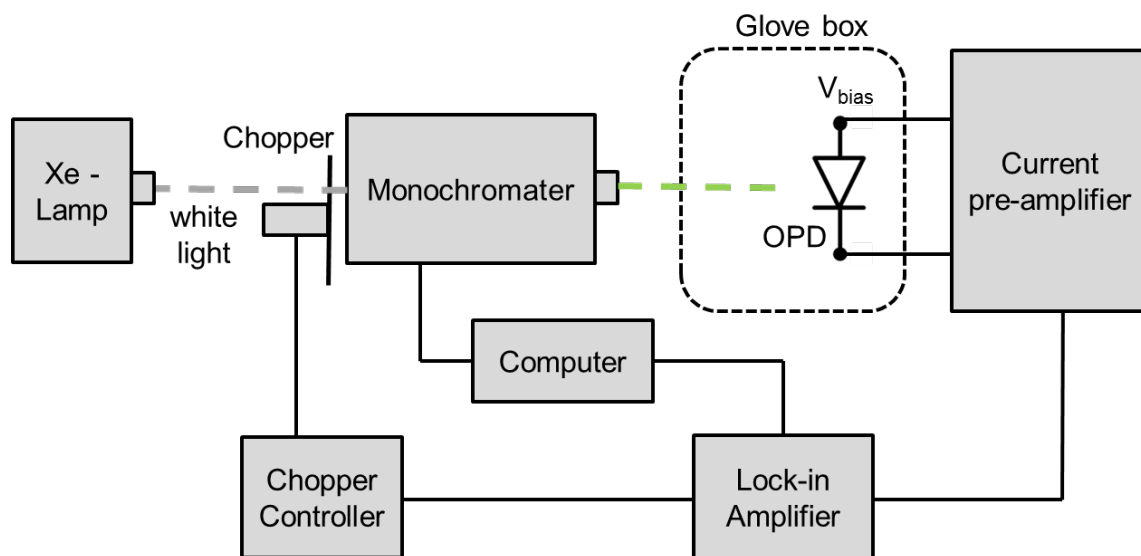
Figure 3.5. Schematic of the EQE measurement setup.

The generated AC photocurrent from the device is converted and amplified to an AC voltage by a current amplifier (KEITHLEY 428) and then detected by a lock-in amplifier (SRS 830, Stanford Research), synced with the light chopper. The current amplifier is able to provide reverse bias directly on the device while the lock-in amplifier exclude a DC signal component (e.g. dark current with bias).

The extracted EQE data can be calculated based on the definition of EQE,

$$EQE = \frac{electrons\ out/sec}{photons\ in/sec} = \frac{current/charge\ of\ one\ electron}{total\ power\ of\ photons/energy\ of\ one\ photon} \qquad (3\text{-}1)$$

Firstly, the photocurrent values [C/s] of the Si photodetector with each wavelength are collected. The responsivity [(C/s)/(J/s)] table provided with the commercial Si photodetector is used to calculate the incident power [J/s] for each wavelength. Meanwhile, the energy of one photon can be derived using the Planck's equation, $E\ [J/photon] = hc\ /\ \lambda$, where h is the planck's constant (6.626 x 10^{-34} J·s) and c is the speed of light in vacuum (3 x 10^8 m/s). Finally we can calculate the number of photons per second [photons/sec] by dividing incident power by E. Next we measure the current value [C/s] of the testing device and divide it by the element charge value, q = 1.6 x 10^{-19} C, yielding the total number of electrons per second [electrons/sec]. Now we can calculate the EQE = [electrons/sec] / [photons/sec].

A UV-enhanced silicon photodetector (UV808, Newport) was used for the light intensity calibration for both photovoltaic J-V and EQE measurement. The temporal response and bandwidth optical measurements were conducted with in-house probe station set-up in ambient atmosphere at room temperature. The green light emitting diode (LED) was used and pulsed by a function generator (HP 8110A). A low-noise current pre-amplifier with bias voltage capability (SR 570, Stanford Research) and an oscilloscope (Agilent MSO7104B) were used for the temporal response and bandwidth measurement. Capacitance – voltage (C-V) measurements were performed in air using HP4284A LCR meter at room temperature in the

dark. The amplitude of the small-signal voltage for the C-V measurement was 25 mV with frequency of 1 kHz.

Transient measurement of the photocurrent is performed in order to characterize the dynamic response of the OPD to pulsed light source. To measure the temporal response, we used a green light-emitting diode (LED) as a light source connected to a function generator (8110A, HP) to generate square light pulses. The output signal was measured by a digital oscilloscope (MSO7104B, Agilent) with 1MΩ input impedance.

The optical simulation of the fabricated OPDs was performed by transfer matrix method to calculate the interference of reflected and trasnmitted light waves at each layer of the device [22,80]. The complex refractive index ($\underline{n}$ = n + ik) of each material is acquired by a spectroscopic ellipsometer (M-2000, J. A. Woollam) with a B-spline fitting function and used in the simulation. The electric field distribution and absorbed optical power distribution is calculated by following the model of Petterson [80] with normal incidence condition.

3.3 Results and Discussion

3.3.1. Device Band Diagram

Figure 3.6 shows schematic band diagram to illustrate how the bilayer interdiffusion can effectively suppress the dark current injection under reverse bias condition. Detailed energy level values for different layers can be found in Chapter 2.3.2. Although other approaches were proposed to suppress the dark current injection such as addition of the hole blocking layer (HBL) (e.g. ZnO) [118,119] or electron blocking layer (EBL) (e.g. Poly[N , N ′ -bis(4-butylphenyl)- N , N ′ -bis(phenyl)-benzidine] (poly-TPD)) [32], they are highly fabrication process dependent since the additional layers can introduce interface states and deteriorate the device performance [120–122].

(a)

Vacuum level

$\Phi_{MoO3} = 6.9eV$

$\Phi_{ITO/PEIE} = 3.6eV$

dark

ITO/ PEIE

LUMO,D

⊖

$\Delta E_{electron} = 2.6eV$

LUMO,A

BHJ

⊖

HOMO,D

⊕

Ag

$\Delta E_{hole} = 1.4eV$

⊕

HOMO,A

MoO_3

$V_{bias} < 0$

(b)

Vacuum level

$\Phi_{MoO3} = 6.9eV$

$\Phi_{ITO/PEIE} = 3.6eV$

dark

⊖

LUMO,D

$\Delta E_{electron} = 3.9eV$

ITO/ PEIE

HOMO,D

LUMO,A

Ag

$\Delta E_{hole} = 2.5eV$

HOMO,A

⊕

MoO_3

$V_{bias} < 0$
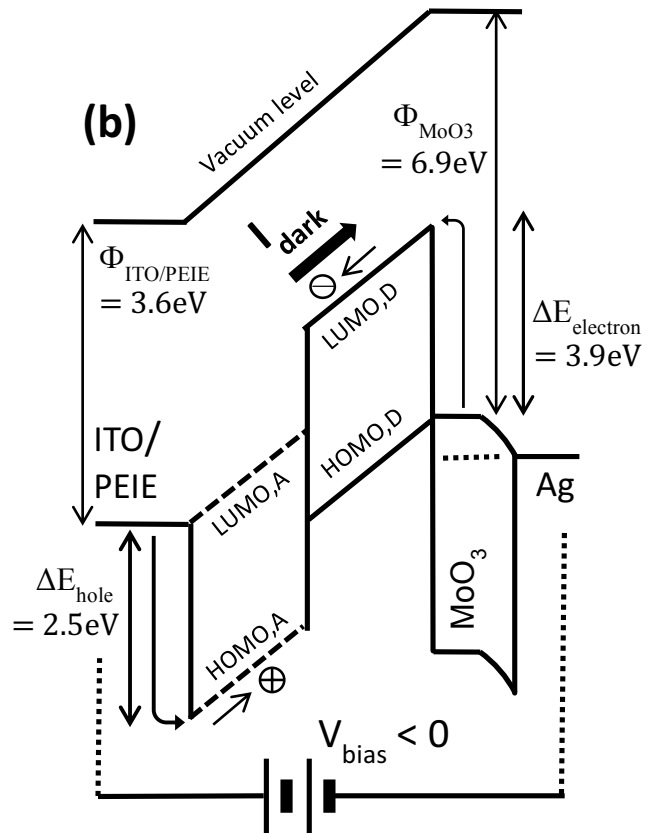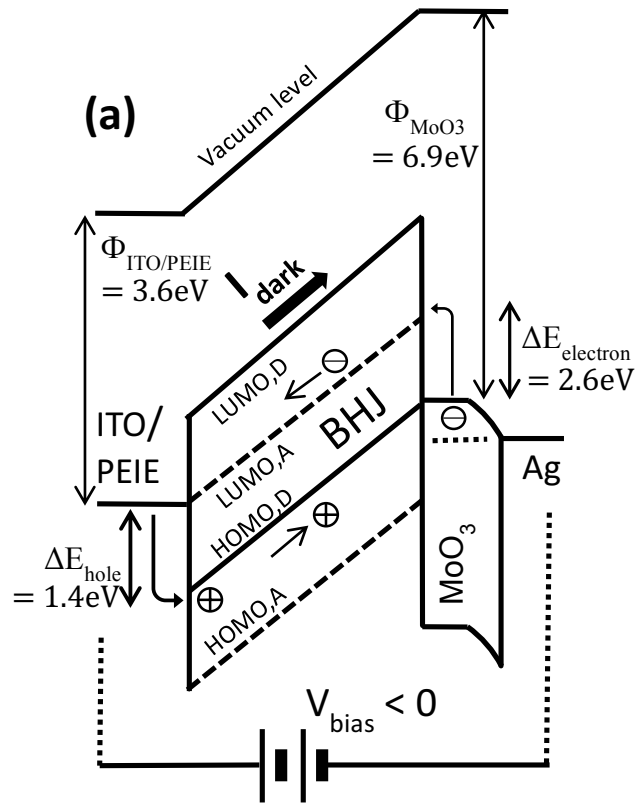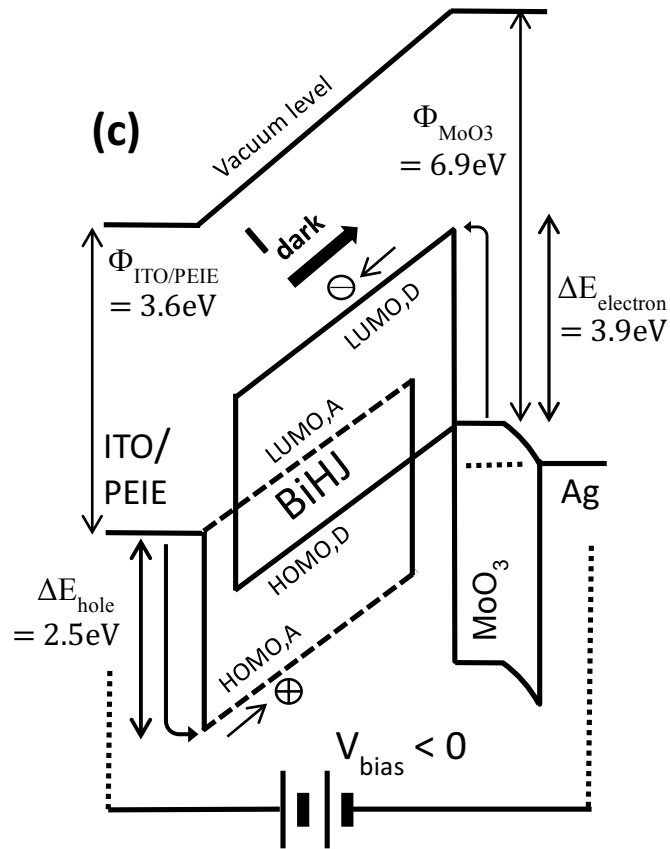
Figure 3.6 Suggested band diagrams of the (a) conventional bulkheterojunction (BHJ) OPD (b) bilayer OPD and (c) bilayer interdiffused heterojunction (BiHJ) OPD with reverse bias under dark condition. The arrows show the carrier injection mechanism at each electrode. LUMO,D and HOMO,D indicate LUMO and HOMO level of electron donor (P3HT) while LUMO,A and HOMO,D corresponds to electron acceptor (PCBM).

These trap states can become the recombination centers at the interface and provide additional dark current components which will increase the shunt leakage current. Theoretically, to suppress the dark current, it is desirable to have only acceptor material at cathode side while only donor material presents at anode side to prevent undesirable carrier injection [2,49]. In the case of the generic BHJ system, both the electron donor and acceptor species are present at the cathode / anode interface, lowering the average charge injection barrier. In the inverted structure, used in this study as shown in Figure 3.6(a), the hole injection barrier at the cathode/ BHJ active layer is about ΔE_{hole} = 1.4 eV (ΔE_{hole} = the highest occupied molecular orbital (HOMO) level of P3HT (5.0 eV)[87] - $\Phi_{ITO/PEIE}$ (3.6 eV)[117]) and the electron injection barrier at the anode/ BHJ active layer is determined as $\Delta E_{electron}$ = 2.6 eV ($\Delta E_{electron}$ = Φ_{MoO3} (6.9 eV)[88] - the lowest

unoccupied molecular orbital (LUMO) level of PCBM (4.3 eV)[87]). A significant increase on the injection barrier can be realized by precisely controlling the vertical segregation of the donor/ acceptor materials by the bilayer structure, Figure 3.6(b). The bilayer of the electron acceptor and donor allows higher injection barriers at the interface with the increased hole injection barrier at the cathode/ PCBM layer as ΔE_{hole} = 2.5 eV (ΔE_{hole} = the highest occupied molecular orbital (HOMO) level of PCBM (6.1 eV)[87] - $\Phi_{ITO/PEIE}$ (3.6 eV)) and the increased electron injection barrier at the anode/ P3HT layer as $\Delta E_{electron}$ = 3.9 eV ($\Delta E_{electron}$ = Φ_{MoO3} (6.9 eV)[88] - the lowest unoccupied molecular orbital (LUMO) level of P3HT (3.0 eV)[87]). The increased ΔE_{hole} and $\Delta E_{electron}$ in the bilayer OPD structure are expected to suppress the device leakage current effectively. Even though the increased injection barriers are achieved through the bilayer concept, the small interface between electron acceptor and donor at the middle of the cell can significantly limit the photo-generated carrier generation due to small diffusion length of excitons on the order of 10 nm. As we described earlier in the introduction chapter, the thermal interdiffusion concept is adapted and depicted in Figure 3.6(c) in order to maximize the area of the electron donor / acceptor mixed layer while preserving the electron donor and acceptor only layers at each electrode. The precise control of the thermal annealing condition for the interdiffusion process is required to yield optimum performance which guarantees both high quantum efficiency and low dark current.

3.3.2. Dark Current Density vs. Voltage Characteristics

The dark current density (J_d) versus applied voltage (V) characteristics for BiHJ OPDs with various thermal annealing conditions are shown in Figure 3.7. The J_d-V curves are fitted with the recursive non-ideal diode equation 2-2 and fits are shown as solid lines.
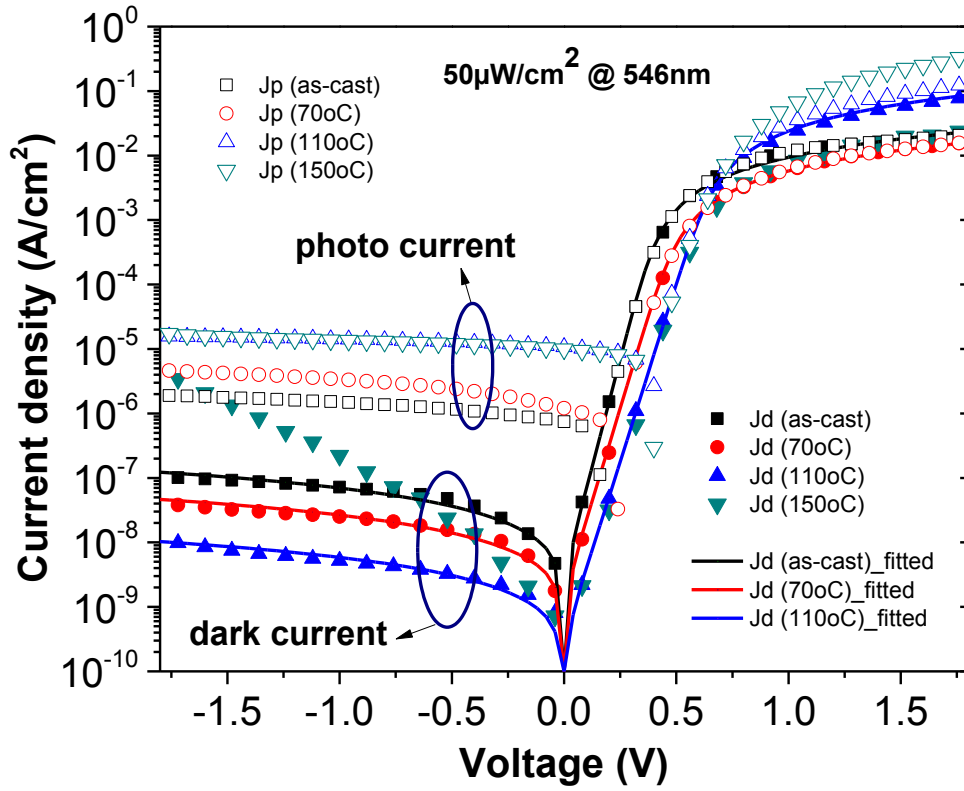
Figure 3.7 Experimental dark and under illumination current density (J) versus voltage (V) characteristics for OPDs with different annealing conditions. The voltage was applied to anode contact and irradiance of 50μW/cm² light illumination with 546nm was used. Solid symbols represent measured dark currents when open symbols are photo responses and the solid lines indicate fitted J-V curves.

Table 3.1 The extacted parameters for the BiHJ OPDs with different annealing conditions

Annealing conditions	J_d (A/cm²) @ -1.5V	RshA (Ωcm²)	RsA (Ωcm²)	n	Jo (A/cm²)
As-cast	9.38×10^{-8}	1.5×10^{7}	55	1.3	3.0×10^{-9}
70 °C	3.32×10^{-8}	4.0×10^{7}	50	1.45	1.5×10^{-9}
110 °C	7.72×10^{-9}	1.8×10^{8}	12	1.5	3.0×10^{-10}

All the parameters are extracted from the fitted dark current plots for T = 299 K and summarized in Table 3.1. We can observe that the J_d at - 1.5 V decreases more than one order of magnitude when the annealing temperature is increased up to 110 °C. It is believed that a higher dark current observed for as-cast device is due to residual solvent molecules that could

introduce undesirable doping or traps resulting in increased recombination – generation (R-G) current under reverse bias [96,123]. As the annealing temperature increases, the residual solvent molecules can be effectively removed decreasing solvent effect. When the annealing temperature increases up to 150 $^{\circ}$C, we clearly observe the sharp increase of the J_d. As verified by Treat et al [115], the elevated temperature accelerates the PCBM interdiffusion into P3HT polymer chains and eventually the PCBM molecules penetrate completely the P3HT polymer layer reaching the counter-electrode (anode). Resulting poorly defined contact between electron acceptor molecules and anode can siginificantly reduce the effective carrier injection barrier leading to sharp increase of the dark current at higher reverse bias, as experimentally observed.

3.3.3 Capacitance – Voltage Characteristics under Dark

The capacitiance – voltage (C-V) characteristics of the as-cast and 110 $^{\circ}$C annealed BiHJ OPDs are shown in Figure 3.8(a); the measured dissipation factor (D = $1/\omega RC$, $\omega = 2\pi f$ and R is device resistance) is also shown. At high reverse bias, the capacitance values for both as-cast and 110 $^{\circ}$C BiHJ devices tend to saturate. This behavior can be explained if we assume that the active layer is fully depleted of majority carriers for large reverse bias [124,125]. In such case the device capacitance becomes equivalent to geometric capacitance, $C_{geo} = \varepsilon\varepsilon_0 A/t$ (where the ε is the dielectric constant of active layer, ε_o is vacuum permittivity, and t is thickness of the active layer between electrodes). The inset in Figure 3.8(a) shows measured capacitance values for both devices at higher reverse bias ranging from -2 V to -4 V. It is interesting to note that the saturated capacitance values of as-cast and 110 $^{\circ}$C devices are slightly different. The measured capacitances for as-cast and 110 $^{\circ}$C devices at -2 V bias are $C_{as\text{-}cast}$ = 153 pF and $C_{110^{\circ}C}$ = 123 pF, respectively.
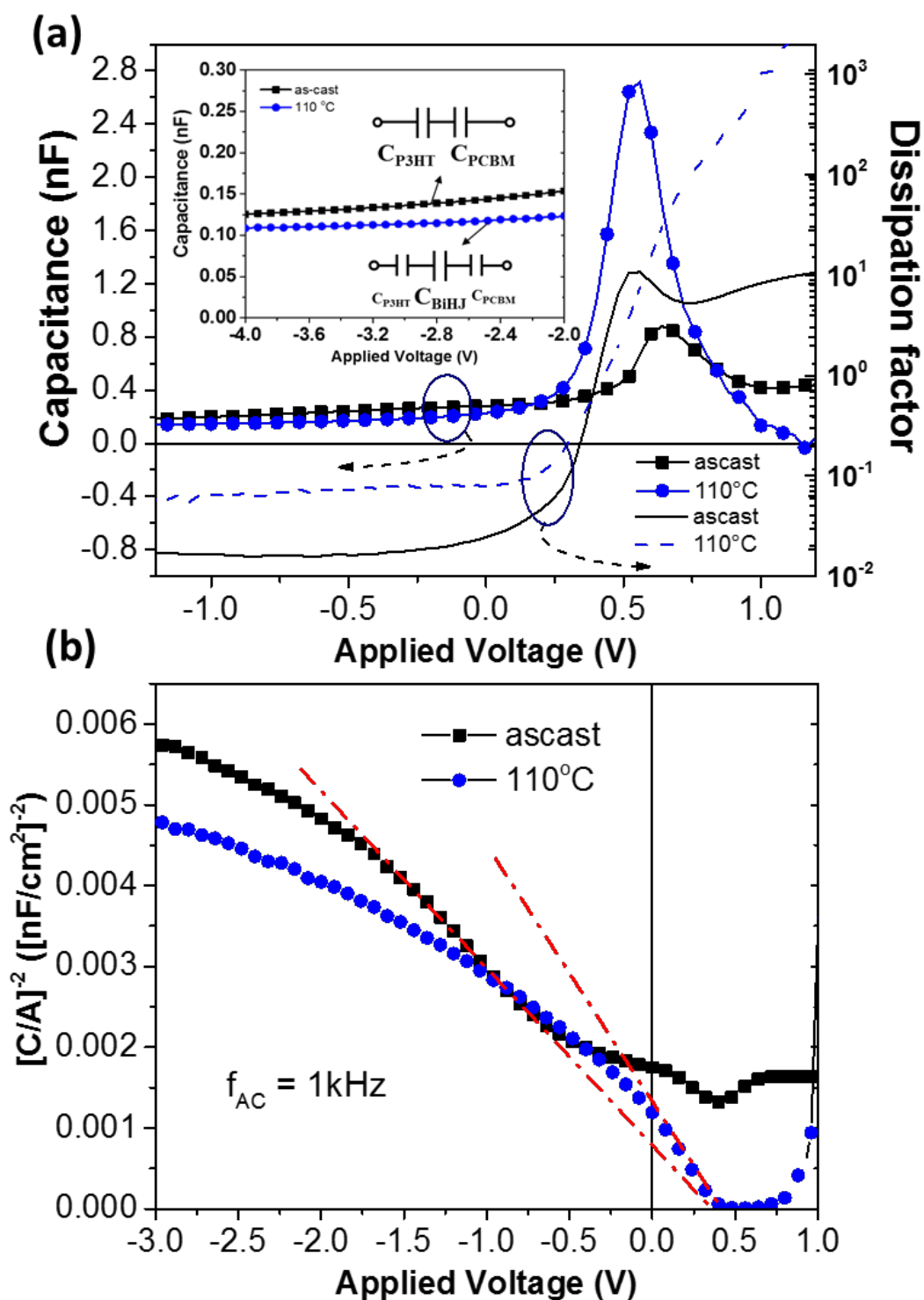
Figure 3.8 (a) C–V characteristics along with dissipation factor plot (b) Mott-Schottky [(C/A)$^{-2}$ – V] characteristics of the BiHJ OPDs for as-cast and 110 ^{o}C annealing conditions.

It can be noticed, when the solvent is removed the thickness of the active layer becomes

thinner. The average thickness reduction of the devices after annealing was about 5 % (e.g. 190

nm to 180 nm) measured by profilometer over 20 devices. This should lead to $C_{110^oC} > C_{as\text{-}cast}$ due to thickness reduction, which is opposite to experimental observation. Therefore to explain experimental data we must assume that change of heterojunction morphology with the annealing introduce a change of the effective value of the dielectric constant. Assuming that $C_{as\text{-}cast}$ is composed of two serially connected capacitors of P3HT and PCBM films with same thickness, we can obtain

$$C_{as-cast} = \frac{C_{P3HT}C_{PCBM}}{C_{P3HT}+C_{PCBM}} = \varepsilon_0 \frac{A}{t/2} \frac{\varepsilon_{P3HT}\varepsilon_{PCBM}}{\varepsilon_{P3HT}+\varepsilon_{PCBM}} \qquad (3\text{-}3)$$

where t is thickness of the total active layer, ε_{P3HT} and ε_{PCBM} are the dielectric constants of P3HT and PCBM films, respectively. When we use $\varepsilon_{P3HT} = 4.4$ [126] and $\varepsilon_{PCBM} = 3.9$ [127], the calculated $C_{as\text{-}cast}$ becomes 151 pF, which matches quite well with the experimental value. On the other hands, 110 ^{o}C device can be regarded as three capacitors connected in series composed of C_{P3HT}, C_{BiHJ} and C_{PCBM}, due to intermixed middle layer by thermal annealing process. If we assume that the interdiffused heterojunction is expanded to most of the volume inside the active layer, the whole capacitance value can be approximated to $C_{110^oC} = C_{BiHJ}$ since smaller capacitance dominates in series connection. Now the capacitance can be simplified as Equation 3-4,

$$C_{110^oC} \approx C_{BiHJ} = \varepsilon_{BiHJ}\varepsilon_0 \frac{A}{t} \qquad (3\text{-}4)$$

where ε_{BiHJ} is the dielectric constant of P3HT:PCBM BiHJ film.

When we use the measured $C_{110^oC} = 123$ pF value and t = 180 nm which is reduced after annealing, the calculated ε_{BiHJ} yields 3.2, which is comparable with $\varepsilon_{BiHJ} = 3.3$ from [124]. We believe that the smaller ε_{BiHJ} of the mixed layer compared to ε_{P3HT} and ε_{PCBM} is partially affected by solvent removal effect (dielectric constant of CB = 5.62) by thermal annealing. This simple analysis is consistent with the idea of fully depleted region at higher reverse bias and formation of the BiHJ layer after thermal annealing.

When the applied voltage increases to forward bias region, the capacitance values of both devices increases and show different peaks with C_{peak} = 2.7 nF at 0. 56 V for 110 °C device and C_{peak} = 0.9 nF at 0.64 V for as-cast device. The capacitance increase can be attributed to the compensation of the depleted carriers formed by built-in electric field inside the device. As the depleted region diminishes, the space charge capacitance disappears and the bulk capacitance (e.g. device series resistance) becomes dominant factor, which can be responsible for the decrease of the capacitance after the peak region [128]. For the high precision C-V measurement system, the upper limit of the dissipation factor D should be kept in the range of < 10, giving the approximate instrumentation error around < 1 % [129]. In case of 110 °C device at higher forward bias, the OPD becomes very conductive yielding the high D value which prevents accurate evaluation of capacitance. In contrast, D value for the as-cast device remained within the acceptable error range even at higher forward bias range. We attribute the difference of the capacitance peak for the both devices to distinct structures of the heterojunction in active layers having different RsA values, Table 3.1.

By using the standard C-V analysis, the Mott-Schottky relationship was plotted in Figure 3.8(b) according to Equation 3-5 [96].

$$\frac{A^2}{C^2} = \frac{2}{q\varepsilon\varepsilon_0 N_{eff}}(V_{bi} - V) \qquad (3-5)$$

where N_{eff} is the effective charge density, V_{bi} is the built-in voltage, and V is the applied voltage. Using A and ε values previously obtained, the 110 °C device yielded V_{bi} = 0.41 V and N_{eff} = 1.44 x 10^{16} cm^{-3}; the V_{bi} and N_{eff} values for as-cast device have not been explicitly extracted because of the unpredictable C^{-2}-V curve.

If the investigated OPD is to be used for X-ray imager application it is important to evaluate the full-well capacity Q_{well} given by [130].

$$Q_{well} = \int_{V_{reset}}^{V_{max}} C_{PD}(V)\, dV \qquad (3-6)$$

where C_{PD} is OPD capacitance, V_{max} and V_{reset} are the maximum and reset bias voltage, respectively. If we assume that the C_{PD} is fully depleted in reverse bias mode, it can be approximately regarded as constant value. When we assume V_{reset} is zero and V_{max} equals V_{bias}, the simplified Q_{well} equation becomes

$$Q_{well} = C_{PD}V_{bias} = \frac{\varepsilon\varepsilon_0 A}{t_{PD}}V_{bias} = \varepsilon\varepsilon_0 A E_{applied} \qquad (3\text{-}7)$$

where V_{bias} is applied reverse bias, t_{PD} is the thickness of the OPD, and $E_{applied}$ is the applied electric field. A dynamic range (DR) of an imager is limited by the charge handling capacity so higher Q_{well} can enhance the imager performance, where DR is defined by

$$DR = 20\log(\frac{I_{max}}{I_{min}}) = 20\log(\frac{Q_{well}^{max}-I_d T_{int}}{\sqrt{\sigma_r^2+qI_{dc}T_{int}}}) \qquad (3\text{-}8)$$

where I_d is dark current, T_{int} is integration time and $\sigma_r{}^2$ is variance of the temporal noise. As shown in Equation 3-7, to increase the Q_{well}, (i) the $E_{applied}$ needs to be enhanced either by increasing V_{bias} or by decreasing t_{PD}; (ii) ε or (iii) A needs to be increased. Our BiHJ OPD device (110 ^{o}C) was able to sustain Q_{well} value of 1.9 pC at $E_{applied}$ = 1.5 V / 180 nm = 8.3 V/μm with low dark current value of 7.72 nA/cm^2. Increase of ε will require new material. Increase of V_{bias} or decrease of t_{PD} could increase I_d. Increase of A will reduce imager resolution. (e.g. pixel size will be larger). All these requirements cannot be satisfied at the same time. Hence there must exist a pixel size and these OPD materials / structure that compromise the criteria.

3.3.4 Figure of Merits of the BiHJ OPDs

In addition to the J_d-V and C-V characterization in the dark, we evaluated the OPD performance under illumination condition with 546 nm wavelength having light intensity of 50 μW/cm^2. The 546 nm wavelength was chosen since it lies in the absorption peak of the

P3HT:PCBM BiHJ film and also corresponds to a typical emission peak of a scintillator on indirect-type X-ray imager [61].

Table 3.2 Comparison of figures of merit of OPDs with different annealing conditions at irradiance of 50μW/cm^2 light illumination with 546 nm wavelength

Annealing conditions	$\mathcal{R}$ (mA/W) @ -1.5V	EQE (%) @ -1.5V	NEP (W/Hz$^{1/2}$) @ -1.5V	D* (cm·Hz$^{1/2}$W^{-1}) @ -1.5V
As-cast	28	8	5.51 x 10^{-13}	1.61 x 10^{11}
70 °C	75	14	1.38 x10^{-13}	6.44 x 10^{11}
110 °C	240	60	1.84 x 10^{-14}	4.82 x 10^{12}
150 °C	243	61	2.59 x 10^{-13}	3.42 x 10^{11}

The J-V semi-log plot under the illumination condition can be found in Figure 3.7. Based on the J-V characteristics, figure of merits (FOMs) of the OPDs (J$_d$, EQE, Responsivity ($\mathcal{R}$), Noise Equivalent Power (NEP) and Specific Detectivity (D*)) are evaluated using Equations 2-3, 2-5 and 2-6 and summarized in Table 3.2 for different annealing temperatures. The detailed derivation methods of the FOMs can be found elsewhere [118]. As we discussed in previous section, while the lowest J$_d$ was achieved with 110 ^{o}C device and the highest J$_d$ value was observed with 150 ^{o}C device at 1.5 V reverse bias, the responsivity values of both devices were similar as $\mathcal{R}$ = 240 mA/W for 110 ^{o}C device and $\mathcal{R}$ = 243 mA/W for 150 ^{o}C device. The comparable $\mathcal{R}$ obtained for the two devices confirms that the annealing temperature of 110 ^{o}C is sufficient to produce interdiffusion layer yielding the maximum photo response, while the higher temperature will extend the interdiffusion layer throughout the device and will reach both contacts leading to high J$_d$. The 110 ^{o}C device showed highest D* = 4.82 x 10^{12} cm·Hz$^{1/2}$W^{-1} due to the lowest dark current value J$_d$ = 7.72 x 10^{-9} A/cm^2 at 1.5 V reverse bias. Beside the photoconductive mode of the photodetector which requires applied reverse bias for charge storage purpose, the unbiased photovoltaic mode has its advantage of low-noise continuous-wave measurement (e.g. Optical Power Meter) which requires minimum level of dark current [96,97]. In the photovoltaic mode, the 110 ^{o}C BiHJ OPD showed J$_d$ (0V) = 3.58 x 10^{-10} A/cm^2

and $\mathcal{R}(0V) = 243$ mA/W, yielding a high detectivity value of $D^* = 1.57 \times 10^{13}$ cm·Hz$^{1/2}$W^{-1} at 546 nm wavelength, which is one of the best detectivity using P3HT/PCBM or other high performance low bandgap polymer BHJ system published so far [2].

Figure 3.9 shows the measured LDR of the BiHJ OPD with 110 °C annealing condition all the way down to noise equivalent power (NEP) at reverse bias of 1.5 V with 546 nm wavelength illumination. The BiHJ OPD device has a linear response with fitting equation, J [A/cm^2] = αP$_{in}$ [μW/cm^2] + β with slope coefficient $\alpha = 0.585$ [A/W] and $\beta = 1.81 \times 10^{-7}$ [A/cm^2], where J is photocurrent and P$_{in}$ is input irradiance.
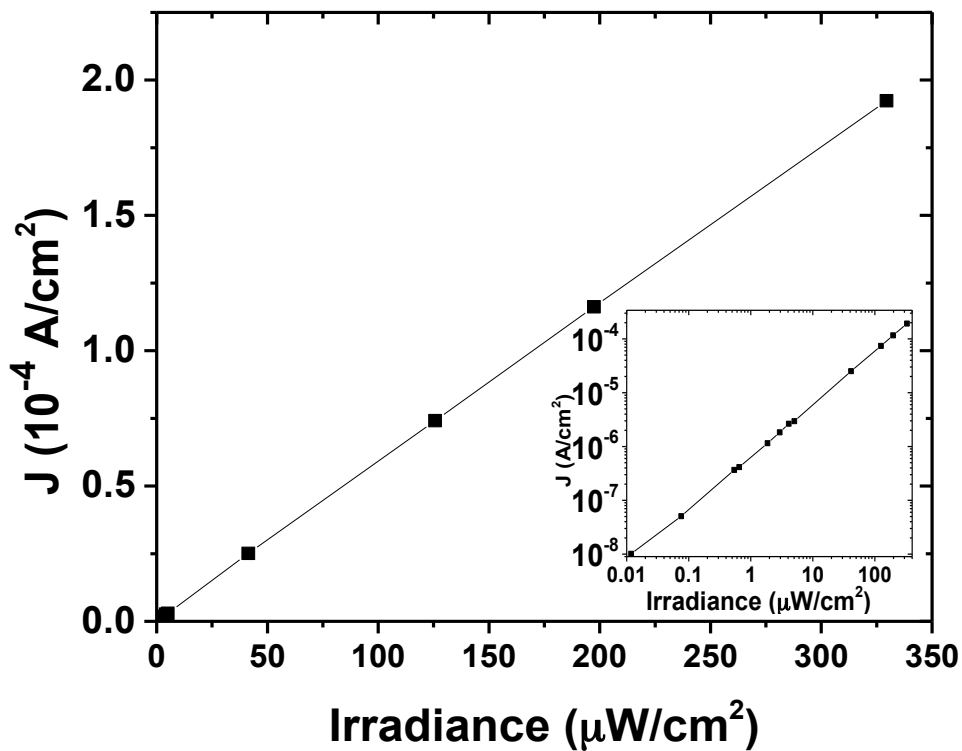
Figure 3.9 Linear dynamic range (LDR) of the BiHJ OPD with 110°C annealing condition under various light intensity at 546nm light wavelength with 1.5V reverse bias. The inset shows the LDR plot in logarithmic scale.
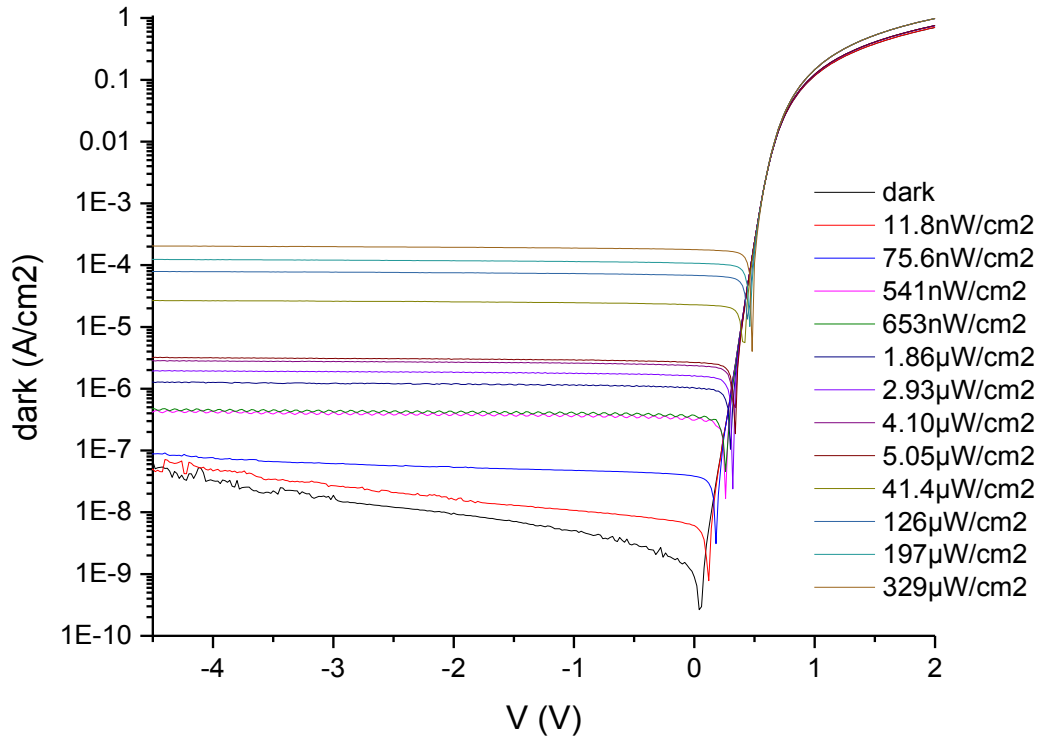
Figure 3.10 J-V curve of the BiHJ OPD with 110 ^{o}C annealing condition under various light intensity at 546nm wavelength.

The full J-V characteristic of the OPD with various 546 nm light intensities can be found in Figure 3.10. The OPD device did not show the photocurrent saturation up to 0.1 W/cm^2 of the light intensity which yields corresponding LDR over 120 dB. This high LDR is significantly higher than InGaAs photodetectors (66dB) and is comparable with a Si photodetector (120dB) [46]. Moreover, for further evaluation of the OPDs, we measured transient response and 3 dB bandwidth characteristics of the 110 ^{o}C BiHJ OPD, as shown in Figure 3.11 and 3.12, respectively. The amplitude of the temporal response increases with higher reverse bias, varied from 0 V to -4 V. The measured rise time t_r and fall time t_f with 4 V reverse bias were 2 ms and 3.9 ms, respectively, which are taken from the transient data as the time it takes to rise (or fall for t_f) from 10 % to 90 % of its final value. The bandwidth (B) is defined as the frequency of the light signal modulation at which the output photo response is -3 dB (half power) lower than

continuous wave response, calculated by the equation, $20\log(V_{out} / V_{in})$. The light intensity of the modulated input signal was kept as 5 µW/cm^2. The measurend 3 dB bandwidth frequency (f_{3dB}) was about 200 Hz, which agrees with the relationship between t_r and f_{3dB} given by the equation $t_r = 0.35 / f_{3dB}$ [97]. The calculated t_r value of 1.75 ms from the equation is close to t_r value of 2 ms measured in Figure 3.11. The measured bandwidth (BW) was ~ 200 Hz at 4 V reverse bias condition with a light intensity of 5 µW/cm^2 at 546 nm wavelength, which is sufficient for typical video applications with a minimum bandwidth of 30 Hz.
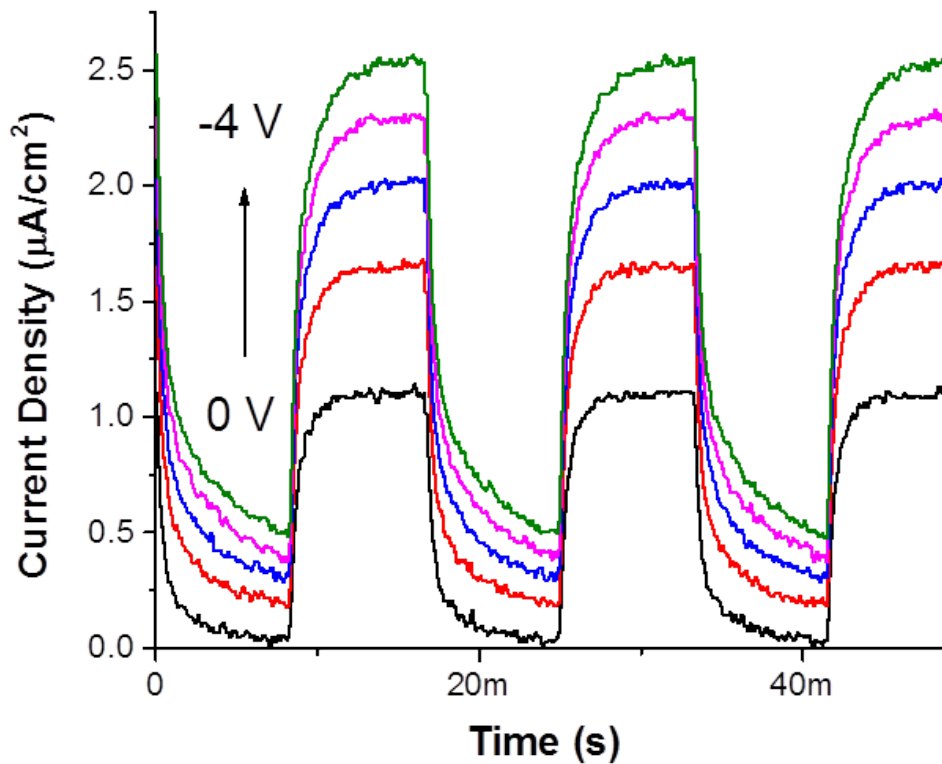
Figure 3.11 Transient responses of the BiHJ OPD with 110°C annealing condition with different reverse biases for light intensity of 5 µW/cm^2.
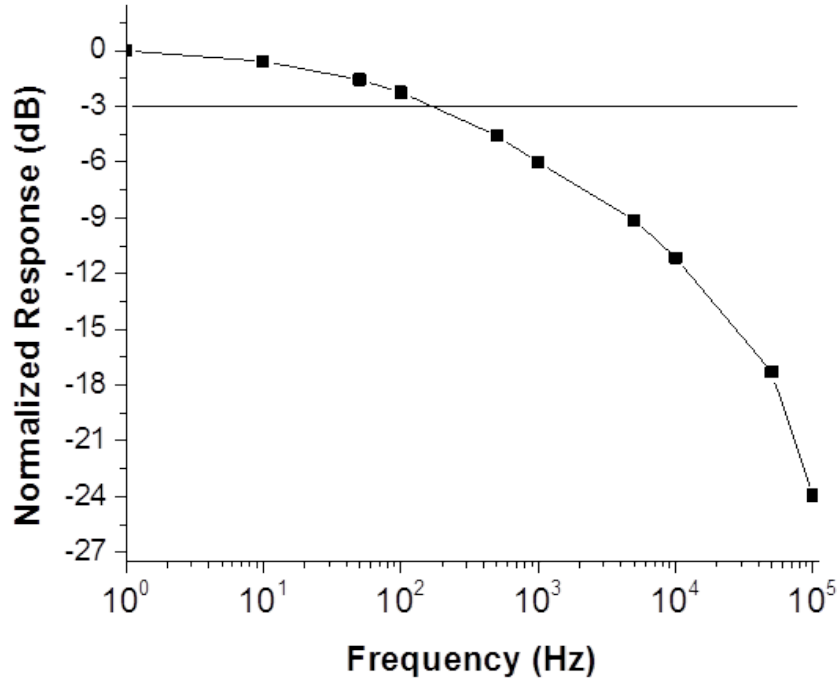
Figure 3.12 Frequency response of the BiHJ OPD with 110 ºC annealing condition with 1.5 V reverse bias condition.

3.3.5. BiHJ Solar Cell Properties

To demonstrate the possibility of the BiHJ OPD for solar cell application, we additionally measured the solar cell performances of the OPDs under 1 sun illumination condition. To evaluate the performance of the solar cell, the power conversion efficiency (PCE) under standard illumination condition (AM 1.5 spectral illumination) should be evaluated. The PCE of an OSC can be determined by three parameters, open circuit voltage (V_{oc}), short circuit current (J_{sc}) and fill factor (FF). Under 1 sun illumination condition, the J-V curve of the OSC will generate the maximum power (P_{max}) at a particular point, which is the product of the maximum current density value J_m and maximum voltage V_m. Now the PCE can be defined as

$$PCE = \frac{P_{max}}{P_{in}} = \frac{J_m V_m}{P_{in}} = \frac{J_{sc} V_{oc} FF}{P_{in}} \qquad (3\text{-}7)$$

where P_{in} is the power of the incident light on the device, and the FF is defined by

67

$$FF = \frac{P_{max}}{J_{sc}V_{oc}} = \frac{J_m V_m}{J_{sc}V_{oc}} \qquad (3\text{-}8)$$

Here, we re-write the full non-ideal diode equation for typical solar cell model,

$$J(V) = J_O \left[\exp\left(\frac{q(V - J(V)R_S A)}{nkT}\right) - 1 \right] + \frac{V - J(V)R_S A}{R_{sh}} - J_{ph} \qquad (3\text{-}9)$$

Equations for Voc and Jsc can be easily deduced by setting the net current of the diode equation 3-9 to zero and the voltage to zero, respectively

$$V_{OC} = \frac{nkT}{q} \ln\left\{ \frac{J_{ph}}{J_o}\left(1 - \frac{V_{OC}}{J_{ph}R_{sh}A}\right) + 1 \right\} \qquad (3\text{-}10)$$

$$J_{SC} = \frac{1}{1 + \frac{R_S}{R_{sh}}} \left[\left\{ J_o \exp\left(-\frac{qJ_{SC}R_S A}{nkT}\right) - 1 \right\} - J_{ph} \right] \qquad (3\text{-}11)$$

where J_{ph} is the photocurrent generated by the incident light.

The measured J-V curves and FOMs for solar cells are shown in Figure 3.13 and Table 3.3, respectively. All the FOMs including Jsc, Voc, FF and PCE are extracted and calculated by Equation mentioned above. As shown in the figure, the as-cast device exhibited a power conversion efficiency (PCE) of 0.48 % with a short circuit current (Jsc) of 1.29 mA/cm^2, open circuit voltage (Voc) of 0.58 V, and a fill factor (FF) of 63.7 %. The BiHJ device with 70 ^{o}C annealing condition gave the similar PCE of 0.49 % with slightly increased Jsc and decereased FF. The 110 ^{o}C annealed BiHJ device showed the best PCE value of 3.59 % mainly due to substantially increased Jsc value of 9.89 mA/cm^2.
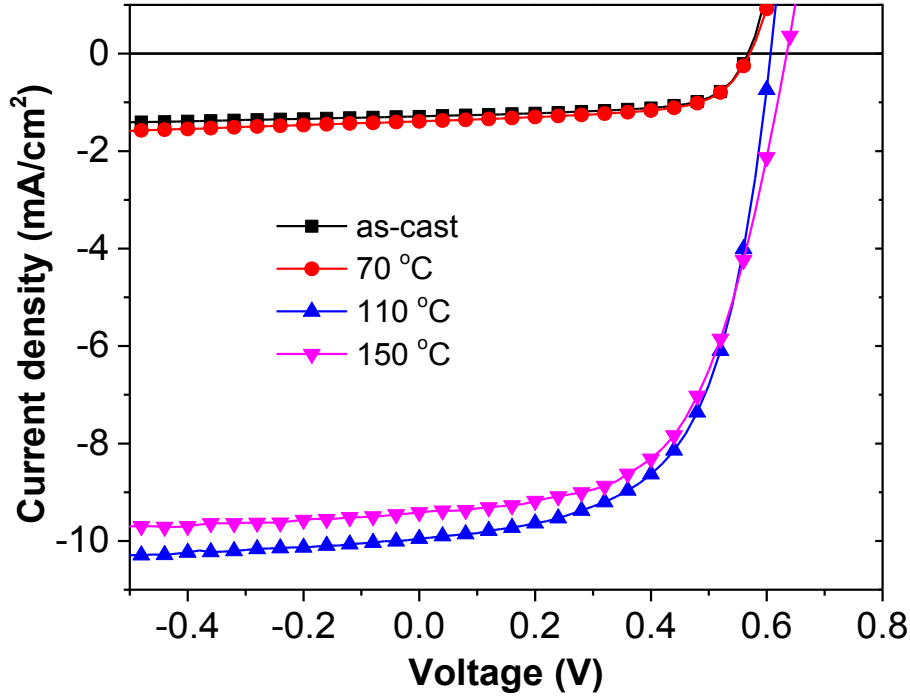
Figure 3. 13 J-V characteristics of the BiHJ OPDs with various annealing temperatures under illumination at 100 mW/cm^2 (AM 1.5G).

Table 3.3 Summary of photovoltaic figures of merit under AM 1.5G condition

Annealing conditions	Jsc (mA/cm^2)	Voc (V)	FF(%)	PCE(%)
As-cast	1.29	0.58	63.7	0.48
70 °C	1.39	0.58	61.1	0.49
110 °C	9.89	0.62	58.2	3.59
150 °C	9.41	0.64	57.2	3.45

The increase of the Voc from 0.58 V for as-cast device to 0.62 V for 110 °C device was 0.04 V, and this increase can be attributed to the decrease of J_o (Table 3.1) and increase of photocurrent J_{ph} as the annealing temperature increases, since $V_{OC} \propto \ln(\frac{J_{ph}}{J_o} + 1)$. The full Voc equation is shown in Equation 1-9. The 150 °C annealed BiHJ device showed slightly lower PCE value of 3.45 % but most of the FOMs were comparable with optimized 110 °C device. It

is noteworthy to emphasize that the PCE value of 3.59 % obtained in this work is one of the best PCE obtained for the modular construction of the bilayer P3HT / PCBM active layers using various approaches [106,109,111,131–136]. Hence the proposed DTS process can also be beneficial for the fabrication of highly efficient organic solar cells based on suggested or any other organic materials.

3.3.6 EQE measurement

Figure 3.14 compares the EQE spectal responses of the as-cast and 110 $^{\circ}$C annealed BiHJ OPDs for various reverse bias conditions of 0 V, 1.5 V, 3 V and 4.5 V. The EQE is defined as the ratio of the number of electrons collected by the external circuit per the number of incident photons for a given wavelength (Equation 3-1). As shown in the figure, the overall EQE of the both OPDs increased with higher reverse bias. The EQE values of the as-cast device were much lower compared to 110 $^{\circ}$C annealed device over all the range of spectrum. The measured result was consistent with the calculated responsivity and EQE values at 546 nm wavelength at -1.5 V (Table 3.2) derived from J-V characteristics in Figure 3.7. The as-cast device showed the peak EQE value for all the bias condition (e.g. EQE = 12 % with -1.5 V) at 435 nm wavelength while the 110 $^{\circ}$C BiHJ OPD showed the highest EQE values (e.g. EQE = 62 % with -4.5 V) at 555 nm wavelength. To clarify the difference in peak EQE locations before /after thermal annealing, photon absorption profile modeling within the BiHJ devices was performed using the transfer matrix method. The photon absorption profile versus position and wavelength was calculated by [80]

$$Q_j(x, \lambda) = \frac{2\pi c \varepsilon_0 k_j n_j}{\lambda} \left| E_j(x) \right|^2 \tag{3-12}$$

where c is the speed of light, and Ej is the electric field when the multilayer is composed of j (j = 1, 2, ..., m) individual layers.
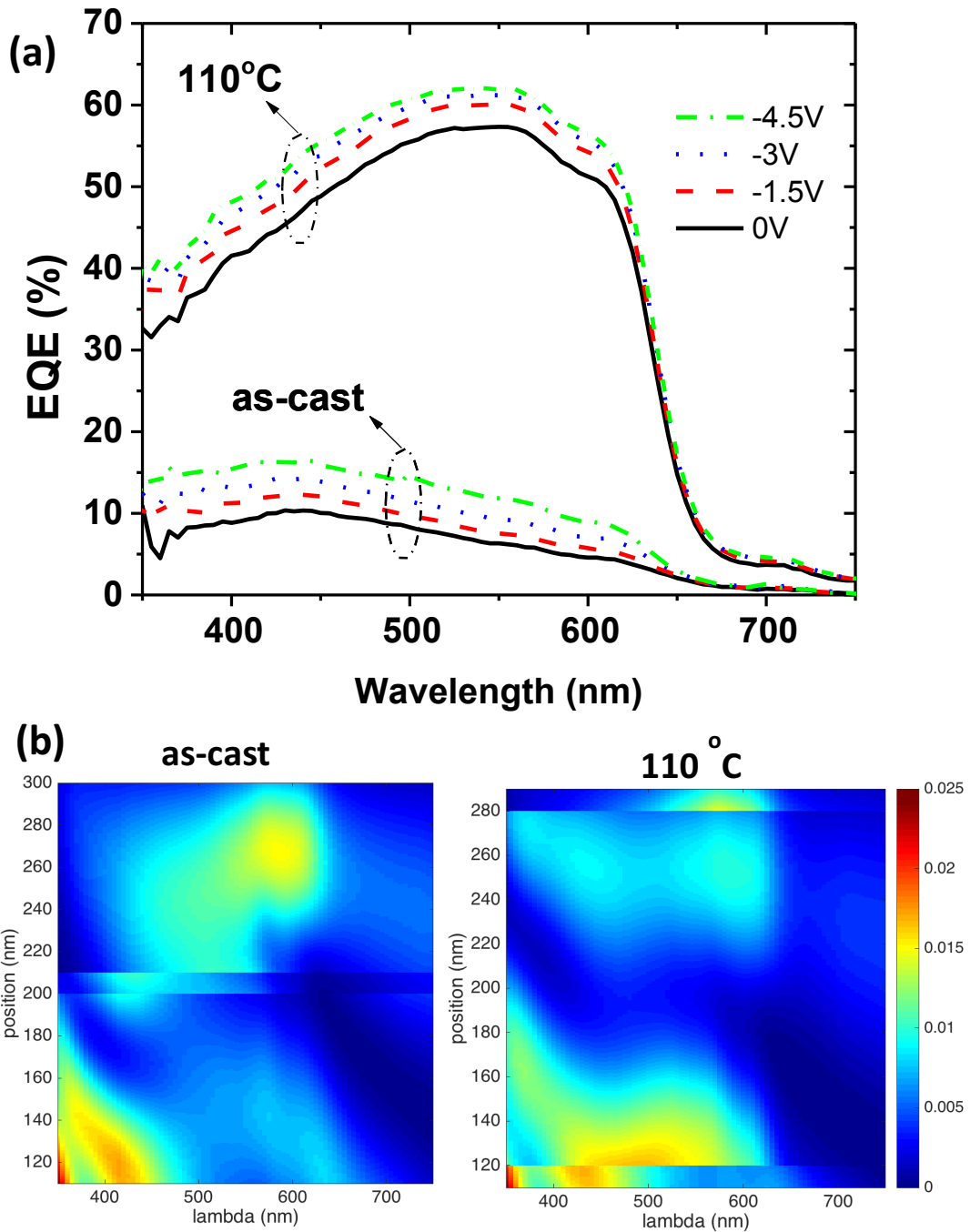
Figure 3.14 (a) EQE spectral response of the BiHJ OPDs under various reverse biases with as-cast and 110 ^{o}C annealing conditions. (b) Absorbed optical power distribution of the BiHJ OPD active layers with as-cast (left) and 110 ^{o}C (right) annealing conditions.

Full structure of the BiHJ OPDs was simulated and Figure 3.14(b) shows the photon absorption distribution inside only the active layers. The complex refractive indices of all the layers (ITO, PEIE, active layers [P3HT, PCBM, BiHJ 110 ^{o}C], MoO$_3$, Ag) were measured by

ellipsometer and representative extinction coefficients (k) for active layers were plotted in Figure 3.15.
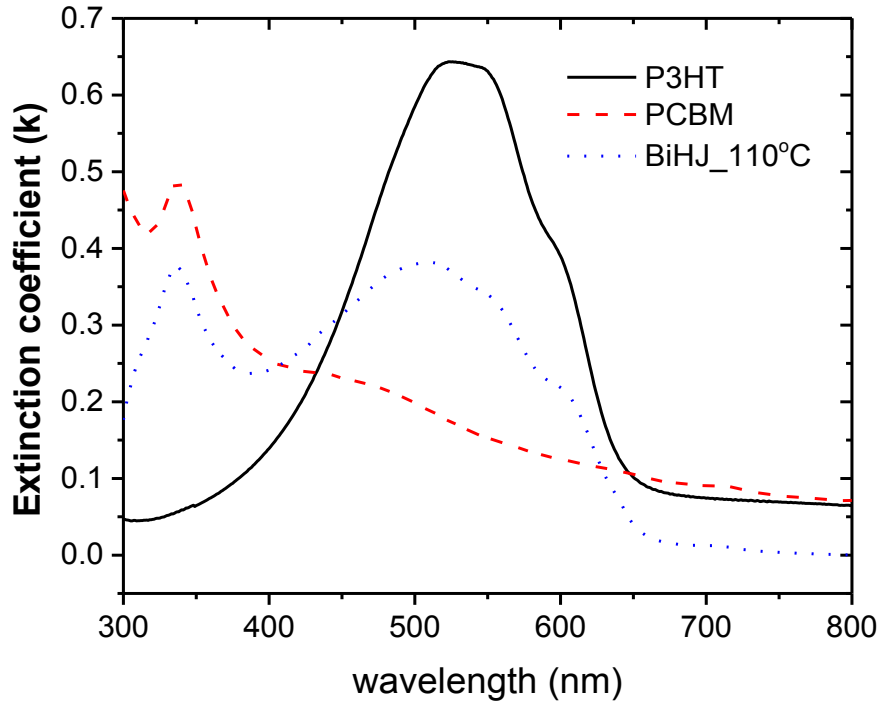
Figure 3.15 Measured extinction coefficient versus wavelength plot of P3HT, PCBM and BiHJ film annealed at 110 ^{o}C.

For the as-cast device simulation, we assumed partially interdiffused BiHJ network during the DTS process, hence included 10 nm of BiHJ layer between 90 nm thickness of P3HT and PCBM layers (total 190 nm thick). The BiHJ 110 ^{o}C device is assumed to have residual 10 nm thick film for each P3HT / PCBM layers after interdiffusion process with 160 nm of BiHJ layer at middle. For the as-cast device, we observe a peak photon absorption of the incident light occurs around 400 ~ 450 nm range at the middle layer of the device and gradually decrease as the wavelength increases. These results are consistent with the experimental EQE results obtained for as-cast device. This similarity indicates that the optical absorption around middle D/A junction generates major portion of the photo-generated charges for the as-cast device. The high absorption profile around 400 nm inside PCBM layer (front side of device) and around 600 nm inside P3HT layer (rear side of device) generates Frenkel excitons which are

immediately undergoing recombination process due to lack of D/A junction; hence do not contribute to photocurrent since the exciton diffusion lengths $L_{ex} = (D_{ex}\tau_{ex})^{1/2}$ (D_{ex} : exciton diffusion coefficient, τ_{ex} : exciton lifetime) for P3HT and PCBM are typically limited to $5 \sim 20$ nm range [137,138] . Meanwhile, BiHJ 110 ^{o}C device showed broad and intense overlapping region of the photon absorption around $500 \sim 600$ nm wavelength at both front and rear regions of the BiHJ layer, where the absorbed photons will directly contibute to charge carriers due to expanded D/A junction through the device volume.

To break down the origin of the enhanced EQE after thermal annealing process, the EQE can be factored into four detailed optical-to-electrical conversion processes [22],

$$EQE(\lambda, V) = \eta_A(\lambda)\eta_{IQE}(\lambda, V) = \eta_A(\lambda)\eta_{Diff}\eta_{CT}(V)\eta_{CC}(V) \qquad (3\text{-}13)$$

where η_{IQE} is the internal quantum efficiency, η_A is the optical absorption efficiency of the incident photons in the active layer resulting in the excitons formation, η_{Diff} is the exciton diffusion efficiency equal to the fraction of excitons reaching the D/A junction, η_{CT} is the charge transfer efficiency for excitons to dissociate into electrons in the PCBM acceptor and holes in the P3HT donor, and η_{CC} is the charge collection efficiency, defined as the fraction of charges collected at the electrodes. The λ is the wavelength of the incident light and V is the applied voltage. η_{CT} can be treated as unity since the offset between the D/A electronic energy levels is large enough for typical organic D/A system and the charge transfer (CT) process occurs in a few hundred femto-seconds which is much shorter than any other competing process [22]. Therefore, the Equation 3-13 now becomes

$$EQE(\lambda, V) \approx \eta_A(\lambda)\eta_{Diff}\eta_{CC}(V) \qquad (3\text{-}14)$$

To evaluate η_A, the absorption spectra of the devices were measured for both as-cast and 110 ^{o}C BiHJ films with 200 nm thickness as shown in Figure 3.16.
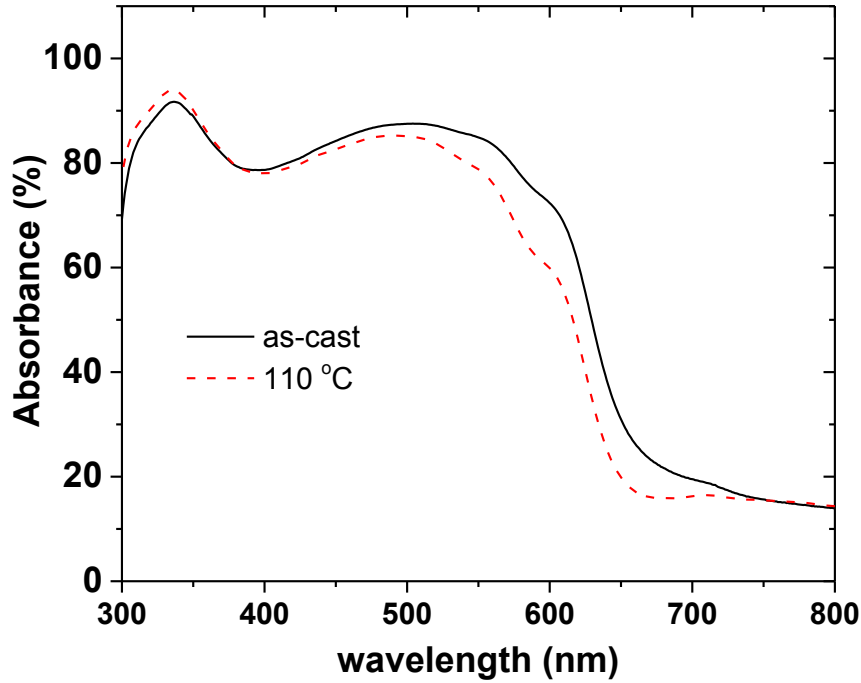
Figure 3.16 Absorbance spectra of as-cast and 110 $^{\circ}$C BiHJ OPD. The thickness of the measured films was 200 nm.

The spectra showed similar absorption behavior over all wavelength region with slight blue-shift around 550 - 650 nm. In the absorption spectra, we clearly see the absorption peak for P3HT in the range of 450 to 550 nm which corresponds to the π-π* transition of the P3HT backbone [139] and peak for PCBM around 345 nm [140]. Based on the measured optical absorption spectra of the films, the absorption coefficients (α) of the as-cast BiHJ, 110 $^{\circ}$C BiHJ including P3HT and PCBM films are plotted in Figure 3.17 versus photon energy. The optical energy gap (E_G) of each film was estimated by the Tauc plot of the absorption spectra in Figure 3.18 [141]. Even though the Tauc analysis cannot be strictly used for organic semiconductors where Bloch's theorem does not hold, it can provide a better estimate of the optical energy gap than the simple absorption spectra. By assuming the active layers are in amorphous 3-D structure which have a parabolic density of state at the band edge, the relationship between the absorptivity and E_G can be described as

$$(\hbar\omega\alpha)^{1/2} \propto (\hbar\omega - E_G) \tag{3-15}$$

74

where $\hbar\omega$ is the photon energy. The Tauc gap (E_G) of the as-cast BiHJ thin film extracted from the figure was determined to be 1.79 ± 0.01 eV when the E_G of 110 °C BiHJ film was 1.83 ± 0.01 eV and E_G for P3HT film was 1.85 ± 0.01 eV.
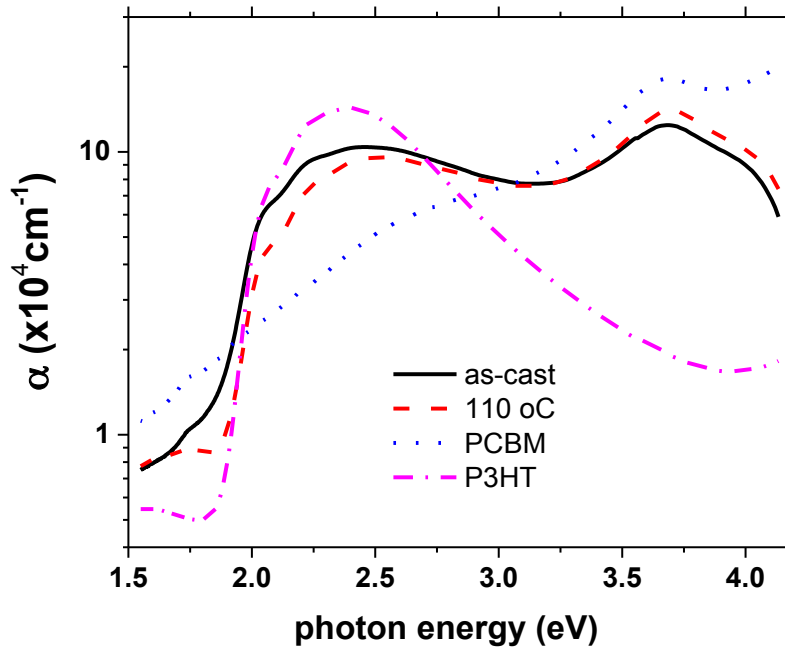
Figure 3.17 Absorption coefficient plot versus photon energy for as-cast, 110 °C, PCBM and P3HT films.
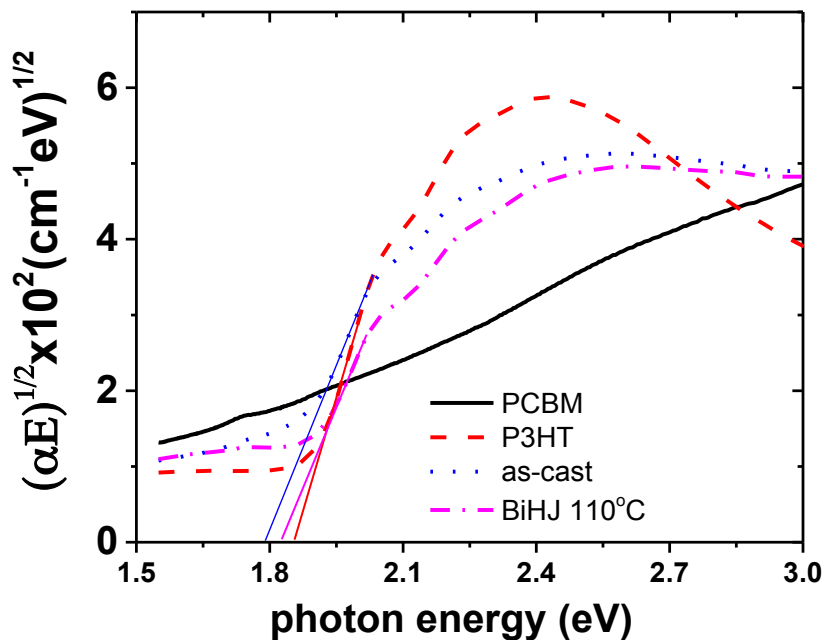
Figure 3.18 Tauc plot versus photon energy for as-cast, 110 °C, PCBM and P3HT films.

Since we observed comparable η_A for both devices, it is obvious that η_A is not dominant factor for the EQE enhancement, but the $\eta_{Diff}\eta_{CC}$. η_{CC} can be defined by following equation [142],

$$\eta_{CC} = \frac{L_d}{t}[1 - exp(-\frac{t}{L_d})] \tag{3-16}$$

where L_d is the charge drift length and t is the thickness of the active layer. In Equation 3-13, it is obvious that $\eta_{CC} \approx 1$ when t << L_d by Taylor expansion, and $\eta_{CC} \approx L_d/t$ for t >> L_d, which tells us that the thinner active layer than the L_d will yield high charge collection efficiency. The L_d, which is a function of the applied voltage can be expressed as,

$$L_d = (\mu_p \tau_p + \mu_n \tau_n)(V_{bi} - V)/t \approx L_{d0}(V_{bi} - V)/V_{bi} \tag{3-17}$$

where $\mu_p(\mu_n)$ is the hole (electron) mobility, $\tau_p(\tau_n)$ is the hole (electron) lifetime, V_{bi} is the built-in potential, and $L_{d0} = L_d(V = 0) = (\mu_p \tau_p + \mu_n \tau_n)V_{bi}/t$ is the charge drift length under short-circuit condition. From Equation 3-16 and 3-17, we see that the η_{CC} can be significantly enhanced by either having thinner active layer or increasing the applied reverse voltage. Meanwhile, the total current density under illumination can be described as J(V) = J_d(V) + J_{ph}(V) when J_{ph}(V) is defined as [143]

$$J_{ph}(V) = q \int EQE(\lambda, V)S(\lambda)\frac{\lambda}{hc}d\lambda \tag{3-18}$$

where S(λ) is power spectrum of the incident light. Equation 3-18 can be rewritten by substituting Equation 3-14,

$$J_{ph}(V) = P_o R_o \eta_{cc}(V) \tag{3-19}$$

where $P_o = \int S(\lambda)d\lambda$ is the incident optical power density and $R_o = \int \frac{q\lambda}{hc}\eta_A(\lambda)\eta_{Diff}d\lambda$ is the responsivity in case η_{cc} equals unity. Now Equation 3-16 can be fitted with J-V characteristics in Figure 3.13 to estimate the η_{CC}. The experimental J_{ph} derived from Figure 3.13 and fitted J_{ph} curves for as-cast and 110 °C devices are plotted in Figure 3.19. The fitting parameters are listed in Table 3.4 and the η_{CC} versus applied reverse voltage up to $-$ 4.5 V is plotted in Figure 3.20.

The calculated η_{CC} under short-circuit (zero bias) was ~ 0.6 for as-cast and ~ 0.9 for 110 °C device. As we increase the applied voltage to -4.5 V, the η_{CC} can approach up to $\eta_{CC}^{as\text{-}cast}$(-4.5V) ≈ 0.94 and η_{CC}^{110oC} (-4.5V) ≈ 0.99.
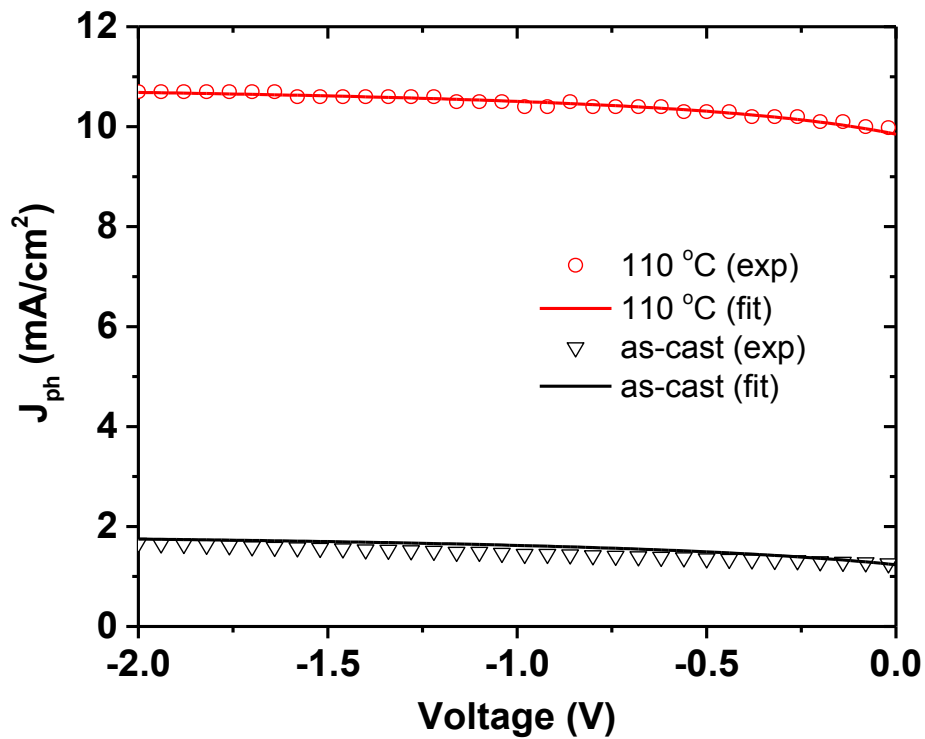
Figure 3.19. Comparison of experimental (open circles and triangles) and simulated photocurrent J_{ph} (solid lines) under 1 sun illumination (Po = 100 mW/cm²).

Table 3.4 Parameters used in fitting the J_{ph}-V characteristics under 1 sun illumination (100 mW/cm²) for the BiHJ OPDs

Fitting Parameters	t (nm)	Po (mW/cm²)	Ro (mA/W)	Lco (nm)	V_{bi} (V)
As-cast	190	100	20	180	0.70
110 °C	180	100	110	800	0.70
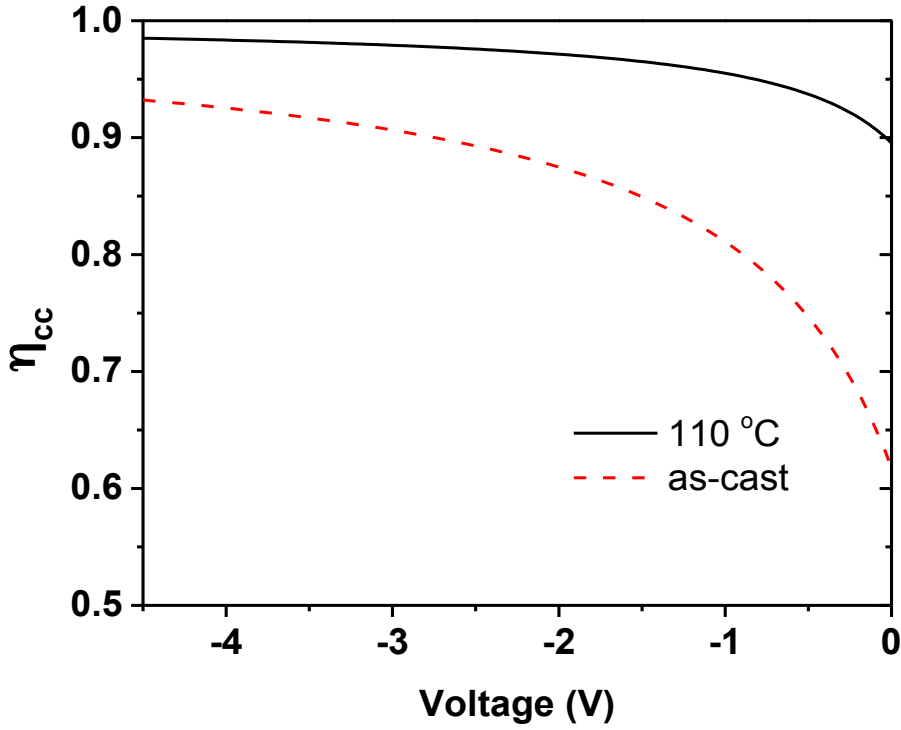
Figure 3.20 The charge collection efficiency versus applied reverse voltage of the as-cast and 110 °C BiHJ OPD.

To estimate the η_{Diff} value for each device, we fix the wavelength to 546 nm for a simple analysis. At λ = 546 nm, the $EQE^{as-cast}$(-4.5V) $\approx$ 0.12 and the $EQE^{110\ oC}$(-4.5V) $\approx$ 0.62. By plugging in $\eta_A^{as-cast}$ (546nm) $\approx$ 0.82 and η_A^{110oC}(546nm) $\approx$ 0.76 to Equation 3-11, we get $\eta_{Diff}\eta_{CC}^{as-cast}$(-4.5V) $\approx$ 0.146 and $\eta_{Diff}\eta_{CC}^{110oC}$(-4.5V) $\approx$ 0.816. The spatial deviation of the absorption efficiency for each device can be neglected since the optical field distribution at 546 nm wavelength in each device is proven to be similar as shown in Figure 3.21. Now when we consider the calculated charge collection efficiency $\eta_{CC}^{as-cast}$(-4.5V) $\approx$ 0.94 and η_{CC}^{110oC}(-4.5V) $\approx$ 0.99, we finally conclude the estimated $\eta_{Diff}^{as-cast}$(546nm) $\approx$ 0.156 and η_{Diff}^{110oC}(546nm) $\approx$ 0.824. Since the η_{Diff} is proportional to the fraction of excitons reaching the D/A junction, the volume of the interdiffused layer can be estimated by the evaluated $\eta_{Diff}^{as-cast}$ and η_{Diff}^{110oC}. If we assume that the effective active layer thickness of the as-cast device which contributes to

78

photo-generated charges as ~ 30 nm including L_{ex}, we can estimate the volume of the interdiffused region after 110 °C thermal annealing becomes approximately η_{Diff}^{110oC}(546nm)/ $\eta_{Diff}^{as-cast}$(546nm) $\approx$ 5.28 times increased, as ~ 160 nm. The result is consistent with the estimated thickness of the interdiffused volume used in the photon absorption profile modeling in Figure 3.14(b).
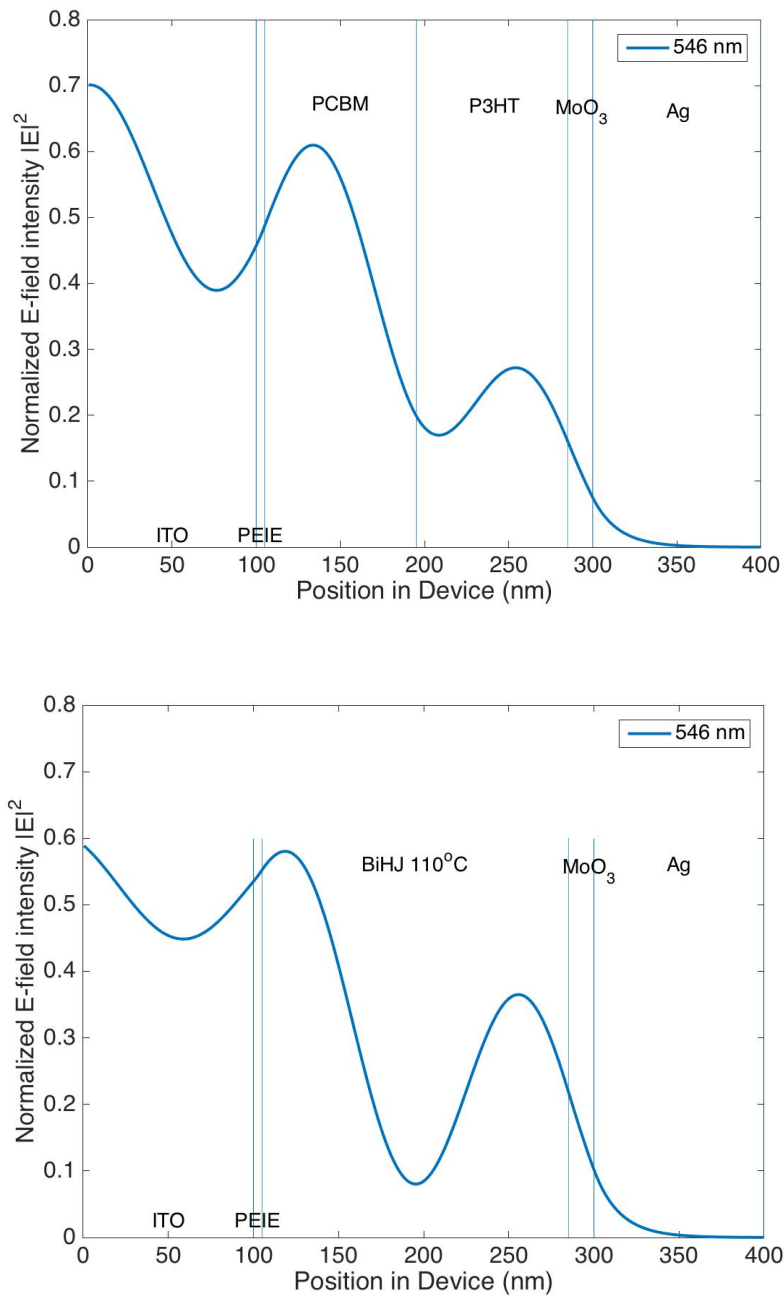
Figure 3.21. Simulated distribution profiles for the E-field intensities in the as-cast (top) and BiHJ 110 °C (bottom) OPDs. The excitation wavelength was fixed to 546 nm.

3.4. Conclusion

In conclusion, we developed a novel transfer printing method called DTS process to fabricate precisely controlled donor/acceptor bilayer organic photodiode which effectively prevents co-existence of the D/A material at the anode and cathode. Post-interdiffusion process was adapted to maximize the D/A interface at the middle of the active layer that is clearly seperated by donor and acceptor materials from respective electrodes. Moreover, the DTS method was able to exclude any contamination of the films during the process which can adversely introduce impurities inside the active layer. The proposed DTS method can be virtually applied to any fullerene / polymer hetrojunction system and it allows more freedom on selecting the solvent system for numerous materials which practically require tedious optimization processes to achieve favorable active layer morphology. Through the effort in this research, we demonstrated OPD with high specific detectivity of 4.82 x 10^{12} cm·$Hz^{1/2}W^{-1}$ at reverse bias of 1.5 V ($E_{applied}$ = 8.3 V/μm) with J_{dark} of 7.7 nA/cm^2 and EQE of 60 % (photoconductive mode) while the D* of 1.57 x 10^{13} cm·$Hz^{1/2}W^{-1}$ could be achieved at zero bias (photovoltaic mode). Additionally, the solar cell performance under simulated 1 sun condition was evaluated, achieving 3.59 % of PCE. In summary, we firmly believe that the proposed DTS process can be beneficial to simplify the complex BHJ morphology optimization process and enhance the reliability and yield of the OPD or OPV fabrication process. Moreover, the realization of the precisely defined bilayer heterojunction device can open a new opportunity to further reveal the physics and properties of the polymer organic heterojunction system.

Chapter 4.
High Performance Low-bandgap Polymer Organic Photodiode with Broadband Absorption with Charge Blocking Layer by Double Transfer Stamping Method

4.1 Introduction

Recently, there has been considerable efforts to use OPDs for image sensor applications associated with complementary metal-oxide-semiconductor [144] or metal-oxide thin film transistor active pixel sensor arrays [61]. Even though the spectrum selectivity of the OPDs can be beneficial to certain application [145], broadband photo-response in visible range of the organic materials is desirable to replace the Si PDs in conventional CMOS based imager. So far, the P3HT:PCBM system has been the most popular choice for the hybrid imagers applications [57,58,61,144]. However, the absorption spectra of P3HT:PCBM suffers from low absorption coefficient and weak photo-response below 620 nm of wavelength [118]. This narrow optical absorption bandwidth compared with their Si based inorganic counterparts hampers their replacement with OPDs for full color imager applications. Therfore, it is highly desirable to adapt a low-bandgap polymer material to extend the absorption spectrum to cover all visible range, including near-IR region.

Among various narrow-bandgap polymers reported so far, a blend of [[2,6′ -4,8-di(5-ethylhexylthienyl)benzo[1,2-b;3,3-b] dithiophene] [3-fluoro-2[(2-ethylhexyl)carbonyl]thieno[3,4-b]thiophenediyl] (PTB7-Th) and [6,6]-phenyl-C_{71}-butyric acid methyl ester ($PC_{70}BM$) has been extensively studied for solar cell applications due to its broadband absorption, high EQE and PCEs around 8 ~ 10 % [146]. Even though there were a

great number of efforts to enhance the performance of organic solar cells using the PTB7-Th polymer [146–149], none of the previous works focused on improvement of the photodetector performance by suppressing dark leakage current and maintaining high quantum efficiency at the same time. Unlike the organic solar cell case which does not focus on the dark current suppression, a photodetector usually requires additional buffer layers such as electron blocking layers (EBL) or hole blocking layers (HBL) to suppress the carrier injections responsible for leakage dark current under reverse bias [49,105,150–152]. The development of the solution for EBL or HBL for the solution-processed organic photodetector can be challenging task, because each solution has to be modified to prevent dissolution or damage of the underlying organic layers.

In previous chapter, we introduced a novel transfer printing method called DTS process to promote thermally induced interdiffusion between donor and acceptor layers to form well-defined BiHJ OPDs having a low dark leakage current and high performance. In this chapter we exploit the applicability of the DTS process for the OPD based on low-band gap polymer material with the goal to achieve a low dark current and a high responsivity at the same time. In this approach, we applied electron acceptor ($PC_{70}BM$) or electron donor (PTB7-Th) materials as HBL or EBL, respectively, which are used for the BHJ mixed active layer in this work. The resulting device is an inverted PTB7-Th:$PC_{70}BM$ BHJ OPD sandwiched between $PC_{70}BM$ HBL and PTB7-Th EBL having dark current density of 5.1 ± 0.2 nA/cm^2, an external quantum efficiency of 48 ± 1 % and a peak specific detectivity of (1.48 ± 0.1) x 10^{13} cm·Hz$^{1/2}$W^{-1} at reverse bias 0.5 V under 700 nm illumination.

4.2. Experimental

4.2.1 Device Fabrication

The ITO-coated glass substrates ($R_{sheet} \approx 10$ Ω/sq) were cleaned by acetone, isopropyl alcohol, and deionized water by sonication for 10 minutes, and subsequently ashed by oxygen plasma for 5 minutes. ZnO sol-gel solution was prepared by dissolving 1 M of zinc acetate dihydrate (Zn(CH$_3$COO)$_2$·2H$_2$O, Sigma Aldrich) as a precursor in 2-methoxyethanol (2ME, Sigma Aldrich) solvent. The 0.5 M of mono-ethanolamine was added as a stabilizer and the mixture was vigorously stirred at a temperature of 70 ^{o}C for 2 hours. The solution was then cooled down and aged for more than 12 hours. The synthesized ZnO solution was spin-coated on top of the cleaned ITO glass substrates with spin-coating speed of 500 rpm for 5 seconds for spreading and 3500 rpm for 50 seconds for film formation. The thermal annealing is done at 150 ^{o}C for 20 minutes, yielding 70 nm ZnO layer. The substrates were transferred into a glove box with nitrogen atmosphere for deposition of photoactive layer. Total three kinds of active layer solution were prepared in glove box: (1) PTB7-Th solution : 10 mg of PTB7-Th (Solarmer) was dissolved in 1.1 mL of CB; (2) PC$_{70}$BM solution : 25 mg of PC$_{70}$BM (Nano-C, purity: > 99.9%) was dissolved in 1 mL of CB; and (3) BHJ solution : 10 mg of PTB7-Th and 17 mg of PC$_{70}$BM was dissolved in 1 mL of CB. All the solutions were stirred by magnetic bar for ~12 hours at 70 ^{o}C to yield homogeneous solutions. PC$_{70}$BM solution was spin-coated with 2000 rpm or 1000 rpm for 1 min to form 50 nm or 90 nm thick film on the top of prepared ZnO / ITO substrate. The spin-cast process allowed enough time for CB solvent to vaporize and no further thermal annealing process was needed. For BHJ layer film deposition, 3 vol% 1,8-diiodooctane (DIO, Sigma-Aldrich) was added to the BHJ solution right before spin-coating process. The mixed solution was spin-coated with 600 or 900 rpm for 2 min to yield 150 nm or 100 nm thick of BHJ film. In case of spin-coating of the BHJ solution on PC$_{70}$PM film, the solution was drop-casted while spinning the substrate to minimize the dissolution of the PC$_{70}$BM film. The transfer of PTB7-Th polymer solution onto BHJ film or PC$_{70}$BM film was performed by the DTS process to prevent the dissolution of the underlying active layer. The detailed description of DTS process is explained in Chapter 3.2.3. Subsequently, the devices

were transferred into thermal evaporator built-in glove box to complete the device fabrication by depositing MoO_3 / Ag anode; Circular shadow mask with 1 mm diameter was used to deposit 25 nm MoO_3 and 100 nm silver electrode.

4.2.2 Device Measurement

The current density – voltage (J-V) measurement of the OPDs under dark and illumination were measured using a solar simulator (Oriel) equipped with Xenon lamp, band pass filters with peak wavelength at 546nm and 720 nm (FWHM = 10 nm) and 4156C semiconductor parameter analyzer located outside the glove box. The measured devices were located inside the glove box and illumination was done through bottom side (glass substrate). The optical intensity of the illuminated monochromatic light was measured by a power meter (70260, Newport). For the solar cell J-V characterization, simulated AM 1.5G illumination at 1 sun intensity (100 mW/cm^2) was used. EQE was measured with a setting of lock-in amplifier (Stanford Research Systems SRS 830), monochromator equipped with a 100W halogen tungsten lamp, light chopper, and UV-enhanced silicon photodetector (Newport UV808) used for calibration. Detailed description of the EQE measurement can be found in Chapter 3.2.4.

To measure the temporal response, a 5 V red dot laser diode (Farhop, 5 mW, 650 nm) was used as a light source connected to a function generator (8110A, HP) to generate square light pulses. The OPD photocurrents were amplified and converted to voltage value by a current pre-amplifier (SR 570, Stanford Research). The voltage bias to the OPDs was applied by the pre-amplifier with High Bandwidth gain mode. The transient output signal was measured by a digital oscilloscope (MSO7104B, Agilent) with 1MΩ input impedance. The schematic of the transient measurement is shown in Figure 4.1.
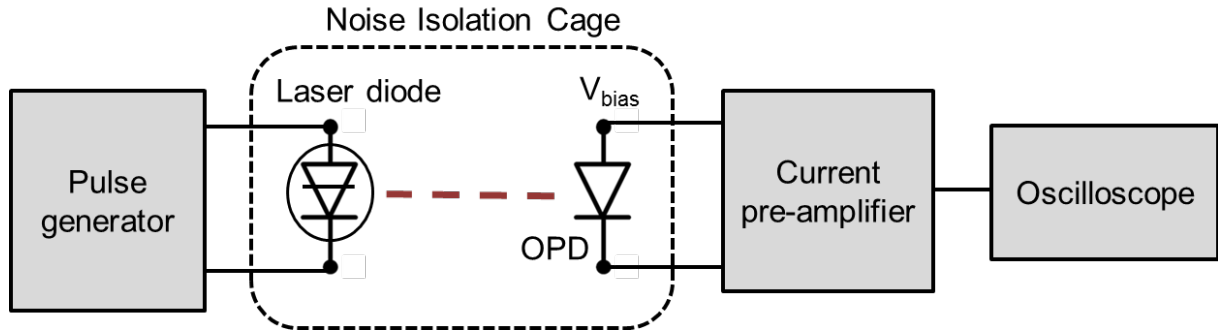
Figure 4.1. Schematic of the transient measurement setup.

To fully characterize the performance of the OPD, the evaluation of noise current is crucial since the lower limit of the photo detection ability is determined by the noise characteristic of the device. The major sources of noise in OPDs can be classified as Johnson (thermal) noise, shot noise (current fluctuations due to the discrete nature of the Poissonian distributed electrons) and low-frequency (flicker) noise [98]. These noise components have no correlation with each other so the total noise current of the OPD can be expressed as

$$i_{noise} = \sqrt{i_J^2 + i_{sh}^2 + i_f^2}$$ (4-1)

where i_J is the Johnson noise , i_{sh} is the shot noise and i_f is the flicker noise current [97].

Figure 4.2 shows the measurement setup used for the noise analysis. The device under test (DUT) is placed on the stage inside a noise-isolated Faraday cage to shield ambient electromagnetic noise. For further shielding of external ambient noise, the DUT is covered by a aluminum foil case. The noise current from the device is first amplified by a current pre-amplifier (SR 570, Stanford Research) which also provides a voltage bias to the device. The first amplified signal was passed through a high-pass filter (HPF) with 0.03 Hz cut-off frequency at +6 dB / octave to remove DC current components of the DUT with low drift gain mode. The pre-amplifier was powered by the ± 12 V batteries to prevent any AC coupled noise inteference from the power source. The final output signal was digitized by a FFT spectrum analyzer (SR760, Stanford Research).
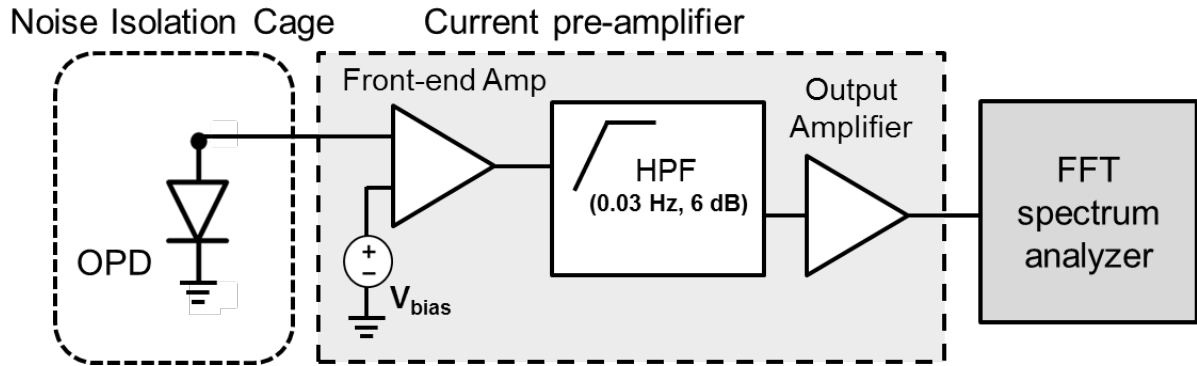
Figure 4.2. Schematic of the noise measurement setup.

To verify the accuracy of the noise measurement set-up, the Johnson current noise of metal-film resistors was measured. Johnson noise, first measured by John B. Johnson [153], is the thermal agitation of the electrons by the random thermal motion of electrons within resistive materials similar to Brownian movement. The thermal noise of a resistor R is directly proportional to the absolute temperature T and can be described as

$$i_j = \sqrt{\frac{4kT\Delta f}{R}} \tag{4-2}$$

where k is the Boltzmann's constant and Δf is the noise bandwidth. Because Equation 4-2 is independent of frequency, the Johnson noise is considered as a white noise source. The Johnson noise may become a dominant noise source when the dark current level of the photodetector is extremely low. (e.g. photovoltaic mode of the photodetector without any external bias to the photodetector).
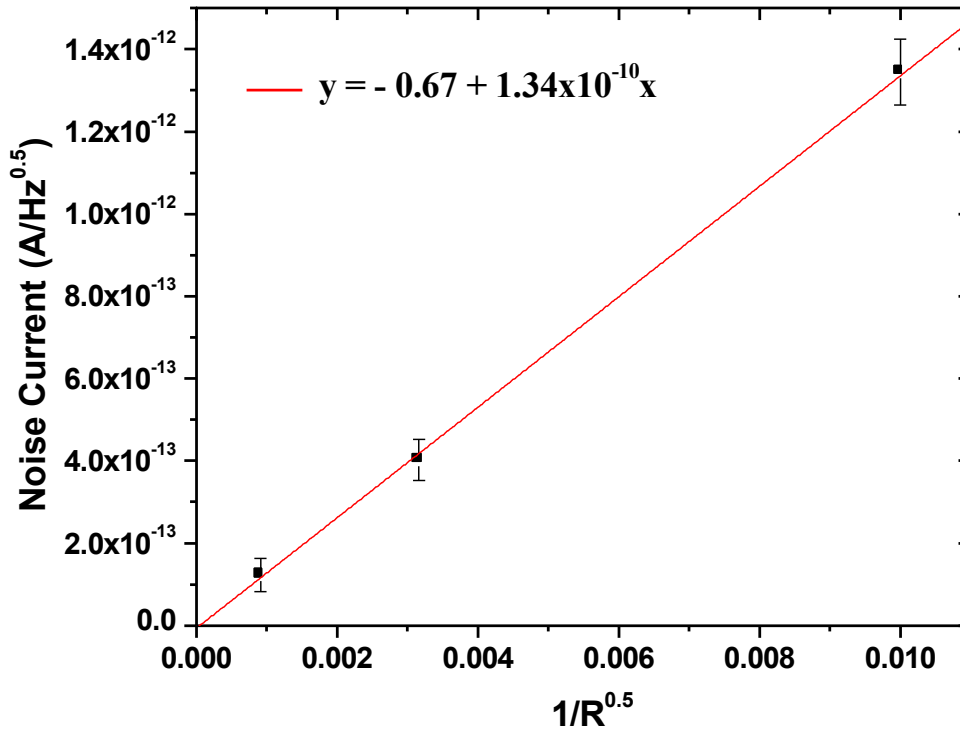
Figure 4.3 Johnson noise measurement with different value of metal-film resistors. The fitted line shows a good agreement with theoretical equation.

When the measured atmosphere temperature inside the Faraday cage was T = 296 K, Equation 4-2 now becomes $i_J = 1.278 \times 10^{-10} / \sqrt{R}$ [A/Hz$^{0.5}$] when R represents the measured resistor values of metal-film resistors. The measured R values were typically 10 kΩ, 100 kΩ and 1.2 MΩ. The measured noise current value for each resistor is plotted with error bar in Figure 4.3. The fitted line can be described by a linear equation, y = -0.67 + (1.34x10^{-10})x when x axis represents $1/\sqrt{R}$ and y axis is converted Johnson noise current in A/Hz$^{0.5}$. The fitted slope of 1.34 x 10^{-10} matched well with the theoretical expected slope value of 1.278 x 10^{-10}, which indicates that the noise measurement set-up is reliable. The lowest noise current value (noise floor) which the measurement set-up could detect was ~ 5 x 10^{-16} A/Hz$^{0.5}$.

4.3. Absorption Spectra of Films

The chemical structures of PTB7-Th polymer and PC$_{70}$BM are shown in Figure 4.4(a) and Figure 4.4(b) shows energy diagram of the different materials used in our OPDs structure. The diagram shows a good alignment of the conduction band of the ZnO layer (4.4eV [86]) with the lowest unoccupied molecular orbital (LUMO) level of PC$_{70}$BM (4.3eV [154]) and the conduction band of the MoO$_3$ layer (5.5eV [88]) with the highest occupied molecular orbital (HOMO) level of PTB7-Th (5.4eV [155]).
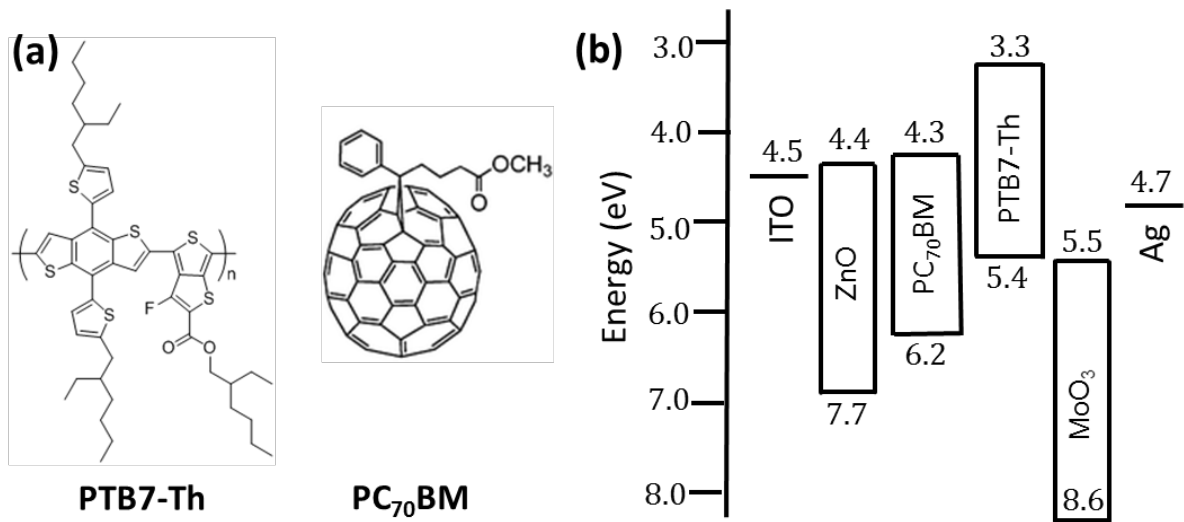
Figure 4.4. (a) Chemical structure of PTB7-Th and PC$_{70}$BM. (b) Energy diagram of the materials used in the OPDs.

As shown in Figure 4.5, the PTB7-Th polymer film absorbs from λ = 300 nm to λ = 800 nm, with a peak of 1.9 x 10^4 cm^{-1} at λ = 700 nm, showing low absorption profile at lower wavelength region. The PC$_{70}$BM shows absorption between λ = 300 nm to λ = 720 nm but decrease gradually from λ = 550 nm. This complementary absorption spectra of PTB7-Th and PC$_{70}$BM result in broad absorption spectrum for PTB7-Th:PC$_{70}$BM BHJ film over all visible range.

The optical energy gap (E$_G$) of the PTB7-Th:PC$_{70}$BM BHJ film was estimated by the Tauc plot of the absorption spectra in Figure 4.6 [141]. By assuming the active layers are in amorphous 3-D structure, the relationship between the absorptivity and E$_G$ can be described by $(\hbar\omega\alpha)^{1/2} \propto (\hbar\omega - E_G)$ where $\hbar\omega$ is the photon energy. The Tauc gap (E$_G$) of the PTB7-

Th:PC$_{70}$BM BHJ film extracted from the figure was 1.50 ± 0.01 eV, which is ~ 0.3 eV lower than P3HT:PCBM BHJ as described in Chapter 3.3.6.
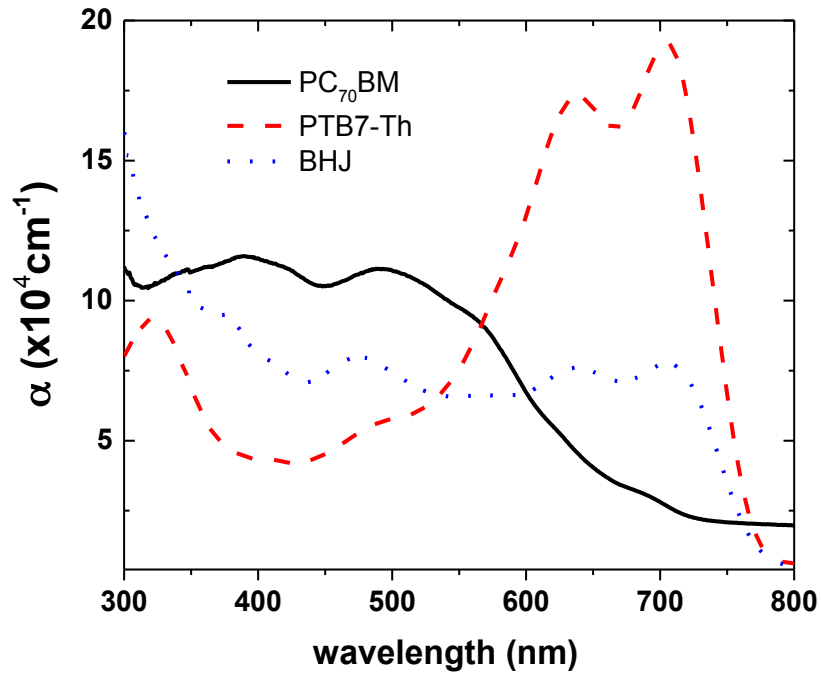
Figure 4.5 Absorption coefficient plot versus wavelength for PC$_{70}$BM , PTB7-Th (transferred), PTB7-Th:PC$_{70}$BM BHJ film.
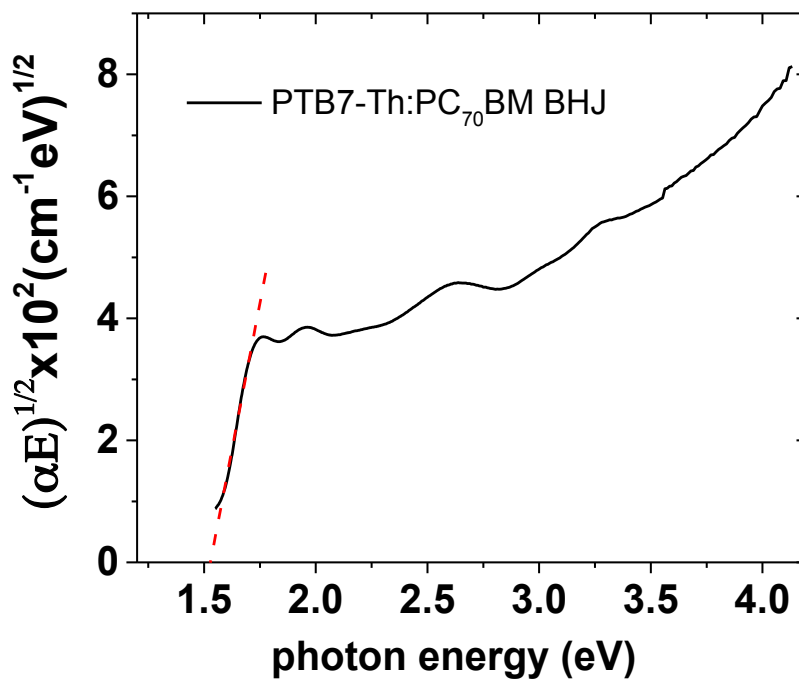
Figure 4.6 Tauc plot versus photon energy for PTB7-Th:PC$_{70}$BM BHJ film.

4.4. Results and Discussion

To evaluate the opto-electronic properties of the OPD, we fabricated and investigated following structures of OPDs :

(i) **D1** : ITO/ ZnO/ PTB7-Th:PC$_{70}$BM 150 nm/ MoO$_3$/ Ag (reference cell)

(ii) **D2** : ITO/ ZnO/ PC$_{70}$BM 90nm/ PTB7-Th 100nm/ MoO$_3$/ Ag

(iii) **D3** : ITO/ ZnO/ PC$_{70}$BM 50nm/ PTB7-Th:PC$_{70}$BM 100nm/ PTB7-Th 50nm/ MoO$_3$/ Ag

(iv) **D3*** : ITO/ ZnO/ PTB7-Th:PC$_{70}$BM 100nm/ PTB7-Th 50nm/ MoO$_3$/ Ag

(v) **D4** : ITO/ ZnO/ PC$_{70}$BM 50nm/ PTB7-Th:PC$_{70}$BM 150nm/ MoO$_3$/ Ag

D1 was the reference cell with typical BHJ active layer and inverted structure. In the device, MoO$_3$ HTL and ZnO ETL are directly in contact with the active layer and no additional buffer layer is employed.

D2 device is the bilayer structure fabricated by DTS process. The thickness of the acceptor layer was precisely controlled to be 90 nm through spin-casting process optimization while polymer layer thickness was adjusted by controlling the concentration of the solution and the stamping pressure during DTS process.

D3 and D3* devices exhibit additional PTB7-Th EBL on top of the active layer, transferred by the DTS process. The difference between D3 compared to D3* was the existence of the additional PC$_{70}$BM HBL on bottom of the active layer. The total thickness (150 nm) of BHJ layer plus EBL in D3* was kept same as BHJ thickness of D1 device to exclude influence of the series resistance associated with the film thickness variation of active region. D4 device is composed of only PC$_{70}$BM HBL layer without EBL layer. For the discussion of the OPD characteristics, D4 device was omitted intentionally since it showed almost identical OPD performance with D1 reference cell. D4 device will be discussed in more detail later as it showed superior photovoltaic performance than other devices. Through investigation of these

various device structure, we were able to determine the D3 OPD has the best yielding the

highest detectivity. Figure 4.7 visualized the device structures of the studied OPDs ; D1, D2

and D3.
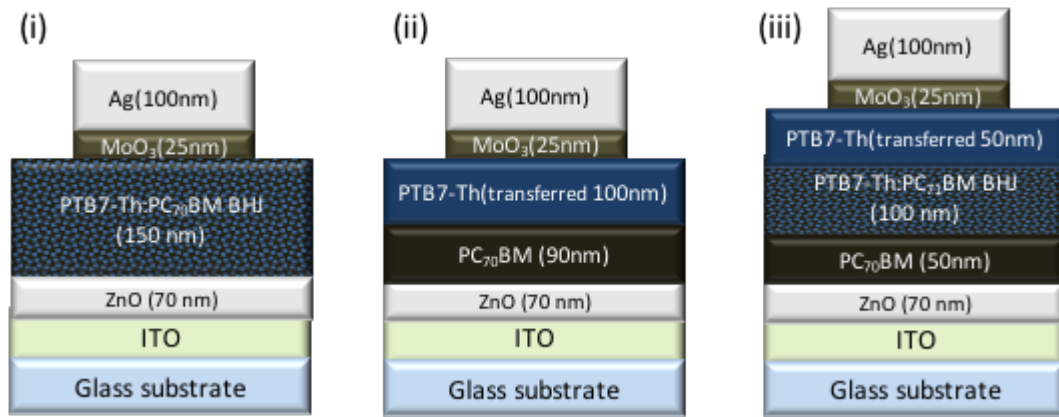
Figure 4.7 Device structures of the selected low bandgap polymer OPDs (i) D1, reference cell with typical BHJ active layer (ii) D2, bilayer cell with DTS method (iii) D3, BHJ active layer cell with hole and electron blocking layers.

The dark current density (J_d) versus applied voltage (V) characteristics of D1, D2, D3

and D3* devices are plotted in Figure 4.8. As shown in the figure, the D1 reference device

without any EBL or HBL showed a large dark current of about 0.43 $\mu A/cm^2$ at reverse bias of

0.5 V, which is one or two orders of magnitude larger than the other devices. In general, high

level of the dark current is not usually suitable for the high performance OPD application [2].

As the first attempt to suppress the dark current, we tried to fabricate a bilayer interdiffused

device D2 using DTS process as we described in Chapter 3. Different annealing conditions after

bilayer formation have been conducted to facilitate the interdiffusion process of the $PC_{70}BM$

fullerene molecules into the polymer material. The post-annealing process with temperatures

of as-cast, 100 ^{o}C, 120 ^{o}C and 140 ^{o}C were done following Experimental procedure described

in Chapter 3. Even though we succeeded to supress the dark current level about 20 times

compared to D1 down to $J_{dark} = 25.3$ nA/cm^2 at - 0.5 V, the various annealing conditions could

not enhance EQE value (~10 %) of D2 devices as shown in Figure 4.9, indicating the

interdiffusion process was not efficient compared to interdiffusion process of P3HT / PCBM

discussed in Chapter 3. This observation implies that the interdiffusion process efficiency between a polymer and fullerene molecules is influenced by the chemical structure or materials properties (e.g. hardness, tensile strength, etc) of the polymer material.
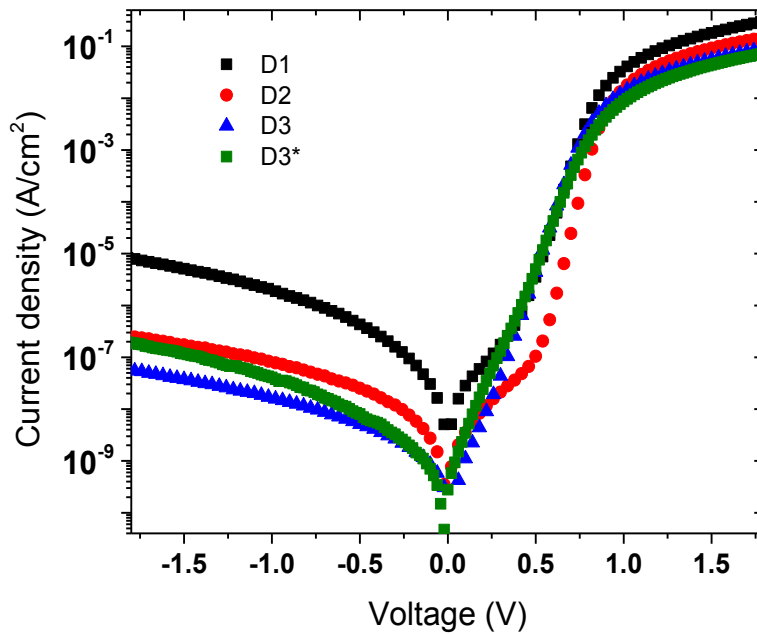
Figure 4.8 J_d-V curves in the dark for BHJ reference cell (D1), Bilayer device (D2), BHJ device with both HBL and EBL (D3) and BHJ device with only EBL (D3*).
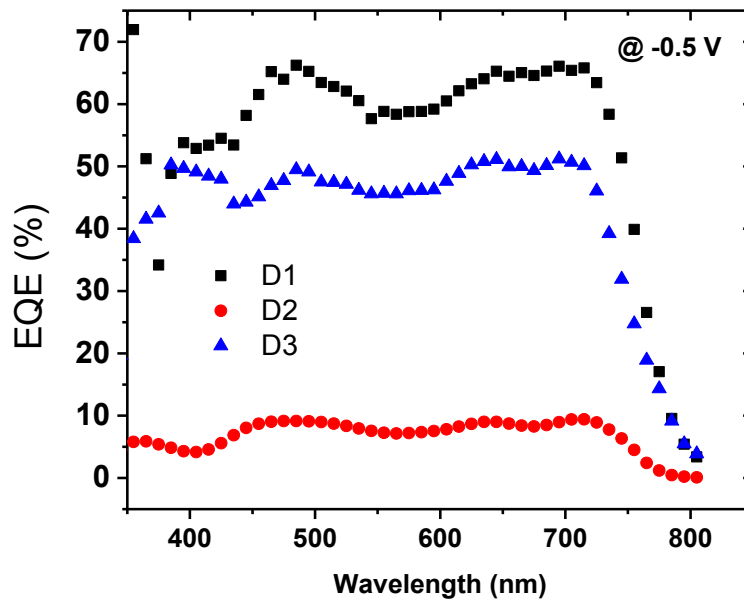
Figure 4.9 EQEs of the BHJ control device (D1), bilayer device (D2) and BHJ device with both EBL and HBL blocking layers (D3) at reverse bias of 0.5 V.

To alleviate the low EQE problem, D3 and D3* devices were fabricated by modifying the D1 structure by adding PTB7-Th EBL using DTS process on top of the BHJ film. As discussed earlier, the D3 device has additional $PC_{70}BM$ HBL compared to D3* device. For D3 and D3* device fabrication, the DTS process is crucial because the PTB7-Th EBL solution can re-dissolve and damage the BHJ layer previously deposited, resulting in unreliable OPD performance. As shown in Figure 4.8, D3 device showed the dark current of about 5.1 nA/cm^2 at reverse bias of 0.5 V when D3* device showed slightly larger J_d = 8 nA/cm^2, demonstrating the effectiveness of electron blocking of the transferred PTB7-Th layer at the anode side. It should be noted that the D3 device with additional $PC_{70}BM$ layer under BHJ layer showed lower dark current level compared to D3* device with BHJ film directly deposited on ZnO buffer layer. The suppression of the dark current of D3 device is associated with the presence of $PC_{70}BM$ layer providing additional hole blocking function to ZnO ETL. Besides the decreased dark current level of D3 compared to D1 device, the forward bias dark current of D3 also decreased, resulting from increased series resistance due to additional PTB7-Th EBL and $PC_{70}BM$ HBL. The measured EQE value of D3 device was consistently around 50 % from 400 nm to 720 nm range which is ~ 15 % smaller than EQE of D1 control device. This is possibly due to the thinner active layer thickness and additional incident light absorption by the PTB7-Th EBL in D3 device which does not contribute to photocurrent generation. The deficiency of the electron acceptor material in the PTB7-Th EBL layer leads to inefficient photo-generated exciton dissociation process and subsequent overall EQE drop. Table 4.1 summarizes the dark current density, EQE and responsivity of the D1, D2, and D3 devices at wavelength 526 nm and 720 nm at reverse bias of 0.5 V. The responsivity $\mathcal{R}$ is directly related to EQE by a factor of $q\lambda/hc$. Since the responsivity is defined as the photocurrent per unit incident optical power, it can be used to determine the photogenerated current in response to the light wavelength of interest.

Table 4.1. J_{dark}, EQE and Responsivity comparison of the devices at wavelength of 546 nm (green light) and 720 nm (near IR) at -0.5 V bias condition

Device	J_{dark} at - 0.5 V	Responsivity at 546nm	EQE at 546 nm	Responsivity at 720nm	EQE at 720 nm
D1	430 nA/cm^2	253 mA/W	57.7 %	375 mA/W	64.6 %
D2	25.3 nA/cm^2	33 mA/W	7.6 %	54 mA/W	9.2 %
D3	5.1 nA/cm^2	200 mA/W	45.6 %	280 mA/W	48.3 %

To justify that the smaller EQE of D3 device compared to reference cell is due to reduced light absorption inside the BHJ layer, the simulation of optical field distributions for the D1 and D3 devices was done for 546 and 720 nm wavelength by Transfer Matrix method [80]. Figure 4.10 shows spatial distributions of the normalized squared optical electric field strength ($|E|^2$) inside D1 and D3 device structures. The chosen 546 and 720 nm wavelengths are typical spectra for indirect X-ray imager or IR detector applications, respectively [156,157]. The E-field profiles are consequence of the optical interference between the incident light from the ITO side and back-reflected light by the metallic Ag electrode. As shown in the figure, the E-field intensity $|E|^2$ for 546 nm and 720 nm wavelength inside D1 device was relatively higher than $|E|^2$ in D3 device. For $\lambda = 546$ nm, the addition of the PTB7-Th EBL spacer between active layer and MoO$_3$ layer resulted in right-shift of the interference maxima to reside in the EBL layer with overall $|E|^2$ decrease about 30 % compared to D1 device. The optical distribution of the 720 nm wavelength inside the active layer in D3 was greatly attenuated due to strong absorption in the PTB7-Th EBL film around $\lambda = 600 \sim 750$ nm region as shown in the absorption coefficient (α) plot of Figure 4.5. These results show consistent trend with EQE graph of Figure 4.9 ; the EQE values at 546 nm and 720 nm of D1 are higher than D3 by about 20 %.
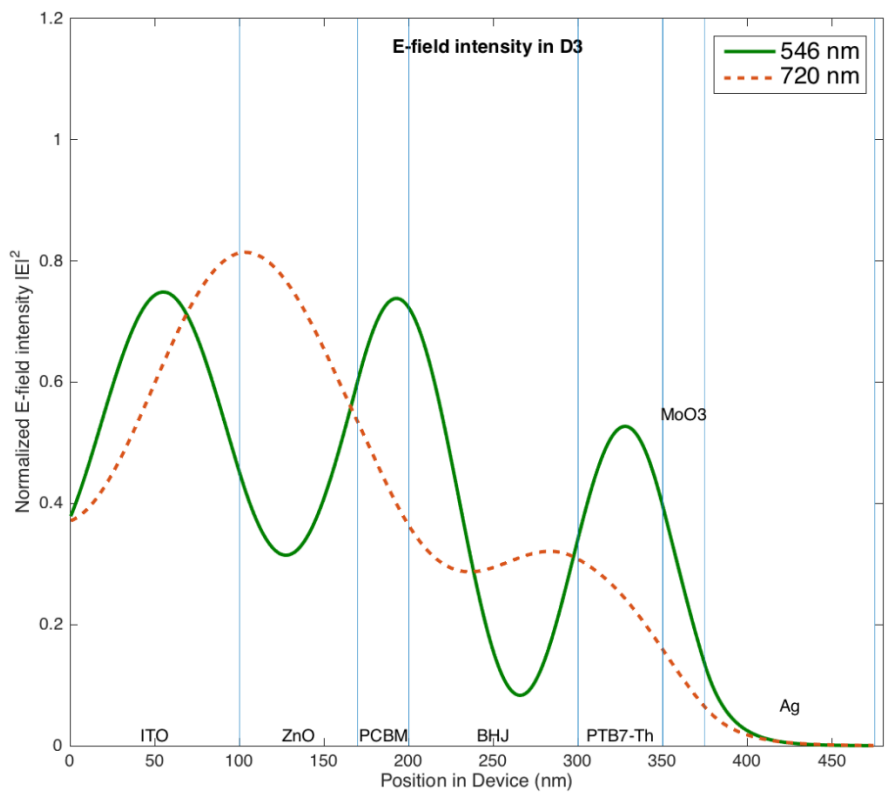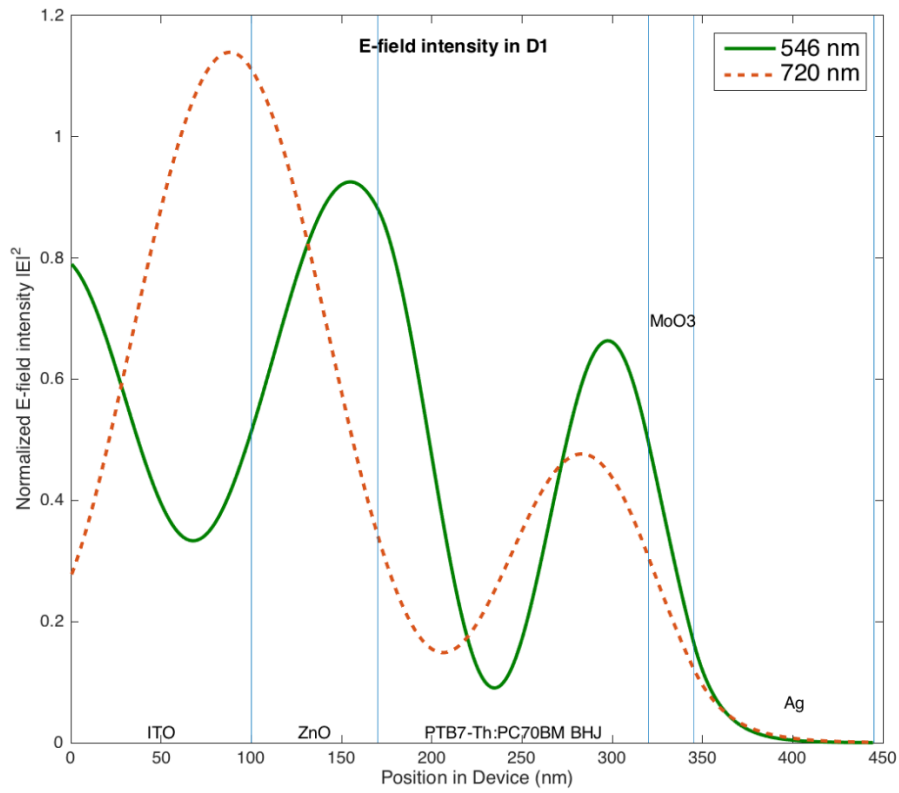
Figure 4.10 Optical distribution profiles of the E-field intensity in D1 (top) and D3 (bottom) devices. The excitation wavelength used were 546 nm (green) and 720 nm (near IR).

After establishing that the BHJ device sandwiched between PC$_{70}$BM HBL and PTB7-Th EBL can have reduced dark current and reasonably high EQE over a broad spectral range, it will be worthwhile to investigate the other OPDs key parameters. The most useful figure of merit to evaluate the OPD performance is specific detectivity D^*, which is the function of external quantum efficiency η, dark current I_d and other noise sources as following

$$D^* = \frac{EQEq\lambda\sqrt{A}}{hc}(i_{noise})^{-1} \quad [cm\sqrt{Hz}/W] \tag{4-3}$$

where A is the area of the OPD and i_{noise} is the noise current such as shot noise, Johnson noise or flicker noise. As shown in Equation 4-3, the high D^* requires a low noise current and high quantum efficiency. For the accurate evaluation of the specific detectivity, it is necessary to determine i_{noise} appropriately.

The noise characteristic of the D3 device is measured using a noise measurement set-up described in Chapter 4.2.2. Figure 4.11 shows comparison of the measured noise current versus dark-current of the D3 device. The noise current is commonly expressed as a summation of the shot noise i_{sh} and thermal noise i_j. It should be noted that the i_{sh} from the dark current is commonly assumed to be the dominant factor on noise, which is not always true and can underestimate the noise level due to additional flicker noise [46]. The shot noise current limit in the plot is calculated by $i_{sh} = \sqrt{2qI_d\Delta f}$ where I$_d$ is the dark current and Δf is the modulated bandwidth. The Johnson noise floor is also included in the plot. The measured dark current value was slightly higher but very close to the shot noise limit, which tells us that the noise of the OPD is dominated by the shot noise. The measured noise current i$_N$ = 5.31 x 10^{-15} A/Hz$^{0.5}$ at - 0.5 V was used to calculate the Noise Equivalent Power, $NEP = (\sqrt{\langle i_N^2 \rangle / \Delta f}) / \mathcal{R}$ of D3 device at 546 nm wavelength. Applying the responsivity value of 0.2 A/W at 546 nm wavelength with - 0.5 V bias, the corresponding NEP was 2.65 x 10^{-14} W/Hz$^{1/2}$ at reverse bias of 0.5 V at 546 nm.
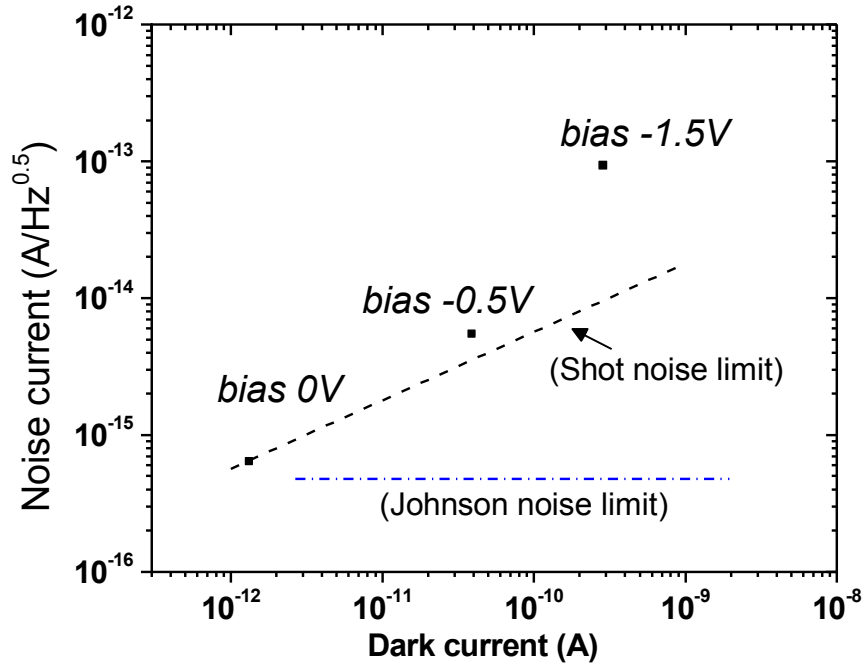
Figure 4.11 Shot noise current comparison with measured dark current of D3.
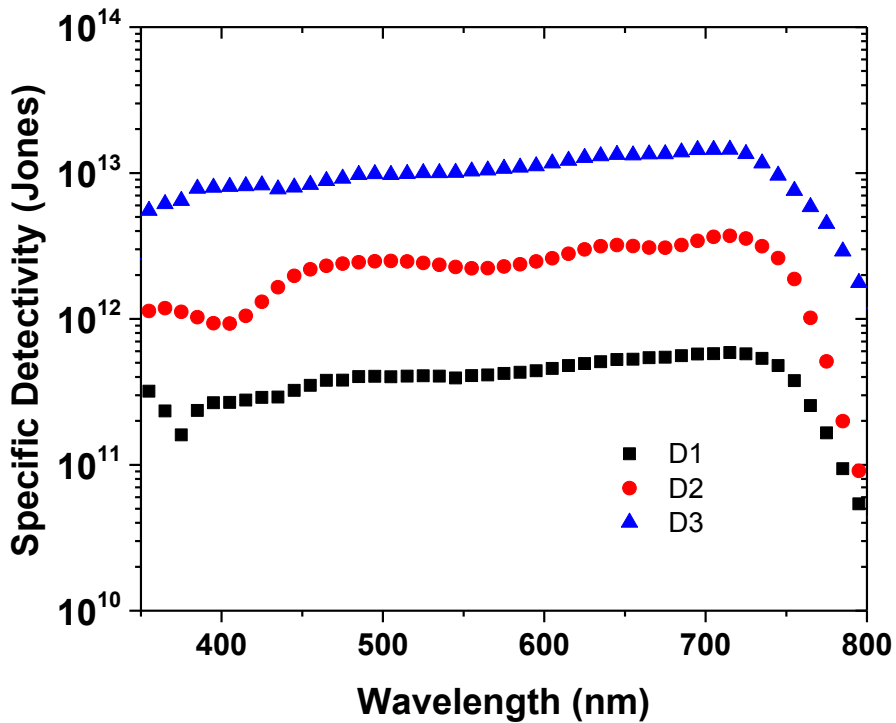
Figure 4.12 The measured specific detectivity as a function of wavelength at − 0.5 V bias condition of D1, D2 and D3 device.

Using the measured noise current at a corresponding reverse bias, the specific detectivity

D^* for D1, D2 and D3 device was calculated and plotted in Figure 4.12. As shown in Table 4.1,

even though the EQE value of D1 was ~ 10 % higher than D3, about two orders of magnitude lower dark current level of D3 device yielded the highest D^* of reaching $\sim 10^{13}$ cm·Hz$^{1/2}$W^{-1} at 0.5 V reverse bias covering all the visible spectral region of 400 nm to 750 nm with highest D^* = 1.48 x 10^{13} cm·Hz$^{1/2}$W^{-1} at 700 nm. This specific detectivity obtained is one of the highest detectivity among organic semiconductor based photodetector published so far [2,48,152,158,159]. The peak specific detectivity of the D2 bilayer device was D^*_{peak}(D2) = 3.56 x 10^{12} cm·Hz$^{1/2}$W^{-1} at 700 nm, which is about one order higher than D^*_{peak}(D1) = 5.93 x 10^{11} cm·Hz$^{1/2}$W^{-1} of the reference cell. Considering the lower EQE value of D2 (less than 10 %) compared to EQE $\simeq$ 60 % of the D1 device (Table 4.1), it is clear that devices having a low dark current (noise current) level can achieve higher detectivity.

Figure 4.13 shows the J-V characteristics of D3 device with various light intensities of the 546 nm wavelength illumination. The figure indicates that the OPD responses to light irradiance down to 960 nW/cm^2, having more capability to detect weaker light intensity at low negative bias region (0 V ~ - 1 V) while the photoresponse is being limited by the dark current at higher bias region over - 2 V. Meanwhile, the photocurrent at positive bias above open circuit voltage has no variation, which indicates the series resistance R_S of the OPD is not affected by the irradiance level. According to the various input irradiance level, The linear dynamic range (*LDR*) of the D3 device is plotted, which is defined as $LDR = 20\log(J^*_{ph}/J_d)$ [dB] where J^*_{ph} is the photocurrent density of the OPD [97]. *LDR* of the D3 device at reverse bias of 0.5 V for 546 nm wavelength was plotted in Figure 4.14, which shows the value over > 90 dB . The measured responsivity with input irradiance variation for 546 nm wavelength is also plotted together. Due to the linear photocurrent generation with light intensity variation, the responsivity of the OPD was also constant at different irradiance levels, which tells us that the OPD performance is quite stable.
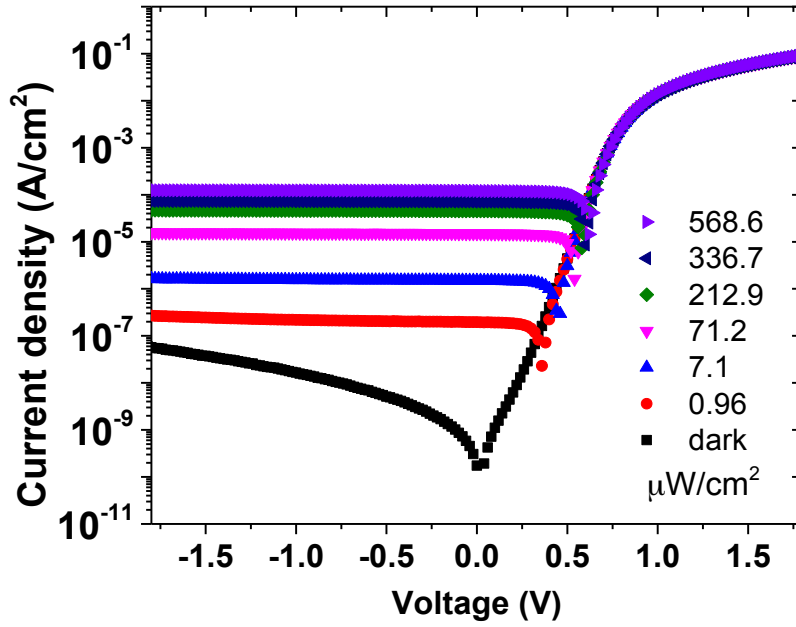
Figure 4.13 Current density versus voltage curve of D3 under various light intensity with 546nm wavelength.
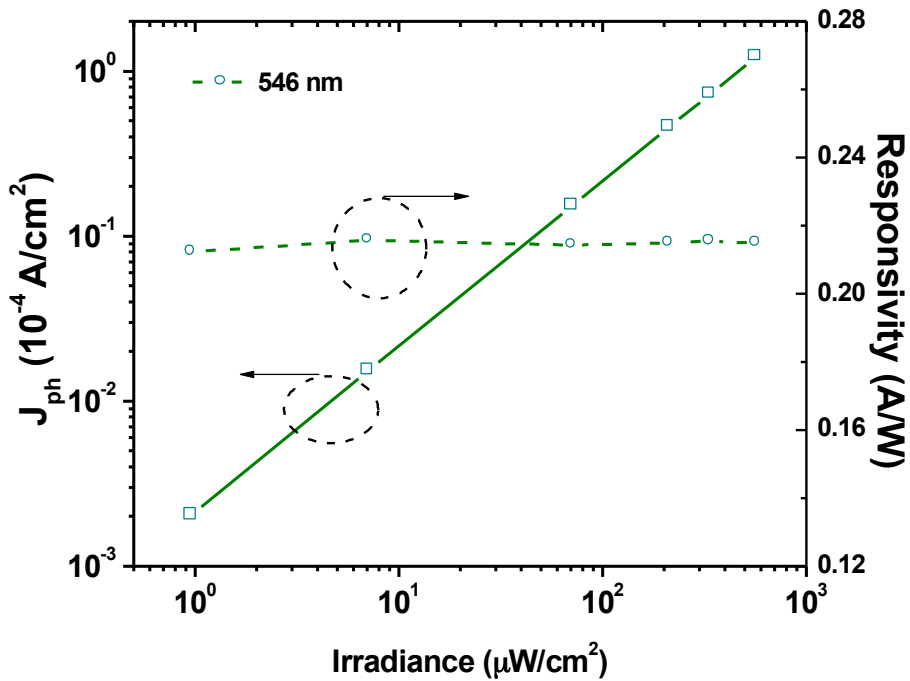
Figure 4.14 Variation of the photocurrent and Responsivity with irradiance of the D3 device under monochromatic light of 546 nm and reverse bias of 0.5V in linear scale.

Transient response and 3 dB bandwidth characteristics of the D3 device were measured

as shown in Figure 4.15. The 3 dB bandwidth is defined as the frequency of the light signal

modulation at which the output photo response is -3 dB half power lower than continuous wave response. The light intensity of the modulated input signal was kept at 5 μW/cm^2. The measured 3 dB bandwidth frequency (f_{3dB}) with reverse bias of 0.5 V was about 700 kHz with the modulated light intensity of 13.2 mW/cm^2.
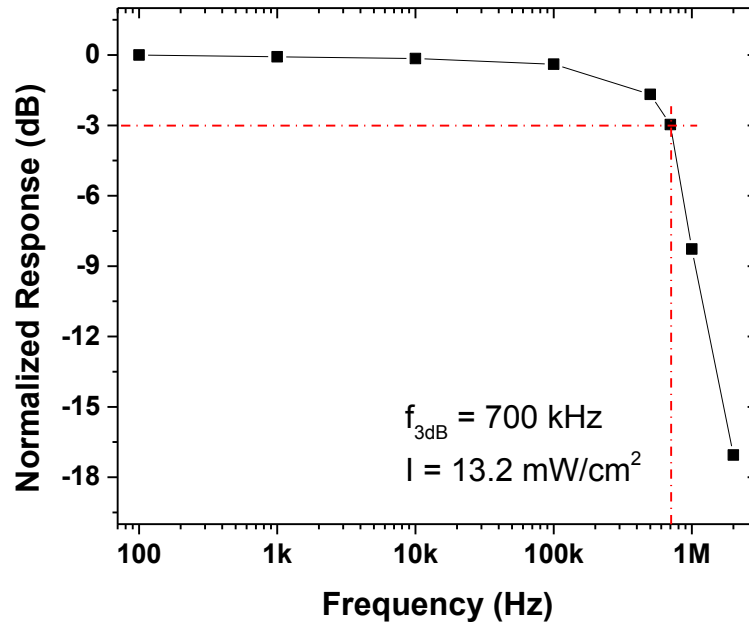
Figure 4.15 3dB bandwidth plot with 650nm laser diode.

Even though we focused on the evaluation and discussion of the OPD characteristics throughout the chapter, it is worthwhile to discuss the solar cell performance of the fabricated devices because one of the OPD structures showed desirably high photovoltaic performance under 1 sun illumination condition (AM 1.5G). The measured photo current density - voltage curves and key photovoltaic parameters of the fabricated devices are shown in Figure 4.16 and Table 4.2, respectively. For the photovoltaic performance comparison, the D4 device, the cell with only PC$_{70}$BM HBL, is included which showed the highest performance with the best PCE of 8.45 %. D1 reference device, without any additional buffer layer exhibited PCE of 6.51 % with the short-circuit current density (Jsc) of 15.63 mA/cm^2, open circuit voltage (Voc) of 0.8 V, and fill factor (FF) of 52.1 %. The bilayer D2 devices exhibited PCE of 0.96 % mainly due

to low Jsc of 2.34 mA/cm^2 with similar Voc = 0.78 V and 53.14 % of FF. The low Jsc of D2 device is originated from low EQE value over the spectrum range as already shown in Figure 4.9. D3 device, which showed the best OPD performance with the highest detectivity, gave PCE = 5.56 % which is slightly lower than reference cell. The smaller PCE was mainly caused by reduced Jsc = 12.51 mA/cm^2. The smaller Jsc is due to the undesirable light absorption in the PTB7-Th EBL layer, which is validated by the optical field distribution comparison in Figure 4.10. Device D4, the BHJ cell with PC$_{70}$BM HBL underneath the active layer, exhibited the best PCE of 8.45 % mainly due to enhanced FF of 67.79 % with similar Voc of 0.8 V and Jsc of 15.58 mA/cm^2. The additional PC$_{70}$BM buffer layer possibly enhanced the balance of charge transport and decreased the contact resistance, resulting in improved FF compared to reference cell [160,161].
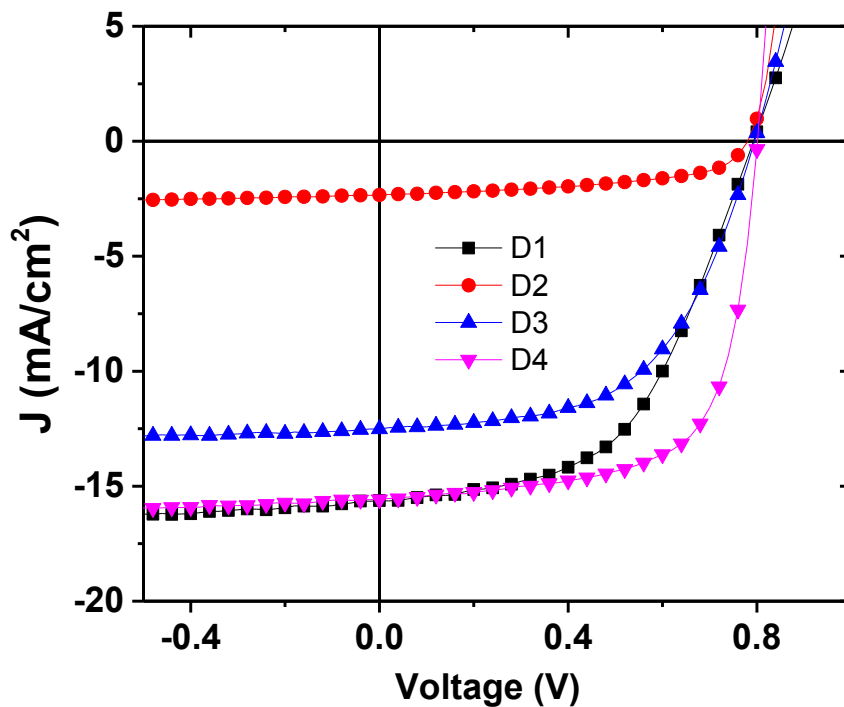
Figure 4.16 J-V characteristics of the OPDs under illumination at 100 mW/cm^2 (AM 1.5G). D4 device is also compared with the other devices already evaluated for OPD performance.

Annealing conditions	Jsc (mA/cm^2)	Voc (V)	FF(%)	PCE(%)
D1	15.63	0.80	52.10	6.51
D2	2.34	0.78	53.14	0.96
D3	12.51	0.80	55.55	5.56
D4	15.58	0.80	67.79	8.45

Table 4.2 Summary of photovoltaic figures of merit under AM 1.5G condition for D1 ~ D4 devices.

4.5. Conclusion

In this chapter, a high performance low-bandgap polymer OPD was fabricated using a PTB7-Th:PC$_{70}$BM BHJ sandwiched between PC$_{70}$BM HBL and PTB7-Th EBL enabled by a novel double transfer stamping (DTS) method. A low dark current of ~ 5 nA/cm^2 at reverse bias 0.5 V was achieved resulting in high specific detectivity of 1.48 x 10^{13} Jones at 700 nm. We elucidate that the reduced dark current by transferring PTB7-Th film is due to efficient charge blocking function of the film under reverse bias by increase of the interfacial barrier at anode side. Further analysis of the device properties revealed that the device with the electron blocking layer has fast frequency response with f$_{-3dB}$ = 700 kHz. A reliable noise measurement for the OPD is performed and the OPD showed *NEP* of 2.65 x 10^{-14} W/Hz$^{1/2}$ with 0.5 V reverse bias at 546 nm. Finally, the optimum structure for the PTB7-Th:PC$_{70}$BM BHJ photovoltaic cell was investigated. We demonstrated that the BHJ device with PC$_{70}$BM HBL showed the best solar cell performance with PCE of 8.45 %. We believe that the performance of the PTB7-Th:PC$_{70}$BM OPD / OPV can be further enhanced by deliberate design of the each active / buffer layer and utilization of the DTS process which enables a reliable film transfer process of the charge blocking layers without damaging preceding layer.

Chapter 5.
Hemispherical Organic Photodiodes Arrays Enabled by Three Dimensional Printed Masks

5.1 Introduction

Most of the current image sensors and cameras are based on flat focal plane array (FPA) technology, which is developed either on flat silicon substrate (CCD, CMOS) or glass substrate (TFT). The planar FPA requires complex multi-element lenses to correct the image surface ; i.e., the Petzval surface. The deviations of the optical system performance lead to a distorted and blurred image due to off-axis aberrations. To correct these problems, additional optical elements and high precision lens system are required, which result in more complex and expensive optical system. Compared to the camera system with the flat FPA, a curved image surface mimicking a spherical human retina provides numerous advantages. The image system with the curved image surface can provide a wide field of view (FOV), a low optical aberration, low 1/f number and less optical lens components which lead to compact, cheaper and lighter camera system. [162–164].

However, the fabrication of image sensors on curved surface has long been a challenging task among researchers due to the difficulty of the development of the fabrication method. To name a few efforts, Yoo et al reported a fabrication of a-Si:H TFT passive pixel sensor (PPS) array on hemispherical surface by maskless laser-write lithography (LWL) method [165]. The successful fabrication of the PPS array on hemispherical surface showed a potential for the fully functional image sensor when it can be possibly integrated with organic photodiode on the top of the array. On the other hand, Xu et al. demonstrated an organic photodetector array on a

hemispherical substrate by cold welding method [55].

In Chapter 3 and 4, we proposed a novel transfer printing method called DTS process which provides a degree of freedom on fabrication of polymer based organic photodiode devices. The PDMS stamps for the DTS process can be not only prepared on flat substrate but also on hemispherical surface if an appropriate substrate is ready. We utilize a customized concave glass substrate already used for the a-Si TFT PPS array fabrication in our lab to fabricate the organic photodetector array on a hemispherical surface [165,166]. To realize the OPD array on a hemispherical surface, we suggest a novel process by combination of the modified transfer stamping process and a stereolithography technique to fabricate a three dimensional (3D) mask for metal electrode deposition.

5.2. Curved Focal Plane Arrays for Imaging Systems

5.2.1 Human eyes and conventional camera system

A vision system of primates such as human eyes is regarded as one of the ideal imaging systems due to its wide field of view (FOV), low aberration, and low f-number. Its simple one-lens imaging system is enabled by the curved retina, located at the back of the eyeball, as shown in Figure 5.1 (a). Compared to the natural imaging system, the artificial imaging system such as CMOS / CCD cameras relies on flat, brittle, silicon-based planar FPAs. Even though both human eyes and artificial cameras resemble in structures which comprise an aperture, optical elements (lenses) and a FPA, the different shapes of the focal plane distinguish the complexity of overall system, especially in number of lens elements. As shown in Figure 5.1(b), in modern digital cameras, due to flat shape of the FPA, multiple lens elements with high precision are required to allow the image surface (Petzval surface) to be flattened so the major optical aberrations such as coma, field curvature, and distortion can be suppressed. This complex lens system became major barrier to develop light-weighted, wide FOV with free of image distortion

imager for next-generation camera systems. Therefore, it is inevitable to investigate a curved imager sensor which can potentially leads to better image quality with less aberration, more compact and simpler optics.
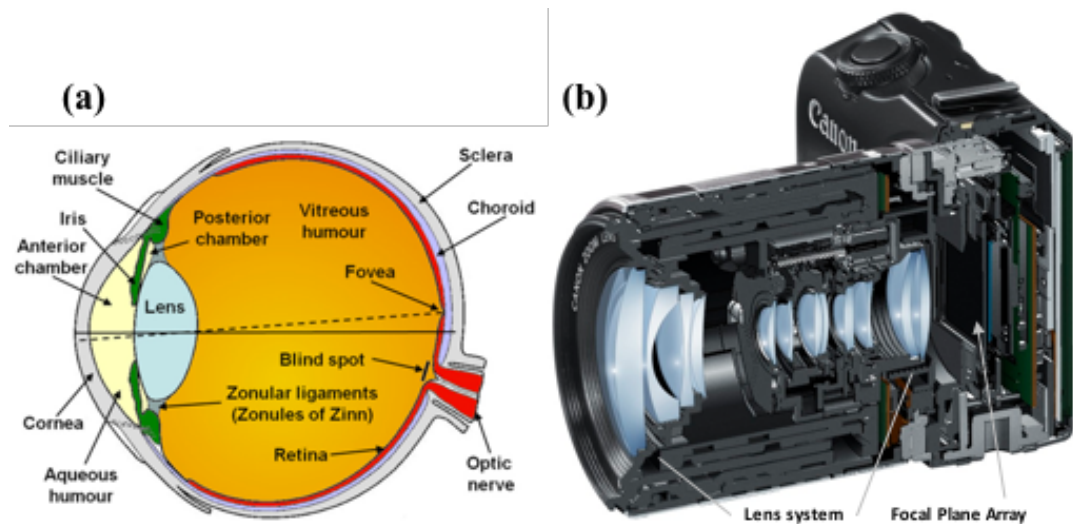
Figure 5.1 Cross sectional view of (a) human eye (image adapted from [167]) (b) modern digital camera system (image supplied by Canon inc. [168]).

5.2.2 Comparison between different camera systems

As we mentioned above, a curved image sensor such as retina has an obvious advantage that can make the lens system much simpler since the edges of the focal plane are about the same distance from the lens as the center. In contrary, the edge of the flat FPA is farther from the lens, while the center is closer, which eventually results in corner blurriness. To emphasize the advantage of the curved FPA system, more analytical comparison between different FPAs and lens systems using optical modeling are illustrated in Figure 5.2.

Total three optical systems considered (Figure 5.2. (a)-(c)) and compared. The optical traces of the three systems are produced using the ray tracing software (Zemax OpticStudio 16®) and the result is shown as image (I)-(III) which are generated from system (a)-(c), respectively [169]. The images are simulated by employing the Image Simulation feature of the software which visualizes geometric aberrations of the modeled optical system which considers

lens properties, object radiance, geometric distortion and spatially-variant PSFs (point spread functions) at various wavelengths. System (a) is Cooke triplet lens system, which is a typical three-lens system for low-end cameras [170]. System (b) consists of a convex lens (r = 18 mm) and a planar FPA with a 10 mm diameter. System (c) has same convex lens with System (a) but with a hemispherical FPA with radius-of-curvature of r = 10 mm. Our glass substrate is used as lens material (refractive index n= 1.5168) for the systems. The excited wavelength for all the systems was λ = 546 nm.
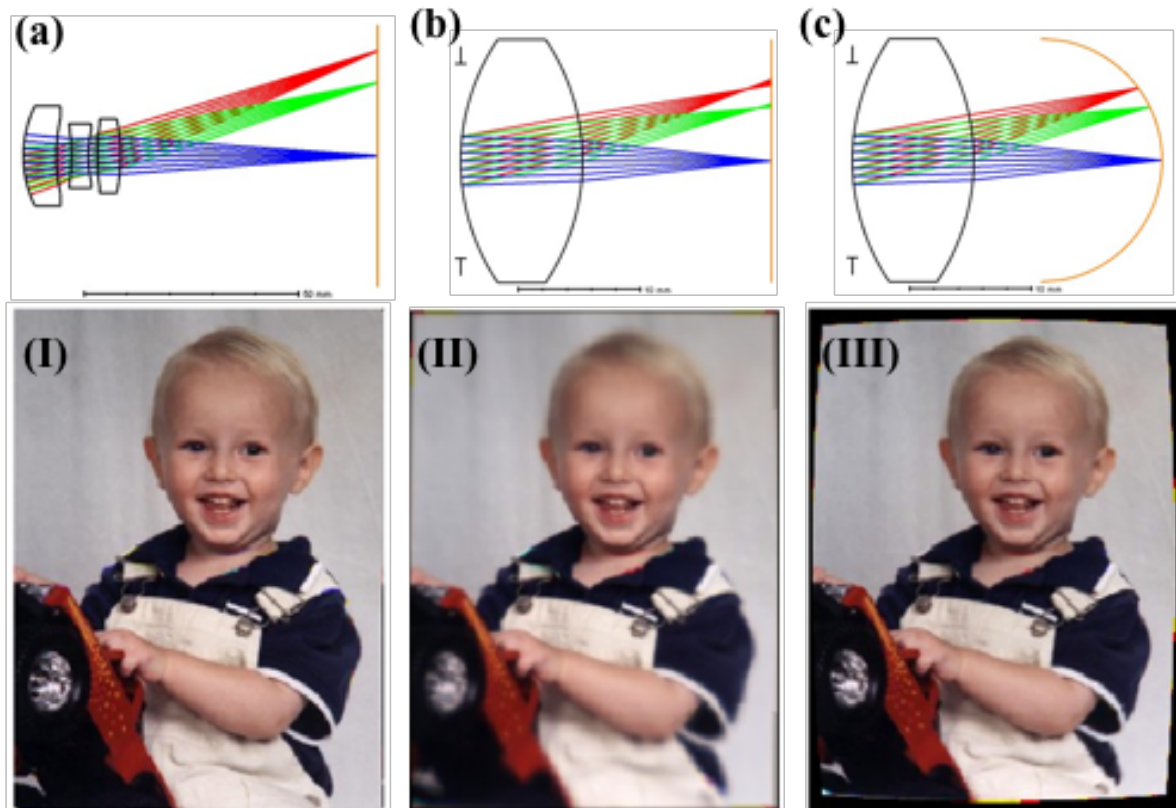
Figure 5.2 Three different optical systems (a) Cooke triplet (b) flat FPA with single lens (c) hemispherical FPA (r = 1 cm) with single lens. (I-III) images generated by corresponding optical systems (a-c), respectively.

As shown in the figure, System (b) with single lens and flat FPA produces an image (II) with blurred boundaries and barrel distortion. However, System (a) and (c) resolved the problem of system (b) and generate images with good quality and suppressed geometric

aberration. Moreover, a curved focal plane of system (c) represents a significant improvement for better imaging capability than system (a) in terms of simplicity of the lens system. Based on the analysis, it is obvious that employing a curved focal plane instead of flat focal plane can significantly reduce the number of lens components required to minimize the optical aberrations, and increase the overall performance of the imaging system.

5.2.3 Challenges to fabricate the curved focal plane array

Despite of many advantages of the hemispherical detector geometry, the realization of this type of curved detector has been suffered from extremely challenging fabrication process compared to well-established process for planar silicon-based FPAs, which comprises conventional patterning, deposition, etching, growth techniques.

The fabrication routes for the curved FPA can be largely categorized into two methods. The first one is patterning the circuit on flat substrate, followed by deforming the substrate into desired curved shape [163,171–173]. This method can be beneficial since it can use the mature semiconductor patterning techniques for silicon wafer before the deformation. However, due to the brittle nature of the conventional substrates such as silicon or glass, the strain that can be induced during the deformation is greatly limited, which otherwise can cause permanent damage to the devices.

Alternatively, the detector circuit can be directly patterned on the prepared curved substrate [55,174–177]. This method introduces no deformation-induced strain, and allows more freedom on the surface geometry. However, it requires special, unconventional patterning techniques to fabricate reliable devices on the curved substrates, which can be potentially quite complicated and unreliable for mass production of such devices. Even though various techniques to fabricate patterned detector arrays on curved surfaces have been reported [164,178–182], very few works have been done to fabricate fully functional detector arrays on

107

the curved substrates [55,176]. Hence, it is worthwhile to develop a new pathway to fabricate reliable photodetector array on hemispherical surface.

5.3. Preparation for the Curved Focal Plane Array Fabrication

To realize the FPA array on curved substrate, it is crucial to develop a reliable method to pattern metal electrodes and active layers on the non-flat surface. In this work, we propose two novel patterning methods to enable the direct fabrication of metal electrodes and organic active layers on hemispherical substrates. For the electrode deposition, a stereolithography technique to fabricate the 3D mask is employed [183–185]. The fabricated 3D shadow mask can be conformally attached to the curved surface for the metal electrode patterning process. The organic active layer on the hemispherical surface also requires non-conventional deposition technique other than typical spin-coating process. Here, we adapt modified transfer stamping process using 3D shaped PDMS stamp.

5.3.1. Stereolithography for 3D Mask Fabrication

The 3D shadow mask model was designed based on the dimension information of the hemispherical substrate shown in Figure 5.3 (a). The glass substrate is fully customized by a manufacturer to have FOV = 120° [165,166]. The prototype 3D shadow mask were modelled by SolidWorks 2016® (Dassault System, USA) CAD software to have total five uniformly distributed arrays (aperture = 1 mm, pitch = 1 mm) to fabricate 5 x 5 array. The solidworks file (.SLDPRT) was converted to .STL format to be compatible with 3D printer's software package. The modeled 3D shadow mask is shown in Figure 5.4 (a).
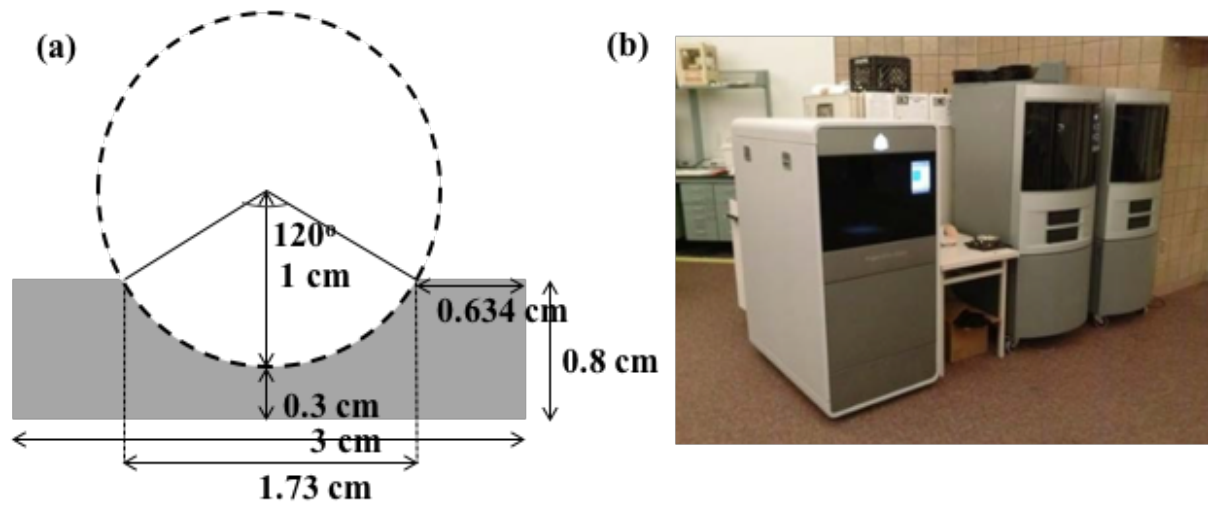
Figure 5.3 (a) Schematic of a hemispherical BK-7 substrate (b) Projet 3500 HDMax 3D printer used for the fabrication of the 3D shadow mask.
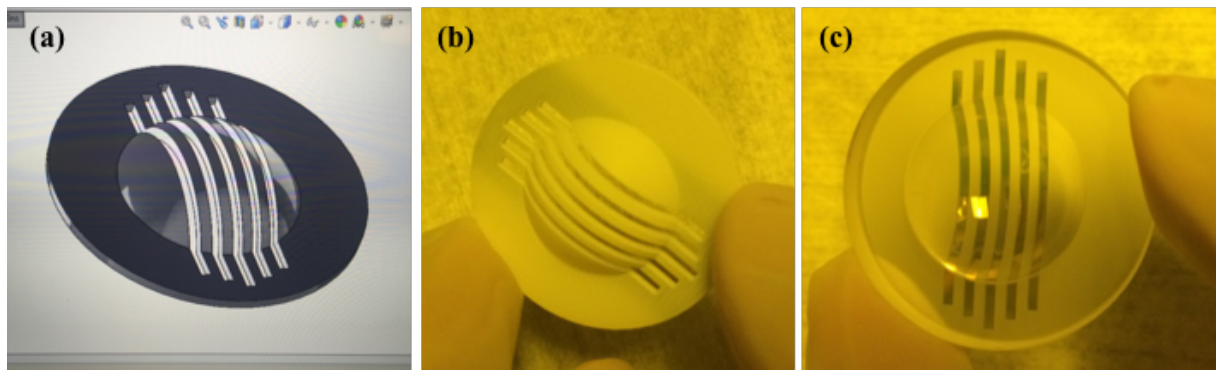
Figure 5.4 (a) Solidworks 3D modeling of the shadow mask (b) 3D printed plastic shadow mask (c) Bottom Au electrode (100 nm) patterned with the 3D shadow mask on the hemispherical substrate.

Projet 3500 HD*Max* (3D Systems, USA) high definition 3D printer (Figure 5.3 (b)) was used for the 3D shadow mask fabrication with 25 μm x-y and 16 μm layer thickness deposition resolution. The imported 3D CAD model of the 3D shadow mask was embedded into the ProJet built-in software with "Ultra High Definition" mode to yield the highest resolution.

The Projet 3D printer is based on multijet printing method (MJP method) [186]. The MJP process technology employs UV bulbs and photo-polymer materials with piezo-printhead technology to deposit the photocurable plastic resin. The print heads have several piezoelectric

nozzle rows arranged in a line. Each layer is exposed to UV for curing for immediate solidification, and the surface is milled to hold tolerance. This process is repeated until fabrication completion. Therefore, they are essentially stereolithography systems [183,187].

For the 3D mask fabrication, VisiJet M3-X (ABS like) resin (3D Systems) with VisiJet S300 Support Wax was used as per manufacturer standard operating protocol (SOP) [188]. The printed substance required several post-processing steps to remove the Support Wax to complete the process : (i) oven treatment at 70 °C for 30 min; (ii) ultrasonic cleaning in a canola oil at 50 °C for 5 minutes; (iii) ultrasonic cleaning in a canola oil at 50 °C combined with flushing devices with a warm canola oil (55°C) for up to 5 minutes; (iv) washing with Decon90 detergent for 5 minutes to flush out oil and remaining wax.

Figure 5.4(b) shows a prototype shadow mask fabricated by a 3D printer. The thickness of the 3D mask was 1mm to sustain the shape of the printed model. The thinner 3D printed shadow mask suffered from deformation due to soft material properties. The printed 3D shadow mask will be utilized for both top /bottom electrode deposition for the curved OPD with 90o vertical overlap to yield total 5x5 arrays. Finer and more precise pattern can be designed and fabricated for smaller pixel array fabrication. The prototype bottom electrode (Au 100 nm) on the hemispherical substrate deposited using the fabricated 3D shadow mask is shown in Figure 5.4(c).

5.3.2. Preparation of elastomeric 3D PDMS stamp

The elastomeric 3D PDMS stamps were prepared by mixing the Sylgard 184 silicone elastomer (Dow Corning) and a curing agent in clean room (53 % relative humidity, 22 °C temperature) environment [116]. The two components were mixed homogenously for 20 minutes and degassed in vacuum chamber at the pressure of ~ 0.4 psi overnight before being poured onto targeted hemispherical substrate. The concave glass substrate itself is utilized as

the mold for the 3D PDMS stamp. The curved glass substrate was placed at the center of a plastic weighing boat and the mixed PDMS solution was poured on the substrate to fully immerse the curved substrate. The PDMS solution was cured at room temperature for three days. The cured 3D PDMS stamps were gently peeled off from the substrate then cut into appropriate form for the stamping (Figure 5.5 (a)). The thickness of the PDMS stamps boundary were typically ~5 mm. The 3D PDMS stamps were attached to backing glass wafers for a conformal transfer process. For the active layer deposition, the modified transfer stamping process was performed by squeezing the active layer solution between a 3D PDMS stamped the hemispherical substrate. By adapting the modified transfer stamping process, we successfully demonstrated a uniform deposition of P3HT:PCBM BHJ film on hemispherical surface and this technique was used for the hemispherical OPD fabrication. Figure 5.5 (b) shows the uniformly printed P3HT:PCBM solution using the fabricated 3D PDMS stamp.
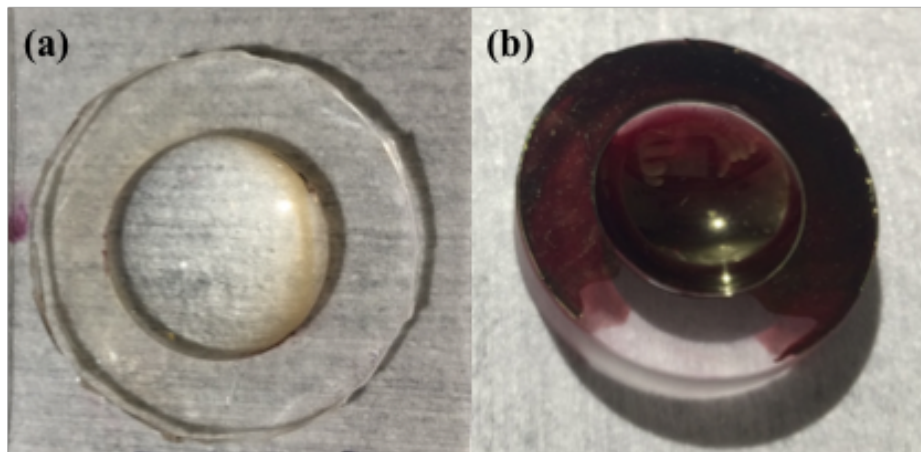
Figure 5.5 (a) Fabricated 3D PDMS stamp for the active layer formation (b) P3HT:PC$_{70}$BM active layer printed on the hemispherical substrate

5.4. Fabrication of Hemispherical Focal Plane Arrays

For the fabrication of the hemispherical FPA, we adapt the 3D shadow mask and 3D PDMS stamp described in previous section. We demonstrate 5 x 5 passive pixel array with 1 mm^2 feature size, which the active layer is perpendicularly sandwiched between bottom Al cathode and top DMD anode stripes. The hemispherical glass substrates were cleaned by

acetone, isopropyl alcohol, and deionized water, and treated by O_2 plasma (80 sccm, 160 mT, 300 W) for one minute subsequently. The prepared 3D shadow mask was attached on the curved substrate and placed inside a thermal evaporator for bottom electrode deposition. 80 nm of aluminum layer was thermally evaporated with the shadow mask with 1 Å/s deposition rate (Figure 5.6(a)). The PEIE solution was prepared by dissolving 5 wt% of PEIE (Sigma Aldrich) in 2-methoxyethanol (2ME, Sigma Aldrich) solvent in ambient atmosphere. The PEIE solution was spray-coated on top of the Al patterned curved substrate to uniformly deposit < 10 nm of PEIE dipole layer and annealed at 100 ^{o}C for 10 minutes in air. The substrates were transferred into a glove box with nitrogen atmosphere for deposition of photoactive layer. 20 mg of P3HT (Rieke Metals) and 20 mg of PCBM (American Dye Source, Purity: >99.5%) were mixed into 1mL of chlorobenzene (CB) and stirred by magnetic bar overnight for the BHJ solution, and filtered by 0.45 μm syringe filter subsequently. Next the BHJ solution was drop-casted on the curved substrate followed by quick squeeze with 3D shaped PDMS stamp to form a uniform BHJ film on the curved substrate. Once the BHJ film formation is completed the BHJ active layer is thermally annealed with temperature of 150 ^{o}C (Figure 5.6(b)). The final thickness of the BHJ active layer was measured by Dektek profilometer yielding 250 ± 20 nm. The BHJ layer formed substrates were transferred into thermal evaporator with the 3D shadow mask on it to deposit 5 nm MoO_3, 15 nm Ag and 35 nm MoO_3 subsequently for the transparent top anode formation. The transparent Ag metal layer needed to be thicker than the optimized DMD electrode in Chapter 2 to prevent the disconnection of the metal strips at the outside edge of the hemispherical dome. The devices were encapsulated with a thin slide glass sealed by UV curable epoxy resin to finish the device fabrication (Figure 5.6(c)). An individual device size was (0.1 x 0.1) cm^2 with square shape with total 5 x 5 array. The picture of completed hemispherical OPD device is shown in Figure 5.7.

(a)

Al electrode

substrate

Radius of curvature: 1 cm

Field of View (w/o lens) : 120 °

(b)

P3HT:PCBM

Al / PEIE

substrate

(c)

Encapsulating glass

DMD top electrode

P3HT:PCBM

Al / PEIE

substrate
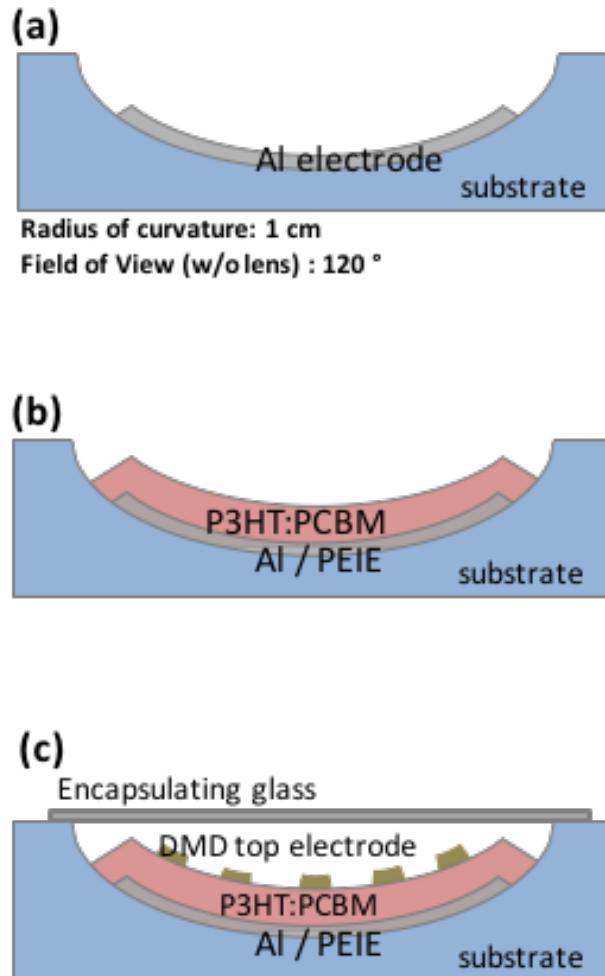
Figure 5.6 Fabrication procedure of the hemispherical organic photodiode (a) bottom cathode deposition (b) electron transporting dipole layer (PEIE) and BHJ active layer formation (c) top DMD anode formation.

Active layer   Bottom cathodes

Top DMD anodes
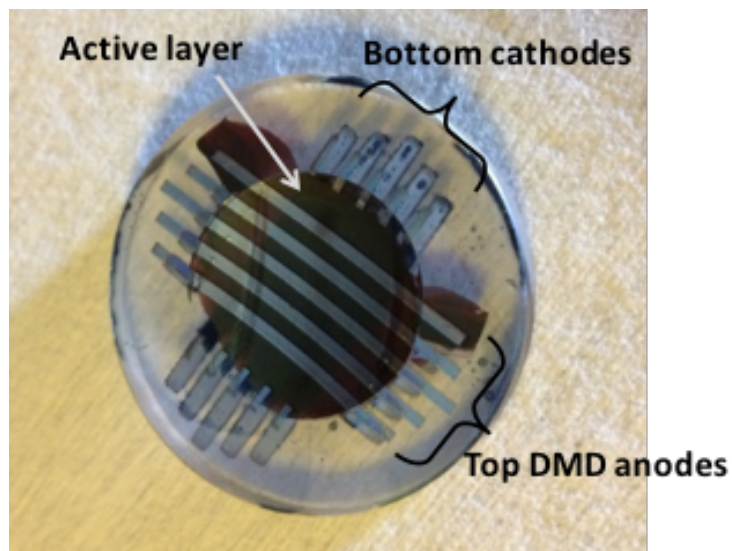
Figure 5.7 Fabricated hemispherical organic photodiode OPD on curved substrate.

5.5. Result and Discussion

The current density - voltage (J-V) characteristics of a fabricated hemispherical OPD device are shown in Figure. 5.9. The irradiance of the illuminated light from the top was 1.63 mW/cm^2 at 546 nm wavelength. The J-V characteristics of the hemispherical OPD under illumination and dark conditions were measured by HP2416A semiconductor measurement system with a probe station in a dark Faraday cage. The probe contacts were made on the flat periphery region of the electrodes outside the hemispherical dome. The dark current density at 1.5 V reverse bias of the OPD was $J_d = 994 \pm 0.6$ nA/cm^2. This value was only ~2 times higher than the DMD top anode OPD device with similar active layer thickness (200 nm) demonstrated in Chapter 2. The measured external quantum efficiency (EQE) of the hemispherical OPD was 17.91 % for $\lambda = 546$ nm at -1.5 V, which was half of the EQE acquired with the 200 nm DMD OPD in Chapter 2. This lower EQE can be attributed to thicker Ag electrode (15 nm) in the top DMD anode which can significantly decrease the optical transmittance of the top transparent anode. However, the thicker electrode was needed to guarantee the connectivity of top thin metal electrode strips on a curved surface. The photodetector performance was evaluated by the specific detectivity $D^* = (A\Delta f)^{1/2}/NEP$, where A is the detector area, Δf is the bandwidth, and NEP is the noise equivalent power previously described in Chapter 2.3.3. The NEP can be fairly approximated to $NEP = (2qI_D)^{1/2}/R$, when we assume the shot noise current associated to the dark current is dominant over the thermal noise under reverse bias [97]. In this case, we obtain $D^* = 1.4 \times 10^{11}$ Jones in a 1 Hz bandwidth at 546 nm wavelength with -1.5 V bias. The D* value obtained here is comparable with the D* of the 200 nm DMD OPD device in Chapter 2 which was slightly higher (1.46×10^{11} Jones). Finally, we evaluate a yield of the hemispherical OPD array as low as ~ 10 % for sample number N > 50. The low yield of the device is possibly due to non-uniform nature of the DMD transparent top anode during thermal evaporation process especially on steep region of periphery side. A modification of the vacuum evaporator

might be needed for more uniform thin metal evaporation process.
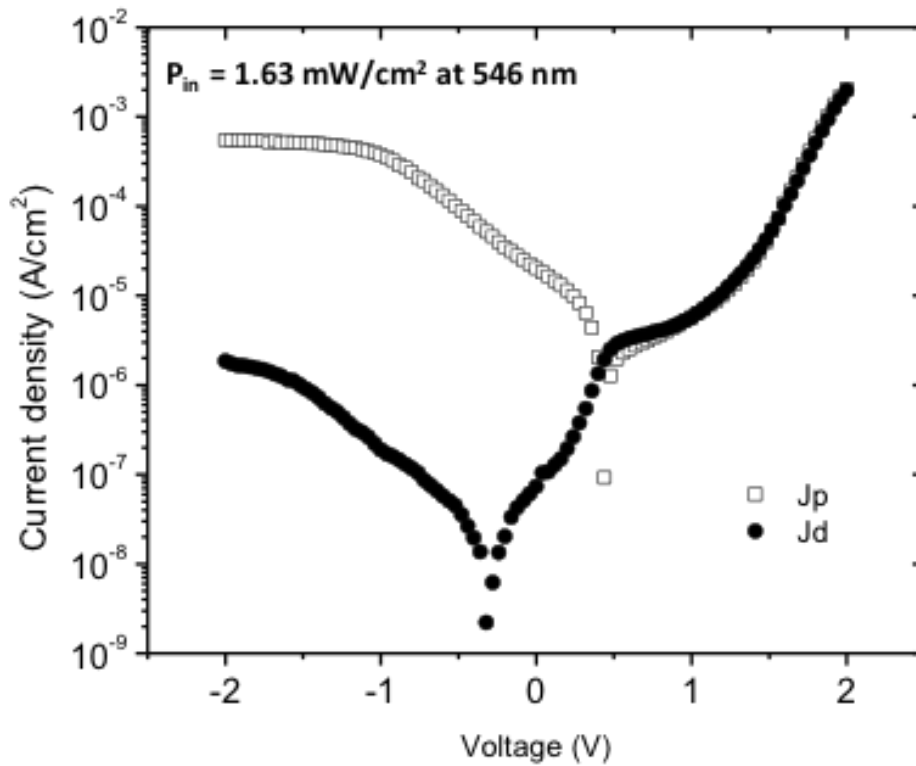
Figure 5.9 Experimental dark and under illumination current density (J) versus voltage (V) characteristics for the hemispherical OPDs. The irradiance of 1.63 mW/cm^2 light illumination with 546 nm was used. Solid symbols represent measured dark currents when open symbols are photo responses.

5.5. Conclusion

In this chapter, for the first time, we have demonstrated a method to fabricate organic photodiode passive arrays on a hemispherical substrate with FOV = 120°. To realize the hemispherical OPD fabrication, two unconventional fabrication process was introduced ; 3D shadow mask fabrication by stereolithography, and 3D PDMS stamp for transfer printing on curved substrate. This technique allows us to directly pattern the device electrodes without excessive strain caused by substrate deformation process. We believe that the developed 3D mask and 3D organic layer transfer printing process can be extended to more complicated applications which can mimic the advanced imaging system such as human eyes.

Chapter 6.
Simulation of Organic Photodiode - Metal Oxide Active Pixel Sensor Circuit with Transimpedance Amplifier

6.1 Introduction

Today the large area digital imaging such as X-ray imaging are based on the active matrix flat panel digital detector technology [189–191]. The most common choice for the commercial flat panel imagers is amorphous silicon thin-film transistors (a-Si TFTs) passive pixel sensor (PPS) technology [192–196]. To increase the sensitivity of the sensor circuit especially for the low dose applications, it is essential that the dynamic range (DR) of the sensor circuit is larger than 30 dB [197]. The a-Si TFT PPS circuitry generally suffers from a high noise (e.g. > 1000 e⁻) since it transmits detected photo-induced signals to a readout circuit without any signal amplification [198]. Moreover, a-Si PPS technology has critical limiting factor : low field-effect mobility (μ_{eff}). The μ_{eff} is less than 1 cm^2/Vs that limits the readout speed or frame per second (FPS) of the pixel array [61,199]. To mitigate the a-Si PPS circuit low signal-to-noise (SNR) ratio, a current-mode active pixel sensor (C-APS) circuit based on a-Si TFT was proposed [193,57]. However, the low mobility of the a-Si TFT limited the effectiveness of the APS circuitry yielding a charge gain of less than 3.2 [57]. To mitigate this issue, the amorphous indium-gallium-zinc oxide (a-IGZO) TFT PPS with a higher $\mu_{eff} = 10 \sim 20$ cm^2/Vs has been proposed for image sensor application by a few groups [200,201]. Furthermore, Zhao et al. proposed a-IGZO TFT APS X-ray imager for digital breast tomosynthesis (DBT) to increase the charge gain and suppress the noise [61]. The proposed a-IGZO TFT based APS imager system exhibited a large charge gain of 31–122 with total noise

of 912 e$^-$ for 50 μm pixel pitch. In addition, Roose et al. reported an APS X-ray backplane with the a-IGZO TFT technology [202].

To further enhance the performance of the APS imager system, it will be beneficial to adapt a new kind of metal oxide TFTs with the higher mobility. Recently, amorphous indium-tin-zinc oxide (a-ITZO) TFTs with even higher $\mu_{eff} > 30$ cm^2/Vs and lower off current $I_{off} < 10^{-14}$ A have been reported by our group and the others [203–205]. These high μ_{eff} and low I_{off} properties are highly desirable to be used for the high-performance X-ray imagers and the next generation image sensor application.

Previously, we have investigated various strategies to enhance the performance of the OPD for the image sensor applications. In the Chapter 2, we proposed that the DMD transparent electrode can be used as top anode for the vertically stacked imager application. In the chapter 3 and 4, a novel DTS method is proposed to effectively suppress the dark current noise and increase the responsivity of the OPD at the same time. By combining both DMD top electrode and DTS method, high performance organic photodiode can be integrated successfully on the active matrix backplane for flat panel imager application.

In this chapter, we propose the study of the vertically integrated OPD and a-ITZO TFT APS with a transimpedance amplifier (TIA) readout circuit. Adaptation of the TIA readout circuit to the OPD with a-ITZO TFT APS array allows cost-effective solution with comparably fast readout with suppressed noise performance for the low-dose, video-rated X-ray imaging system [202]. This simple "current-to-voltage converter" allows considerably faster and resonably higher gain with simpler and cheaper circuit schematic. Various conditions of the a-ITZO APS and the TIA are simulated to evaluate the circuit performance. Voltage gain (Av), linearity, charge-to-current conversion gain (K), and electron-to-voltage conversion gain (G) are calculated and discussed.

6.2 Device Fabrication

6.2.1 Amorphous Indium-Tin-Zinc Oxide TFTs

The detailed fabrication process of the a-ITZO TFT used in this modeling can be found elsewhere [203]. To briefly describe the process, a gate electrode (Mo) and a 470-nm-thick amorphous silicon dioxide (SiO_2) as a gate insulator are deposited using plasma-enhanced chemical vapor deposition (PECVD). Next, a 30-nm-thick a-ITZO film is deposited by DC sputtering with an O_2 flow ratio of 5%, subsequently patterned by a wet etching process, and then annealed at 300 °C. Afterward, the S/D electrodes (Mo) are deposited by sputtering and patterned by phosphoric acid, acetic acid, and nitric acid (PAN) etchant. Finally, an organic or inorganic film as a passivation layer is deposited over the a-ITZO TFT to finish the fabrication process. Figure 6.1(a) shows a cross-sectional view of the fabricated a-ITZO TFT.

6.2.2 Organic Photodiodes

The BiHJ OPD fabrication process on the APS backplane is briefly explained here. 100 nm ITO layer is deposited on top of the Mo Source / Drain electrode to be used as bottom cathode electrode. A synthesized ZnO solution was spin-coated on top of the patterned cathode layer with spin-coating speed of 2000 rpm for 30 seconds and annealed at 150 ^{o}C for 20 minutes, yielding 40nm thickness of ZnO layer. Next, a 90nm thick PCBM electron acceptor layer is deposited by spin coating process. Subsequently, a 90-nm-thick P3HT electron donor film is transferred by DTS process on PCBM/ZnO/ITO/Mo substrate. The P3HT/PCBM/ZnO/ITO/Mo substrate is subsequently annealed at 110 °C to facilitate a interdiffusion process between P3HT and PCBM (P3HT/interdiffusion hetero- junction/PCBM/PEIE/ITO/Mo). Finally, a 15 nm MoO_3, a 10 nm Ag, and a 35 nm MoO_3 are sequentially deposited on the top of the active layer to form a transparent anode electrode. The OPD is illuminated through the top transparent anode.

Figure 6.1(b) shows the cross-sectional view of the BiHJ OPD with DMD top transparent anode.

A cross-sectional view of the vertically stacked OPD-APS is shown in Figure 6.1(c).
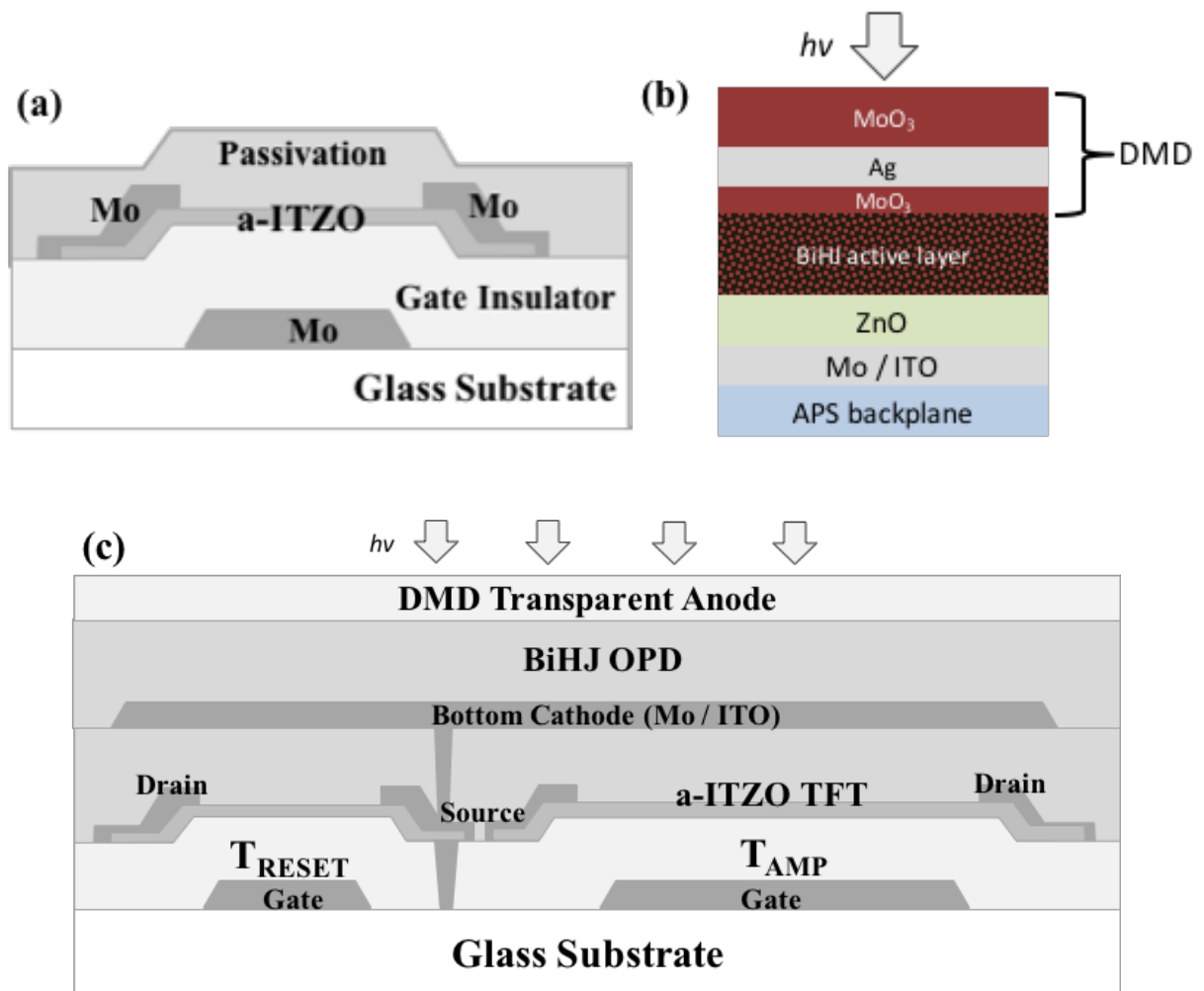
Figure 6.1 Cross-sectional view of (a) a-ITZO TFT (b) DMD OPDs descirbed in the chapter (c) Schematic cross-sectional view of vertically integrated OPD-APS pixel.

6.3. Device Characteristics and SPICE Models

6.3.1 Amorphous Indium-Tin-Zinc Oxide TFTs

The data points of Figure 6.2 (a) and (b) show the measured a-ITZO TFT with 35 μm/ 15 μm (W/L) transfer (drain current vs. gate-to-source voltage; I_D vs. V_{GS}) and output (drain current vs. drain-to-source voltage; I_D vs. V_{DS}) characteristics, respectively. The TFT transfer characteristic is obtained by sweeping V_{GS} from -20 V to 20 V as V_{DS} is set to 0.1 V and 20 V referring to linear and saturation regions, respectively. The TFT output characteristic is acquired by sweeping V_{DS} from 0 V to 20 V while V_{GS} is from 0 V to 20 V. The field-effect mobility as a function of V_{GS} in linear (μ_{EFF_lin}) region and in saturation region (μ_{EFF_sat}) can be calculated by the equations

$$\mu_{EFF_{lin}} = \frac{L}{W C_{ox} V_{DS}} \frac{\partial I_{D_{lin}}}{\partial V_{GS}} \tag{6-1}$$

$$\mu_{EFF_{sat}} = \frac{2L}{W C_{ox}} \left(\frac{\partial (I_{D_{sat}})^{\frac{1}{2}}}{\partial V_{GS}} \right)^2 \tag{6-2}$$

where I_{D_lin} is drain currents in linear region, I_{D_sat} is drain currents in saturation region, L is the channel length, W is the channel width, and C_{OX} is the gate capacitance per unit area. C_{OX} can be computed by $C_{OX} = \varepsilon_r \varepsilon_0 / T_{OX}$ where ε_r is the relative permittivity of SiO_2, ε_0 is the vacuum permittivity, and T_{OX} is the thickness of SiO_2, so C_{OX} is 7.34 nF/cm^2.

Extracted values of μ_{EFF_lin} and μ_{EFF_sat} are 27.59 and 31.19 cm^2/Vs, respectively, at $V_{GS} = 10$ V. The device mobility is gate voltage dependent. Substhreshold swing (SS) can be estimated by $SS = [\partial(\log I_D)/\partial V_{GS}]^{-1}$. Minimum SS is 153 mV/dec. I_{OFF} is lower than 10^{-14} A. With the linear fitting method based on 10 % to 90 % of maximum I_D of transfer characteristics in linear scale, the extracted initial V_{th} is -0.93 V. The extracted field effect mobility, SS and I_{OFF} were comparable or even higher than previously published works [204–208]. Table 6.1 summarizes the comparison of the electrical properties of this work with literatures.

Table 6.1 Comparison of the electrical properties of a-ITZO TFTs

	Fukumoto et al. [205]	Ryu et al. [206]	Tseng et al. [208]	Junho et al. [204]	This work
μ_{EFF} (cm$_2$/Vs)	30.9	24.6	33.2	22.4	31.19
SS (mV/dec)	210	230	220	440	153
V_{th} (V)	0.97	0.20	0.27	0.75	- 0.93
I_{OFF} (A)	1×10^{-14}	1×10^{-13}	2×10^{-14}	1×10^{-13}	$< 10^{-14}$
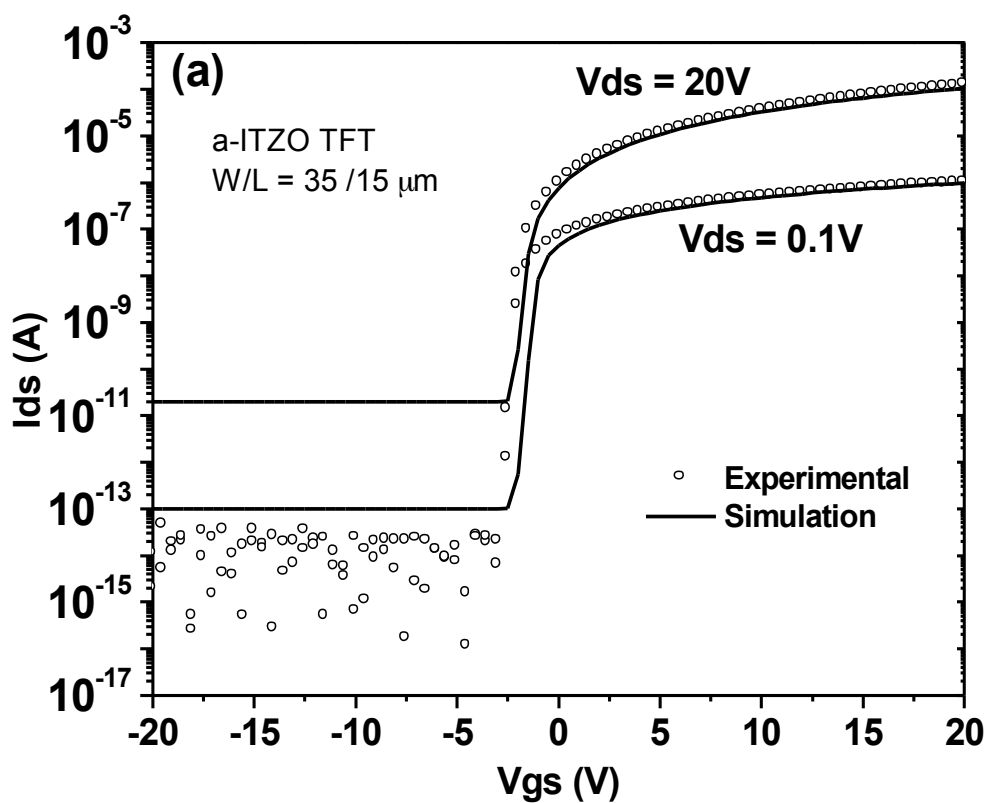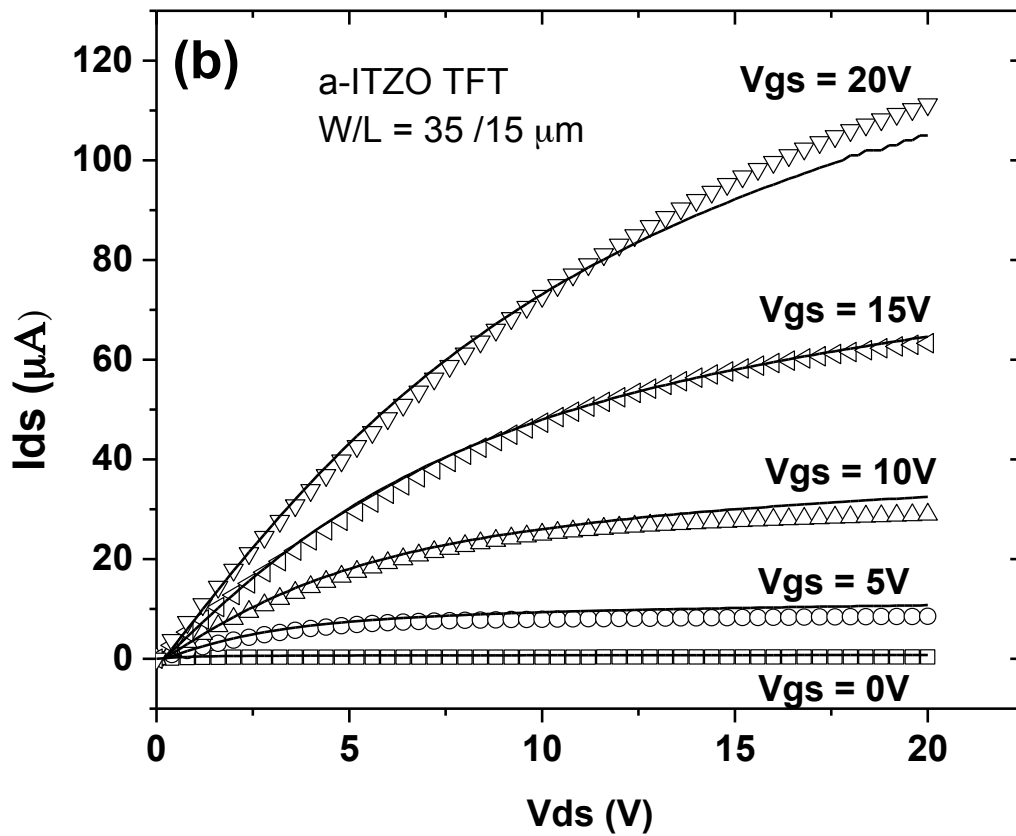
Figure 6.2 Current - voltage (I-V) characteristics of the a-ITZO TFT used in the model (a) Transfer curve (b) Output curve (the data adapted from [209]).

6.3.2 SPICE Model for a-ITZO TFTs

An a-ITZO TFT model for SILVACO SmartSpice$^©$ is established using Rensselaer Polytechnic Institute (RPI) a-Si TFT model (LEVEL = 35), which is based on a number of equations developed for above-threshold, subthreshold, and leakage regions of a TFT. The detailed procedure is described in [210]. The above-threshold region is related to zero bias threshold voltage (VTO), power law mobility parameter (GAMMA), characteristic voltage for field-effect mobility (VAA), saturation modulation parameter (ALPHASAT), channel modulation parameter (LAMBDA), knee shape parameter (M), electron band mobility (MUBAND), transition width parameter (DELTA), and convergency parameter (VMIN). The subthreshold region is influenced by flat-band voltage (VFB), characteristic voltage of deep

states (V0), midgap density of states (GMIN), dark Fermi level position (DEF0), and effective conduction band density of states (NC). The leakage region is associated with zero bias leakage current (IOL), hole leakage current drain voltage parameter (VDSL), hole leakage current gate voltage parameter (VGSL), and minimum leakage current (SIGMA0). Relative permittivities of gate insulator (EPSI) and substrate (EPS) are material-related parameters. Gate insulator thickness (TOX) is device-geometry-related parameter. Extraction of these parameters is discussed in [209] and obtained. The parameters are given in Table 6.2. The solid lines of figure 6.1 show a good fit between the experimental TFT data and the simulated curves based on the extracted parameters, ensuring the accuracy of the circuit simulations.

Table 6.2 SPICE parameters for the a-ITZO TFT

Above-Threshold region			
Parameter	Value	Parameter	Value
VTO	1 (V)	GAMMA	0.1509
VAA	1627.2 (V)	ALPHASAT	0.526
LAMBDA	0.0069 (V)	M	1.59
MUBAND	0.005 (m^2/Vs)	DELTA	5
VMIN	0.05		
Subthreshold region			
Parameter	Value	Parameter	Value
VFB	-2 (V)	V0	0.3992 (V)
GMIN	4.96×10^{20} ($m^{-3}eV^{-1}$)	DEF0	1.5 (eV)
NC	5×10^{24} (m^{-3})		
Leakage region			
Parameter	Value	Parameter	Value
IOL	1×10^{-12} (A)	VDSL	1000 (V)
VGSL	100 (V)	SIGMA0	1×10^{-18} (A/V)
Others			
Parameter	Value	Parameter	Value
EPSI	3.9	EPS	10
TOX	4.7×10^{-7} (m)		

6.3.3 SPICE Model for Organic Photodiodes

The SPICE model for the 110 ^{o}C annealed BiHJ OPD in Chapter 3 is modeled using an equivalent circuit model described in Figure 6.3 (b) [209]. In the figure, D is a basic diode, R_S is a series resistor, R_{SH} is a shunt resistor, C_{PD} is a photodiode capacitance, and I_{PH} is a current source emulating photocurrents. The model equation used to calculate and extract the device physical parameters has been described in Chapter 3.

The reverse-biased current is affected by R_{SH}, the transition between the forward-biased region and the reverse-biased region is determined by the diode (ideality factor, n, and saturation current density, J_S), and the forward-biased current is associated with R_S. Matlab and SmartSpice are both used to evaluate and extract physical parameters for the OPD. Table 6.3 lists the PDs parameters that have been extracted from Chapter 3.3. The OPD area is modeled to be 50 μm x 50 μm pixel pitch. The fitted curve shown in Figure 6.3 (a) agrees well with the experimental I-V.
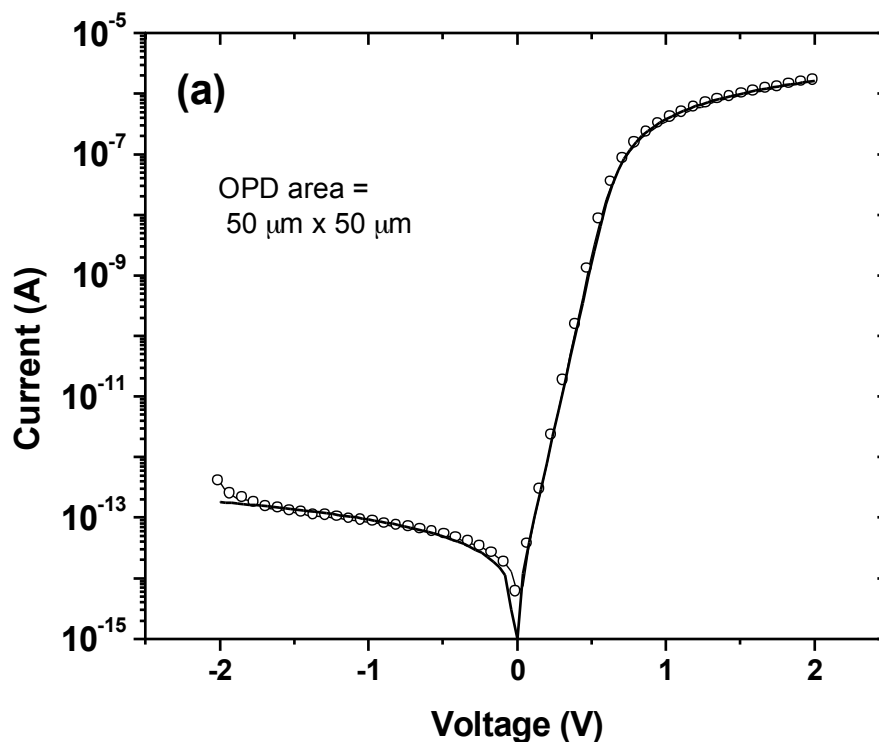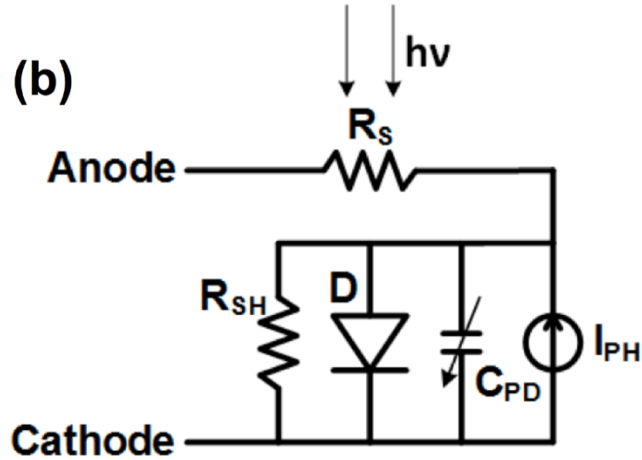
Figure 6.3 (a) Current - voltage (I-V) characteristics of the BiHJ OPD used in the model (b) Equivalent OPD model (figure adapted from [209]).

Table 6.3 SPICE parameters for the OPDs

Parameter	Value	Parameter	Value
Diode version	LEVEL = 1	R_{SH}	1.8×10^8 (Ω/cm^2)
Js	0.3×10^{-9} (A/cm^2)	C_{PD}	0.21 (pF) @ -5V
n	1.52	I_{PH}	$0 \sim 100$ (pA)
R_S	12 (Ω/cm^2)		

6.4. OPD-APS and Transimpedance Amplifier

One possible choice for the a-ITZO APS readout circuit is the charge integrator that has a fast readout ability [193,57,211]. However, the discrete design of the switched charge integrator could be impractical for a low noise and precision applications because of the switching noise of the reset switch, which is caused by the injection of charge across the parasitic gate-to-source, gate-to-drain, and source-to-drain capacitances of the FET switches [212–214]. A special design such as differential readout [215,216] or correlated double sampling (CDS) [217–219] is needed for the noise cancellation for a high performance charge integrator. Alternative readout circuit is a transimpdedance amplifier [202,212,220–225]. One possible advantage of the TIA is that there is no need for a large integration feedback capacitor

(typically larger than ~ 5 nF), which can reduce the readout circuit cost and area [202]. Another advantage of the TIA is removal of the feedback reset switch, which simplifies the readout circuits further and reduce the reset switching noise [212,226,227].

Figure 6.4 shows the pixel sensor schematics and corresponding timing diagrams for the a-ITZO APS and the TIA readout circuit. APS consists of one PD, and three a-ITZO TFTs (T_{RST}, T_{AMP}, and T_{READ}). The PD detects photo-induced signals (electrons) generated by photons absorbed by the OPD layer. The C_{PIX} ($C_{PD} + C_{ST}$) stores detected photo-induced signals. T_{RST} is used to remove photo-induced signals stored in C_{PIX} (i.e. to reset the gate voltage of T_{AMP}, V_{IN}, to its initial value). T_{AMP} is used to amplify detected photo-induced signals. T_{READ} controls the transfer of amplified photo-induced signals from the pixel sensor to the external readout circuit. The output current I_{OUT} of the individual pixel flows through the column bus data line which include typically line capacitance, C_{DATA}. Finally, the output current I_{OUT} is converted to voltage V_{OUT} by the TIA readout circuit for signal post-processing.
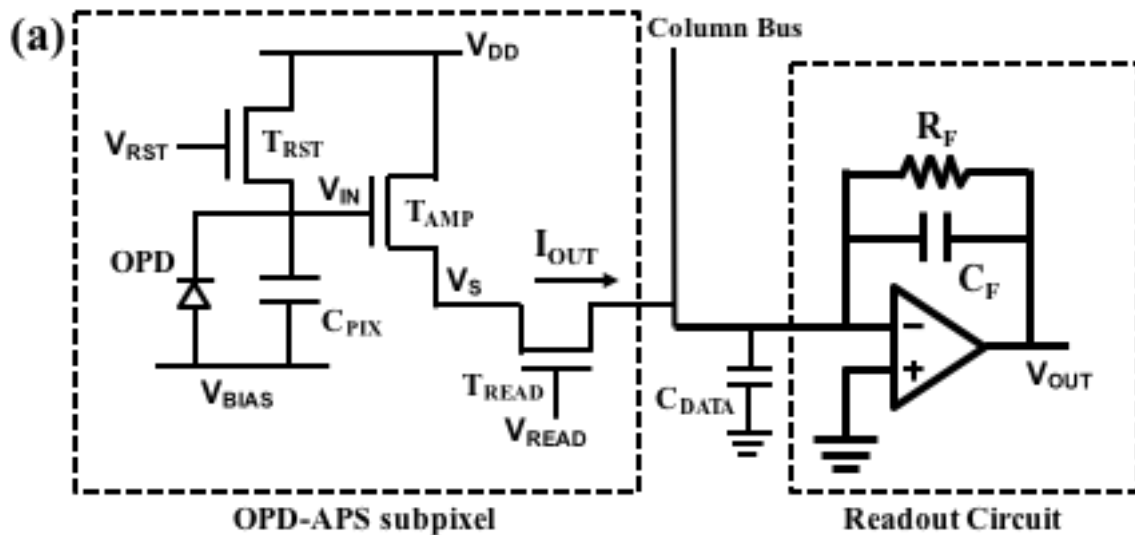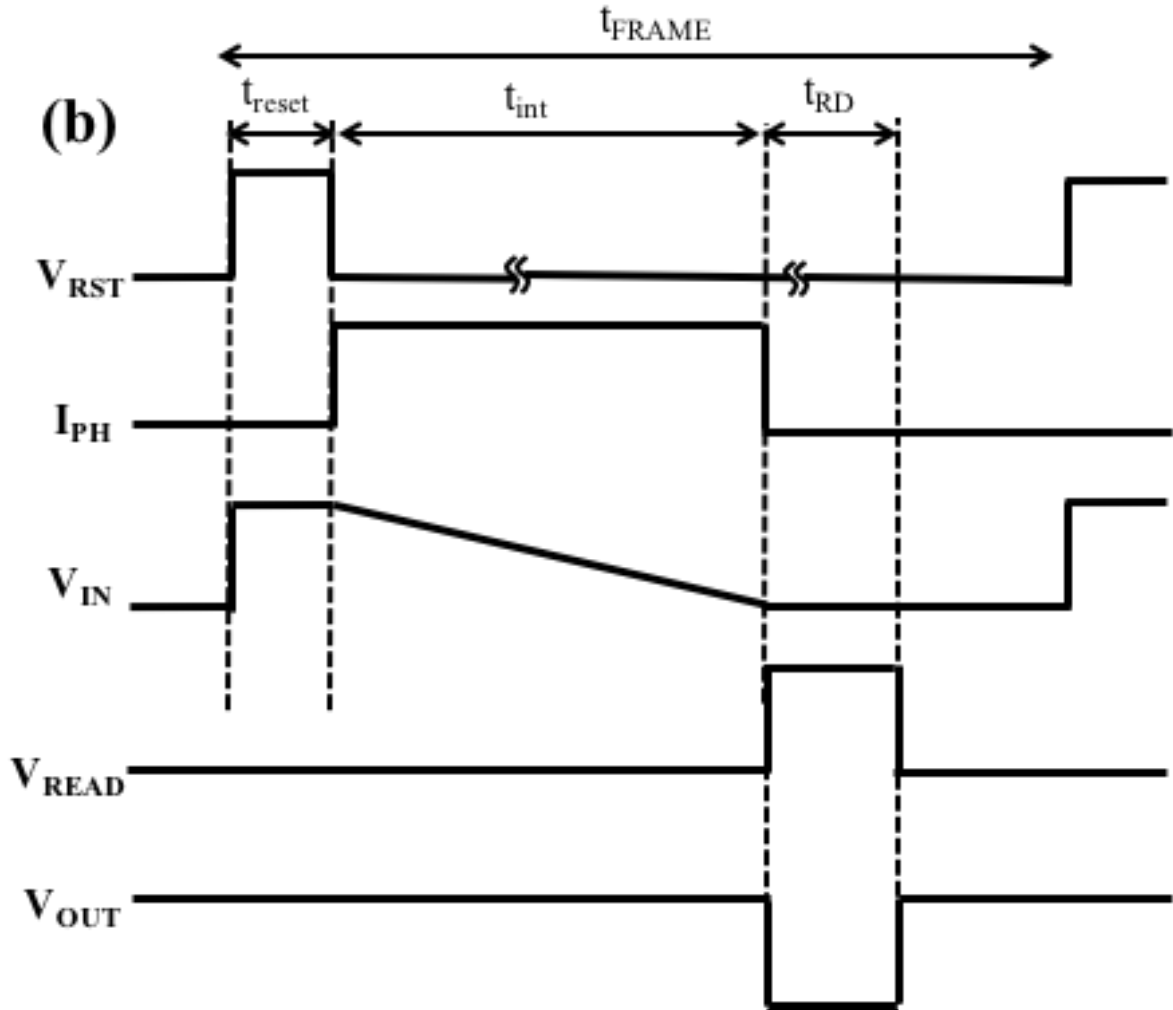
Figure 6.4 (a) Proposed top anode APS circuit schematic with transimpedance amplifier readout circuit. The APS pixel consists of three transistors (T_{RESET}, T_{READ} and T_{AMP}) with an OPD with a capacitance of C_{PD}. (b) An example of the driving/ reading scheme. t_{FRAME}, t_{reset}, t_{int} and t_{RD} are the frame time of operation, reset time, integration time and readout time, respectively. Note that the V_{out} signal is synced with t_{RD}.

6.4.1 Operation Principle

Reset period: The reset switch T_{RST} is turned on by setting V_{RST} to high (10 V) and V_{READ} is kept low (-5 V) to switch off T_{READ} to isolate APS from the TIA readout circuit. The turned-on T_{RST} resets the gate node (V_{IN}) of T_{AMP} to V_{DD}. A reverse-biased condition for OPD ($V_{cathode} = V_{DD} = 10V$, $V_{anode} = V_{BIAS} = 5$ V) is kept to ensure the OPD works in photoconductive mode. The V_{OUT} is maintained at the ground level by the shunting feedback R_F network to virtual ground of the OP Amp.

Integration period: V_{READ} are kept low to isolate the APS from the TIA readout circuit and T_{RST} is switched off by setting V_{RST} low (-5 V) during integration period t_{int}. During t_{int}, the input light signal (e.g. green light emitted from scintillator excited by X-rays) are absorbed by OPD and generate excitons [228]. These excitons are dissociated into polarons at the donor / acceptor junction which are separated into electrons and holes by the electrical field inside OPD formed by reverse bias . The generated holes and electrons move toward anode and cathode, respectively, to discharge C_{PIX} and decrease the V_{IN} during integration period.

Readout period: After integration period, T_{READ} is turned on by setting V_{READ} high (10 V) during a readout time t_{RD}, which connects the APS to the TIA circuit for further signal amplification. The V_{IN} modulated by the end of integration period determines the amount of the current I_{OUT} produced by T_{AMP}, which flows into the TIA external circuit through T_{RD}. Since V_{DD} = 10 V is higher than V_{IN} - V_{TH_AMP} (threshold voltage of T_{AMP}) at the end of Integration stage, the channel of T_{AMP} is to be pinched off and operated in saturation region [229]. Therefore, I_{OUT} can be expressed as:

$$I_{OUT} = \mu_{eff} C_{ox} \frac{W}{2L} \left(V_{IN} - V_S - V_{TH\_AMP} \right)^2 \qquad (6\text{-}3)$$

where μ_{eff} is the field-effect mobility, V_S is source voltage of T_{AMP}, and W and L are the channel width and length of T_{AMP}, respectively.

The readout TIA circuit consists of an op-amp, a shunt feedback resistor RF, and a stabilizing feedback capacitor CF as shown in Figure 6.4(a). The transfer function of output voltage V_{out} can be simply expressed as

$$V_{OUT} = -I_{OUT} \frac{R_F}{1+j2\pi f R_F C_F} \qquad (6\text{-}4)$$

where *f* is the operation frequency of the current. The transfer function simply converts the current I_{OUT} to output voltage V_{OUT} based on Ohm's Law at low frequency (e.g. below cutoff frequency $f_{cut\text{-}off}$ = $1/2\pi R_F C_F$),

$$V_{OUT} = -I_{OUT}R_F \qquad\qquad (6\text{-}5)$$

However, the integration of the TIA with the pixel circuit having the feedback loop should be carefully designed to stabilize the whole circuit. The capacitance C_F between the OP Amps inverting input and V_{OUT} stabilizes the circuit against potential oscillation problem or gain peaking due to impedance mismatch when operating frequency varies [212,227]. The effect of C_F and R_F variation on the TIA circuit performance will be discussed in the following section in more detail.

6.4.2 Simulation Results and Discussion

SmartSpice is used to evaluate the APS TIA circuit performances. Table 6.4 lists circuit parameters used for the OPD-APS TIA evaluation. In the simulation, integration time t_{INT} is set to 100 ms (10 FPS) which is suitable for typical X-ray imager read-out operation [230]. The t_{RESET} was set to 100 µs and the T_{READ} is on for $t_{RD} = 20$ µs, which is typical timings of a rolling shutter readout method [231].

Table 6.4 SPICE parameters for the a-ITZO TFT APS with the Transimpedance Amplifier

Parameter	Value	Parameter	Value
V_{DD}	10 (V)	I_{PH}	$0 \sim 14$ (pA)
V_{BIAS}	5 (V)	t_{RESET}	100 (µs)
V_{RS}	-5 / 10 (V)	t_{INT}	100 (ms)
V_{RD}	-5 / 10 (V)	t_{RD}	20 (µs)
T_{RST} (W/L)	10 / 3,4,5 (µm)	t_{FRAME}	100.2 (ms)
T_{AMP} (W/L)	36 / 3,4,5 (µm)	R_F	500, 250 (kΩ)
T_{READ} (W/L)	36 / 3,4,5 (µm)	C_F	5 (pF)
C_{ST}	$0 \sim 0.4$ (pF)	C_{DATA}	50 (pF)

The SPICE model for the transimpedance amplifier was modified from the switched

integrator (Burr-Brown ACF2101) model provided by the supplier [213]. To optimize the performance of the TIA for the OPD-APS circuit, it is essential to choose appropriate value of the feedback components R_F and C_F for the TIA design while considering operation frequency (in this simulation, 10 FPS). If the feedback loop is inappropriately designed by choosing wrong R_F and C_F value, the TIA is prone to oscillation due to phase shifts [226]. Therefore, detailed analysis for the system is required for the optimum performance. This is out of scope of this initial studies. Figure 6.5 (a) shows the V_{OUT} of the TIA with various C_F value of 0, 5 and 10 pF. The R_F was set to 500 kΩ and no I_{ph} was induced for the simulation. The justification for the choice of R_F value with $I_{ph} = 0$ is explained in below paragraph. As it is shown in the figure, overshooting oscillation swing from -17 V to 12 V was observed with no phase compensation capacitor $C_F = 0$ pF). This oscillation behavior can induce huge error during the readout period which makes the TIA circuit unusable. The oscillation behavior also presents with $I_{ph} \neq 0$ case so the I_{ph} value is not directly related to the oscillation phenomena. When $C_F = 5$ pF is used, the oscillation is suppressed and stable V_{OUT} was achieved during the readout time period. If C_F increases to 10 pF, the time constant $\tau = R_F C_F$ becomes 5 μs, which is not fast enough to achieve desirable V_{OUT} during the readout time. Therefore, it is very important to choose the correct C_F value to prevent the possible oscillation problem when designing TIA circuit. The adjustment of C_F value needs to be carefully done by considering the R_F value together.

Meanwhile, it is important to choose the correct R_F value which will maximize the output voltage and charge gain. The small difference in I_{OUT} associated with small I_{ph} to be produced at low X-ray dose can have increased dynamic range by choosing high R_F value to amplify the current. However, the maximum voltage range of the TIA circuit is limited by the supply voltage of the amplifier. In our simulation, the supply voltage to the OP Amp was V_{CC+} = 18 V and V_{CC-} = -18 V so the maximum achievable V_{OUT} saturated at - 17 V which is limited by V_{CC-} when $R_F = 600$ kΩ with $C_F = 5$ pF, as can be seen in Figure 6.5 (b). The V_{OUT} increased linearly with increasing R_F value, starting from $V_{OUT} = -3$ V with $R_F = 100$ kΩ, reaching V_{OUT}

= -14 V with R_F = 500 kΩ. Based on the analysis of the dependence of R_F and C_F value on TIA circuit, we choose C_F = 5 pF and R_F = 500 kΩ as optimum feedback components throughout the analysis in the following sections. The different I_{ph} values will not alter the optimum R_F value because the V_{OUT} decreases with higher I_{ph} in the APS, which is not affecting V_{OUT} saturation. The analysis with R_F = 250 kΩ will be also included to discuss the feedback resistor effect on output performance.
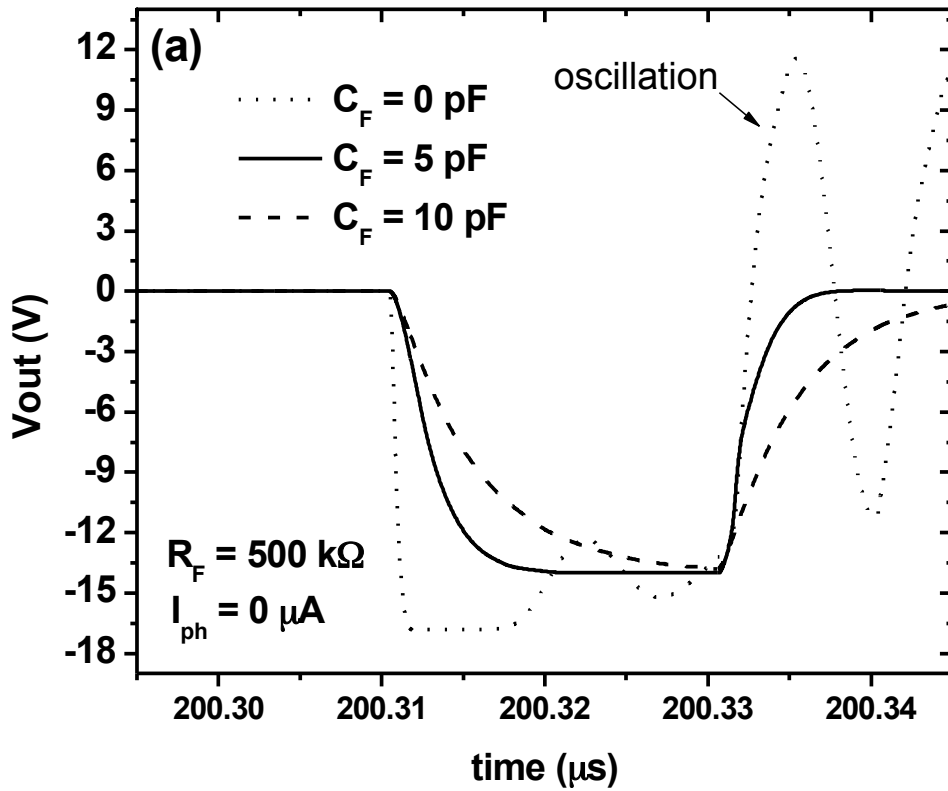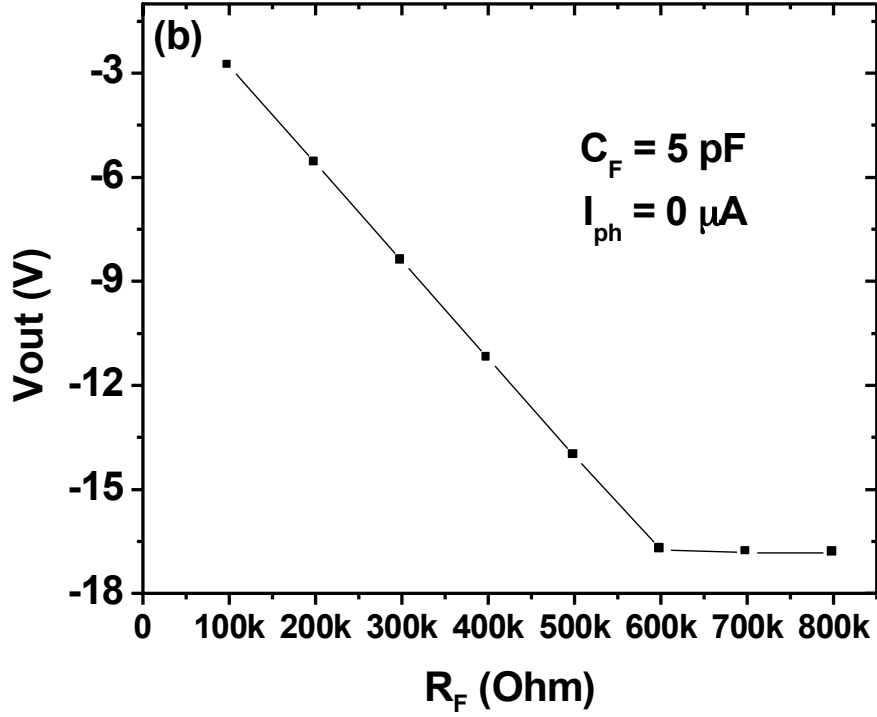
Figure 6.5 (a) Output voltage waveform with different feedback capacitance value with fixed $R_F = 500$ kΩ. (b) V_{OUT} - R_F plot with fixed $C_F = 5$ pF and $I_{ph} = 0$ μA.

Figure 6.6 (a) shows the V_{IN} waveforms of the APS TIA during the integration period t_{INT}. I_{ph} was varied from 0 pA (dark state when only OPD dark current (I_{DARK}) exists) to 14 pA for which V_{IN} saturates before t_{INT} reaches 100 ms. The V_{IN} is essentially the gate voltage of T_{AMP} and it determines the transconductance ($g_m = \Delta I_{ds}/\Delta V_{gs}$) of T_{AMP}. At the beginning of the T_{INT} period, V_{IN} is reset to 9 V, due to 1 V voltage drop in the on-state T_{RST} during reset stage. The discharging behavior of V_{IN} signal during t_{INT} period is a function of C_{PIX}, and it can be described as,

$$\Delta V_{IN} = \frac{\Delta Q_P}{C_{PIX}} \tag{6-5}$$

where $\Delta Q_P = (I_{DARK} + I_{ph})\, t_{INT}$ is the change in the input signal charge on $C_{PIX} = C_{PD} + C_{ST}$ due to induced light and corresponding I_{ph}. The C_{PIX} value with zero C_{ST} in the simulation was 0.21 pF which is the measured value of the BiHJ OPD. The maximum ΔV_{IN} in this configuration at

the end of t_{INT} was 4.5 V and it can be potentially increased if C_{PIX} is decreased as indicated in Equation 6-5.

Figure 6.6 (b) shows V_{OUT} waveforms of the APS TIA circuit during t_{RD} period with R_F = 500 kΩ and C_F = 5 pF. As shown in the figure, the transimpedance amplifier read-out scheme of the I_{out} signal enables very fast (< 10 μs) signal amplification to given V_{OUT} level. The V_{OUT} signal is inversely proportional to the amount of I_{ph} and the saturation occurs at 12 pA, which is limited by V_{IN} saturation behavior. While the V_{OUT} is inversely proportional to I_{ph} value, the rise time t_{RISE} and fall time t_{FALL} are related to the time constant $\tau = R_F C_F$. With R_F = 500 kΩ and C_F = 5 pF, the calculated τ is 2.5 μs resulting in $t_{RISE} \approx t_{FALL} \approx 4.8$ μs, independent with induced I_{PH} value.
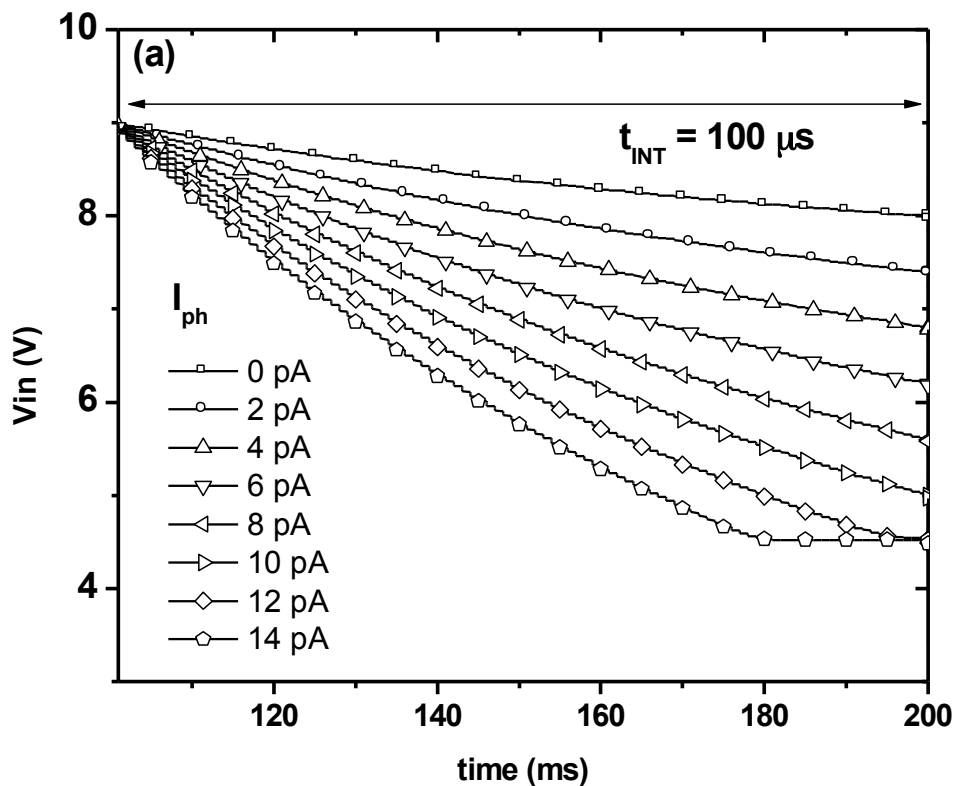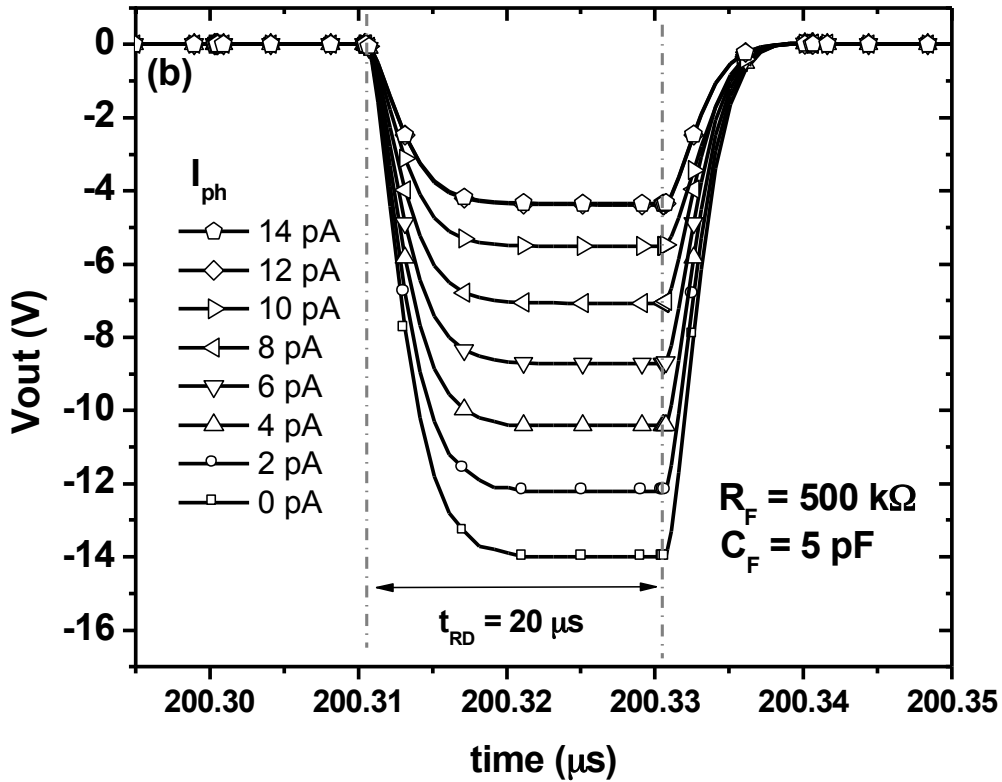
Figure 6.6 Voltage waveforms of the a-ITZO TFT APS with TIA under various photo current (I_{ph}) values ranging from 0 pA to 14 pA (a) Vin during t_{INT} (b) V_{OUT} during t_{RD}.

Figure 6.7(a) shows the linearity relation between V_{IN} vs V_{OUT} of the APS TIA. In this case, 250 kΩ feedback resistor along with 500 kΩ R_F were considered to evaluate the R_F dependence on voltage gain and linearity. Owing to a consistent saturation region operation of T_{AMP} (constant transconductance, g_m) which is a typical characteristic of source follower, the APS TIA produces a highly linear relation between V_{IN} and V_{OUT}. The non-linearity is calculated by fitting the curve according to the adjusted R-squared model [232]. The residual non-linearity was 0.17 % for both R_F = 500 kΩ and 250 kΩ cases. This results indicate that the source-follower type APS with TIA is attractive pixel circuit for the X-ray imagers. The same residual non-linearity for both R_F values also confirms that the linearity is not related to the external readout components.

The voltage gain, Av defined by Av = ΔVout / ΔVin was 3.03 for R_F = 500 kΩ and 1.52

for R_F = 250 kΩ for the APS TIA circuit. The Av reduction is expected since V_{OUT} is linearly proportional to R_F value. As mentioned earlier, the R_F value should be carefully adjusted not to exceed the supply voltage limit of the OP Amp which will eventually result in voltage clipping.

Figure 6.7(b) shows the variation of V_{OUT} and I_{OUT} with the amount of electrons (Q_{pd}) between the a-ITZO APS TIA with and OPD when R_F = 500 kΩ. For V_{OUT} extraction for both Figure 6.7(a) and 6.7(b), the value at steady-state (e.g. t = 200.325 μs) was chosen. Charge-to-voltage conversion gain, G, in the unit of V/pC defined as voltage variation caused by 1 pC photo-induced charge can be calculated by

$$G = \left| \frac{\Delta V_{OUT}}{\Delta Q_{pd}} \right| \tag{6-5}$$

where ΔQ_{PD} is the charge variation induced by OPD currents, I_{ph} and $\Delta e_{PD} = \Delta Q_{PD}/q$, where q is electron charge. Alternatively, Charge-to-current conversion gain, K, in the unit of μA/pC can be defined as ΔI_{OUT} caused by 1 pC photo-induced charge.

$$K = \left| \frac{\Delta I_{OUT}}{\Delta Q_{pd}} \right| \tag{6-6}$$
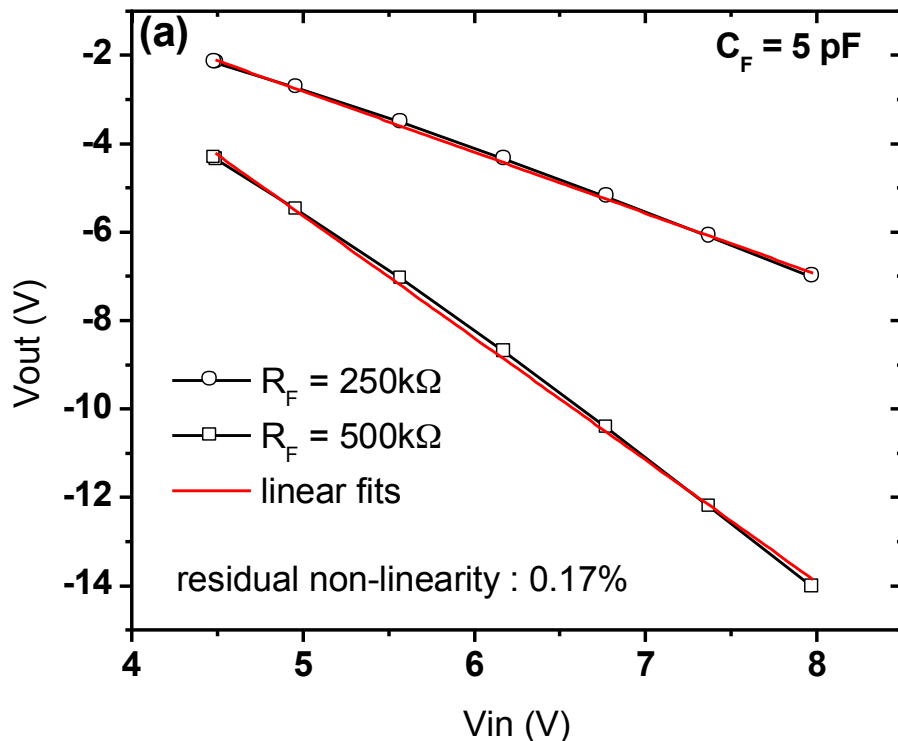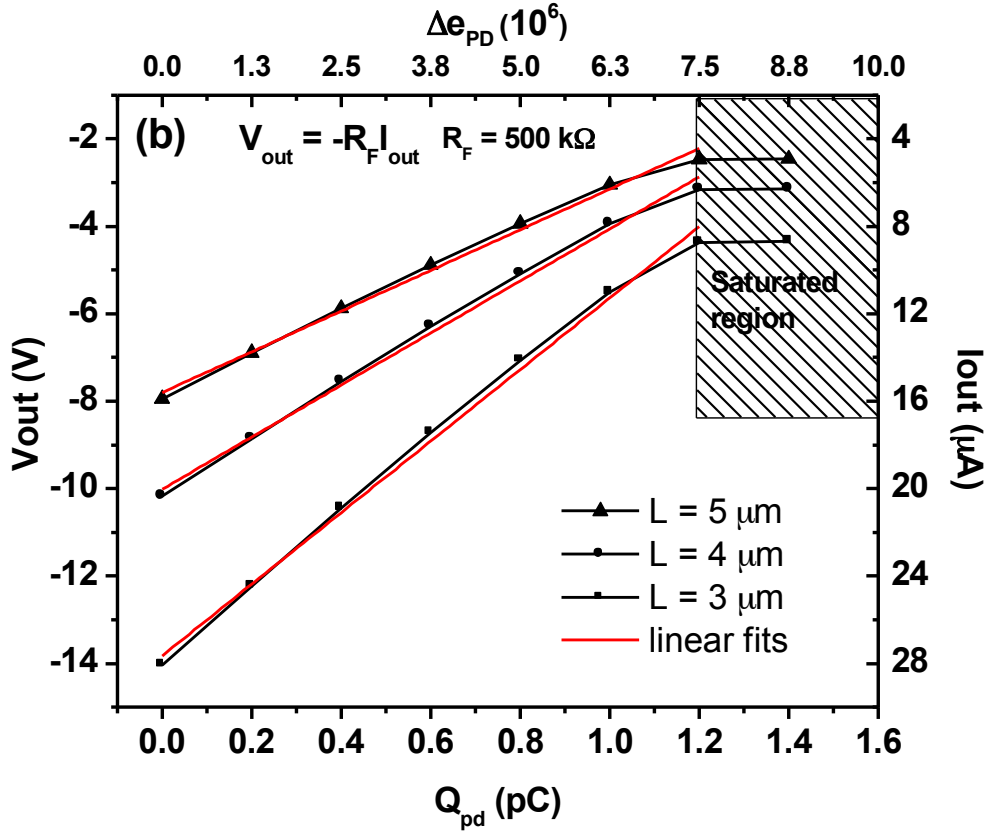
Figure 6.7 (a) Input voltage – output voltage (V_{IN} vs V_{OUT}) linearity plot (Av) (b) charge-to-voltage conversion gain (G) and charge-to-current gain (K) plot of the a-ITZO APS with TIA

The G and K are essentially the slope of the V_{OUT} or I_{OUT} vs Q_{pd} plot of non-saturated region in Figure 6.7(b) and the relationship between I_{OUT} and V_{OUT} can be simply defined by Equation 6-4. TFTs used in this work have channel length (critical dimension, CD) of 3 μm, higher CD can lead to higher production yield and uniformity [202]. The TFT channel length can have impact on the APS TIA properties. Figure 6.7 (b) shows charge-to-voltage conversion gain, G, for CD = 3, 4 and 5 μm. The R_F value was fixed to 500 kΩ in this analysis. The different CD values yielded decreasing G from 9.1 V/pC, 6.6 V/pC and 5.3 V/pC, respectively. Interestingly, increasing CD also adversely affected the input charge (Q_{pd}) - V_{OUT} linearity behavior. The non-linearity of the Q_{pd}-V_{OUT} was calculated excluding the saturated region due to the C_{PIX} limit. The maximum remaining non-linearity for CD = 5 μm case was 0.65 %, which is enhanced to 0.43 % when CD is decreased to 3 μm. The linearity decrease with higher CD is

possibly due to weaker channel inversion with the longer channel length. The calculated K for each CD value was 18.2, 13.3 and 10.5 μA/pC for CD = 3, 4 and 5 μm, respectively. The G and K comparison with different CDs and R_F value were plotted in Figure 6.8.
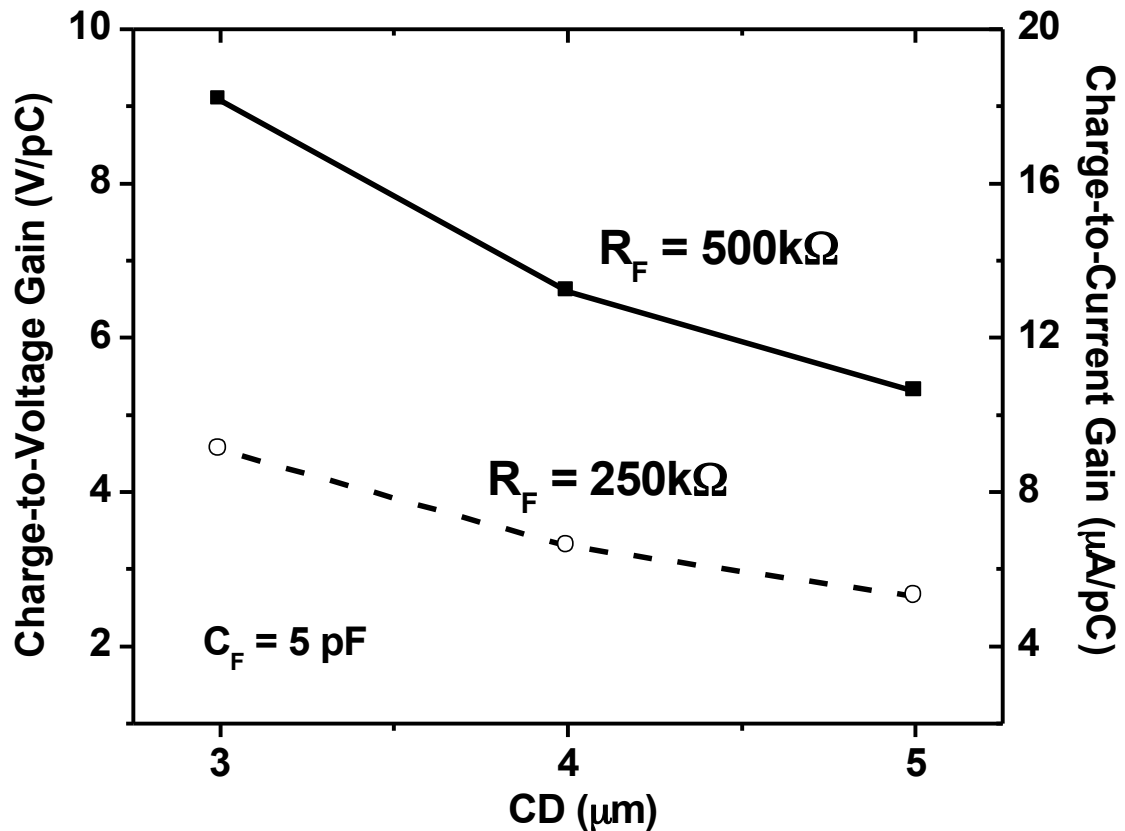
Figure 6.8 Effect of channel length scaling and the feedback resistor on charge-to-voltage gain.

For the readers' information, a summary table of performance comparison with previous works on APS imager is given in Table 6.5. When we compare the proposed readout system with the previous works, it showed superior charge-to-current gain of 18 μA/pC and remaining non-linearity of 0.48 % except the work by Roose et al [202], which showed higher charge-to-current gain (K) of 59 μA/pC. However, it is worthwhile to emphasize that the gain (K or G) in our simulation can be further enhanced by increasing supplying voltage range (V_{DD}) or modulating TFT I_{ds}-V_{ds} output curve. For example, if the V_{DD} value in our system is increased

from 10 V to 20 V, the forced current by the V_{DD} through the T_{AMP} will be amplified further resulting in charge-to-current gain increase from 18 µA/pC to 25 µA/pC. Alternatively, the W/L ratio of the TFT can be increased or V_{th} can be adjusted to increase output current (g_m) of T_{AMP}. The range of the C_{PIX} for both work was comparable (Roose et al. : 0.22 pF ~ 0.44 pF, this work : 0.21 pF ~ 0.61 pF) so the K difference affected by C_{PIX} value can be neglected.

Table 6.5 A summary table of performance comparison with previous works

	Karim et al. [193]	Tedde et al. [57]	Zhang et al. [233]	Roose et al. [202]	Proposed System
Detector	a-Si:H pin	OPD	Current source	Current source	OPD
TFT Technology	a-Si:H	a-Si:H	a-IGZO	a-IGZO	a-ITZO
Pixel pitch	250 µm (102 ppi)	150 µm (169 ppi)	135 µm (195 ppi)	100 µm (254 ppi)	50 µm (508 ppi)
Critical Dimension	25 µm	4 µm	4 µm	3 µm	3 µm
Operating principle	Source output	Source output	Source output	Drain output	Source output
Readout circuit	Charge Integrator (C_{FB}=10pF)	Charge Integrator (C_{FB}=100pF)	Charge Integrator (C_{FB}=100pF)	Transimpedance Amplifier (R_F = 20kΩ)	Transimpedance Amplifier (R_F = 300kΩ)
Charge-to-current Gain	0.43 µA/pC	0.35 µA/pC	0.011 µA/pC	59 µA/pC	18 µA/pC
Remaining non-linearity	1.77 %	2.08 %	0.95 %	0.33 %	0.48 %
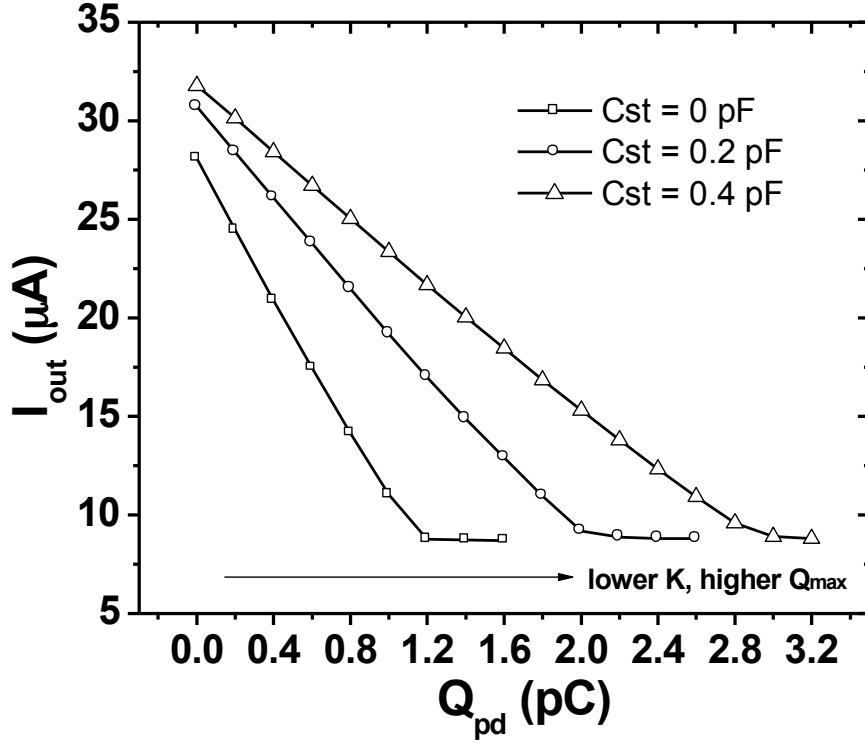
Figure 6.9 Output current I_{OUT} for different storage capacitances C_{ST}. Total C_{PIX} is calculated as $C_{PIX} = C_{PD}$ (0.21 pF) $+ C_{ST}$.

The another design rule to increase the charge-to-current gain is by decreasing C_{PIX} [193]. Figure 6.9 shows that higher $C_{PIX} = C_{PD} + C_{ST}$ will result in lower K based on Equation 6-5, $\Delta V_{IN} = \Delta Q_P / C_{PIX}$. For the different C_{ST} value of 0 pF, 0.2 pF, and 0.4 pF, the K value is calculated as 18.21 μA/pC, 11.48 μA/pC, and 8.36 μA/pC, respectively. Even though higher C_{PIX} can decrease K and G due to slower V_{IN} change, it can increase the capacity Q_{MAX} of the a-ITZO APS. Therefore, C_{PIX} must be carefully determined to achieve an acceptable K and Q_{MAX} for a certain imaging application.

Finally, the dynamic range, DR = 20log(Q_{max} / Q_{min}) was evaluated. Q_{max} can be calculated by $Q_{MAX} = I_{SAT}t_{INT}$ where I_{SAT} is the maximum I_{PH} that the APS TIA can detect. Q_{max} for the OPD is 7.5×10^6 e⁻, from Figure 6.7 (b). Similarly, Q_{min} can be determined by $Q_{min} = I_{DARK}t_{INT}/q$. Q_{min} for the OPD is 2.43×10^5 e⁻. From the evaluated Q_{max} and Q_{max}, the calculated DR was about 30 dB.

6.5. Conclusion

In this chapter, we proposed a vertically OPD stacked a-ITZO TFT APS with a transimpedance amplifier. We evaluated the applicability of the organic photodiode in combination with the a-ITZO thin film transistor active pixel sensor circuit and transimpedance amplifier circuit to imager. It is demonstrated that the a-ITZO TFT APS with TIA readout circuit can yield max G = 9.1 V/pC, K = 18.2 μA/pC with DR = 30 dB. A remaining non-linearity for CD = 3 μm and RF = 300 kΩ was 0.43%. Additionally, we demonstrate a transimpedance approach for the readout IC to reduce the integration cost by eliminating the integrating capacitor. Overall, we demonstrated the a-ITZO TFT APS with TIA is another possible approach for the next generation x-ray imager applications.

Chapter 7.
Final Remarks and Future Works

7.1 Summary of Results and Conclusions

The attempts to use organic based optoelectronic devices in many applications are tremendously increasing as the Internet of Things (IoT) and wearable device technology emerges as next industry trends. Especially, the huge focus on organic photodetectors and image sensors is being made due to the importance to be able to see and communicate with each devices for autonomous industry. In this context, the aim of this thesis was to investigate the strategies for high performance organic photodiodes which is applicable to the large-area / conformal image sensor for medical or next-generation imager applications. To achieve this goal, several key requirements were tackled and presented in each chapter. To be brief, we have investigated and presented followings :

† The development and optical analysis of DMD top transparent anode for inverted organic photodiode and imager application

† The direct modification of the bilayer heterojunction active layer by novel double transfer stamping (DTS) method for high performance OPD

† The employment of the DTS process to low-bandgap polymer donor material with electron blocking layer

† OPD fabrication on hemispherical concave substrate by 3D printed mask and 3D PDMS stamp

† Simulation and modeling of OPD performance integrated on metal oxide active pixel sensor circuit with transimpedance amplifier external circuit.

First of all, in order to enable the vertical integration of the OPD on active matrix array, we demonstrated a top-anode, top-illumination organic photodetector with engineered MoO_3/ Ag/ MoO_3 Dielectric/ Metal/ Dielectric (DMD) semi-transparent electrode that could be used for large area imager or optoelectronic communication. It is confirmed that the optimized DMD transparent electrode with 5 nm MoO_3/ 10 nm Ag/ 35 nm MoO_3 DMD structure showed maximum optical transmittance of 85.7% with R_{sheet} = 6.2 Ω/sq, which outperforms conventional ITO values used in such applications. More detailed optical simulation and experimental measurement are done to investigate the effect of the DMD semi-transparent electrode on OPD. Another merit of the inverted OPDs is enhanced air stability of the OPD due to stable top metal electrode. The proposed DMD anode demonstrated in the chapter can be a new standard for low-cost, high performance OPD for next generation.

To suppress the dark current without sacrificing the high external quantum efficiency, a novel double transfer stamping (DTS) method is developed for the inverted OPD structure. The DTS method allowed efficient interdiffusion of the electron acceptor molecules into the electron donor polymer induced by thermal annealing process, which eventually produce optimum morphology for the heterojunction active layer, with well-defined electron donor / acceptor layers to prevent the presence of each material on cathode and anode. Precise analysis of the bilayer interdiffused organic photodiode is performed by capacitance - voltage, current - voltage, EQE measurement and optical modeling methodology. Performance parameters of the OPD were critically calculated and discussed which gave us very high specific detectivity of 4.8 x 10^{12} Jones at a reverse bias of 1.5 V at a wavelength of 546 nm. The organic photodiodes also showed a very high linear dynamic range of > 120 dB.

We also demonstrated a high performance low-bandgap polymer OPD with broadband spectrum using DTS method. Because one of the biggest advantage of the OPD is the variety of organic materials, it is legit to investigate higher performance low-bandgap polymer materials which potentially yield better OPD characteristics. Besides the popular P3HT:PCBM

BHJ or BiHJ system, we investigated the OPD performance of PTB7-Th:PC$_{70}$BM BHJ active layer with inverted structure. For the higher performance OPD to produce lower dark current and higher responsivity, various approaches of the device structure employing hole blocking layer (HBL) or / and electron blocking layer (EBL) were investigated. A very low dark current of ~ 5 nA/cm^2 at reverse bias 0.5 V was achieved with BHJ active layer sandwiched between both HBL and EBL resulting in high specific detectivity of 1.48 x 10^{13} Jones at 700 nm, which is significantly high value comparable with commercially available inorganic photodiode counterparts. In addition, critical noise current measurement of the OPD was done to evaluate more accurate Noise Equivalent Power (NEP) value. It turned out that the shot noise is dominant over the thermal noise in the OPD verified by the in-depth noise analysis. Further analysis frequency response of the OPD was conducted and the acquired 3 dB cut-off frequency was f. $_{3dB}$ = 700 kHz. Moreover, the alternative optimum structure for the PTB7-Th:PC$_{70}$BM BHJ photovoltaic cell was also investigated which gave us the best PCE of 8.45 % with PC$_{70}$BM HBL employed. More deliberate design of the device structure can deliver higher performance OPD / OPV cell with developed DTS method.

The other attractive character of the organic polymer semiconductor is its processability on arbitrary surface. To investigate this benefit for the various OPD applications, we successfully fabricated hemispherical organic photodiode arrays on curved concave glass substrate. To achieve the goal, we developed a novel 3D shadow mask by additive manufacturing process (stereolithography) for the electrode deposition and 3D shaped PDMS stamp for organic active layer formation. The techniques allowed the direct patterning of the OPD devices on hemispherical substrates without excessive strain or deformation. It is believed that the developed 3D mask and 3D organic layer transfer printing process can be further utilized to various optoelectronic device applications which require free form factor on arbitrary substrates.

Lastly, based on the aforementioned accomplishments for the high performance OPD development, a thorough simulation of the OPD stacked a-ITZO TFT active pixel sensor (APS) pixel with external transimpedance amplifier (TIA) readout circuit was performed. We especially investigated the applicability of the organic photodiode we developed for the imager application with a-ITZO thin film transistor active pixel sensor circuit and transimpedance amplifier circuit. Various parameters such as feedback capacitance and resistance was considered and optimized to produce high output voltage with affordable dynamic range. Charge-to-current gain (K) and charge-to-voltage gain (K) was critically calculated in various scenarios of the system and maximum K and G value obtained was 18.2 μA/pC and 9.1 V/pC, respectively. The transimpedance amplifier approach for the readout IC can potentially decrease the integration cost of the readout circuits by eliminating the large-value integrating capacitor and complex reset switch configuration. To sum up, we demonstrated that the OPD stacked a-ITZO TFT APS with TIA can be a promising technology for the next generation high performance imager application.

7.2 Recommendations for Future Work

There are still more works to be done to prove that the organic photodiode is promising alternative for the next generation imager application. We propose following topics as suggested future works for the potential future researchers.

· Organic photodiode integration on CMOS imager

Although it is shown that organic photodiodes have many possibilities to be used for the imager applications, actual demonstration of the large area imager integrated with organic photodetector was not accomplished in this work. We suggest to develop a hybrid CMOS image sensor vertically integrated with solution-processable organic photodetectors. The suggested CMOS image sensor technology is mature, and already in market. Therefore, the fabrication of

the hybrid organic-CMOS image sensor can be easier and more accessible than other undeveloped next - generation imagers such as OPD stacked IGZO TFT APS image sensor.

· Spectral imager with structured color filter

We previously demonstrated that DMD structure can be a great alternative of the top transparent electrode for the OPD imager applications. By modifying the DMD structure to metal/DMD (MDMD) structure, we can further extend the functionality of the DMD transparent top electrode to color filtered electrodes at the same time by employing structured Fabry-Perot cavity. By finely tuning the optical cavity induced by the MDMD structure, it is possible to create the structured RGB color filter array which can be potentially used for next-generation colored image sensor. To accomplish this goal, we suggest to do the following : An optical simulation and optimization of the DMDM color filter ; fabrication of the DMDM color filter on glass substrate by various deposition method including thermal evaporation and solution processing ; Integration of the DMDM color filter with organic photodetector and active matrix backplane.

· Fabrication of active matrix array on a spherical substrate by 3D mask approach

A passive matrix array using cross-bar approach was successfully demonstrated in the thesis. However, for fully functional OPD imager, it is necessary to integrate active matrix array such as passive pixel sensor (PPS) or active pixel sensor (APS) on the hemispherical substrate. For this purpose, it is suggested to investigate the possibility to use 3D mask concept for patterning finer density circuits by conventional / unconventional patterning technology such as photolithography, spin-coating, spray-coating, or etc. Moreover, further investigation and optimization for the deposition condition of organic active layer and top transparent electrode need to be followed. Finally, proper optical lens design and testing methodology should be explored to evaluate the performance of the fabricated device.

APPENDIX A

Influence of Series Resistance in Large Area Solar Cells

Practical large area solar cell devices suffer from resistive losses, which should be minimized to maintain the performance of the devices. We will quantify the effect of series resistance, Rs by computing the resistive power loss. In small area devices, organic semiconducting active layers contribute more to the resistive power loss than other factors. However, as the size of the devices increases, the Rs of the transparent electrodes becomes the main factor of the resistive loss. The total resistive power loss per unit area is given by

$$P_R = \frac{R_S(J_{max}A)^2}{A} = R_S A J_{max}^2, \tag{A-1}$$

where P_R is the total resistive power loss per unit area, R_S is the series resistance in the device, J_{max} the current density, and A the area of the devices. Rs in organic solar cell contains the the resistances of the anode, active layer, contacts, and cathode:

$$R_S = R_{anode} + R_{active} + R_{contacts} + R_{cathode}, \tag{A-2}$$

where R_{active} and $R_{contacts}$ are the series resistances of active layer and contacts of each layer, respectively. When we assume the conventional structure of organic solar cell, cathode side is the reflective metal and the anode side is the transparent electrode. R_{active} and $R_{contacts}$ does not increase with area scaling since they are vertical components in the cell which have the same carrier travel distance regardless of cell area. Furthermore, the metal cathode has negligible series resistance as compared to transparent anode electrode such as ITO, with typical conductivity ratio of ~100:1. Therefore, the main factor that determines the resistive loss with increasing device size is the resistance of transparent electrode. Figure A.1 shows each component inside the cell graphically.
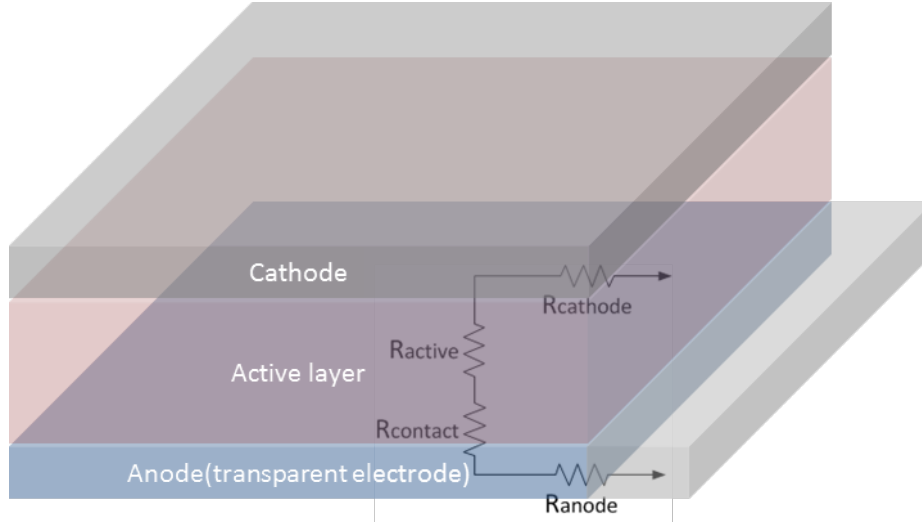
Figure A.1 Description of series resistance components inside conventional OPV cells.

The effect of the series resistance can be studied in more detail with the non-ideal equivalent circuit model, which is widely acceptable for both inorganic solar cells and organic solar cells [234]. With the parasitic resistances included, the diode equation becomes,

$$J(V) = J_o \left(e^{\frac{q(V - J(V)R_S A)}{nkT}} - 1 \right) + \frac{V - J(V)R_S A}{R_{sh}A} - J_{ph} \qquad (A\text{-}3)$$

where J_o is the reverse saturation current, V is the applied voltage, J is the current density of the cell, n is the diode ideality factor, k is Boltzmann's constant, T is temperature, R_s is series resistance, R_{sh} is shunt resistance and J_{ph} is the photocurrent generated by the cell. The parameters J_o, n, R_s, R_{sh} and J_{ph} can be obtained by fitting the diode model to the experimental J-V data from actual OPV devices under illuminated and dark conditions. Servaites *et al.* [235] showed the impact of Rs on the performance of large area P3HT:PCBM BHJ OPVs using ITO anode. Figure A.2 shows the effect of Rs variation on the J-V curves for the P3HT:PCBM test cell. In the graph, Rs is the only parameter that changes and all the other parameters in Equation A-3 are kept constant. The results show that the resistive losses due to Rs remain negligible with cell areas under ~0.1 cm^2. However, as cell area increases over 0.2 cm^2, the efficiency

starts to drop significantly due to steep increase of anode series resistance. Figure A.2(b) show

the relationship between anode conductivity and cell area on power conversion efficiency of

the P3HT:PCBM device, illustrating the importance of the anode conductivity as the cell size

increases.

a.
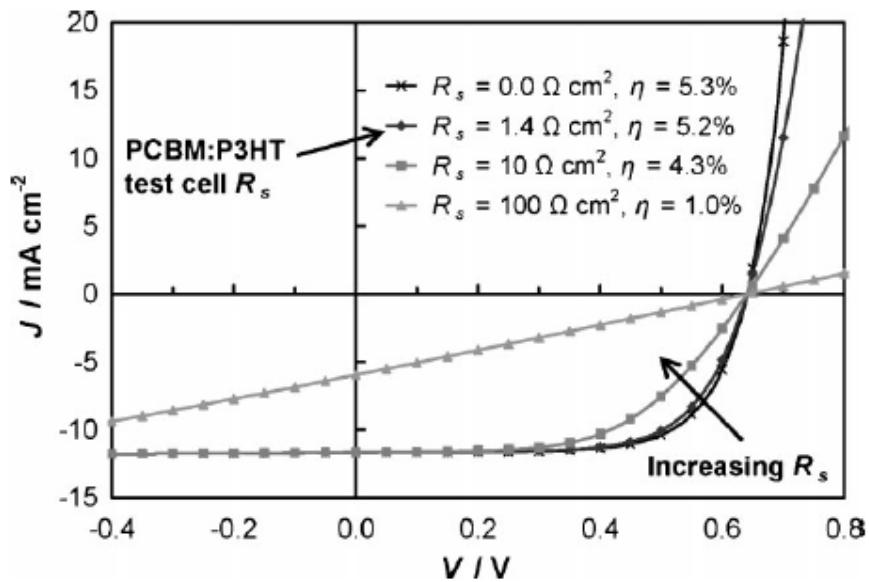
b.
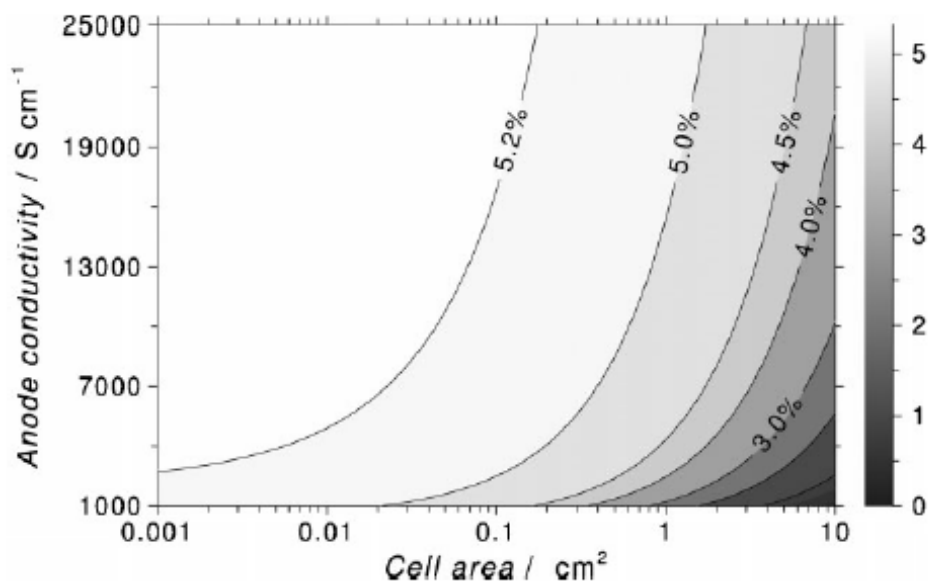
Figure A.2 (a) The effect of Rs variation on projected J-V characteristics for the P3HT:PCBM test cell. (b) The effect of anode conductivity and cell area on cell power conversion efficiency for the P3HT:PCBM test cell.

A.1 Design Strategy of Transparent Electrode for Low Series Resistance

To reduce the series resistance of the transparent electrode of the large area OPVs, metal grid patterns can be added to the anode side to reduce the resistive loss. Deliberate design of electrode geometry is imperative. Several strategies have been employed to reduce the negative effect of the series resistance on OPVs including bus bar design [236] , ring type design [237], stripe type design [238], and deep trench type metal grating design with conductive polymer [239]. Stripe design of the large area OPVs is the most popular type due to its simplicity and adaptability to roll-to-roll process. The resistive losses from relatively high resistance of the transparent electrode can be minimized by reducing the travel distance of the photo-generated charges at the transparent electrode. The simplest way to achieve this is by putting at least one side of metal lines as close as possible to the regions of photocurrent generation. In other words, the width of the PV cell stripe should be kept narrow with the contacts put on the long sides while the length of the stripe does not matter as long as each layer of the solar cell device has no defects or discontinuities. The effects of the width of the stripe in organic solar cells were investigated by Lungenschmied *et al*. [240]. They calculated theoretical power conversion efficiencies of a P3HT:PCBM BHJ cells with two cases of ITO sheet resistance, 15 ohm/sq. and 60 ohm/sq.. As shown in Fig A.3, the rapid decrease of the power conversion efficiency with increasing width of the rectangular solar cell can be observed while the length of the device kept same, indicating that the performance of stripe typed large area OPV devices are mainly affected by the width of the stripes as a result of the series resistance of the the transparent electrode.
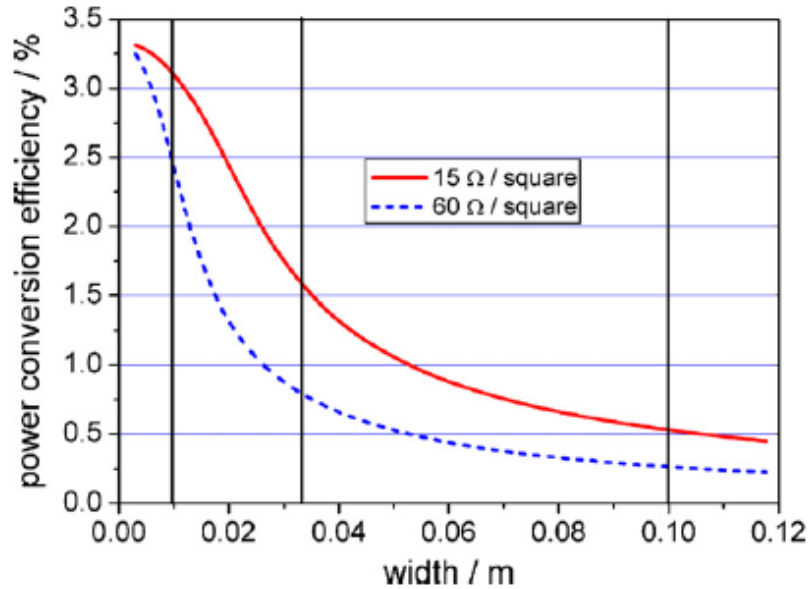
Figure A.3 Calculated power conversion efficiency of a P3HT:PCBM-based single rectangular organic solar cell as a function of the width of the electrode. Two cases are shown, an ITO sheet resistance of 15Ohm/sq.(solid line) and 60 ohm/sq.(dashed line).

Another effective way to reduce the Rs of transparent electrode is the combination of metal mesh and PEDOT:PSS to serve as transparent electrode [241]. By increasing the metal width and reducing the mesh period, the sheet resistance can be made smaller than the conventional ITO electrode. A trade-off between the optical transmittance and electrical conductivity still exists, though much smaller than that of ITO. This trade-off can be further compensated by embedding high aspect-ratio metal mesh into conductive polymer, which eliminates the low optical transmittance problem without sacrificing the conductivity. Kuang *et al.* [239] fabricated a nanoscale metallic grating with optical transparency over 80% and low electrical resistance under 2.4 ohm/sq.. To make the structure, a polyurethane (PU) grating structure was prepared for oblique metal deposition and argon ion milling process to get the metal layers on the PU sidewalls. The typical sheet resistance of the patterned structures with gold and silver were 9.6 ohm/sq.and 3.2 ohm/sq., respectively, which are lower than the sheet resistance of ITO for typical applications of OPVs and OLEDs.

A.2 Fine Metal Mesh Design for the Transparent Electrode

Previously we have demonstrated normal type OPVs by using fine transparent metal mesh electrodes (TME) made by nanoimprinting [241] and transfer-printing techniques [242]. Recently we fabricated TME by conventional photolithography technique and successfully fabricated inverted type OPVs with the TMEs using aluminum and silver with 150 um cell size and 5 um line width (Figure A.4). The thickness of the patterned TMEs for both metals was 50nm. Figure A.5 shows the UV-vis transmittance spectra from 200nm to 1100nm wavelength range of the TME. The transmittance of Ag TME substrate was 85%, which is comparable with ITO glass. The transmittance of Al TME was 80%, which is slightly low than ITO glass and Ag TME substrate.Inverted solar cells were fabricated with structure shown in Figure A.6. On the TME substrates, PEDOT:PSS was spun-coated to planarize the TME patterns. Polyethylenimine ethoxylated (PEIE) solution was coated subsequently to reduce the work-function of the PEDOT:PSS for it to function as a cathode for extracting electrons. Both P3HT:PC$_{61}$BM and a low bandgap polymer PIDT-phanQ:PC$_{71}$BM [243] bulk heterojunction system were used to fabricate the solar cells. MoO$_3$ and silver were deposited sequentially for the anode formation.
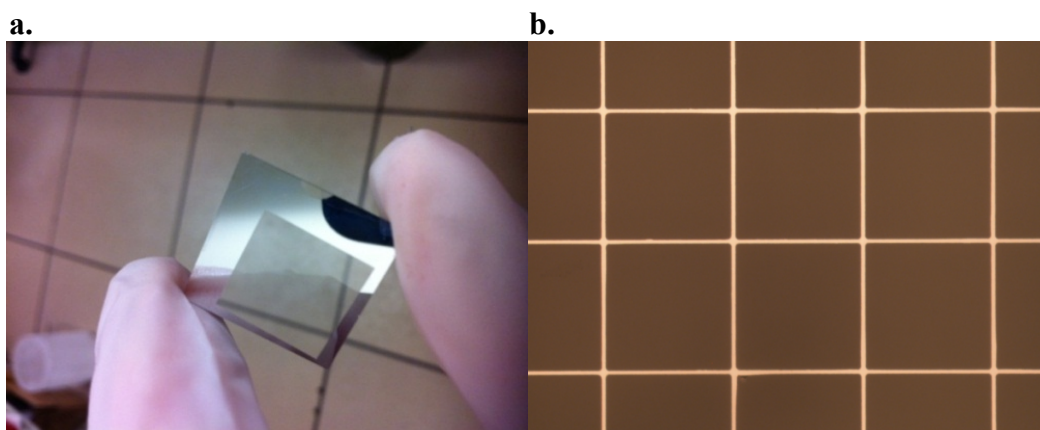
Figure A.4 (a) The fabricated transparent metal electrode on glass (b) The optical microscope image of the fabricated transparent silver electrode. The line width of silver is 5um and the distance between lines is 150um.
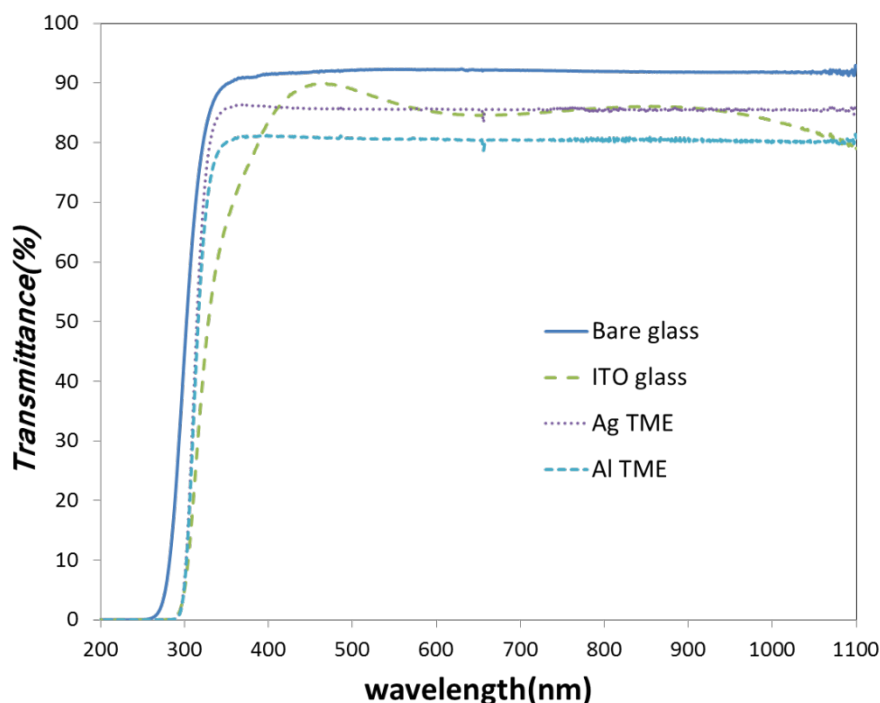
Figure. A.5 UV-Vis transmittance spectra of bare glass, ITO glass, and the transparent Ag, Al mesh electrodes.
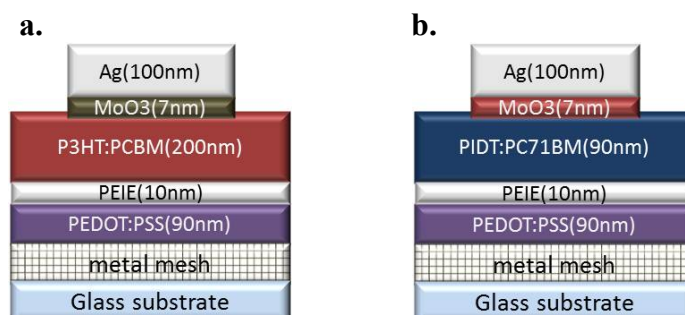
Figure A.6 The device structure of the inverted TME solar cell for (a) P3HT:PCBM bulk heterojunction (b) PIDT-phanQ:PC71BM bulk heterojunction.

To compare the performance of the TME substrates for organic solar cell application two PEDOT:PSS materials with different conductivity, pristine PH500 (σ = 0.2 S/cm) and PH1000 (σ = 0.4 S/cm) purchased from HC Starck , were used to compare the performance of Al and Ag TME electrodes. The current density versus voltage characteristics are shown in Figure A.7. The figures of merits are summarized in Table A.1. When we compare the P3HT:PC$_{61}$BM BHJ device with Al TME and Ag TME, the OPV with Ag TME showed superior performance than Al TME due to the higher conductivity of Ag. In Table A.2, the Ag

TME based OPV devices were compared with ITO based OPV devices for the PIDT-phanQ:$PC_{71}BM$ BHJ system. The OPV with Ag TME showed the best performance with higher current density and fill factor compared to the OPV with Al TME and ITO electrode. One of the reasons is that Ag TME with PH500 show the lowest Rs. Once again these results show the importance of Rs in determining the OPV overall efficiency.
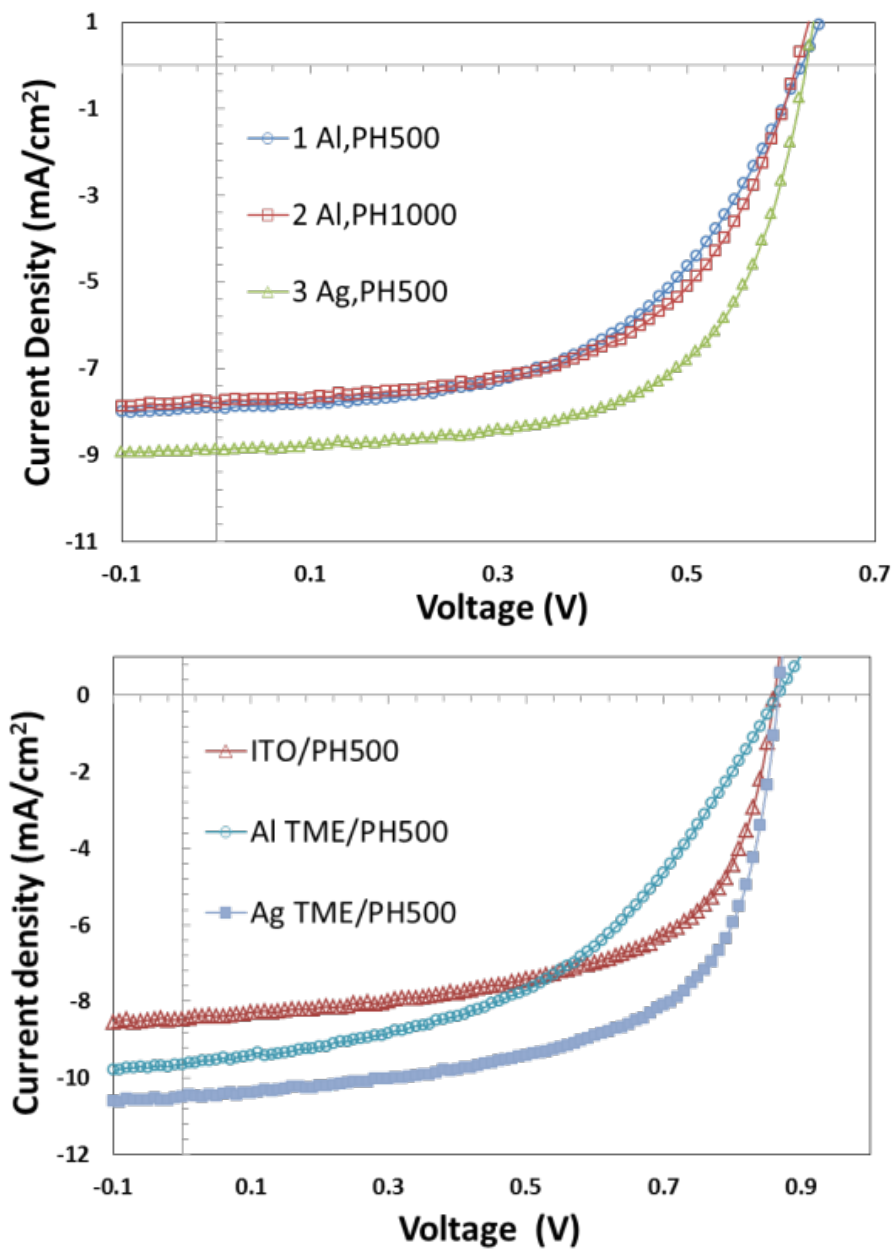
Figure A.7 J-V characteristics of organic solar cells fabricated using different transparent metal electrodes (top) P3HT:PCBM BHJ inverted cells with Al TME/PH500, Al TME/PH1000, and Ag TME/PH500 (bottom) PIDT-phanQ:PC71BM BHJ inverted cells with ITO glass/PH500, Al TME/PH500 and Ag TME/PH500.

Table A.1   Device characteristics of solar cells fabricated by transparent metal mesh of (a) P3HT:PCBM BHJ inverted cell

P3HT:PCBM	Jsc (mA/cm^2)	Voc (V)	FF (%)	PCE (%)	Rs (Ωcm^2)	Rsh (Ωcm^2)
Al TME/PH500	7.90	0.63	52.46	2.62	19.52	3588.17
Al TME/PH1000	8.20	0.63	56.22	2.89	11.85	767.65
Ag TME/PH500	9.01	0.64	61.57	3.53	6.29	1932.42

Table A.2   Device characteristics of solar cells fabricated by transparent metal mesh of PIDT-phanQ :PC71BM BHJ inverted cell

P3HT:PCBM	Jsc (mA/cm^2)	Voc (V)	FF (%)	PCE (%)	Rs (Ωcm^2)	Rsh (Ωcm^2)
ITO/PH500	8.53	0.87	59.62	4.41	5.95	1320.41
Al TME/PH500	9.66	0.88	46.90	3.99	32.10	591.74
Ag TME/PH500	10.54	0.88	61.49	5.68	4.14	1927.38

A.3 Conclusions

This chapter described the influence of the series resistance in large area solar cell / photodetector. Metal mesh structures in combination with conductive polymers was also introduced as the ITO-free transparent electrode. Finally, successful fabrication of the organic solar cells using transparent metal mesh electrodes was demonstrated.

APPENDIX B

Origin of Shunt Leakage in Organic Solar Cells with Inverted Structure

B.1. Introduction

Large area organic solar cell module has become huge interest in the organic photovoltaics field because the organic solar cell proved itself that it can be a great alternative for low-cost, high-throughput solar cells with efficiency higher than ~10% [1]. Recently, there were numerous efforts among researchers to fabricate large area organic solar cell modules with decent efficiency. When the thin film organic solar cell gets larger, not only series resistance but also the shunt leakage current through the buffer layers become dominant factor which hinders the solar cell module maintains the optimum performance. There were many efforts to analyze the series resistance issue in organic solar cells so far and several groups achieved significant results for the series resistance analysis on large area solar cell module [239,244–248]. However, not that many researchers focused on the shunt resistance issues so far and the research on the shunt leakage on the organic thin film solar cell remains still insufficient. There were several papers mentioning about shunt leakage for solar cells but they mainly focused on inorganic solar cells or theoretical works [121,249–251].

In this chapter, we systematically analyze the effect of shunt defect on electron transfer layer by intentional shunt holes formation on ZnO electron transfer layer of inverted organic solar cells. We found that the defect on the buffer layer reduces open circuit voltage and power conversion efficiency significantly due to increased dark saturation leakage current through the shunting defect site.

B.2. Experimental

Device Fabrication : ITO substrates (Delta Technologies, LTD) were cleaned by acetone, IPA, and DI water by sonication for 5 minutes for each process, and treated by O2 plasma for 3 minutes subsequently. The ZnO sol-gel solution was prepared by dissolving 0.5 M of zinc acetate dihydrate ($Zn(CH_3COO)_2 \cdot 2H_2O$) as a precursor in 2-methoxyethanol (2ME) solvent. 0.5 M of mono-ethanolamine was added as a stabilizer and the mixture was vigorously stirred at a temperature of 60 ^{o}C for 4 hours. The solution was then cooled down and aged for more than 24 hours. The synthesized ZnO solution was spin-coated on top of the ITO layer with spin-coating speed of 3000 rpm for 30 seconds and annealed at 150 ^{o}C for 20 minutes, yielding 40nm thickness of ZnO layer. To pattern the shunting holes on ZnO layer, we used conventional lithography process using photomasks with various densities of holes. After forming the various areas of holes on ZnO layers, the substrates were transferred to a glove box with nitrogen atmosphere for deposition of photoactive layer. 20 mg of regioregular P3HT and 16mg of PCBM (American Dye Source, Purity: > 99.5%) were mixed into Chlorobenzene and stirred by magnetic bar overnight. The solution was filtered by 0.45 um syringe filter and then spin-coated onto the ZnO layer to give an active layer thickness of 100nm. After annealing at 160 ^{o}C for 8 minutes, the substrates were transferred into thermal evaporator with shadow mask on it to deposit 7 nm MoO_3 and 100 nm of silver to finish the fabrication. The device size was 0.785 mm^2 with circular shape of 1 mm diameter.

Device Measurement : A solar simulator(Oriel) equipped with Xenon lamp and AM 1.5G filter at intensity of 100mW/cm^2, was used for the current density-voltage (J-V) characteristic measurement. The system was calibrated with a NREL certified reference silicon photodiode. The current versus voltage (I-V) characteristics of all the PV cells were measured by Keithley 2400 system.

B.3. Results and Discussion

Figure B.1(a) shows schematic of the inverted organic solar cell with possible shunt paths on buffer layers. In this study, as shown in Figure B.1(b), we intentionally patterned the shunt holes on ZnO electron transfer layer with densities of 1%, 5% and 20% with periodical holes pattern with 3 um diameter (Figure B.1(c)). The current density versus voltage (J-V) measurement of the inverted solar cells with various shunt hole sizes under 1 sun illumination are presented in Figure B.2.
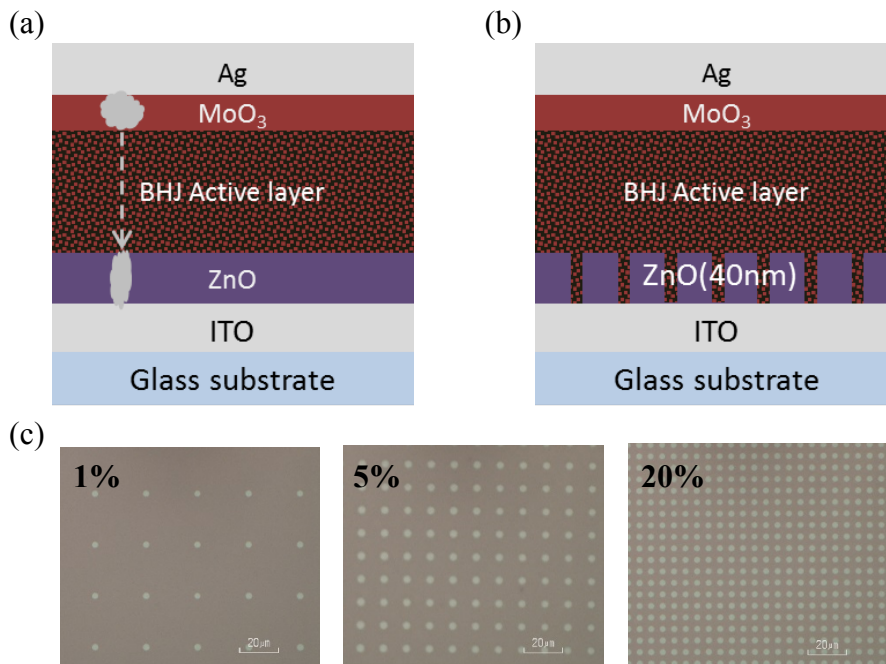
Figure B.1 (a) Schematic of the possible localized shunt leakage in OPV cells, (b) Schematic of the OPV cells with intentional shunt holes formation, (c) Optical microscope picture of ZnO layers on ITO substrate with various hole areas of 1%, 5% and 20%.

The device parameters including short circuit current (Jsc), open circuit voltage (Voc), fill factor (FF), power conversion efficiency (PCE), series resistance (Rs) and sheet resistance (Rsh) are summarized in Table B.1. The control device with no intentional shunt holes on ZnO layer gave us the Voc value of 0.62V, which is the typical value of the P3HT:PCBM inverted solar cells. As the shunt holes area increases, the V_{OC} starts to decrease significantly from 0.57

V of 1 % shunt holes device to 0.50 V for 5 % shunt hole device and 0.40V for 20 % shunt hole

device, respectively.
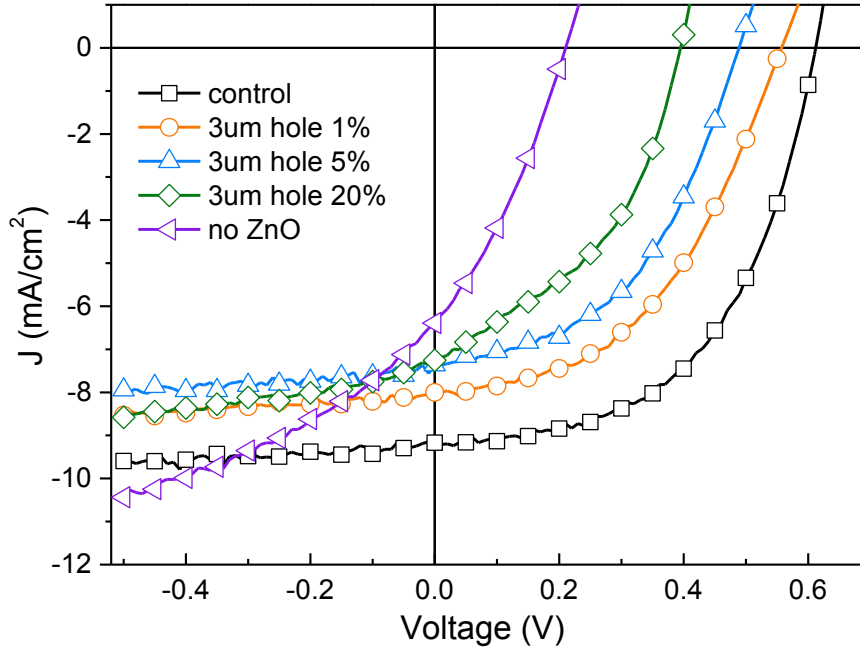
Figure B.2. Current density (J) versus voltage (V) characteristics under 1 sun condition for various shunt hole densities on ZnO electron transfer layers.

Table B.1. Summary of device performance of P3HT:PCBM based inverted solar cells with various shunt hole densities on ZnO electron transfer layer

	Jsc (mA/cm^2)	Voc (V)	FF (%)	PCE (%)	Rs (Ωcm^2)	Rsh (Ωcm^2)
control	9.17	0.62	52.84	3.00	9.88	737.84
3um hole 1%	8.00	0.57	45.73	2.09	26.66	510.93
3um hole 5%	7.36	0.50	46.73	1.72	23.43	381.55
3um hole 20%	7.25	0.40	41.59	1.21	13.66	146.04

This reduction of the Voc was essentially due to the shunt resistance decrease which is

reduced about four times from R_{sh} = 737.84 Ωcm^2 of control device to R_{sh} = 146.04 Ωcm^2 for

20% shunt hole device. To clarify the origin of the Voc and R_{sh} reduction, the dark current

density was measured according to voltage. The graph for dark current density versus voltage (J_{dark}-V) measurement is shown in Figure B.3. From the graph, we can clearly see the dark current density at reverse bias significantly increases when the area of shunt holes increases. Control device with no shunt holes shows dark current density of $2x10^{-3}$ mA/cm^2 at - 0.5 V. However, the device with only 1% area of shunt holes shows the dark current density of $1X10^{-2}$ mA/cm^2 which is one order of the magnitude larger than control device. The devices with 5% and 20% area of shunt holes showed dark currents of $8x10^{-2}$ mA/cm^2 and $2x10^{-1}$ mA/cm^2 at - 0.5 V, respectively, which is significantly higher than the dark current of the control device which has no shunt defect. This result proves that the increased dark saturation current is closely related to open circuit voltage and shunt resistance reduction.
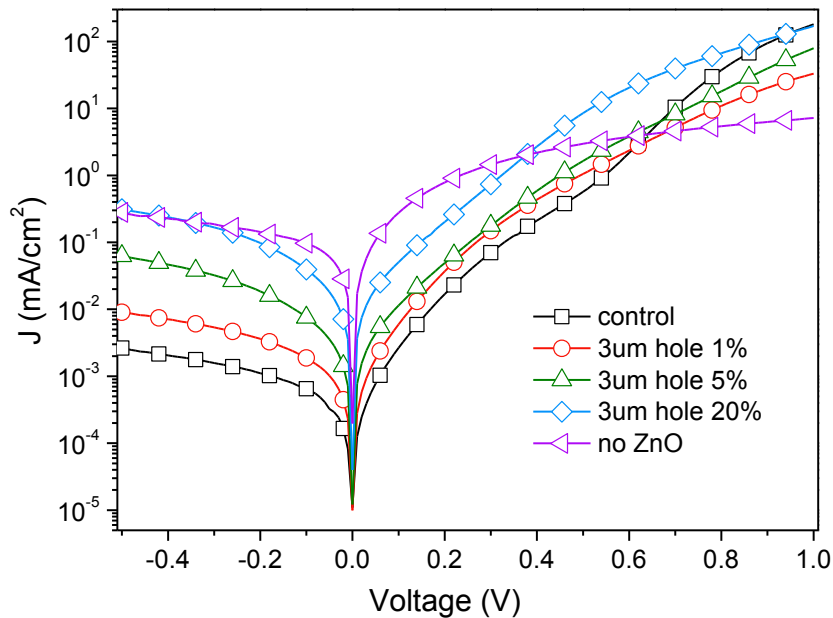
Figure B.3. Dark saturation current density (J_{dark}) versus voltage (V) characteristics of the solar cells with various shunt hole densities on ZnO electron transfer layers.

To elucidate the relationship between open circuit voltage and dark saturation current reduction with increasing shunt hole areas, we utilize the non-ideal diode equation B-1 which has been generously accepted in organic solar cell research.

Table B.2. Comparison of calculated and measured dark saturation current J_o of the solar cell devices with various shunt hole densities on ZnO electron transfer layer

	Voc (V)	Rsh (Ωcm^2)	Calculated J_o (mA/cm^2)	Measured J_o (mA/cm^2)
control	0.62	737.84	3.2×10^{-5}	4.5×10^{-5}
3um hole 1%	0.57	510.93	6.9×10^{-5}	7.8×10^{-5}
3um hole 5%	0.50	381.55	2.31×10^{-4}	1.4×10^{-4}
3um hole 20%	0.40	146.04	2.4×10^{-3}	2.0×10^{-3}

$$J(V) = J_o \left[\exp\left(\frac{q(V - J(V)R_S)}{nkT} \right) - 1 \right] + \frac{V - J(V)R_S}{R_{sh}} - J_{ph}(V) \qquad (B\text{-}1)$$

where J is total current, J_o is reverse dark saturation current, n is ideality factor, k is Boltzmann constant, T is temperature, R_S is series resistance, R_{sh} is shunt resistance and J_{ph} is photocurrent. Equation B-1 can be used to fit the experimental data by adapting appropriate fitting parameters such as J_o, R_S, R_{sh} and n. When we put the total current value to zero, the equation B-1 can be modified in terms of the open circuit voltage, yielding,

$$V_{OC} = \frac{nkT}{q} \ln \left[\frac{J_{ph}(V_{OC})}{J_o} + 1 - \frac{V_{OC}}{R_{sh}J_o} \right] \qquad (B\text{-}2)$$

Table B.2 shows the comparison of calculated and measured values of J_o of the solar cell devices with 0%, 1%, 5% and 20% shunt hole areas. We observed that the calculated dark saturation current values match with the measured values with minor errors. This analysis proves that the V_{OC} reduction is directly related to the dark saturation current increase due to the increased leakage recombination current through the shunt holes in ZnO buffer layers.

We also investigated the behavior of V_{OC} reduction with illuminated condition by comparing the experimental data with simulated photovoltaic J-V curves. The simulated J-V curves with 1 sun illumination were calculated by linear superposition of the data extracted from control device with ZnO buffer layer and the device without ZnO layer. For example, the

simulated J-V characteristic for the device with 5% shunt hole area was obtained by linearly summing up the J-V data of the control device with ZnO buffer layer scaled by 95% and the data of the device without ZnO layer scaled by 5%. The simulated result for the devices with 5% and 20% shunt areas was compared with the experimental result of the corresponding devices with 3 um shunt holes.
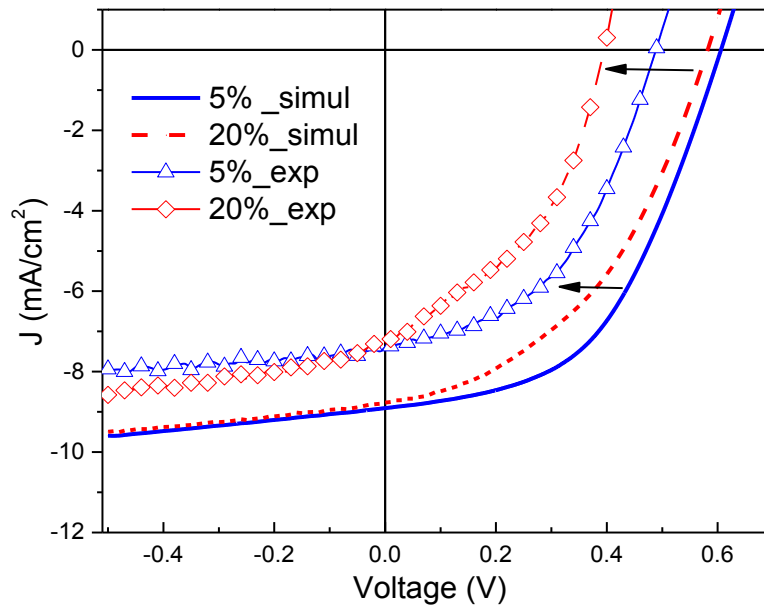
Figure B.4. Comparison of J-V characteristics under 1 sun illumination for simulated and experimental data with shunt hole densities of 5% and 20%

Table B.3. Comparison of open circuit voltage and shunt resistance of simulated data and experimental data for 3um shunt holes with 5% and 20% areas on ZnO layers of solar cell devices

3% holes	Simulation		Experimental		Voc Deviation	Rsh Deviation
	Voc (V)	Rsh (Ωcm^2)	Voc (V)	Rsh (Ωcm^2)		
5% shunt	0.60	465.74	0.50	381.55	0.10 V	84.19 Ωcm^2
20% shunt	0.55	229.11	0.40	146.04	0.15 V	83.07 Ωcm^2

As shown in Figure B.4, the experimental J-V characteristics showed apparent divergence with the simulated result. When the simulated data yields V_{OC} reduction of 0.02 V and 0.07 V for 5% and 20% shunt hole devices, respectively, compared to control device, the actual devices showed huge deviation of V_{OC} value with 0.12 V and 0.22 V for each device. The shunt resistance difference between simulated and experimental device was also apparently large. Table B.3 summarizes the comparison of the simulated and experimental results and their deviation. To explain this large deviation between simulated and experimental results, we suspect the shunt holes have funneling effect which makes the effective shunt holes much bigger to attract more photogenerated charges near the holes, due to the lower contact resistance of no ZnO area compared to the resistance of area with ZnO buffer layer.

B.4. Conclusion

In this chapter, we systematically analyzed the effect of shunting holes on buffer layer of organic thin film solar cells with inverted structure. To find out the origin of the V_{OC} reduction with increasing shunting areas, the dark saturation current versus voltage characteristics was exploited to establish the direct relationship between open circuit voltage reduction and dark current increase. We also compared the experimental result with simulated data of the solar cell devices with various shunt hole areas and huge discrepancy between the data was observed. This study tells us that even the small percentage of shunting leakage areas such as pinholes or particle defects deteriorates the overall performance of the solar cell due to the crowding effect of recombination current on the shunt defects making the effective site of the shunting leakage area bigger. To realize the scale up of the organic solar cell devices from laboratory level to industrial size, it would be crucial to establish the robust design of the buffer layers for organic solar cell structure.

BIBLIOGRAPHY

[1] L. Dou, J. You, Z. Hong, Z. Xu, G. Li, R.A. Street, Y. Yang, 25th anniversary article : a decade of organic/polymeric photovoltaic research, Adv. Mater. 25 (2013) 6642–71.

[2] K.-J. Baeg, M. Binda, D. Natali, M. Caironi, Y.-Y. Noh, Organic light detectors : photodiodes and phototransistors, Adv. Mater. 25 (2013) 4267–95.

[3] Z. Bao, Materials and fabrication needs for low-cost organic transistor circuits, Adv. Mater. 12 (2000) 227–230.

[4] M.C. Hamilton, J. Kanicki, Organic polymer thin-film transistor photosensors, IEEE J. Sel. Top. Quantum Electron. 10 (2004) 840–848.

[5] T. Tsujimura, OLED displays fundamentals and applications, John Wiley & Sons, 2012.

[6] J. Wang, F. Zhang, J. Zhang, W. Tang, A. Tang, H. Peng, Z. Xu, F. Teng, Y. Wang, Key issues and recent progress of high efficient organic light-emitting diodes, J. Photochem. Photobiol. C Photochem. Rev. 17 (2013) 69–104.

[7] Y. Hong, J.-Y. Nahm, J. Kanicki, Optoelectrical properties of four amorphous silicon thin-film transistors 200 dpi active-matrix organic polymer light-emitting display, Appl. Phys. Lett. 83 (2003) 3233.

[8] G. Yu, J. Gao, J.C.J. Hummelen, F. Wudl, A.J. Heeger, Polymer photovoltaic cells: enhanced efficiencies via a network of internal donor-acceptor heterojunctions, Science (80-.). 270 (1995) 1789–1791.

[9] C.W. Tang, Two-layer organic photovoltaic cell, Appl. Phys. Lett. 48 (1986) 183.

[10] P. Peumans, V. Bulovic, S.R. Forrest, Efficient, high-bandwidth organic multilayer photodetectors, Appl. Phys. Lett. 76 (2000) 3855–3857.

[11] P. Rebello, L. Costa, V. Ferro, Development of all-organic antenna printed for passive UHF RFID application, in: 2014 IEEE Bras. RFID, IEEE, 2014: pp. 57–60.

[12] H.-J. Shin, K.-M. Park, S. Takasugi, S.-H. Choi, Y.-S. Jeong, H.-D. Choi, I.-J. Kim, H.-S. Kim, H.-W. Lee, C.-H. Oh, 45-2: Advanced OLED Display Technologies for Large-Size Semi-Flexible TVs, SID Symp. Dig. Tech. Pap. 47 (2016) 609–612.

[13] Y. Galagan, R. Andriesse, Third generation photovoltaics, InTech, 2012.

[14] http://www.japanbullet.com/technology/new-organic-transistor-can-be-sterilized-at-150-degrees-c, (n.d.).

[15] http://www.osadirect.com/news/article/980/isorg-and-plastic-logic-co-develop-the-worlds-first-organic-image-sensor-on-plastic/, (n.d.).

[16] J. hyuk Lee, H.D. Kim, C.H. Lee, H.-J. Chung, S.C. Kim, S.S. Kim, The technological trends of future AMOLED, in: Proc. SPIE, International Society for Optics and Photonics, 2009: p. 74150O–1.

[17] Y.-H. Tak, C.-W. Han, H.-S. Kim, B.-C. Kim, J.-W. Kim, T.-S. Kim, B.-S. Kim, C.-H. Oh, S.-Y. Cha, B.-C. Ahn, Novel technologies for commercialized 55-inch WRGB OLED TV, Proc. SPIE - Int. Soc. Opt. Eng. 8829 (2013) 88290R.

[18] P. Stallinga, Electrical characterization of organic electronic materials and devices, John Wiley & Sons, 2009.

[19] J.E. Lennard-Jones, Cohesion, Proc. Phys. Soc. 43 (1931) 461–482.

[20] A. Köhler, H. Bässler, Electronic Processes in Organic Semiconductors: An Introduction., John Wiley & Sons, 2015.

[21] M. Pope, C.E. Swenberg, Electronic processes in organic crystals and polymers, 2nd ed., Oxford University Press, New York, 1999.

[22] P. Peumans, A. Yakimov, S.R. Forrest, Small molecular weight organic thin-film photodetectors and solar cells, J. Appl. Phys. 93 (2003) 3693.

[23] T. Förster, Delocalized excitation and excitation transfer., Florida State University, Talahassee Flor., 1965.

[24] S.R. Forrest, The limits to organic photovoltaic cell efficiency, MRS Bull. 30 (2005) 28–32.

[25] S. Forrest, EECS 598 Organic electronics : fundamentals to applications, Lecture Notes, (2016).

[26] S. Forrest, Ultrathin organic films grown by organic molecular beam deposition and related techniques, Chem. Rev. 97 (1997) 1793–1896.

[27] H. Klauk, ed., Organic electronics: materials, manufacturing, and applications, John Wiley & Sons, 2006.

[28] https://stuff.mit.edu/afs/athena.mit.edu/course/3/3.082/www/team2_f02/, (n.d.).

[29] K.P. Gritsenko, A.M. Krasovsky, Thin-film deposition of polymers by vacuum degradation, Chem. Rev. 103 (2003) 3607–3649.

[30] D.B. Hall, P. Underhill, J.M. Torkelson, Spin coating of thin and ultrathin polymer films, Polym. Eng. Sci. 38 (1998) 2039–2045.

[31] F. Guo, Z. Xiao, J. Huang, Fullerene photodetectors with a linear dynamic range of 90 dB enabled by a cross-linkable buffer layer, Adv. Opt. Mater. 1 (2013) 289–294.

[32] X. Zhou, D. Yang, D. Ma, Extremely low dark current, high responsivity, all-polymer photodetectors with spectral response from 300 nm to 1000 nm, Adv. Opt. Mater. 3 (2015) 1570–1576.

[33] M.S. Kim, D.H. Lee, Y.H. Cha, K.B. Kim, S.H. Jung, J.K. Lee, O. Beom-Hoan, S.G. Lee, S.G. Park, Preparation of fluoropolymer structures for orthogonal processing of diverse material by Micro-Contact Printing, Microelectron. Eng. 123 (2014) 33–37.

[34] J.C. Aguirre, S.A. Hawks, A.S. Ferreira, P. Yee, S. Subramaniyan, S.A. Jenekhe, S.H. Tolbert, B.J. Schwartz, Sequential processing for organic photovoltaics: Design rules for morphology control by tailored semi-orthogonal solvent blends, Adv. Energy Mater. 5 (2015) 1–11.

[35] H. Youn, H. Kim, L.J. Guo, Low-cost fabrication of organic photovoltaics and polymer LEDs, Low-cost nanomaterials, green energy and technology, Springer, 2014.

[36] A. Teichler, J. Perelaer, U.S. Schubert, Inkjet printing of organic electronics – comparison of deposition techniques and state-of-the-art developments, J. Mater. Chem. C. 1 (2013) 1910.

[37] S.-H. Jung, J.-J. Kim, H.-J. Kim, High performance inkjet printed phosphorescent

organic light emitting diodes based on small molecules commonly used in vacuum processes, Thin Solid Films. 520 (2012) 6954–6958.

[38] M. Singh, H.M. Haverinen, P. Dhagat, G.E. Jabbour, Inkjet printing-process and its applications, Adv. Mater. 22 (2010) 673–685.

[39] M. Bale, J.C. Carter, C.J. Creighton, H.J. Gregory, P.H. Lyon, P. Ng, L. Webb, A. Wehrum, Ink-jet printing: The route to production of full-color P-OLED displays, J. Soc. Inf. Disp. 14 (2006) 453.

[40] T. Shimoda, K. Morii, S. Seki, H. Kiguchi, Inkjet printing of light-emitting polymer displays, MRS Bull. 28 (2003) 821–827.

[41] P.. Blazdell, J.R.. Evans, Application of a continuous ink jet printer to solid freeforming of ceramics, J. Mater. Process. Technol. 99 (2000) 94–102.

[42] A. Asai, Three-dimensional calculation of bubble growth and drop ejection in a bubble jet printer, J. Fluids Eng. 114 (1992) 638.

[43] Heliatek sets new Organic Photovoltaic world record efficiency of 13.2%. (2016, Feb 02). Retrieved from http://www.heliatek.com/en/press/press-releases/details/heliatek-sets-new-organic-photovoltaic-world-record-efficiency-of-13-2, (n.d.).

[44] M.T. Dang, L. Hirsch, G. Wantz, P3HT:PCBM, best seller in polymer photovoltaic research, Adv. Mater. 23 (2011) 3597–3602.

[45] L. Dou, Y. Liu, Z. Hong, G. Li, Y. Yang, Low-bandgap near-IR conjugated polymers / molecules for organic electronics, Chem. Rev. 115 (2015) 12633–12665.

[46] X. Gong, M. Tong, Y. Xia, W. Cai, J.S. Moon, Y. Cao, G. Yu, C.-L. Shieh, B. Nilsson, A.J. Heeger, High-detectivity polymer photodetectors with spectral response from 300 nm to 1450 nm., Science. 325 (2009) 1665–7.

[47] C.H. Cheung, D.Y. Kim, J. Subbiah, C.M. Amb, J.R. Reynolds, F. So, Solution processed polymer near-infrared photodiode with electron and hole blockers, IEEE Trans. Electron Devices. 61 (2014) 3852–3857.

[48] A. Pierre, I. Deckman, P.B. Lechêne, A.C. Arias, High detectivity all-printed organic photodiodes, Adv. Mater. 27 (2015) 6411–6417.

[49] P.E. Keivanidis, S.-H.H. Khong, P.K.H. Ho, N.C. Greenham, R.H. Friend, All-solution based device engineering of multilayer polymeric photodiodes: Minimizing dark current, Appl. Phys. Lett. 94 (2009) 173303.

[50] F. Guo, B. Yang, Y. Yuan, Z. Xiao, Q. Dong, Y. Bi, J. Huang, A nanocomposite ultraviolet photodetector based on interfacial trap-controlled charge injection, Nat. Nanotechnol. 7 (2012) 798–802.

[51] X. Hu, K. Wang, C. Liu, T. Meng, Y. Dong, S. Liu, F. Huang, X. Gong, Y. Cao, High-detectivity inverted near-infrared polymer photodetectors using cross-linkable conjugated polyfluorene as an electron extraction layer, J. Mater. Chem. C. 2 (2014) 9592–9598.

[52] A. Kumar, D. Moet, J.-L. van der Steen, A. Tripathi, F.G. Rodriguez, J. Maas, M. Simon, W. Reutten, A. Douglas, R. Raaijmakers, P.E. Malinowski, K. Myny, U. Shafique, R. Andriessen, P. Heremans, G. Gelinck, J. Van Der Steen, X-ray imaging sensor arrays on foil using solution processed organic photodiodes and organic transistors, 9137 (2014) 91370Q.

[53] T. Rauch, M. Boberl, U. Lemmer, W. Heiss, O. Hayden, M. Bo, W.H. and O.H. berl , Sandro F. Tedde, Jens Fu rst, Maksym V. Kovalenko, Gu nter Hesser, Uli Lemmer, Near-infrared imaging with quantum-dot- sensitized organic photodiodes, Nat. Photonics. 3 (2009) 332–336.

[54] N. Martino, D. Ghezzi, F. Benfenati, G. Lanzani, M.R. Antognazza, J.M. Chem, N. Martino, D. Ghezzi, F. Benfenati, G. Lanzani, M.R. Antognazza, Organic semiconductors for artificial vision, J. Mater. Chem. B. 1 (2013) 3768–3780.

[55] X. Xu, M. Davanco, X. Qi, S.R. Forrest, Direct transfer patterning on three dimensionally deformed surfaces at micrometer resolutions and its application to hemispherical focal plane detector arrays, Org. Electron. 9 (2008) 1122–1127.

[56] T.N. Ng, W.S. Wong, M.L. Chabinyc, S. Sambandan, R.A. Street, Flexible image sensor array with bulk heterojunction organic photodiode, Appl. Phys. Lett. 92 (2008) 213303.

[57] S. Tedde, E.S. Zaus, J. Fürst, D. Henseler, P. Lugli, Active pixel concept combined with organic photodiode for imaging devices, IEEE Electron Device Lett. 28 (2007) 893–895.

[58] G.H. Gelinck, A. Kumar, D. Moet, J. Van Der Steen, U. Shafique, P.E. Malinowski, K. Myny, B.P. Rand, M. Simon, W. Rütten, A. Douglas, J. Jorritsma, P. Heremans, R. Andriessen, X-ray imager using solution processed organic transistor arrays and bulk heterojunction photodiodes on thin, flexible plastic substrate, Org. Electron. 14 (2013) 2602–2609.

[59] F. Arca, E. Kohlstädt, S.F. Tedde, P. Lugli, O. Hayden, Large active area organic photodiodes for short-pulse X-ray detection, IEEE Trans. Electron Devices. 60 (2013) 1663–1667.

[60] T. Agostinelli, M. Campoy-Quiles, J.C. Blakesley, R. Speller, D.D.C. Bradley, J. Nelson, A polymer/fullerene based photodetector with extremely low dark current for X-ray medical imaging applications, Appl. Phys. Lett. 93 (2008) 203305.

[61] C. Zhao, J. Kanicki, Amorphous In–Ga–Zn–O thin-film transistor active pixel sensor x-ray imager for digital breast tomosynthesis, Med. Phys. 41 (2014) 91902.

[62] B. Zimmermann, U. Würfel, M. Niggemann, Longterm stability of efficient inverted P3HT:PCBM solar cells, Sol. Energy Mater. Sol. Cells. 93 (2009) 491–496.

[63] Z. He, C. Zhong, S. Su, M. Xu, H. Wu, Y. Cao, Enhanced power-conversion efficiency in polymer solar cells using an inverted device structure, Nat. Photonics. 6 (2012) 593–597.

[64] S.K. Hau, H.-L. Yip, N.S. Baek, J. Zou, K. O'Malley, A.K.-Y. Jen, Air-stable inverted flexible polymer solar cells using zinc oxide nanoparticles as an electron selective layer, Appl. Phys. Lett. 92 (2008) 253301.

[65] A.K.K. Kyaw, X.W. Sun, C.Y. Jiang, G.Q. Lo, D.W. Zhao, D.L. Kwong, An inverted organic solar cell employing a sol-gel derived ZnO electron selective layer and thermal evaporated MoO3 hole selective layer, Appl. Phys. Lett. 93 (2008) 221107.

[66] G. Li, C.-W. Chu, V. Shrotriya, J. Huang, Y. Yang, Efficient inverted polymer solar cells, Appl. Phys. Lett. 88 (2006) 253503.

[67] X. Liu, H. Wang, T. Yang, W. Zhang, I.-F. Hsieh, S.Z.D.D. Cheng, X. Gong, Solution-processed near-infrared polymer photodetectors with an inverted device structure, Org.

Electron. 13 (2012) 2929–2934.

[68] J. Jeong, S. Nam, H. Kim, Y. Kim, Inverted organic photodetectors with ZnO electron-collecting buffer layers and polymer bulk heterojunction active layers, IEEE J. Sel. Top. Quantum Electron. PP (2014) 1–1.

[69] D. Baierl, B. Fabel, P. Gabos, L. Pancheri, P. Lugli, G. Scarpa, Solution-processable inverted organic photodetectors using oxygen plasma treatment, Org. Electron. 11 (2010) 1199–1206.

[70] D. Baierl, B. Fabel, P. Lugli, G. Scarpa, Efficient indium-tin-oxide (ITO) free top-absorbing organic photodetector with highly transparent polymer top electrode, Org. Electron. 12 (2011) 1669–1673.

[71] M. Jørgensen, K. Norrman, F.C. Krebs, Stability/degradation of polymer solar cells, Sol. Energy Mater. Sol. Cells. 92 (2008) 686–714.

[72] C. Zhang, D. Zhao, D. Gu, H. Kim, T. Ling, Y.K.R. Wu, L.J. Guo, An ultrathin, smooth, and low-loss Al-doped Ag film and its application as a transparent electrode in organic photovoltaics, Adv. Mater. 26 (2014) 5696–5701.

[73] C.-C. Chueh, S.-C. Chien, H.-L. Yip, J.F. Salinas, C.-Z. Li, K.-S. Chen, F.-C. Chen, W.-C. Chen, A.K.-Y. Jen, Toward high-performance semi-transparent polymer solar cells : optimization of ultra-thin light absorbing layer and transparent cathode architecture, Adv. Energy Mater. 3 (2013) 417–423.

[74] K. Hong, K. Kim, S. Kim, I. Lee, H. Cho, S. Yoo, H.W. Choi, N. Lee, Y. Tak, J. Lee, Optical properties of WO3 / Ag / WO3 multilayer as transparent cathode in top-emitting organic light emitting diodes, J. Phys. Chem. C. 115 (2011) 3453–3459.

[75] B. Tian, G. Williams, D. Ban, H. Aziz, Transparent organic light-emitting devices using a MoO3/Ag/ MoO3 cathode, J. Appl. Phys. 110 (2011) 104507.

[76] T. Winkler, H. Schmidt, H. Flügge, F. Nikolayzik, I. Baumann, S. Schmale, T. Weimann, P. Hinze, H.-H. Johannes, T. Rabe, S. Hamwi, T. Riedl, W. Kowalsky, Efficient large area semitransparent organic solar cells based on highly transparent and conductive ZTO/Ag/ZTO multilayer top electrodes, Org. Electron. 12 (2011) 1612–1618.

[77] J.Y. Lee, K.-T. Lee, S. Seo, L.J. Guo, Decorative power generating panels creating angle insensitive transmissive colors., Sci. Rep. 4 (2014) 4192.

[78] K. Lee, J.Y. Lee, S. Seo, L.J. Guo, Colored ultrathin hybrid photovoltaics with high quantum efficiency, Light Sci. Appl. 3 (2014) e215.

[79] G. Li, V. Shrotriya, J. Huang, Y. Yao, T. Moriarty, K. Emery, Y. Yang, High-efficiency solution processable polymer photovoltaic cells by self-organization of polymer blends, Nat. Mater. 4 (2005) 864–868.

[80] L.A.A. Pettersson, L.S. Roman, O. Inganäs, Modeling photocurrent action spectra of photovoltaic devices based on organic thin films, J. Appl. Phys. 86 (1999) 487.

[81] A. Macleod, The admittance diagram, Soc. Vac. Coaters Bull. Spring (2008) 22–26.

[82] D. Yao, M. Gu, X. Liu, S. Huang, B. Liu, C. Ni, Fabrication and Performance of Columnar CsI (Tl) Scintillation Films With Single Preferred Orientation, 60 (2013) 1632–1636.

[83] D. Nguyen, S. Vedraine, L. Cattin, P. Torchio, M. Morsli, F. Flory, J.C. Bernède,

Effect of the thickness of the MoO 3 layers on optical properties of MoO 3 / Ag / MoO 3 multilayer structures, J. Appl. Phys. 112 (2012) 63505.

[84] C.C. Lee, S.H. Chen, C.C. Jaing, Optical monitoring of silver-based transparent heat mirrors., Appl. Opt. 35 (1996) 5698–703.

[85] K.-T. Lee, S. Seo, J.Y. Lee, L.J. Guo, Ultrathin metal-semiconductor-metal resonator for angle invariant visible band transmission filters, Appl. Phys. Lett. 104 (2014) 231112.

[86] A. Janotti, C.G. Van de Walle, Fundamentals of zinc oxide as a semiconductor, Reports Prog. Phys. 72 (2009) 126501.

[87] I. Hwang, D. Moses, A.J. Heeger, Photoinduced carrier generation in P3HT / PCBM bulk heterojunction materials, J. Phys. Chem. C. 112 (2008) 4350–4354.

[88] A. Kahn, J. Meyer, A. Kahn, Electronic structure of molybdenum-oxide films and associated charge injection mechanisms in organic devices, J. Photonics Energy. 1 (2011) 11109.

[89] P.E. Keivanidis, P.K.H. Ho, R.H. Friend, N.C. Greenham, The dependence of device dark current on the active-layer morphology of solution-processed organic photodetectors, Adv. Funct. Mater. 20 (2010) 3895–3903.

[90] C. Deibel, V. Dyakonov, Polymer–fullerene bulk heterojunction solar cells, Reports Prog. Phys. 73 (2010) 96401.

[91] B.C. Grabmaier, Crystal scintillators, IEEE Trans. Nucl. Sci. NS-31 (1984) 372–376.

[92] V.D. Mihailetchi, P.W.M. Blom, J.C. Hummelen, M.T. Rispens, Cathode dependence of the open-circuit voltage of polymer : fullerene bulk heterojunction solar cells, J. Appl. Phys. 94 (2003) 6849–6854.

[93] C. Waldauf, M.C. Scharber, P. Schilinsky, J.A. Hauch, C.J. Brabec, Physics of organic bulk heterojunction devices for photovoltaic applications, J. Appl. Phys. 99 (2006) 104503.

[94] G. a. H. Wetzelaer, M. Kuik, M. Lenes, P.W.M. Blom, Origin of the dark-current ideality factor in polymer:fullerene bulk heterojunction solar cells, Appl. Phys. Lett. 99 (2011) 153506.

[95] R.A. Street, M. Schoendorf, A. Roy, J.H. Lee, Interface state recombination in organic solar cells, Phys. Rev. B. 81 (2010) 205307.

[96] S. M. Sze, Physics of semiconductor devices, Wiley-Interscience, 2007.

[97] J.-M. Liu, Photonic devices, Cambridge University Press, 2005.

[98] P. Bhattacharya, Semiconductor optoelectronic devices, Upper Saddle River, NJ: Prentice-Hall, 1997.

[99] S.F. Tedde, J. Kern, T. Sterzl, J. Fu, P. Lugli, O. Hayden, Fully spray coated organic photodiodes, Nano Lett. 9 (2009) 980–983.

[100] B. Arredondo, C. De Dios, R. Vergaz, a. R.R. Criado, B. Romero, B. Zimmermann, U. Würfel, C. de Dios, Performance of ITO-free inverted organic bulk heterojunction photodetectors: Comparison with standard device architecture, Org. Electron. 14 (2013) 2484–2490.

[101] Y. Huang, E.J. Kramer, A.J. Heeger, G.C. Bazan, Bulk heterojunction solar cells:

morphology and performance relationships., Chem. Rev. 114 (2014) 7006–7043.

[102] M.A. Ruderer, S. Guo, R. Meier, H.Y. Chiang, V. Körstgens, J. Wiedersich, J. Perlich, S. V. Roth, P. Müller-Buschbaum, Solvent-induced morphology in polymer-based systems for organic photovoltaics, Adv. Funct. Mater. 21 (2011) 3382–3391.

[103] J.J. Jasieniak, N.D. Treat, C.R. McNeill, B.J.T. de Villers, E. Della Gaspera, M.L. Chabinyc, Interfacial characteristics of efficient bulk heterojunction solar cells fabricated on MoOx anode interlayers, Adv. Mater. (2015) n/a-n/a.

[104] H.J. Park, M.G. Kang, S.H. Ahn, L.J. Guo, A facile route to polymer solar cells with optimum morphology readily applicable to a roll-to-roll process without sacrificing high device performance, Adv. Mater. 22 (2010) 247–253.

[105] M. Binda, A. Iacchetti, D. Natali, L. Beverina, M. Sassi, M. Sampietro, High detectivity squaraine-based near infrared photodetector with nA/cm2 dark current, Appl. Phys. Lett. 98 (2011) 73303.

[106] L. Xie, S. Yoon, Y.J. Cho, K. Kim, Effective protection of sequential solution-processed polymer/fullerene bilayer solar cell against charge recombination and degradation, Org. Electron. 25 (2015) 212–218.

[107] V.S. Gevaerts, L.J.A. Koster, M.M. Wienk, R. a J. Janssen, Discriminating between bilayer and bulk heterojunction polymer:fullerene solar cells using the external quantum efficiency., ACS Appl. Mater. Interfaces. 3 (2011) 3252–5.

[108] H. Kong, J. Sinha, D. Hoeft, S.B. Kirschner, D.H. Reich, H.E. Katz, Solution processable organic p-n junction bilayer vertical photodiodes, Org. Electron. Physics, Mater. Appl. 14 (2013) 703–710.

[109] X. Lin, J. Seok, S. Yoon, T. Kim, B. Kim, K. Kim, Morphological investigation of P3HT/PCBM heterojunction and its effects on the performance of bilayer organic solar cells, Synth. Met. 196 (2014) 145–150.

[110] A. Tada, Y. Geng, Q. Wei, K. Hashimoto, K. Tajima, Tailoring organic heterojunction interfaces in bilayer polymer photovoltaic devices., Nat. Mater. 10 (2011) 450–5.

[111] D. Chen, F. Liu, C. Wang, A. Nakahara, T.P. Russell, Bulk heterojunction photovoltaic active layers via bilayer interdiffusion, Nano Lett. 11 (2011) 2071–2078.

[112] H.W. Ro, B. Akgun, B.T. O'Connor, M. Hammond, R.J. Kline, C.R. Snyder, S.K. Satija, A.L. Ayzner, M.F. Toney, C.L. Soles, D.M. DeLongchamp, Poly(3-hexylthiophene) and [6,6]-phenyl-C61-butyric acid methyl ester mixing in organic solar cells, Macromolecules. 45 (2012) 6587–6599.

[113] D. Leman, M.A. Kelly, S. Ness, S. Engmann, A. Herzing, C. Snyder, H.W. Ro, R.J. Kline, D.M. DeLongchamp, L.J. Richter, In situ characterization of polymer–fullerene bilayer stability, Macromolecules. 48 (2015) 383–392.

[114] B.L. Chen, P. Degenaar, D.D.C. Bradley, Polymer transfer printing : Application to layer coating , pattern definition , and diode dark current blocking, Adv. Mater. 20 (2008) 1679–1683.

[115] N.D. Treat, M.A. Brady, G. Smith, M.F. Toney, E.J. Kramer, C.J. Hawker, M.L. Chabinyc, Interdiffusion of PCBM and P3HT reveals miscibility in a photovoltaically active blend, Adv. Energy Mater. 1 (2011) 82–89.

[116] Y. Xia, G.M. Whitesides, Soft lithography, Annu. Rev. Mater. Sci. 28 (1998) 153–184.

[117] Y. Zhou, C. Fuentes-Hernandez, J. Shim, J. Meyer, A.J. Giordano, H. Li, P. Winget, T. Papadopoulos, H. Cheun, J. Kim, M. Fenoll, A. Dindar, W. Haske, E. Najafabadi, T.M. Khan, H. Sojoudi, S. Barlow, S. Graham, J.-L. Brédas, S.R. Marder, A. Kahn, B. Kippelen, A universal method to produce low-work function electrodes for organic electronics., Science. 336 (2012) 327–32.

[118] H. Kim, K.-T. Lee, C. Zhao, L.J. Guo, J. Kanicki, Top illuminated organic photodetectors with dielectric/metal/dielectric transparent anode, Org. Electron. 20 (2015) 103–111.

[119] H.-L. Yip, A.K.-Y. Jen, Recent advances in solution-processed interfacial materials for efficient and stable polymer solar cells, Energy Environ. Sci. 5 (2012) 5994.

[120] F. Arca, S.F. Tedde, M. Sramek, J. Rauh, P. Lugli, O. Hayden, Interface trap states in organic photodiodes., Sci. Rep. 3 (2013) 1324.

[121] S. Dongaonkar, J.D. Servaites, G.M. Ford, S. Loser, J. Moore, R.M. Gelfand, H. Mohseni, H.W. Hillhouse, R. Agrawal, M.A. Ratner, T.J. Marks, M.S. Lundstrom, M.A. Alam, Universality of non-ohmic shunt leakage in thin-film solar cells, J. Appl. Phys. 108 (2010) 124509.

[122] B.V. Popescu, D.H. Popescu, P. Lugli, S. Locci, F. Arca, S.F. Tedde, M. Sramek, O. Hayden, Modeling and simulation of organic photodetectors for low light intensity applications, IEEE Trans. Electron Devices. 60 (2013) 1975–1981.

[123] Robert F. Pierret, Semicondutor device fundamentals, Addison-Wesley, 1996.

[124] M. Mingebach, C. Deibel, V. Dyakonov, Built-in potential and validity of the Mott-Schottky analysis in organic bulk heterojunction solar cells, Phys. Rev. B - Condens. Matter Mater. Phys. 84 (2011) 1–4.

[125] P.P. Boix, M.M. Wienk, R.A.J. Janssen, G. Garcia-Belmonte, Open-circuit voltage limitation in low-bandgap diketopyrrolopyrrole-based polymer solar cells processed from different solvents, J. Phys. Chem. C. 115 (2011) 15075–15080.

[126] Y.-S.S. Cho, R.R. Franklin, Conducting polymer material characterization using high frequency planar transmission line measurement, Trans. Electr. Electron. Mater. 13 (2012) 237–240.

[127] F. Jahani, S. Torabi, R.C. Chiechi, L. Jan, A. Koster, J.C. Hummelen, Fullerene derivatives with increased dielectric constants., Chem. Commun. 50 (2014) 10645–7.

[128] J. Kanicki, ed., Amorphous and microcrystalline semiconductor devices: materials and device physics vol. 2., Artech House, 1992.

[129] D.K. Schroder, Semiconductor material and device characterization, John Wiley & Sons, 2006.

[130] J. Nakamura, Image sensors and signal processing for digital still cameras, Taylor & Francis, CRC Press, Inc., 2005.

[131] T.A.M. Ferenczi, J. Nelson, C. Belton, A.M. Ballantyne, M. Campoy-Quiles, F.M. Braun, D.D.C. Bradley, Planar heterojunction organic photovoltaic diodes via a novel stamp transfer process, J. Phys. Condens. Matter. 20 (2008) 475203.

[132] J.-H. Huang, Z.-Y. Ho, T.-H. Kuo, D. Kekuda, C.-W. Chu, K.-C. Ho, Fabrication of multilayer organic solar cells through a stamping technique, J. Mater. Chem. 19 (2009) 4077.

[133] B. Jung, K. Kim, J. Kim, S. Kim, E. Kim, W. Kim, Inter-diffused ordered bulk heterojunction organic photovoltaics: Optimized morphology for efficient exciton dissociation and charge transport, Sol. Energy Mater. Sol. Cells. 120 (2014) 675–684.

[134] J.Y. Oh, W.S. Jang, T. Il Lee, J.M. Myoung, H.K. Baik, Driving vertical phase separation in a bulk-heterojunction by inserting a poly(3-hexylthiophene) layer for highly efficient organic solar cells, Appl. Phys. Lett. 98 (2011) 1–4.

[135] M. Casalegno, D. Kotowski, A. Bernardi, S. Luzzati, R. Po, G. Raos, The effect of donor content on the efficiency of P3HT:PCBM bilayers: optical and photocurrent spectral data analyses, Phys. Chem. Chem. Phys. 17 (2015) 2447–2456.

[136] M.K. Wong, K.Y. Wong, Investigation of the factors affecting the power conversion efficiency of all-solution-processed "bilayer" P3HT:PCBM solar cells, Synth. Met. 170 (2013) 1–6.

[137] P.E. Shaw, A. Ruseckas, I.D.W. Samuel, Exciton diffusion measurements in poly(3-hexylthiophene), Adv. Mater. 20 (2008) 3516–3520.

[138] G.F. Burkhard, E.T. Hoke, S.R. Scully, M.D. McGehee, Incomplete exciton harvesting from fullerenes in bulk heterojunction solar cells, Nano Lett. 9 (2009) 4037–4041.

[139] H. Sirringhaus, P.J. Brown, R.H. Friend, M.M. Nielsen, Two-dimensional charge transport in self-organized, high-mobility conjugated polymers, (1999) 685–688.

[140] V. Shrotriya, J. Ouyang, R.J. Tseng, G. Li, Y. Yang, Absorption spectra modification in poly(3-hexylthiophene):methanofullerene blend thin films, Chem. Phys. Lett. 411 (2005) 138–143.

[141] J. Tauc, Amorphous and liquid semiconductors, Plenum Press, 1974.

[142] J. Xue, B.P. Rand, S. Uchida, S.R. Forrest, A hybrid planar-mixed molecular heterojunction photovoltaic cell, Adv. Mater. 17 (2005) 66–71.

[143] B.P. Rand, D.P. Burk, S.R. Forrest, Offset energies at organic semiconductor heterojunctions and their influence on the open-circuit voltage of thin-film solar cells, Phys. Rev. B - Condens. Matter Mater. Phys. 75 (2007) 1–11.

[144] D. Baierl, L. Pancheri, M. Schmidt, D. Stoppa, G.-F. Dalla Betta, G. Scarpa, P. Lugli, A hybrid CMOS-imager with a solution-processable polymer as photoactive layer, Nat. Commun. 3 (2012) 1175.

[145] D.S. Leem, K.H. Lee, K.B. Park, S.J. Lim, K.S. Kim, Y.W. Jin, S. Lee, Low dark current small molecule organic photodetectors with selective response to green light, Appl. Phys. Lett. 103 (2013).

[146] J. Kong, I.-W. Hwang, K. Lee, Top-down approach for nanophase reconstruction in bulk heterojunction solar cells, Adv. Mater. 26 (2014) 6275–6283.

[147] S.H. Liao, H.J. Jhuo, Y.S. Cheng, S.A. Chen, Fullerene derivative-doped zinc oxide nanofilm as the cathode of inverted polymer solar cells with low-bandgap polymer (PTB7-Th) for high performance, Adv. Mater. 25 (2013) 4766–4771.

[148] B.A.E. Courtright, S.A. Jenekhe, Polyethylenimine interfacial layers in inverted organic photovoltaic devices: effects of ethoxylation and molecular weight on efficiency and temporal stability, ACS Appl. Mater. Interfaces. 7 (2015) 26167–26175.

[149] J. Jeong, J. Seo, S. Nam, H. Han, H. Kim, T.D. Anthopoulos, D.D.C. Bradley, Y. Kim, Significant stability enhancement in high-efficiency polymer:fullerene bulk

heterojunction solar cells by blocking ultraviolet photons from solar light, Adv. Sci. (2015) 1500269.

[150] J.R. Manders, T.-H. Lai, Y. An, W. Xu, J. Lee, D.Y. Kim, G. Bosman, F. So, Low-noise multispectral photodetectors made from all solution-processed inorganic semiconductors, Adv. Funct. Mater. 24 (2014) 7205–7210.

[151] S. Valouch, C. Hönes, S.W. Kettlitz, N. Christ, H. Do, M.F.G. Klein, H. Kalt, A. Colsmann, U. Lemmer, Solution processed small molecule organic interfacial layers for low dark current polymer photodiodes, Org. Electron. 13 (2012) 2727–2732.

[152] E. Saracco, B. Bouthinon, J. Verilhac, C. Celle, N. Chevalier, D. Mariolle, O. Dhez, J. Simonato, Work function tuning for high-performance solution- processed organic photodetectors with inverted structure, (2013) 6534–6538.

[153] J.B. Johnson, Thermal agitation of electricity in conductors, Nature. 119 (1927) 50–51.

[154] P. Fuchs, A. Paracchino, H. Hagendorfer, L. Kranz, T. Geiger, Y.E. Romanyuk, A.N. Tiwari, F. Nüesch, Indium-free PTB7/PC71BM polymer solar cells with solution-processed Al:ZnO electrodes on PET substrates, Int. J. Photoenergy. 2016 (2016) 1–6.

[155] Quality control datasheet, catalog number : ZP-007, Solarmer Energy, Inc, (n.d.).

[156] M. Hoheisel, Review of X-ray detectors for medical imaging, (n.d.).

[157] A. Rogalski, Infrared detectors: status and trends, Prog. Quantum Electron. 27 (2003) 59–210.

[158] I.K. Kim, B.N. Pal, M. Ullah, P.L. Burn, S.-C. Lo, P. Meredith, E.B. Namdas, High-performance, solution-processed non-polymeric organic photodiodes, Adv. Opt. Mater. 3 (2014) n/a-n/a.

[159] Y. Fang, F. Guo, Z. Xiao, J. Huang, Large gain, low noise nanocomposite ultraviolet photodetectors with a linear dynamic range of 120 dB, Adv. Opt. Mater. 2 (2014) 348–353.

[160] H.J. Park, H. Kim, J.Y. Lee, T. Lee, L.J. Guo, Optimization of polymer photovoltaic cells with bulk heterojunction layers hundreds of nanometers thick: modifying the morphology and cathode interface, Energy Environ. Sci. 6 (2013) 2203.

[161] B. Qi, J. Wang, Fill factor in organic solar cells., Phys. Chem. Chem. Phys. 15 (2013) 8972–82.

[162] L.P. Lee, L.P. Lee, R. Szema, Inspirations from biological optics for advanced photonic systems, Science (80-.). 1148 (2010) 1148–1151.

[163] S.-B. Rim, P.B. Catrysse, R. Dinyari, K. Huang, P. Peumans, The optical advantages of curved focal plane arrays, Opt. Express. 16 (2008) 4965.

[164] H.-C. Jin, J.R. Abelson, M.K. Erhardt, R.G. Nuzzo, Soft lithographic fabrication of an image sensor array on a curved substrate, J. Vac. Sci. Technol. B Microelectron. Nanom. Struct. 22 (2004) 2548.

[165] G. Yoo, T. Fung, D. Radtke, M. Stumpf, U. Zeitner, J. Kanicki, Hemispherical thin-film transistor passive pixel sensors, Sensors Actuators A Phys. 158 (2010) 280–283.

[166] G. Yoo, H. Lee, D. Radtke, M. Stumpf, U. Zeitner, J. Kanicki, A maskless laser-write lithography processing of thin-film transistors on a hemispherical surface, Microelectron. Eng. 87 (2010) 83–87.

[167] E. Allen, S. Triantaphillidou, The manual of photography (tenth edition), Tenth Edit, Elsevier, 2011.

[168] www.pcworld.idg.com.au/review/canon/eos_m_interchangeable_lens_camera_preview /431375, (n.d.).

[169] J.M. Geary, Introduction to lens design : with practical ZEMAX examples, Willmann-Bell, Willmann-Bell Richmond, 2002.

[170] M.J. Kidger, Fundamental optical design, SPIE, 2001.

[171] K. Itonaga, T. Arimura, K. Matsumoto, G. Kondo, K. Terahata, S. Makimoto, M. Baba, Y. Honda, S. Bori, T. Kai, K. Kasahara, M. Nagano, M. Kimura, Y. Kinoshita, E. Kishida, T. Baba, S. Baba, Y. Nomura, N. Tanabe, N. Kimizuka, Y. Matoba, T. Takachi, E. Takagi, T. Haruta, N. Ikebe, K. Matsuda, T. Niimi, T. Ezaki, T. Hirayama, A novel curved CMOS image sensor integrated with imaging system, in: 2014 Symp. VLSI Technol. Dig. Tech. Pap., IEEE, 2014: pp. 1–2.

[172] R. Dinyari, J.D. Loudin, P. Huie, D. Palanker, P. Peumans, A curvable silicon retinal implant, Tech. Dig. - Int. Electron Devices Meet. IEDM. (2009) 595–598.

[173] D. Dumas, M. Fendler, N. Baier, J. Primot, E. le Coarer, Curved focal plane detector array for wide field cameras, Appl. Opt. 51 (2012) 5419.

[174] S.R. Forrest, X. Xu, C.K. Renshaw, M. Hack, J. Brown, A 10×10 all-organic passive pixel sensor array, 2010 IEEE Photinic Soc. 23rd Annu. Meet. (2010) 369–370.

[175] X. Xu, M. Mihnev, A. Taylor, S.R. Forrest, Organic photodetector arrays with indium tin oxide electrodes patterned using directly transferred metal masks, Appl. Phys. Lett. 94 (2009) 9–12.

[176] H.C. Ko, M.P. Stoykovich, J. Song, V. Malyarchuk, W.M. Choi, C.-J. Yu, J.B. Geddes III, J. Xiao, S. Wang, Y. Huang, J.A. Rogers, A hemispherical electronic eye camera based on compressible silicon optoelectronics., Nature. 454 (2008) 748–53.

[177] T.F. O'Connor, A. V. Zaretski, B. a. Shiravi, S. Savagatrup, A.D. Printz, M.I. Diaz, D.J. Lipomi, Stretching and conformal bonding of organic solar cells to hemispherical surfaces, Energy Environ. Sci. 7 (2014) 370.

[178] K.E. Paul, M. Prentiss, G.M. Whitesides, Patterning spherical surfaces at the two-hundred-nanometer scale using soft lithography, Adv. Funct. Mater. 13 (2003) 259–263.

[179] J. Huang, P.F. Miller, J.S. Wilson, A.J. de Mello, J.C. de Mello, D.D.C. Bradley, Investigation of the effects of doping and post-deposition treatments on the conductivity, morphology, and work function of poly(3,4-ethylenedioxythiophene)/poly(styrene sulfonate) films, Adv. Funct. Mater. 15 (2005) 290–296.

[180] K. Takechi, M. Nakata, T. Eguchi, H. Yamaguchi, S. Kaneko, Temperature-dependent transfer characteristics of amorphous InGaZnO4 thin-film transistors, Jpn. J. Appl. Phys. 48 (2009).

[181] W.M. Choi, O.O. Park, A soft-imprint technique for direct fabrication of submicron scale patterns using a surface-modified PDMS mold, Microelectron. Eng. 70 (2003) 131–136.

[182] P. Ruchhoeft, M. Colburn, B. Choi, H. Nounu, S. Johnson, T. Bailey, S. Damle, M. Stewart, J. Ekerdt, S. V. Sreenivasan, J.C. Wolfe, C.G. Willson, Patterning curved

surfaces: Template generation by ion beam proximity lithography and relief transfer by step and flash imprint lithography, J. Vac. Sci. Technol. B Microelectron. Nanom. Struct. Process. Meas. Phenom. (1999).

[183] M. Vaezi, H. Seitz, S. Yang, A review on 3D micro-additive manufacturing technologies, Int. J. Adv. Manuf. Technol. 67 (2013) 1721–1754.

[184] D.I. Wimpenny, P.M. Pandey, L.J. Kumar, Advances in 3D printing & additive manufacturing technologies, 2017.

[185] T.J. Snyder, M. Andrews, M. Weislogel, P. Moeck, J. Stone-Sundberg, D. Birkes, M.P. Hoffert, A. Lindeman, J. Morrill, O. Fercak, S. Friedman, J. Gunderson, A. Ha, J. McCollister, Y.K. Chen, J. Geile, A. Wollman, B. Attari, N. Botnen, V. Vuppuluri, J. Shim, W. Kaminsky, D. Adams, J. Graft, 3D systems' technology overview and new applications in manufacturing, engineering, science, and education, 3d Print. Addit. Manuf. 1 (2014) 169–176.

[186] C. Duty, Additive manufacturing, Siemens. (2013).

[187] K. Ikuta, S. Maruo, S. Kojima, New micro stereo lithography for freely movable 3D micro structure-super IH process with submicron resolution, MEMS 98. Proceedings., Elev. Annu. Int. Work. (1998) 290–295.

[188] 3D Systems, ProJet® 3500 SD & HD professional 3D printers, 2014.

[189] M.J. Yaffe, J.A. Rowlands, X-ray detectors for digital radiography, Phys. Med. Biol. 42 (1997) 1–39.

[190] A.C. Konstantinidis, M.B. Szafraniec, R.D. Speller, A. Olivo, The Dexela 2923 CMOS X-ray detector: A flat panel detector based on CMOS active pixel sensors for medical imaging applications, Nucl. Instruments Methods Phys. Res. Sect. A Accel. Spectrometers, Detect. Assoc. Equip. 689 (2012) 12–21.

[191] J.-P. Moy, Large area X-ray detectors based on amorphous silicon technology, Thin Solid Films. 337 (1999) 213–221.

[192] J.T. Rahnl, F. Lemmi, J.P. Lu, P. Meil, R.B. Apte, R.A. Street, R. Lujan, R.L. Weisfield, J.A. Heanue, High resolution x-ray imaging using amorphous silicon flat-panel arrays, IEEE Trans. Nucl. Sci. 46 (1999) 457–461.

[193] K.S. Karim, A. Nathan, S. Member, J.A. Rowlands, Amorphous silicon active pixel sensor readout circuit for digital imaging, IEEE Trans. Electron Devices. 50 (2003) 200–208.

[194] A. Nathan, B. Park, A. Sazonov, S. Tao, I. Chan, P. Servati, K. Karim, T. Charania, D. Striakhilev, Q. Ma, R.V.. Murthy, Amorphous silicon detector and thin film transistor technology for large-area imaging of X-rays, Microelectronics J. 31 (2000) 883–891.

[195] R.. Street, R.. Apte, T. Granberg, P. Mei, S.. Ready, K.. Shah, R.. Weisfield, High performance amorphous silicon image sensor arrays, J. Non. Cryst. Solids. 227–230 (1998) 1306–1310.

[196] R.L. Weisfield, W. Yao, T. Speaker, K. Zhou, R.E. Colbeth, C. Proano, Performance analysis of a 127-micron pixel large-area TFT/photodiode array with boosted fill factor, in: International Society for Optics and Photonics, 2004: p. 338.

[197] W. Zhao, W.G. Ji, A. Debrie, J. a. Rowlands, Imaging performance of amorphous selenium based flat-panel detectors for digital mammography: Characterization of a small area prototype detector, Med. Phys. 30 (2003) 254.

[198] R.L. Weisfield, N.R. Bennett, Electronic noise analysis of a 127-micron pixel TFT/photodiode array, Phys. Med. Imaging, Proc. SPIE. 4320 (2001) 209–218.

[199] A. Nathan, S. Lee, S. Jeon, J. Robertson, Amorphous oxide semiconductor TFTs for displays and imaging, J. Disp. Technol. 10 (2014) 917–927.

[200] T. Sakai, H. Seo, S. Aihara, M. Kubota, N. Egami, D. Wang, M. Furuta, A 128x96 pixel, 50 µm pixel pitch transparent readout circuit using amorphous In–Ga–Zn–O thin-film transistor array with indium–tin oxide electrodes for an organic image sensor, Jpn. J. Appl. Phys. 51 (2012) 10202.

[201] S. Jeon, S. Park, I. Song, J.-H. Hur, J. Park, H. Kim, S. Kim, S. Kim, H. Yin, U. Chung, E. Lee, C. Kim, Nanometer-scale oxide thin film transistor with potential for high-density image sensor applications, ACS Appl. Mater. Interfaces. 3 (2011) 1–6.

[202] F. De Roose, K. Myny, S. Steudel, M. Willigems, S. Smout, T. Piessens, J. Genoe, W. Dehaene, A flexible thin-film pixel array with a charge-to-current gain of 59µA/pC and 0.33% nonlinearity and a cost effective readout circuit for large-area X-ray imaging, in: Dig. Tech. Pap. - IEEE Int. Solid-State Circuits Conf., IEEE, 2016: pp. 296–297.

[203] M. Nakata, C. Zhao, J. Kanicki, DC sputtered amorphous In–Sn–Zn–O thin-film transistors: Electrical properties and stability, Solid. State. Electron. 116 (2016) 22–29.

[204] J.L. Junho Song, Jun Hyung Lim, Byung Du Ahn, High mobility oxide TFTs for future LCD applications, SID 2013 Dig. 10.3 (2013) 93–96.

[205] E. Fukumoto, T. Arai, N. Morosawa, K. Tokunaga, Y. Terai, T. Fujimori, T. Sasaoka, High-mobility oxide TFT for circuit integration of AMOLEDs, J. Soc. Inf. Disp. 19 (2011) 867.

[206] M.K. Ryu, S. Yang, S.-H.K. Park, C.-S. Hwang, J.K. Jeong, Impact of Sn/Zn ratio on the gate bias and temperature-induced instability of Zn-In-Sn-O thin film transistors, Appl. Phys. Lett. 95 (2009) 173508.

[207] M.K. Ryu, S. Yang, S.-H.K. Park, C.-S. Hwang, J.K. Jeong, High performance thin film transistor with cosputtered amorphous Zn–In–Sn–O channel: Combinatorial approach, Appl. Phys. Lett. 95 (2009) 72104.

[208] W.-H. Tseng, S.-W. Fang, C.-Y. Lu, H.-Y. Chuang, F.-W. Chang, G.-Y. Lin, T.-W. Chen, K.-H. Ma, H.-S. Chen, T.-K. Chen, Y.-H. Chen, J.-Y. Lee, T.-H. Shih, H.-C. Ting, C.-Y. Chen, Y.-H. Lin, H.-J. Hong, The effect of nitrous oxide plasma treatment on the bias temperature stress of metal oxide thin film transistors with high mobility, Solid. State. Electron. 103 (2015) 173–177.

[209] M.-H. Cheng, C. Zhao, C.-L. Huang, H. Kim, M. Nakata, J. Kanicki, Amorphous InSnZnO thin-film transistor voltage-mode active pixel sensor circuits for indirect X-ray imagers, IEEE Trans. Electron Devices. 63 (2016) 1–9;

[210] H.C. Slade, Device and material characterization and analytic modeling of amorphous silicon thin film transistors, Univ. Virginia, Charlottesville, VA, 1997.

[211] F. De Roose, S. Steudel, P.E. Malinowski, K. Myny, A. Xhakoni, G. Gielen, J. Genoe, W. Dehaene, Active pixel concepts for high-resolution large area imagers, in: Int. Image Sens. Soc., International Image Sensor Society, 2015: pp. 139–141.

[212] C. Henn, Application Bulletin : Comparison of noise performance between a FET transimpedance amplifier and a switched integrator, Burr-Brown Corp. GmbH. 3197 (1994) 1–4.

[213] ACF2010 datasheet : low noise , dual switched integrator, in: Burr-Brown Corp. GmbH, 1990.

[214] https://www.hamamatsu.com/resources/pdf/ssd/charge_amp_kacc9001e.pdf, (n.d.).

[215] M. Massarotto, A. Carlosena, A.J. Lopez-Martin, Two-stage differential charge and transresistance amplifiers, IEEE Trans. Instrum. Meas. 57 (2008) 309–320.

[216] H. Rödjegård, A. Lööf, A differential charge-transfer readout circuit for multiple output capacitive sensors, Sensors Actuators A Phys. 119 (2005) 309–315.

[217] O. Oliaei, Noise analysis of correlated double sampling sc integrators with a hold capacitor, IEEE Trans. Circuits Syst. I Fundam. Theory Appl. 50 (2003) 1198–1202.

[218] H.M. Wey, W. Guggenbuhl, An improved correlated double sampling circuit for low noise charge coupled devices, IEEE Trans. Circuits Syst. 37 (1990) 1559–1565.

[219] C.C. Enz, G.C. Temes, Circuit techniques for reducing the effects of op-amp imperfections: autozeroing, correlated double sampling, and chopper stabilization, Proc. IEEE. 84 (1996) 1584–1614.

[220] L.B. Oliveira, C.M. Leitao, M.M. Silva, Noise performance of a regulated cascode transimpedance amplifier for radiation detectors, IEEE Trans. Circuits Syst. I Regul. Pap. 59 (2012) 1841–1848.

[221] K. Iniewski, Electronics for radiation detection, CRC Press, 2011.

[222] L.J. Kozlowski, Low-noise capacitive transimpedance amplifier performance versus alternative IR detector interface schemes in submicron CMOS, in: E.R. Fossum (Ed.), International Society for Optics and Photonics, 1996: pp. 2–11.

[223] G. Gurun, P. Hasler, F.L. Degertekin, Front-end receiver electronics for high-frequency monolithic CMUT-on-CMOS imaging arrays, IEEE Trans. Ultrason. Ferroelectr. Freq. Control. 58 (2011) 1658–1668.

[224] A. Basu, R.W. Robucci, P.E. Hasler, A low-power, compact, adaptive logarithmic transimpedance amplifier operating over seven decades of current, IEEE Trans. Circuits Syst. I Regul. Pap. 54 (2007) 2167–2177.

[225] K. Ogawa, E.L. Chinnock, GaAs f.e.t. transimpedance front-end design for a wideband optical receiver, Electron. Lett. 15 (1979) 650.

[226] A. Bhat, Application note : stabilize your transimpedance amplifier, in: Maxim Integr., 2012.

[227] E. Sackinger, The transimpedance limit, IEEE Trans. Circuits Syst. I Regul. Pap. 57 (2010) 1848–1856.

[228] S. Takada, M. Ihama, M. Inuiya, T. Komatsu, T. Saito, CMOS color image sensor with overlaid organic photoconductive layers having narrow absorption band, Proc. SPIE. 6502 (2007) 1–11.

[229] A.S. Sedra, K.C. Smith, Microelectronic circuits, Oxford University Press, 1998.

[230] M. Bissonnette, M. Hansroul, E. Masson, S. Savard, S. Cadieux, P. Warmoes, D. Gravel, J. Agopyan, B. Polischuk, W. Haerer, T. Mertelmeier, J.Y. Lo, Y. Chen, J.T. Dobbins III, J.L. Jesneck, S. Singh, Digital breast tomosynthesis using an amorphous selenium flat panel detector, in: M.J. Flynn (Ed.), Med. Imaging. Int. Soc. Opt. Photonics, International Society for Optics and Photonics, 2005: p. 529.

[231] C. Zhao, A.C. Konstantinidis, Y. Zheng, T. Anaxagoras, R.D. Speller, J. Kanicki, 50 μm pixel pitch wafer-scale CMOS active pixel sensor x-ray detector for digital breast tomosynthesis, Phys. Med. Biol. 60 (2015) 8977–9001.

[232] P. Dalgaard, Introductory statistics with R., Springer Science & Business Media, 2008.

[233] R. Zhang, L. Bie, T.-C. Fung, E.K.-H. Yu, C. Zhao, J. Kanicki, High performance amorphous metal-oxide semiconductors thin-film passive and active pixel sensors, 2013 IEEE Int. Electron Devices Meet. 4 (2013) 27.3.1-27.3.4.

[234] A. Cheknane, H.S. Hilal, F. Djeffal, B. Benyoucef, J.-P. Charles, An equivalent circuit approach to organic solar cell modelling, Microelectronics J. 39 (2008) 1173–1180.

[235] J.D. Servaites, S. Yeganeh, T.J. Marks, M.A. Ratner, Efficiency enhancement in organic photovoltaic cells: consequences of optimizing series resistance, Adv. Funct. Mater. 20 (2010) 97–104.

[236] S. Choi, W.J. Potscavage, B. Kippelen, Area-scaling of organic solar cells, J. Appl. Phys. 106 (2009) 54507.

[237] F.C. Krebs, M. Jørgensen, K. Norrman, O. Hagemann, J. Alstrup, T.D. Nielsen, J. Fyenbo, K. Larsen, J. Kristensen, A complete process for production of flexible large area polymer solar cells entirely using screen printing—First public demonstration, Sol. Energy Mater. Sol. Cells. 93 (2009) 422–441.

[238] D. Angmo, M. Hösel, F.C. Krebs, All solution processing of ITO-free organic solar cell modules directly on barrier foil, Sol. Energy Mater. Sol. Cells. 107 (2012) 329–336.

[239] P. Kuang, J.-M. Park, W. Leung, R.C. Mahadevapuram, K.S. Nalwa, T.-G. Kim, S. Chaudhary, K.-M. Ho, K. Constant, A new architecture for transparent electrodes: relieving the trade-off between electrical conductivity and optical transmittance., Adv. Mater. 23 (2011) 2469–73.

[240] C. Lungenschmied, G. Dennler, H. Neugebauer, S.N. Sariciftci, M. Glatthaar, T. Meyer, A. Meyer, Flexible, long-lived, large-area, organic solar cells, Sol. Energy Mater. Sol. Cells. 91 (2007) 379–384.

[241] M.-G. Kang, M.-S. Kim, J. Kim, L.J. Guo, Organic solar cells using nanoimprinted transparent metal electrodes, Adv. Mater. 20 (2008) 4408–4413.

[242] M.-G. Kang, H. Joon Park, S. Hyun Ahn, L. Jay Guo, Transparent Cu nanowire mesh electrode on flexible substrates fabricated by transfer printing and its application in organic solar cells, 2010.

[243] K.M. O'Malley, C.-Z. Li, H. Yip, A.K.-Y. Jen, Enhanced open-circuit voltage in high performance polymer/fullerene bulk-heterojunction solar cells by cathode modification with a C60 surfactant, Adv. Energy Mater. 2 (2012) 82–86.

[244] J.D. Servaites, M. a. Ratner, T.J. Marks, Organic solar cells: A new look at traditional models, Energy Environ. Sci. 4 (2011) 4410.

[245] W.-I. Jeong, J. Lee, S.-Y. Park, J.-W. Kang, J.-J. Kim, Reduction of collection efficiency of charge carriers with increasing cell size in polymer bulk heterojunction solar cells, Adv. Funct. Mater. 21 (2011) 343–347.

[246] A.K. Pandey, J.M. Nunzi, B. Ratier, A. Moliton, Size effect on organic optoelectronics devices: Example of photovoltaic cell efficiency, Phys. Lett. A. 372 (2008) 1333–1336.

[247] H. Jin, A. Pivrikas, K.H. Lee, M. Aljada, M. Hambsch, P.L. Burn, P. Meredith, Factors

influencing the efficiency of current collection in large area, monolithic organic solar cells, Adv. Energy Mater. 2 (2012) 1338–1342.

[248] A. Manor, E. a. Katz, T. Tromholt, B. Hirsch, F.C. Krebs, Origin of size effect on efficiency of organic photovoltaics, J. Appl. Phys. 109 (2011) 74508.

[249] S. Dongaonkar, Y. Karthik, D. Wang, M. Frei, S. Mahapatra, S. Member, M.A. Alam, On the nature of shunt leakage in amorphous silicon p-i-n solar cells, 31 (2010) 1266–1268.

[250] Y.-K. Liao, S.-Y. Kuo, M.-Y. Hsieh, F.-I. Lai, M.-H. Kao, S.-J. Cheng, D.-W. Chiou, T.-P. Hsieh, H.-C. Kuo, A look into the origin of shunt leakage current of Cu(In,Ga)Se2 solar cells via experimental and simulation methods, Sol. Energy Mater. Sol. Cells. 117 (2013) 145–151.

[251] V. Karpov, A. Compaan, D. Shvydka, Random diode arrays and mesoscale physics of large-area semiconductor devices, Phys. Rev. B. 69 (2004) 45325.